

FLORIDA STATE UNIVERSITY
COLLEGE OF ARTS AND SCIENCES

PHOTOPRODUCTION OF $K^0\bar{K}^0$ WITH THE GLUEX EXPERIMENT

By

GABRIEL A. RODRÍGUEZ LINERA

A Dissertation submitted to the
Department of Physics
in partial fulfillment of the
requirements for the degree of
Doctor of Philosophy

2024

Copyright © 2024 Gabriel A. Rodríguez Linera. All Rights Reserved.

Gabriel A. Rodríguez Linera defended this dissertation on 2024.
The members of the supervisory committee were:

Sean Dobbs
Professor Directing Dissertation

Martin Bauer
University Representative

Paul Eugenio
Committee Member

Simon Capstick
Committee Member

Mark Spieker
Committee Member

The Graduate School has verified and approved the above-named committee members, and certifies that the dissertation has been approved in accordance with university requirements.

ACKNOWLEDGMENTS

The number of people whom deserve to be acknowledged is to large to completely list. Know that I appreciate all of you not only in how you have formed me a physicist but, more importantly, how you have formed a part of my life. Thank you.

As this dissertation is the culmination of my time here at Florida State university I would like to first thank my adviser Dr. Sean Dobbs for his guidance and mentorship throughout all these years. I could not have accomplished what I have done without your guidance. I still remember the first time you told me to "ssh into scigrid" and wondering what "ssh" and "scigrid" are. I am pleased acknowledge that I now know what "ssh" and "scigrid" (and a lot more!) are. Non of this would have happened if not for the Bridge Program here at FSU, co-lead by Dr. Simon Capstick who is also one of my committee members and has been very helpful in understanding hadron physics through the years. This dissertation would also not be possible without the other members of my committee: Dr. Paul Eugenio, Dr. Mark Spieker, and Dr. Martin Bauer. It has been a pleasure to meet and interact with the rest of the physics faculty at FSU. Special mention goes to Dr. Volker Crede and Dr. Jorge Piekarewicz whom have been very supportive throughout the years. Thank you all.

I could not have done this without the support of my family in Puerto Rico, my new family in Switzerland, or my Tallahassee family. To my lovely wife Damaris, I love you and look forward to the rest of our lives together. A mi familia: mami, papi, Kenny, Ednita, madrina, Robbie y las nenas, Tío Paco, Titi Sheila y Ariana. Los quiero y los aprecio. One of the things I will continue to cherish for the rest of my life is the family I have made here in Tallahassee: Jesse, Chris, Edmundo, Lawrence, Donovan, Eli, Katerina, Dr. Mr. Person Benetti, Vignesh, Sahana, Gustavo, Ron, Mario, ... Like I said, to many people. I look forward to spending more time with my new Swiss family in the coming years.

TABLE OF CONTENTS

List of Tables	vii
List of Figures	viii
Abstract	xx
1 Introduction	1
1.1 The Standard Model of Particle Physics	1
1.2 Quantum Chromodynamics	1
1.3 The Constituent Quark Model	3
1.4 Lattice QCD	6
1.5 The Search for Hybrid Mesons	8
1.6 Glueball Hunting	9
1.7 Scattering Experiments and Regge Phenomenology	11
1.8 The $K\bar{K}$ Spectrum	13
1.9 Photoproduction and the GlueX Experiment	15
2 Previous Measurements and Theoretical Predictions	17
2.1 $\phi(1020)$ Photoproduction	17
2.1.1 High Energy Photoproduction	18
2.1.2 Low Energy Photoproduction	18
2.1.3 Theoretical Prediction at $E_\gamma \sim 8.5$ GeV	21
2.1.4 Summary	21
2.2 $K_S K_L$ Final State	23
2.2.1 Established Excited Vector Meson	23
2.2.2 $K_S K_L$ in e^+e^- Collisions	23
2.2.3 $K\bar{K}$ Photoproduction	24
2.2.4 The $\phi(2170)$	26
2.3 $K_S K_S$ Measurements	28
2.3.1 CLAS Collaboration	29
2.3.2 ZEUS Collaboration	30
2.3.3 BESIII Collaboration	30
2.3.4 JPAC Collaboration	31
3 The GlueX Experiment	34
3.1 The Photon Beam	34
3.1.1 Producing a tagged photon beam	35
3.1.2 Beam polarization and flux	37
3.2 GlueX Detector	39
3.2.1 Solenoid Magnet	40
3.2.2 Target and Start Counter	41
3.2.3 Charged Particle Reconstruction	41
3.2.4 Neutral Particle Reconstruction	43

3.2.5	Particle Identification	44
3.2.6	The DIRC detector	46
3.2.7	Trigger and Data Acquisition	47
4	Data Analysis	49
4.1	Overview	49
4.1.1	Datasets and Simulation	49
4.1.2	Beam energy and Mandelstam-t	50
4.1.3	Accidental Subtraction	52
4.1.4	Missing Mass	52
4.1.5	Kinematic Fitting	53
4.1.6	Flight Significance	54
4.1.7	Understanding Backgrounds with Monte Carlo	55
4.2	$\phi \rightarrow K_S K_L$ Event Selections	55
4.2.1	Mandelstam-t	56
4.2.2	Extra Tracks and Showers	56
4.2.3	Missing Mass	57
4.2.4	Flight Significance and χ^2/ndf	59
4.2.5	Background Studies with bggen	61
4.2.6	$\phi(1020)$ Data Sample	63
4.3	High Mass $K_S K_L$ Event Selections	63
4.3.1	Recoil Proton Vertex and RF-Time	64
4.3.2	Mandelstam-t	64
4.3.3	Extra Tracks and Showers	64
4.3.4	Flight Significance and χ^2/ndf	66
4.3.5	Missing and $\pi^+\pi^-$ Mass Distributions	69
4.3.6	Background Studies with bggen	69
4.3.7	$K_S K_L$ Data Sample	71
4.4	$K_S K_S$ Event Selections	71
4.4.1	Fiducial Event Selections	71
4.4.2	Mandelstam-t Distribution	72
4.4.3	Flight Significance and χ^2/ndf	72
4.4.4	$\pi^+\pi^-$ Invariant Mass Distribution	74
4.4.5	$K_S K_S$ Data Set	74
5	Theoretical Formalism	78
5.1	Coordinate System	79
5.2	Spin Density Matrix Elements	80
5.3	Partial Wave Analysis	84
5.4	The Dynamical Amplitude	86
6	$\phi(1020)$ Photoproduction	89
6.1	Spin Density Matrix Elements at GlueX	89
6.1.1	Methodology	89
6.1.2	Nominal Measurement	90

6.1.3	Bootstrap Uncertainties	90
6.1.4	Estimating Systematic Uncertainties: Event Selections	94
6.1.5	Estimating Systematic Uncertainties: Independent Data Sets	95
6.1.6	Estimating Systematic Uncertainties: Other Test	107
6.1.7	Summary of Systematic Studies	112
6.1.8	Final Result	112
6.1.9	Interpretation of $\phi(1020)$ Spin-Density Matrix Elements	116
6.2	Differential Cross Section at $E_\gamma = 8.2 - 8.8$ GeV	121
7	High Mass $K_S K_L$ Photoproduction	123
7.1	The One Dimensional $K_S K_L$ Invariant Mass Distribution	123
7.2	Partial Wave Analysis	127
7.2.1	Angular Distributions	127
7.2.2	Baryon Contributions	129
7.2.3	Methodology	129
7.2.4	Assuming Only Spin-1 Contributions	132
7.2.5	Exploring Spin-3 Contributions	133
8	$K_S K_S$ Photoproduction	142
8.1	The $K_S K_S$ Invariant Mass Distribution	142
8.2	Partial Wave Analysis	145
8.2.1	Angular Distributions and Baryon Contributions	145
8.2.2	Amplitude Analysis	146
9	Conclusion	154
Appendix		
A	Two Body Kinematics	157
B	Beam Polarization Parameters	159
C	Systematic tests of $\phi(1020)$ Spin-Density Matrix Elements	160
D	High Mass $K_S K_L$ Partial Wave Analysis	174
	References	192
	Biographical Sketch	200

LIST OF TABLES

1.1	Quantum numbers and names of conventional $q\bar{q}$ mesons.	5
2.1	$\phi(1020)$ SDME measurements by SLAC [1] and the Omega Photon Collaboration [2].	19
2.2	Established vector mesons below 2 GeV [3].	23
2.3	Resonances identified in J/ψ decays by the analysis of BESIII and JPAC.	32
4.1	Summary of datasets used for each analysis.	51
4.2	Summary of simulation samples. More details of the MCWrapper configuration can be found on the MCWrapper Records webpage.	51
4.3	Fraction of bggen events after nominal event selections in the range $0.99 < M(K_S K_L) < 1.075$ GeV.	61
4.4	List of nominal event selections for $\phi(1020) \rightarrow K_S K_L$	64
4.5	Fraction of bggen events after nominal event selections in the range $1.1 < M(K_S K_L) < 2.0$ GeV.	70
4.6	List of event selections for $K_S K_L$ events above $\phi(1020)$	72
4.7	List of event selections for $K_S K_S$ events.	76
6.1	Sources of systematic uncertainty which have been investigated.	116
7.1	(Above) List of well-established vector mesons and the PDG average for their mass and width [3]. (Below) Mass and width parameters were obtained from a fit to data for each model discussed in the text.	126
7.2	Mass and width for the third Breit-Wigner parameters obtained from fit to data using models 3 and 4 and parameters for $\phi(2170)$. One set of parameters is the PDG average [3] and the other set of parameters are those reported by the BESIII Collaboration in $K^+ K^-$ [4] and $K_S K_L$ [5] decays.	127
7.3	Percent contribution from each F-wave m-projection from a fit with all P-waves plus the indicated F-wave m-projection. The largest contributing waves account for 10% of the total intensity.	137
8.1	Parameters of the $a_2(1700)$ and $f_0(1710)$ taken from the PDG [6]. $BW_3^{J=0}$ is a part of the F_1 model.	144
B.1	Polarization angle luminosity and fraction of GlueX-I data for each run period.	159

LIST OF FIGURES

1.1	(Left) An illustration of The Standard Model of Particle Physics. The bottom left (green) boxes contain the leptons, and the top left (purple) boxes contain the quarks. The vertical column (red) displays all of the gauge bosons, responsible for mediating the fundamental forces. The far right (yellow) box contains the Higgs Boson. (Right) Several measurements of α_s as a function of the energy scale Q [3].	2
1.2	Depiction of different hadrons.	3
1.3	(Left) pseudoscalar (0^-) meson nonet and (right) vector (1^-) meson nonet. Vertical lines indicate the isospin projection, diagonal lines indicate the charge, and horizontal lines indicate the strangeness. Figure taken from Ref [7].	5
1.4	LQCD prediction for the light meson spectrum (green/black) isoscalar mesons and (blue) vector meson [8]. States with an orange outline can be interpreted as hybrid mesons. The three columns on the right are states with exotic J^{PC} quantum numbers. Dashed orange boxes have been drawn over the hybrid nonets.	7
1.5	Various predictions for the lightest scalar, tensor, and pseudoscalar glueball. The scalar glueball is consistently found to be the lightest. Figure is taken from Ref [9]. The reference numbers indicated on the legend refer to the reference numbers inside the original paper.	8
1.6	Coupled-channel fit performed by JPAC [10] to the $\eta^{(\prime)}\pi^-$ P-wave ($J = 1$) spectrum published by the COMPASS Collaboration [11].	10
1.7	Partial wave analysis results of $J/\psi \rightarrow \gamma\eta\eta'$ from the BESIII Collaboration [12]. $\langle Y_l^0 \rangle$ corresponds to the parent particle with spin l	10
1.8	(Left) Diagram of a two body scattering process $1 + 2 \rightarrow 3 + 4$. (Right) Production of an intermediate state X in a t -channel exchange process followed by an n body decay of state X . Both figures have been taken from Ref. [7].	12
1.9	(Left) Chew-Frautschi plot for ground state mesons and the Pomeron [7]. (Right) The total cross section for hadronic, γp and $\gamma\gamma$ processes as a function of \sqrt{s} [3].	14
1.10	$K^0 - \bar{K}^0$ mixing due to the weak interaction [13].	15
1.11	Allowed meson decays to $K\bar{K}$ divided by $(I)J^{PC}$ and final state kaon pairs.	16
2.1	(Left) $\phi(1020)$ SDMEs as a function of $t - t_{min}$ in the Gottfried-Jackson frame. The beam energy range is $2.37 < E_\gamma < 2.77$ GeV. (Right) SDMEs as a function of beam energy in the Gottfried-Jackson frame with $t - t_{min} < -0.05$ GeV ² . Data in open circles comes from a previous LEPS measurement [14]. In both cases the red and	

	green curves are model calculations which included Pomeron, π and η exchange [15]. The difference between the two curves is the strength of the Pomeron coupling.	20
2.2	$\phi(1020)$ SDMEs measured by CLAS [16] (black points) and LEPS [14] (blue points) at 2 GeV beam energy in the Helicity frame.	20
2.3	JPAC model for Spin Density Matrix Elements of $\rho(770)$, $\omega(782)$, and $\phi(1020)$ pho- toproduction at $E_\gamma = 8.5$ GeV.	22
2.4	(Left) The $e^+e^- \rightarrow K_S K_L$ cross section measured by various experiments. (Middle) $e^+e^- \rightarrow K_S K_L$ events after event selections and background subtraction, BaBar data. (Right) Fitted cross sections measured by the BaBar Collaboration [17].	24
2.5	(Left) Photoproduction of K^+K^- at measured by the Omega Photo Collaboration [2]. (Right) Photoproduction of K^+K^- measured by the E401 Experiment [18].	25
2.6	K^+K^- invariant mass distribution measure by the FOCUS Collaboration [19].	27
2.7	(Left) $K^{*0}K_S$ and K^*K mass distributions measured by FOCUS. No evidence for a resonances around 1.7 GeV was found [19]. (Right) Relative cross section of $\phi(1020)$ to $K^+K^-(1750)$ (referred to as $X(1750)$ in the text).	27
2.8	(Left) $e^+e^- \rightarrow \phi(1020)\pi^+\pi^-$ cross section as a function of center of mass energy mea- sured by (black) Belle and (green) Babar [20]. (Right) The $\phi(1020)\pi^+\pi^-$ differential cross section measured by GlueX [21].	28
2.9	(Left) Photoproduction of a hadron X produced in a t-channel exchange as could be seen by GlueX and CLAS. (Middle) Production of a hadron X in ep collider via a virtual photon as could be seen by ZEUS. (Right) Radiative decay of J/ψ as could be seen by BESIII.	28
2.10	(Top) Invariant mass spectrum of $K_S K_S$ published by CLAS[22]. (Bottom) Monte Carlo simulation of pure S-wave (right) and D-wave (left) with the CLAS detector.	29
2.11	Invariant mass distribution of $K_S K_S$ published by ZEUS [23].	31
2.12	Comparison of mass dependent (MD) and mass independent (MI) analysis by the BESIII Collaboration[24]. The MD results are shown in solid black line while solid black markers and open red markers are ambiguous solutions for the MI analysis.	32
2.13	Coupled-channel fit by JPAC[25] to $J/\psi \rightarrow \gamma\pi^0\pi^0/\gamma K_S K_S$ BESIII [26, 24] data.	33
3.1	Schematic image of CEBAF and the four halls housed at Jefferson Lab.	35
3.2	Diagram of the Hall D photon production beamline.	35
3.3	Schematic diagram of the tagger system.	36

3.4	(Top) Photon flux as a function of beam energy for PARA (0/90°) and PERP (−45/45°) diamond orientations and for the aluminum radiator. (Bottom) Polarization fraction as a function of beam energy for PARA nad PERP diamond orientations, the aluminum radiator produces an unpolarized photon beam. An increase in the photon flux is seen where the polarization fraction is enhanced. We refer to the beam energy range between 8.2–8.8 GeV as the coherent peak.	38
3.5	Schematic of the Pair Spectrometer. Figure taken from Ref. [27].	39
3.6	Schematic of the GlueX beamline and spectrometer.	40
3.7	Liquid hydrogen target cell. Dimensions are in mm.	41
3.8	(Left) Picture of CDC before completion. (Right) Diagram of each CDC layer, straws parallel to the beam line are shown in black, straws with +6° stereo angle are shown in red and straws with −6° stereo angle are shown in blue. Figures taken from Ref.[28].	42
3.9	(Left) Picture of the fully assembled FDC. (Right) Rendition of one FDC chamber. From top to bottom: upstream cathode, wire frame, downstream cathode and ground plane that separates the chambers.	42
3.10	Three dimensional rendition of the BCAL. Figure taken from Ref. [29].	44
3.11	(Left) Picture of the FCAL inside Hall D. (Right) Components of an FCAL block.	45
3.12	Start Counter and target. The photon beam exits through the conically shaped end of the SC, see Ref. [30].	45
3.13	(Left) Picture of TOF being lifted into place. (Right) Velocity vs. momentum of positively charged tracks. Bands correspond to e^+ , π^+ , K^+ and p for the TOF detector.	46
3.14	(Left) Picture of the installed DIRC detector, figure taken from Ref. [31]. (Right) Log-likelihood difference distribution for 4000 π/K events with 3.5 GeV momentum. The π/K separation is at a 3σ level. Figure taken from Ref. [32].	47
3.15	Schematic data acquisition system for GlueX [33].	48
4.1	Diagram of reactions of interest. (Left) A photon incident on a stationary proton (p) interact producing a recoil proton (p') and two K_S particles at the production vertex (red circle). K_S particles travel some distance before decaying to a $\pi^+\pi^-$ pair, producing a detached vertex. (Right) A photon incident on a stationary proton produces a recoil proton, a K_S and a K_L at the production vertex. The K_L is not detected and the K_S again decays to a $\pi^+\pi^-$ pair.	50
4.2	(Left) Kinematic fit χ^2 distribution for simulated channels with and without a K_S in the final state. (Right) Flight Significance for simulated data with and without a K_S in the final state.	55

4.3	Mandelstam-t distribution for data (black) and scaled Monte Carlo (red) after all event selections. The Mandelstam-t distribution was modeled as e^{-bt} with $b = 4.4 \text{ GeV}^{-2}$	56
4.4	(Left) Number of unused charged tracks and (right) number of unused neutral showers for simulated $K_S K_L p$ and $K_S K_S p$ events.	57
4.5	Same as Figure 4.4 with (left) at most two unused neutral showers and (right) zero extra charged tracks.	58
4.6	(Left) Number of unused tracks for data (black) and MC (red) are in good agreement after event selections. (Right) Number of unused showers for data (black) and MC (red) after event selections. This variable is not well modeled in MC but we will see evidence that this does not strongly affect the angular distributions. In both cases, the shaded green area indicates the selection that will be placed on the data.	58
4.7	Missing mass for GLUEX-I data (black) compared to Monte Carlo (red) after all event selections. Vertical lines indicate the selection placed on this variable which removes 6.5% of the data.	59
4.8	(Left) χ^2/ndf distribution for GlueX-I data (black) and Monte Carlo data (red). A vertical line indicates the selection that will be placed on the data. (Right) Flight Significance distribution for GlueX-I (black) and Monte Carlo (red). The shaded green area indicates the selection that will be placed on the data.	60
4.9	(Left) Fit to the $\pi^+\pi^-$ invariant mass spectrum with Eq. 4.11. The shaded green area indicated a 2σ window around the mean. This plot includes events with $M(K_S K_L) < 1.1 \text{ GeV}$. (Right) $\pi^+\pi^-$ invariant mass for GlueX-I data (black) and Monte Carlo (red) after cuts. This plot includes the event selection $1.005 < M(K_S K_L) < 1.04 \text{ GeV}$ and shows that background is negligible inside the $\phi(1020)$ region.	61
4.10	Purity, yield, statistical significance and signal-to-background as a function of selecting on Flight Significance for various χ^2/ndf selections.	62
4.11	Stacked histogram of invariant mass for all topologies after relevant event selections in Table 4.4. The left plot is in a linear scale while the right plot is in a log-y scale.	62
4.12	$K_S K_L$ invariant mass distribution after nominal events selections for GlueX-I (black points) and Monte Carlo (red points). The shaded green area indicates the nominal selection for measuring the Spin Density Matrix Elements.	63
4.13	$K_S K_L$ invariant mass distribution with the event selections listed in Table 4.4.	65
4.14	(Left) The RF time spectrum. The green shaded area are in-time events and the violet shaded area are out-of-time events which are used for accidental subtraction. (Right) Recoil proton z-vertex.	65

4.15	(Left) $-t$ distribution for signal events (black points) and $\pi\pi$ sideband events (shaded red). Below the dashed vertical line at 0.2 GeV^2 the data is dominated by background events. (Middle) $-t$ distribution for bggen data divided by topology. Low $-t$ events are dominated by topologies with no K_S in the topology. (Right) $-t$ distribution for data and MC.	66
4.16	Number of unused tracks for (left) bggen data separated by topology and (right) data/MC comparison.	66
4.17	Number of unused showers for (left) bggen data separated by topology and (right) data/MC comparison.	67
4.18	(Left) χ^2/ndf distribution for GLUEX-I data (black) and Monte Carlo data (red). A vertical line indicates the selection that will be placed on the data. (Right) Flight Significance distribution for GLUEX-I (black) and Monte Carlo (red). The shaded green area indicates the selection that will be placed on the data.	67
4.19	Purity, yield, statistical significance and signal to background as a function of selecting on Flight Significance for various χ^2/ndf selections.	68
4.20	(Left) Data and scaled MC for the missing mass distribution. Vertical lines and green shaded area indicate the selection of the data. (Right) Data and scaled MC for the $\pi^+\pi^-$ invariant mass distribution. Solid vertical lines indicate the signal region and dashed vertical lines indicate the sideband regions.	69
4.21	$K_S K_L$ invariant mass distribution from bggen MC divided by topology.	70
4.22	(Black) $K_S K_L$ invariant mass distribution after all event selections and sideband subtraction. (Red) Reconstruction efficiency as a function of $K_S K_L$ invariant mass. . . .	71
4.23	(Top left) RF time spectrum. The green shaded area are in-time events and the violet shaded area are out-of-time events. (Top right) Recoil proton z-vertex. (Bottom) Missing mass squared distribution and solid vertical lines indicate the selection of the data.	73
4.24	Mandelstam-t distribution for data (black) and MC (red). Data shows a change in slope at $-t \approx 0.4 \text{ GeV}^2$ which may indicate a change in the dominant production mechanism.	73
4.25	(Left) χ^2/ndf distribution for GlueX-I data (black) and Monte Carlo data (red). A vertical line indicates the selection that will be placed on the data. (Right) Flight Significance distribution for GlueX-I (black) and Monte Carlo (red). The shaded green area indicates the selection that will be placed on the data.	74
4.26	Purity, yield, statistical significance and signal to background as a function of selecting on Flight Significance of K_S^1 (FS^1) for various selections on the Flight Significance of K_S^2 (FS^2) selections with $\chi^2/ndf = 4.2$	75

4.27	(Left) One dimensional $\pi^+\pi^-$ invariant mass distribution fitted with Eq. 4.11. The red line is the total fit while the blue and black lines are the signal and background, respectively. (Right) Two-dimensional $\pi^+\pi^-$ invariant mass distribution. The green circle indicates the signal region and has a radius of 2σ . The red circles indicate the sideband region. The inner red circle has a radius of 4σ and the outer red circle has a radius $\sqrt{24}\sigma$. The radius of the outermost red circle was chosen to make the signal and background areas equal.	76
4.28	$K_S K_S$ invariant mass distribution. Structure is observed at threshold, ~ 1.25 GeV, ~ 1.5 GeV and ~ 1.7 GeV. Known states that may contribute are included with iso-scalars ($f_{0/2}$) in blue and iso-vectors ($a_{0/2}$) in red.	77
5.1	(Left) t -channel production of an intermediate state X in a t -channel exchange process followed by an n body decay of state X . This figure has been taken from Ref. [7]. (Right) Definition of the angles in the helicity frame. The reaction plane xz , containing the momenta of the photon beam (γ), the nucleon target (p), and the recoiling nucleon (p'), is in blue. θ and ϕ are the polar and azimuthal angles of the η . The polarization vector of the photon forms an angle Φ with the reaction plane. Figure is taken from Ref. [34].	79
5.2	(Left) Modulus square of the Breit-Wigner amplitude (Eq. 5.48) for various ℓ , mass $m_0 = 1.3$ GeV, and width $\Gamma_0 = 0.1$ GeV. (Right) Modulus square of Flatté amplitude (Eq. 5.51) with mass $m_0 = 0.980$ GeV, $g_i = g_{\eta\pi} = 0.353$ GeV and $g_i = g_2 = g_{K\bar{K}} = 0.311$ GeV.	87
6.1	Spin Density Matrix Elements for $\phi(1020) \rightarrow K_S K_L$. Only statistical uncertainties obtained from MINUIT are shown.	91
6.2	Distribution of SDMEs for 500 bootstrap iterations for the first $-t$ bin ($-t \approx 0.15$ GeV ²).	92
6.3	SDMEs with uncertainties obtained from MINUIT and using the bootstrap method. The mean value for both distributions is obtained from MINUIT.	93
6.4	Distributions for all event selections after nominal cuts (excluding the plotted variable). Solid vertical lines indicate the nominal selection and dashed vertical lines indicate variations that are tested.	95
6.5	Spin-Density Matrix Elements for the nominal data set and three variations on the $\pi^+\pi^-$ invariant mass selection.	96
6.6	Barlow significance test for each $\pi\pi$ invariant mass variation as a function of $-t$. Horizontal lines indicate $\pm 4\sigma_{Barlow}$	97
6.7	Spin-Density Matrix Elements as a function of $-t$ for lower/upper half of the $M(K_S K_L)$ distribution. The nominal results are drawn as a blue box. Only uncertainties from MINUIT are shown.	99

6.8	Pull for the lower/upper half of the $M(K_S K_L)$ distribution as a function of $-t$. Horizontal lines indicate $\pm 1\sigma$	100
6.9	Spin-Density Matrix Elements as a function of $-t$ in bins of photon beam energy. The nominal results are drawn as a blue box. Only uncertainties from MINUIT are shown.	101
6.10	Pull for each beam energy bin as a function of $-t$. Horizontal lines indicate $\pm 1\sigma$	102
6.11	Spin-Density Matrix Elements as a function of $-t$ for 0/90 and 45/−45 diamond orientations. The nominal results are drawn as a blue box. Only uncertainties from MINUIT are shown.	103
6.12	Pull distributions for 0/90 and 45/−45 diamond orientations as a function of $-t$. Horizontal lines indicate $\pm 1\sigma$	104
6.13	Spin-Density Matrix Elements as a function of $-t$ for each run period and full Phase-I data. The nominal results are drawn as a blue box. Only uncertainties from MINUIT are shown.	105
6.14	Pull for each run period as a function of $-t$. Horizontal lines indicate $\pm 1\sigma$	106
6.15	Spin-Density Matrix Elements as a function of $-t$ for GlueX-I and Spring 2020 data. The nominal results are drawn as a blue box. Only uncertainties from MINUIT are shown.	108
6.16	Pull for each run period as a function of $-t$. Horizontal lines indicate $\pm 1\sigma$	109
6.17	Spin-Density Matrix Elements as a function of $-t$ for polarization angle at the nominal value and offset by $\pm 1\sigma$. The nominal results are drawn as a blue box. Only uncertainties from MINUIT are shown.	110
6.18	Percent difference for polarization angle offset by $\pm 1\sigma$ as a function of $-t$. Horizontal lines indicate $\pm 1\sigma$	111
6.19	Spin-Density Matrix Elements as a function of $-t$ for an MC input-output test. Only uncertainties from MINUIT are shown. The ρ_{00}^0 term is systematically above the generated value. Fitting this term with a constant we find the offset to be by 0.0075 ± 0.0005	113
6.20	(Black) SDMEs with bootstrap uncertainties and (red) total systematic uncertainty.	114
6.21	Spin-Density Matrix Elements for photoproduction of $\phi(1020) \rightarrow K_S K_L$ at $E_\gamma = 8.2\text{--}8.8$. The plotted uncertainties correspond to statistical and systematic uncertainties added in quadrature. The JPAC model is shown in dashed blue lines. The solid horizontal indicates s-channel helicity conservation.	115
6.22	Combinations of $\phi(1020)$ SDMEs for (black points) GlueX measurement, (black line) SCHC and, (blue) JPAC model. All ρ^U combinations are consistent with zero indi-	

	cating a negligible contribution from unnatural parity exchange. The ρ^N terms show some structure: ρ_{11}^N and ρ_{00}^N are consistent with SCHC while ρ_{1-1}^N and ρ_{10}^N deviate from SCHC indicating the contribution of a natural parity exchange other than the Pomeron. The JPAC model deviates from SCHC due to π and η exchange which the data suggests are negligible.	118
6.23	Parity asymmetry of $\phi(1020)$ photoproduction for (black points) GlueX measurement, (black line) SCHC and, (blue) JPAC model. The GlueX measurement shows a fairly flat behavior which is systematically below $P_\sigma = 1$	119
6.24	Combinations of $\phi(1020)$ SDMEs for (black points) GlueX measurement, (black line) SCHC, and (blue) JPAC model.	120
6.25	Mandelstam-t distribution and reconstruction efficiency.	121
6.26	(Black) $\phi(1020)$ differential cross section and (red) fit to data with an exponential model. The integrated cross section in the $-t$ range 0.15–1.0 GeV ² is estimated to be 295.7 ± 0.4 nb.	122
7.1	(Black) $K_S K_L$ invariant mass spectrum and (red) efficiency.	123
7.2	(Left) Fit to data using model 1, see Eq 7.1. (Right) Fit to data using model 2, see Eq 7.2.	125
7.3	(Left) Fit to data using model 3, see Eq 7.3. (Right) Fit to data using model 4, see Eq 7.4.	125
7.4	Polar angle distributions for (left) $\ell = 1$ amplitudes and (right) $\ell = 3$ amplitudes. . . .	128
7.5	Acceptance corrected $K_S K_L$ invariant mass vs. (left) $\cos(\theta)$ and (right) ϕ in the Helicity frame.	128
7.6	(Top left) $K_L p$ invariant mass distribution, the peak near 1.75 GeV is possibly due to the $\Sigma^+(1775)$. (Top right) $K_S p$ invariant mass distribution, there is some structure below ~ 2.2 GeV but no clear sign of a Σ^+ contribution. (Bottom left) $\pi^+ p$ and (bottom right) $\pi^- p$ invariant mass distributions, no sign of a baryon contribution is observed in the mass spectrum.	130
7.7	Results for Partial Wave Analysis assuming only contributions from spin-1 resonances. Each panel shows the (point) total intensity and (crosses) the intensity of the indicated partial wave.	134
7.8	(Points) Total intensity, (red) positive reflectivity contribution, and (blue) negative reflectivity contribution for fit with all $\ell = 1$ amplitudes and no $\ell = 3$ amplitude. . . .	135
7.9	(Top left) Polar angle and (top right) azimuthal angle of K_S in the \mathcal{H} frame, (bottom left) polarization angle, and (bottom right) $\psi = \phi - \Phi$ angle. These angular distributions are for the first $K_S K_L$ invariant mass bin.	135

7.10	(Top left) Polar angle and (top right) azimuthal angle of K_S in the \mathcal{H} frame, (bottom left) polarization angle, and (bottom right) $\psi = \phi - \Phi$ angle. These angular distributions are for the ninth $K_S K_L$ invariant mass bin.	136
7.11	(Top left) Polar angle and (top right) azimuthal angle of K_S in the \mathcal{H} frame, (bottom left) polarization angle, and (bottom right) $\psi = \phi - \Phi$ angle. These angular distributions are for the twentieth $K_S K_L$ invariant mass bin.	136
7.12	(Top left) Polar angle and (top right) azimuthal angle of K_S in the \mathcal{H} frame, (bottom left) polarization angle, and (bottom right) $\psi = \phi - \Phi$ angle. These angular distributions are for the twenty-fourth $K_S K_L$ invariant mass bin.	137
7.13	(Top left) Polar angle and (top right) azimuthal angle of K_S in the \mathcal{H} frame, (bottom left) polarization angle, and (bottom right) $\psi = \phi - \Phi$ angle. These angular distributions are for the twenty-fourth $K_S K_L$ invariant mass bin. Three fits to data are shown: (violet) all P-wave amplitudes, (red) all P-wave and F_0^+ , and (blue) all P-wave and F_0^- . 138	
7.14	(Top left) Polar angle and (top right) azimuthal angle of K_S in the \mathcal{H} frame, (bottom left) polarization angle, and (bottom right) $\psi = \phi - \Phi$ angle. These angular distributions are for the twenty-fourth $K_S K_L$ invariant mass bin. Three fits to data are shown: (violet) all P-wave amplitudes, (red) all P-wave and F_3^+ , and (blue) all P-wave and F_3^- . 139	
7.15	(Top left) Polar angle and (top right) azimuthal angle of K_S in the \mathcal{H} frame, (bottom left) polarization angle, and (bottom right) $\psi = \phi - \Phi$ angle. These angular distributions are for the twenty-fourth $K_S K_L$ invariant mass bin. Three fits to data are shown: (violet) all P-wave amplitudes, (red) all P-wave and F_1^+ , and (blue) all P-wave and F_1^- . 140	
7.16	(Top left) Polar angle and (top right) azimuthal angle of K_S in the \mathcal{H} frame, (bottom left) polarization angle, and (bottom right) $\psi = \phi - \Phi$ angle. These angular distributions are for the twenty-fourth $K_S K_L$ invariant mass bin. Three fits to data are shown: (violet) all P-wave amplitudes, (red) all P-wave and F_2^+ , and (blue) all P-wave and F_2^- . 141	
8.1	$K_S K_S$ invariant mass spectrum in the coherent beam $E_\gamma = 8.2 - 8.8$ GeV and at $-t = 0.1 - 0.4$ GeV. Several well established (blue) iso-vector and (red) iso-scalar mesons that may decay to $K_S K_S$ are shown.	142
8.2	(Left) Fit to data with model F_1 . The mass and width of the third Breit-Wigner are 1.770 ± 0.006 GeV and 0.094 ± 0.012 GeV respectively. (Right) Fit to data with model F_2	144
8.3	(Left) Polar angle distribution for $\ell_m = 0_m = S_m$ and $\ell_m = 2_m = D_m$. (Right) Acceptance corrected distribution of $M(K_S K_S)$ vs. $\cos(\theta)$ in the Helicity system. . . .	145
8.4	(Left) $K_S p$ invariant mass distribution. The peak at ~ 1.7 GeV is due to a $\Sigma^+ \rightarrow K_S p$ possibly the $\Sigma^+(1775)$. (Right) $M(K_S K_S)$ vs. $\cos(\theta)$ in the Helicity system after removing events below 2.0 GeV in the $K_S p$ invariant mass.	146

8.5	PWA of the $K_S K_S$ system using the TMD wave-set. Each panel includes the (black) total intensity and the intensity for the indicated ℓ_m amplitude with (red) positive reflectivity and (blue) negative reflectivity.	148
8.6	PWA of the $K_S K_S$ system using the minimum reasonable wave-set. Each panel includes the (black) total intensity and the intensity for the indicated ℓ_m amplitude with (red) positive reflectivity and (blue) negative reflectivity.	149
8.7	Comparison of (violet) fit to (black) data with (left) the S_0^\pm and D_2^+ wave set and (right) the TMD wave set. (From top to bottom) Polar angle and azimuthal angle of K_S in the \mathcal{H} frame, polarization angle, and (bottom right) $\psi = \phi - \Phi$ angle. These results correspond to the 2 nd bin. The likelihoods obtained are ($S_0^\pm + D_2^+$) -5199 and (TMD) -5220.	150
8.8	Comparison of (violet) fit to (black) data with (left) the S_0^\pm and D_2^+ wave set and (right) the TMD wave set. (From top to bottom) Polar angle and azimuthal angle of K_S in the \mathcal{H} frame, polarization angle, and (bottom right) $\psi = \phi - \Phi$ angle. These results correspond to the 6 th bin. The likelihoods obtained are ($S_0^\pm + D_2^+$) -4508 and (TMD) -4526.	151
8.9	Comparison of (violet) fit to (black) data with (left) the S_0^\pm and D_2^+ wave set and (right) the TMD wave set. (From top to bottom) Polar angle and azimuthal angle of K_S in the \mathcal{H} frame, polarization angle, and (bottom right) $\psi = \phi - \Phi$ angle. These results correspond to the 11 th bin. The likelihoods obtained are ($S_0^\pm + D_2^+$) -3165 and (TMD) -3184.	152
8.10	Comparison of (violet) fit to (black) data with (left) the S_0^\pm and D_2^+ wave set and (right) the TMD wave set. (From top to bottom) Polar angle and azimuthal angle of K_S in the \mathcal{H} frame, polarization angle, and (bottom right) $\psi = \phi - \Phi$ angle. These results correspond to the 15 th bin. The likelihoods obtained are ($S_0^\pm + D_2^+$) -1644 and (TMD) -1659.	153
A.1	Diagram of a two body scattering process $1 + 2 \rightarrow 3 + 4$. Figure is taken from Ref. [7]	158
C.1	Spin-Density Matrix Elements for the nominal data set and three variations on the missing mass selection.	160
C.2	Barlow significance test for each missing mass variation as a function of $-t$. Horizontal lines indicate $\pm 4\sigma_{Barlow}$	161
C.3	Spin-Density Matrix Elements for the nominal data set and three variations on the $K_S K_L$ invariant mass selection.	162
C.4	Barlow significance test for each $K_S K_L$ invariant mass variation as a function of $-t$. Horizontal lines indicate $\pm 4\sigma_{Barlow}$	163
C.5	Spin-Density Matrix Elements for the nominal data set and three variations on the χ^2/ndf selection.	164

C.6	Barlow significance test for each χ^2/ndf variation as a function of $-t$. Horizontal lines indicate $\pm 4\sigma_{\text{Barlow}}$	165
C.7	Spin-Density Matrix Elements for the nominal data set and three variations on the FS selection.	166
C.8	Barlow significance test for each FS variation as a function of $-t$. Horizontal lines indicate $\pm 4\sigma_{\text{Barlow}}$	167
C.9	Spin-Density Matrix Elements for the nominal data set and three variations on the proton z-vertex selection.	168
C.10	Barlow significance test for each proton z-vertex variation as a function of $-t$. Horizontal lines indicate $\pm 4\sigma_{\text{Barlow}}$	169
C.11	Spin-Density Matrix Elements for the nominal data set and three variations on the number of unused tracks selection.	170
C.12	Barlow significance test for each number of unused tracks variation as a function of $-t$. Horizontal lines indicate $\pm 4\sigma_{\text{Barlow}}$	171
C.13	Spin-Density Matrix Elements for the nominal data set and three variations on the number of unused showers selection.	172
C.14	Barlow significance test for each number of unused showers variation as a function of $-t$. Horizontal lines indicate $\pm 4\sigma_{\text{Barlow}}$	173
D.1	Comparison of $\cos\theta$ in the helicity frame for (violet) fit to (black) data. The fit includes all $\ell = 1$ amplitudes but no $\ell = 3$ amplitudes.	174
D.2	Comparison of ϕ in the helicity frame for (violet) fit to (black) data. The fit includes all $\ell = 1$ amplitudes but no $\ell = 3$ amplitudes.	175
D.3	Comparison of Φ in the helicity frame for (violet) fit to (black) data. The fit includes all $\ell = 1$ amplitudes but no $\ell = 3$ amplitudes.	176
D.4	Comparison of $\Psi = \phi - \Phi$ in the helicity frame for (violet) fit to (black) data. The fit includes all $\ell = 1$ amplitudes but no $\ell = 3$ amplitudes.	177
D.5	Fit to data including all P-wave amplitudes and a F_0^+ amplitude. Points indicate the total intensity and crosses indicate the indicated partial wave.	178
D.6	Fit to data including all P-wave amplitudes and a F_0^- amplitude. Points indicate the total intensity and crosses indicate the indicated partial wave.	179
D.7	Fit to data including all P-wave amplitudes and a F_{-1}^+ amplitude. Points indicate the total intensity and crosses indicate the indicated partial wave.	180

D.8	Fit to data including all P-wave amplitudes and a F_{-1}^- amplitude. Points indicate the total intensity and crosses indicate the indicated partial wave.	181
D.9	Fit to data including all P-wave amplitudes and a F_1^+ amplitude. Points indicate the total intensity and crosses indicate the indicated partial wave.	182
D.10	Fit to data including all P-wave amplitudes and a F_1^- amplitude. Points indicate the total intensity and crosses indicate the indicated partial wave.	183
D.11	Fit to data including all P-wave amplitudes and a F_{-2}^+ amplitude. Points indicate the total intensity and crosses indicate the indicated partial wave.	184
D.12	Fit to data including all P-wave amplitudes and a F_{-2}^- amplitude. Points indicate the total intensity and crosses indicate the indicated partial wave.	185
D.13	Fit to data including all P-wave amplitudes and a F_2^+ amplitude. Points indicate the total intensity and crosses indicate the indicated partial wave.	186
D.14	Fit to data including all P-wave amplitudes and a F_2^- amplitude. Points indicate the total intensity and crosses indicate the indicated partial wave.	187
D.15	Fit to data including all P-wave amplitudes and a F_{-3}^+ amplitude. Points indicate the total intensity and crosses indicate the indicated partial wave.	188
D.16	Fit to data including all P-wave amplitudes and a F_{-3}^- amplitude. Points indicate the total intensity and crosses indicate the indicated partial wave.	189
D.17	Fit to data including all P-wave amplitudes and a F_3^+ amplitude. Points indicate the total intensity and crosses indicate the indicated partial wave.	190
D.18	Fit to data including all P-wave amplitudes and a F_3^- amplitude. Points indicate the total intensity and crosses indicate the indicated partial wave.	191

ABSTRACT

In this dissertation, we study photoproduction of $K^0\bar{K}^0$ through the $K_S K_L p$ and $K_S K_S p$ final states with the GlueX Phase-I (GlueX-I) data set. We measure the spin-density matrix elements (SDMEs) and differential cross section of $\phi(1020) \rightarrow K_S K_L$ to better understand photoproduction of light vector mesons. A mass independent Partial Wave Analysis (PWA) of the $K_S K_L$ and $K_S K_S$ meson spectrum below 2 GeV is also undertaken to study the meson spectrum with $\mathbf{J}^{PC} = \text{even}^{++}$ and odd^{--} .

The $\phi(1020)$ differential cross section is measured at $E_\gamma = 8.2 - 8.8$ GeV and $-t = 0.15 - 1.00$ GeV². The differential cross section is well described by an exponential decay with slope 4.44 ± 0.01 GeV⁻² and the integrated cross section is determined to be 295.7 ± 0.4 nb, only statistical uncertainties are quoted. Both measurements are consistent and far more precise than the previous measurement by Ballam et al. [1]. The $\phi(1020)$ SDMEs were measured in nine bins of $-t$ in the same range. At low $-t$, we find the data were consistent with s-channel helicity conservation, SCHC, i. e. the only non-zero SDMEs were $\rho_{1-1}^1 = -\text{Im}(\rho_{1-1}^2) = 1/2$. At higher $-t$, the SDMEs deviate from SCHC and the measurements indicate this is due to natural parity exchange since we observe that the SDMEs are consistent with zero unnatural exchange. We also find that the contribution from helicity double-flip amplitudes is consistent with zero. The measured SDMEs are in poor agreement with theoretical predictions put forward by JPAC [35]. These measurements will serve as input to refine models of production processes, which will be essential for the interpretation of possible signals of exotic mesons in GlueX.

Analysis of the spectrum above the $\phi(1020)$ indicates the presence of at least three particles at ~ 1.50 , ~ 1.75 , and 2.20 GeV. We employ simple parametrizations of the resonance line shape based on relativistic Breit-Wigner functions considering cases with and without interference. The resonance at ~ 1.50 GeV is not identified as any specific resonance, but could be due to interference between the $\rho(1450)$ and $\omega(1420)$. Our models favor the resonance at ~ 1.75 GeV as the $X(1750)$ rather than the $\phi(1680)$. We find that introducing a third Breit-Wigner into the models improves the fit quality with the χ^2/ndf going from 1.75 to 1.59 and 1.41 to 1.18 for models without and with interference respectively. A PWA of the $K_S K_L$ spectrum indicates that the spectrum is consistent with exclusively spin-1 contribution up to ~ 1.6 GeV. Above ~ 1.6 GeV we find evidence for a

small spin-3 contribution. We also find that the spectrum predominantly positive reflectivity up to ~ 1.6 GeV, after which the spectrum becomes a nearly equal mix of both.

The $K_S K_S$ system shows a rich spectrum with multiple resonance structures but is more statistically limited than the $K_S K_L$ system. Modelling the line shape we find evidence at greater than 10σ level in favor of a resonance at ~ 1.75 GeV. The model parameters suggest this resonance is the $f_0(1710)$. The PWA of the $K_S K_S$ system was inconclusive. However, using a small set of amplitudes suggests that the spin-2 contribution to the spectrum is primarily in the range $1.2 - 1.6$ GeV, where $f_2(1270)$, $a_2(1320)$ and $f'_2(1525)$ are expected.

CHAPTER 1

INTRODUCTION

1.1 The Standard Model of Particle Physics

The modern view of physics posits that there are four fundamental forces: gravity, electromagnetism, the weak force, and the strong force. The Standard Model (SM) of elementary particles, see Figure 1.1, describes all the smallest constituents of matter and the forces that govern their interactions, excluding gravity. Matter is composed of three generations of fermions, spin-half particles called quarks and leptons. Each generation has two quarks, one with electric charge $-\frac{1}{3}$ and another with $\frac{2}{3}$, and two leptons, one with electric charge -1 and another with 0 . The main difference between generations is the masses of the particles. The Higgs boson, a spin-0 particle, is responsible for giving mass to all fundamental particles. Forces are mediated by gauge bosons, spin-1 particles. The electromagnetic force is mediated by the photon (γ) and the weak force is mediated by the Z^0 and W^\pm bosons. These two forces are described by the electroweak theory. The final particle in the SM is the gluon (g) which is, like the photon, massless and has no electric charge. However, unlike the photon, gluons carry color charge and can therefore interact with other gluons. Only quarks and gluons interact through the strong force and the theory that describes this interaction is Quantum Chromodynamics.

1.2 Quantum Chromodynamics

Quantum Chromodynamics (QCD) is the theory of the strong force, which governs the interactions of quarks and gluons. QCD is a quantum field theory that falls under the category of non-abelian gauge theories, with symmetry group $SU_{\text{color}}(3)$. Color refers to the three types of “color charge” that quarks and gluons carry, hence the name chromodynamics. QCD exhibits three special features that are unique to the strong force: (1) color confinement, (2) asymptotic freedom, and (3) dynamic chiral symmetry breaking. Dynamic chiral symmetry breaking, and not the Higgs boson, accounts for more than 98% of visible matter in the Universe [36]. The running of the strong coupling constant, see Figure 1.1, $\alpha_S(Q^2)$, where Q is the momentum transfer

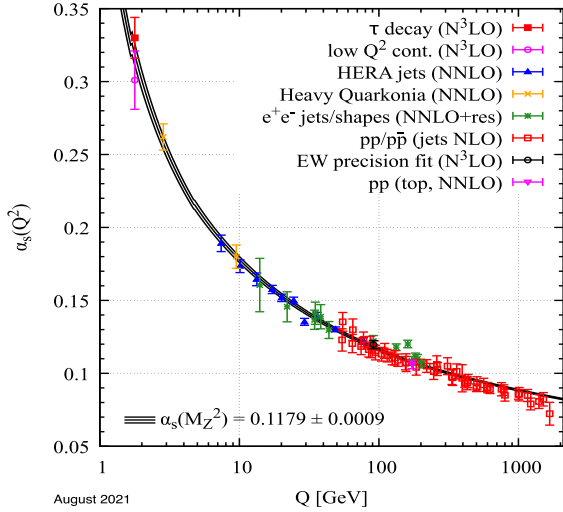
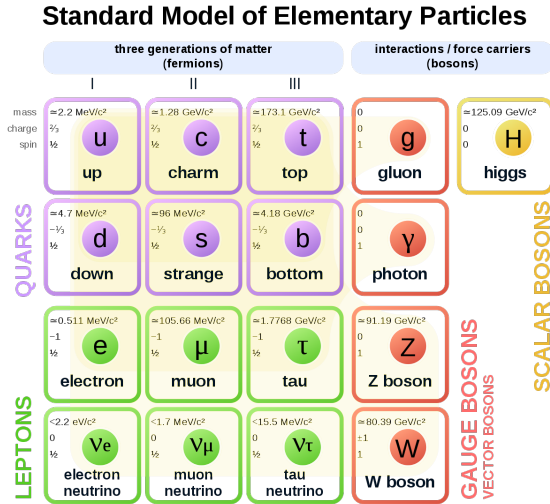


Figure 1.1: (Left) An illustration of The Standard Model of Particle Physics. The bottom left (green) boxes contain the leptons, and the top left (purple) boxes contain the quarks. The vertical column (red) displays all of the gauge bosons, responsible for mediating the fundamental forces. The far right (yellow) box contains the Higgs Boson. (Right) Several measurements of α_s as a function of the energy scale Q [3].

squared, encodes the underlying dynamics of hadron physics giving rise to color confinement and asymptotic freedom [37]. The phenomena of color confinement explain why quarks have not been observed as free particles in nature; instead, quarks are found inside color-neutral bound states called hadrons. Therefore, predictions of the hadron spectrum are an explicit and direct test of our understanding of the confinement mechanism as a result of the low energy dynamics of QCD [38]. Most well established hadrons can be classified as three quark states (qqq) called baryons, like the proton and neutron, or quark-antiquark ($q\bar{q}$) states called mesons. However, other kinds of states are consistent with QCD, such as hybrid mesons ($q\bar{q}g$) or glueballs (gg). Each of these hadrons is depicted in Figure 1.2. This dissertation contributes to the field of hadron spectroscopy, which aims to establish the existence and determine the properties of hadrons. In particular, we contribute to the study of (conventional) mesons, hybrid mesons, and glueballs.

At low- Q , the strong coupling α_s is no longer small, and perturbative calculations are no longer reliable. For this reason, multiple approximation schemes have been developed with varying degrees of rigor and success. Broadly speaking, these schemes can be divided into two classes: phenomenological (or model building) and Lattice QCD (LQCD). In Section 1.3 we will discuss the

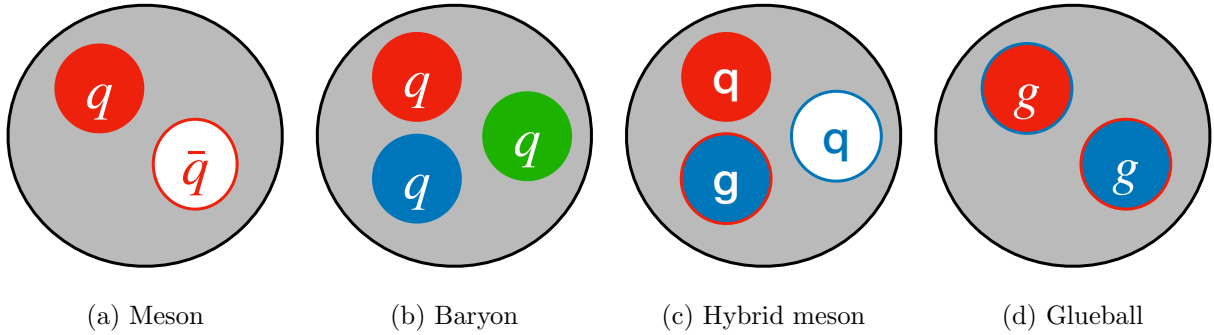


Figure 1.2: Depiction of different hadrons.

Constituent Quark Model (CQM) which, as the name suggests, is a phenomenological approach. Many variations fall under this name, we will discuss the general ideas that are central to the CQM. LQCD is a computational approach in which the full QCD theory is calculated in a discrete space-time lattice. We will discuss this approach in Section 1.4.

1.3 The Constituent Quark Model

The term quark model typically refers to a class of models that describes hadrons as composed of color-neutral bound states of quarks. In 1964 Murray Gell-Mann [39] and George Zweig [40] independently proposed that hadrons are formed by members of a flavor symmetry $SU_{\text{flavor}}(3)$. Following Gell-Mann we call them quarks, and the flavors are called up (u), down (d), and strange (s). This symmetry is not exact due to the different quark masses but has made a large number of very good predictions and provides a framework for classifying mesons and baryons [41].

In the quark model, mesons are bound states of a quark-antiquark ($q\bar{q}$) pair. The total spin of the system is thus $\mathbf{J} = \mathbf{S} \oplus \mathbf{L}$ where \mathbf{S} is the total spin, 0 or 1, and \mathbf{L} is the relative orbital angular momentum between the $q\bar{q}$ pair. For a given \mathbf{S} and \mathbf{L} , the total angular momentum can take the values $\mathbf{J} = |\mathbf{L} - \mathbf{S}|, |\mathbf{L} - \mathbf{S} + 1|, \dots, |\mathbf{L} + \mathbf{S}|$. The quantum numbers: parity (\mathbf{P}), charge conjugation (\mathbf{C}) and G-parity (\mathbf{G}) are conserved in strong decays and are related to \mathbf{S} and \mathbf{L} by the relations

$$P = (-1)^{L+1} \quad C = (-1)^{S+L} \quad G = (-1)^{S+L+1}. \quad (1.1)$$

States with $P = (-1)^J$ are called natural parity states and those with $P = (-1)^{J+1}$ are called unnatural parity states. Another important symmetry of the strong force is isospin (**I**). This is a symmetry of the u and d quarks which is nearly conserved in strong decays because $m_d - m_u \ll \Lambda_{QCD}$ [42]. Eq. 1.1 imply that the following \mathbf{J}^{PC} combinations are allowed

$$0^{-+}, 0^{++}, 1^{--}, 1^{+-}, 1^{-+}, 2^{--}, 2^{-+}, 2^{++}, 3^{--}, 3^{+-}, 3^{-+}, \dots$$

while the following are not

$$0^{--}, 0^{+-}, 1^{-+}, 2^{+-}, 3^{-+}, \dots$$

Mesons with the later quantum numbers are explicitly exotic mesons.

Since mesons are a $q\bar{q}$ pair we can form nine mesons with the same \mathbf{J}^{PC} . With the $SU_{\text{flavor}}(3)$ group we can build the nine mesons

$$\mathbf{3} \otimes \bar{\mathbf{3}} = \mathbf{1} \oplus \mathbf{8}.$$

The collection of nine mesons are called a nonet which is composed of an octet (**8**) and a singlet (**1**). Figures 1.3 show the pseudoscalar and vector nonets. The nonet has four isospin-1/2, three isospin-1 and two isospin-0 particles. Because $SU_{\text{flavor}}(3)$ is a broken symmetry, the two isospin-0 states of a nonet are not necessarily the physical states [41]. These two can mix to form the physical states we observe in nature. Following Ref. [3] we call the isospin-0 member of the octet and singlet ψ_8 and ψ_1 respectively with

$$\begin{aligned} \psi_8 &= \frac{1}{\sqrt{6}} (u\bar{u} + s\bar{s} - 2s\bar{s}) \\ \psi_1 &= \frac{1}{\sqrt{3}} (u\bar{u} + s\bar{s} + s\bar{s}) \end{aligned} \tag{1.2}$$

and the physical states are f and f' . These states are related by the mixing angle θ as

$$\begin{pmatrix} f' \\ f \end{pmatrix} = \begin{pmatrix} \cos(\theta) & \sin(\theta) \\ -\sin(\theta) & \cos(\theta) \end{pmatrix} \begin{pmatrix} \psi_8 \\ \psi_1 \end{pmatrix}. \tag{1.3}$$

The particles shown in Figure 1.3 are the physical states. In the case of ideal mixing f is pure $u\bar{u} + d\bar{d}$ and f' is pure $s\bar{s}$. This is nearly the case for $\omega(782)$ and $\phi(1020)$ with the later being nearly pure $s\bar{s}$. Members of a nonet are assigned names based on their \mathbf{IJ}^{PC} quantum number and whether they are mainly the singlet or octet member, see Table 1.1.

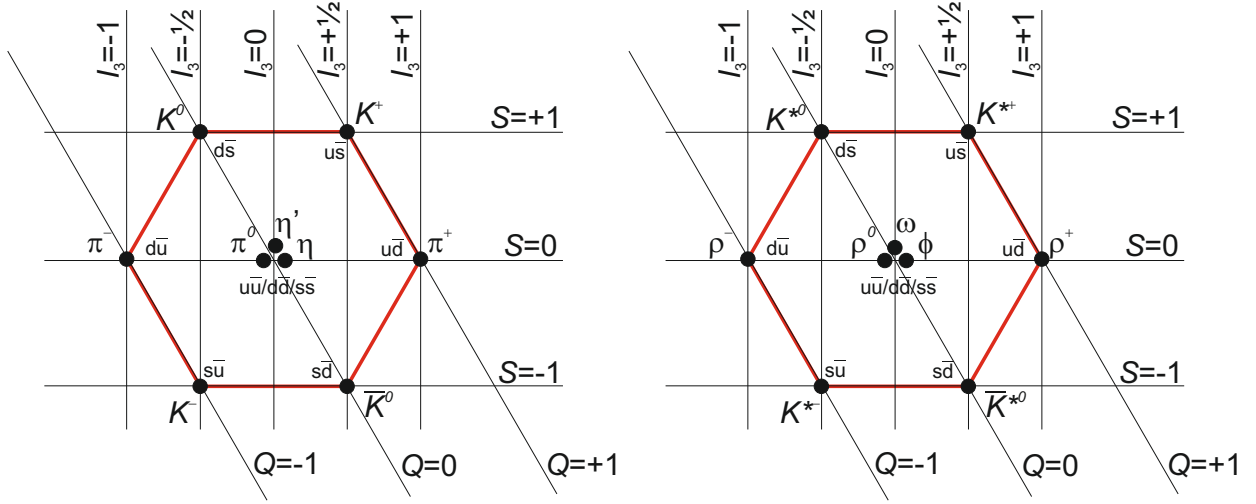


Figure 1.3: (Left) pseudoscalar (0^-) meson nonet and (right) vector (1^-) meson nonet. Vertical lines indicate the isospin projection, diagonal lines indicate the charge, and horizontal lines indicate the strangeness. Figure taken from Ref [7].

Table 1.1: Quantum numbers and names of conventional $q\bar{q}$ mesons.

		J^{PC}	$I = 1$	$I = 0 (n\bar{n})$	$I = 0 (s\bar{s})$	Strange ($n\bar{s}/\bar{n}s$)	Name
$L = 0$	$S = 0$	0^{-+}	π	η	η'	K	pseudoscalar
	$S = +1$	1^{--}	ρ	ω	ϕ	K^*	vector
$L = 1$	$S = 0$	1^{+-}	b_1	h	h'	K_1	pseudovector
	$S = 1$	0^{++}	a_0	f_0	f'_0	K_0^*	scalar
		1^{++}	a_1	f_1	f'_1	K_1	axial vector
		2^{++}	a_2	f_2	f'_2	K_2^*	tensor

1.4 Lattice QCD

Lattice QCD is presently the only available rigorous ab-initio method that can consistently describe the physics of binding and decay of hadrons [7]. Calculations are performed numerically using the full QCD theory on a discretized Euclidean space-time lattice. The lattice spacing a leads to a momentum cut-off proportional to $1/a$. Quark fields are placed at the lattice sites and gluon fields are located at the edges. The calculations are performed using Monte Carlo techniques that require large computational resources that are only available to supercomputers. Multiple approximations are used to reduce the cost of performing these computations. For example, many calculations use large u and d masses in order to reduce the number of quark-antiquark loops that are necessary in the calculations. Typically, the u and d masses used in calculations are expressed in terms of the pion mass¹. Three limits are taken after performing the calculation: the limit $a \rightarrow 0$, extend to infinite space-time volume, and extrapolate to the real u and d masses.

Many state-of-the-art LQCD calculations for ground state hadrons are performed at or close to the physical u and d quark masses. This reduces uncertainties introduced from extrapolations to real world conditions. For excited hadron resonances, calculations still need to be done at unphysical u and d quark masses. However, great progress has been made in calculations of the excited hadron spectrum. Figure 1.4 shows a LQCD calculation of the light meson spectrum [8] (excluding kaons). The scalar (0^{++}) mesons were not considered because of complications in interpreting the spectrum. For mesons with conventional J^{PC} quantum numbers, the spectrum is qualitatively similar to predictions from the CQM [7]. Additionally, four hybrid meson nonets are predicted, one nonet has explicitly exotic quantum numbers while three have conventional quantum numbers. This and other LQCD calculations are important inputs in the experimental search for hybrid mesons at GlueX.

LQCD techniques have been employed to study the glueball spectrum. Figure 1.5 shows several calculations for the lightest scalar 0^{++} , tensor 2^{++} , and pseudoscalar 0^{-+} glueballs [9]. Although the details of each calculation vary, a consistent trend emerges across them. The scalar glueball is the lightest with a mass around $1.3 - 2.0$ GeV, whereas the tensor and pseudoscalar glueballs are similar in mass and heavier than the scalar glueball. LQCD calculations dating back to 1990 [43]

¹The physical pion mass is ~ 140 MeV

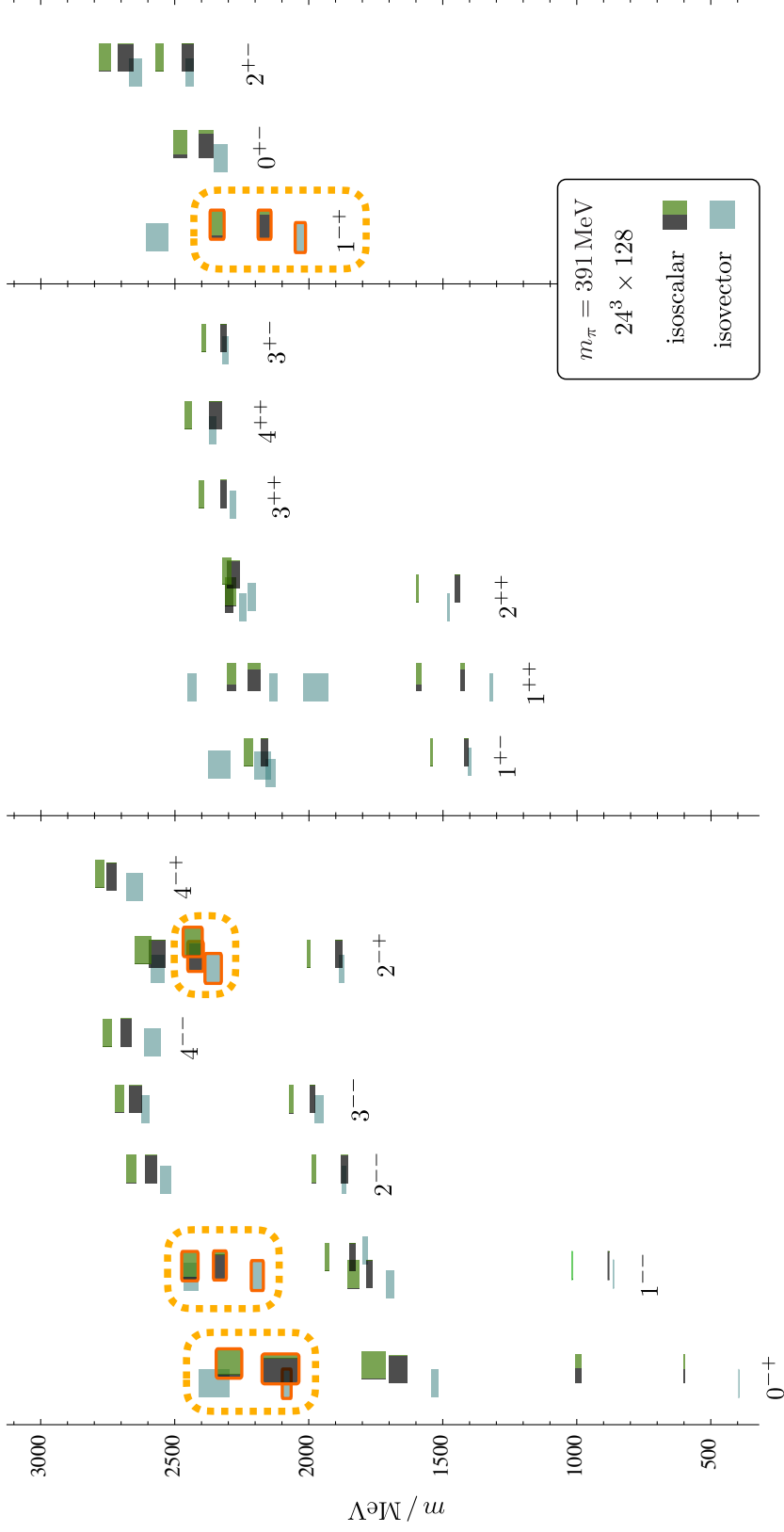


Figure 1.4: LQCD prediction for the light meson spectrum (green/black) isoscalar mesons and (blue) vector meson [8]. States with an orange outline can be interpreted as hybrid mesons. The three columns on the right are states with exotic J^{PC} quantum numbers. Dashed orange boxes have been drawn over the hybrid nonets.

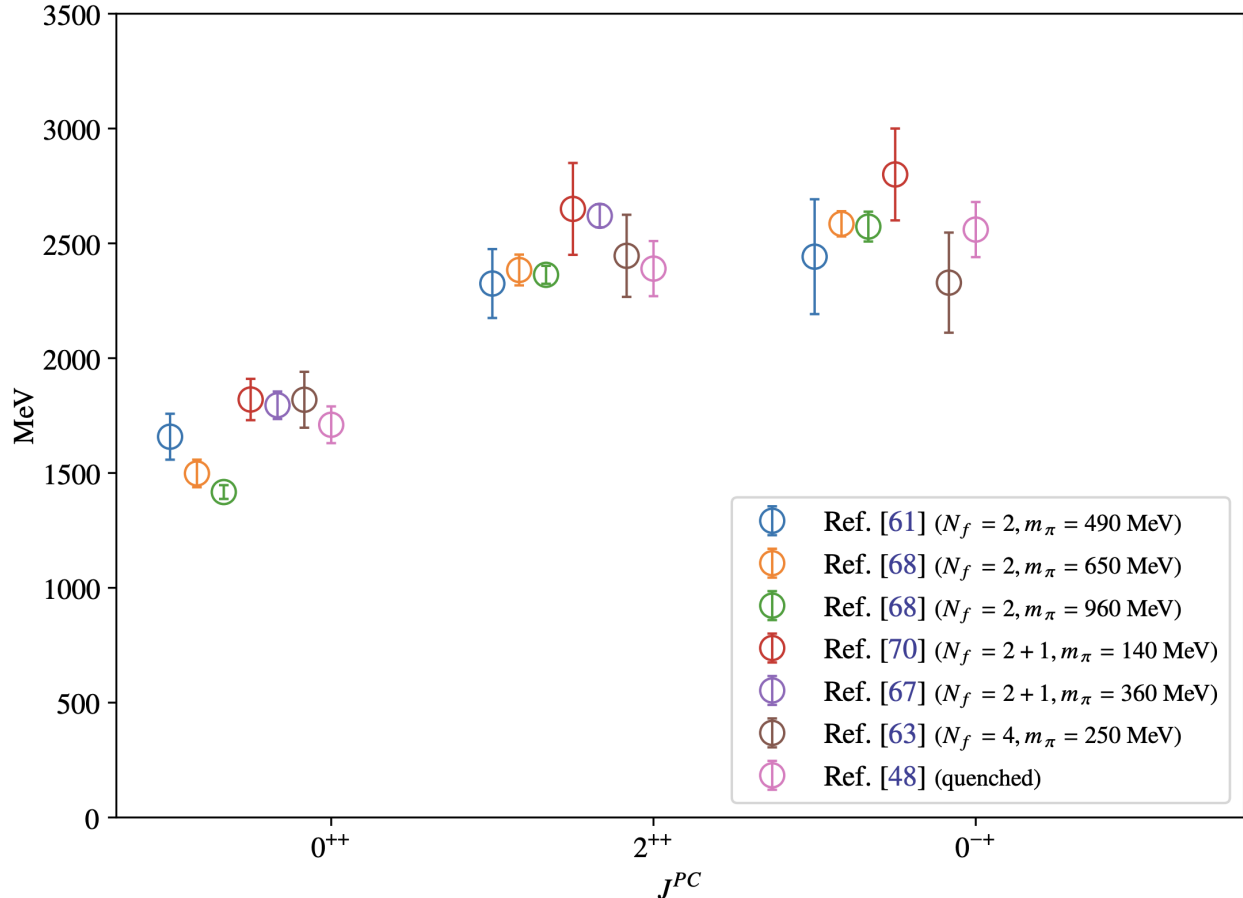


Figure 1.5: Various predictions for the lightest scalar, tensor, and pseudoscalar glueball. The scalar glueball is consistently found to be the lightest. Figure is taken from Ref [9]. The reference numbers indicated on the legend refer to the reference numbers inside the original paper.

have predicted that the scalar glueball is the lightest such state generating a great deal of interest for “glueball hunting” in the so-called scalar sector.

1.5 The Search for Hybrid Mesons

In the light meson sector, the search for hybrid mesons ($q\bar{q}g$ states) has focused on establishing the existence of states with explicitly exotic quantum numbers. Such states are prohibited by the CQM and are therefore smoking gun evidence for their non- $q\bar{q}$ microscopic nature. In recent years, promising evidence for the observation of two hybrid mesons with exotic quantum numbers has emerged. The COMPASS Collaboration studied the reactions $\pi^- p \rightarrow \eta^{(\prime)} \pi^- p$ [11]. The J^{PC}

quantum numbers accessible to the $\eta^{(\prime)}\pi$ system are: 0^{++} , 1^{-+} , 2^{++} , \dots where the 1^{-+} (i.e. a π_1) is not accessible to a $q\bar{q}$ state. The COMPASS paper included a Partial Wave Analysis in which the $\eta^{(\prime)}\pi$ mass spectrum was decomposed by spin contributions. A clear $J = 1$ contribution was observed in both reactions. However, a simple interpretation of the results suggested the existence of two mesons, a $\pi_1(1400) \rightarrow \eta\pi$ and a $\pi(1600) \rightarrow \eta'\pi$. A follow-up analysis by the Joint Physics Analysis Center (JPAC) performed a couple-channel analysis which was able to show that both reactions can be well modeled by a single pole, and therefore a single π_1 [10]. Another analysis used a K-matrix approach to model data from Crystal Barrel, COMPASS, and 11 different $\pi\pi$ scattering datasets and confirmed that the COMPASS data can be described with a single pole. The BESIII Collaboration observed a 1^{-+} isoscalar state in $J/\psi \rightarrow \gamma\eta\eta'$ [12]. Figure 1.7 shows the spin-0 and spin-1 components of the BESIII fit. The 1^{-+} isoscalar state was found to have a mass and width around 1.855 and 0.188 GeV, respectively, and a 19σ statistical significance. Whether this is the isoscalar from the octet or singlet (i.e. η_1 or η'_1) is an open question. In either case, it is natural to interpret this state as an isoscalar partner of the π_1 .

The observation of two hybrid mesons strengthens LQCD predictions of a hybrid nonet with $\mathbf{J}^{PC} = 1^{-+}$. Although the observed mesons are lighter than LQCD predicts. LQCD also predicts the existence of other hybrid nonets with conventional \mathbf{J}^{PC} quantum numbers. Establishing such states is more complicated since one would have to distinguish a hybrid meson from a conventional $q\bar{q}$ meson. The search could be made more complicated if the hybrid and $q\bar{q}$ states mix. Despite the challenge, the goal of the GlueX Experiment is to map the spectrum of hybrid mesons. Among the hybrid mesons with conventional quantum numbers, the 1^{--} hybrid mesons are the most promising since vector mesons are produced copiously.

1.6 Glueball Hunting

We review some aspects of glueball searches, for a more expansive review of the subject see Ref. [44]. The light meson scalar sector has attracted a lot of attention in the search for glueballs. Calculations consistently find the scalar glueball has a mass of 1.3 – 2.0 GeV while experimentally there is evidence for three isoscalar scalar (f_0) states². This situation is intriguing because the CQM can only accommodate two f_0 states with mass in the range 1.3 – 2.0. The combination of

²Glueballs are made purely of gluons and are therefore isoscalar, like for example, the f_0 mesons.

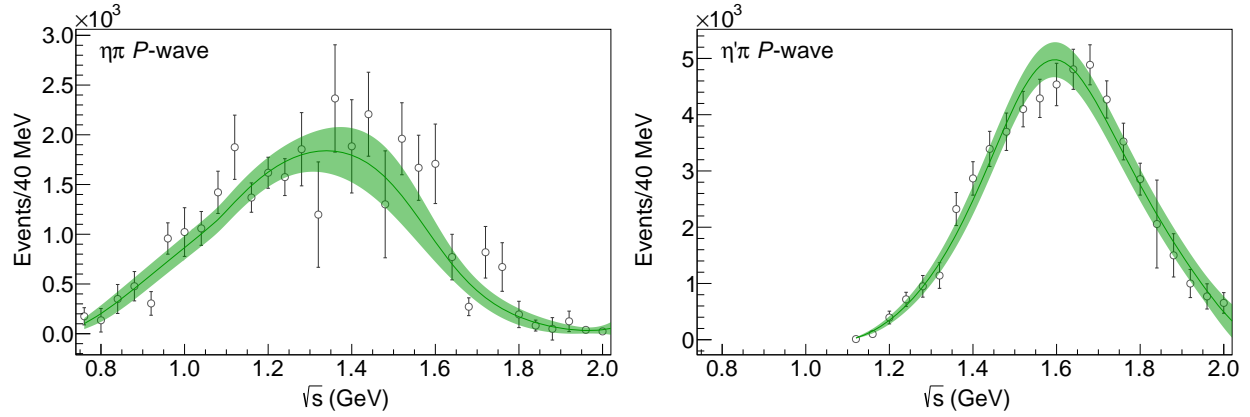


Figure 1.6: Coupled-channel fit performed by JPAC [10] to the $\eta^{(\prime)}\pi^-$ P-wave ($J = 1$) spectrum published by the COMPASS Collaboration [11].

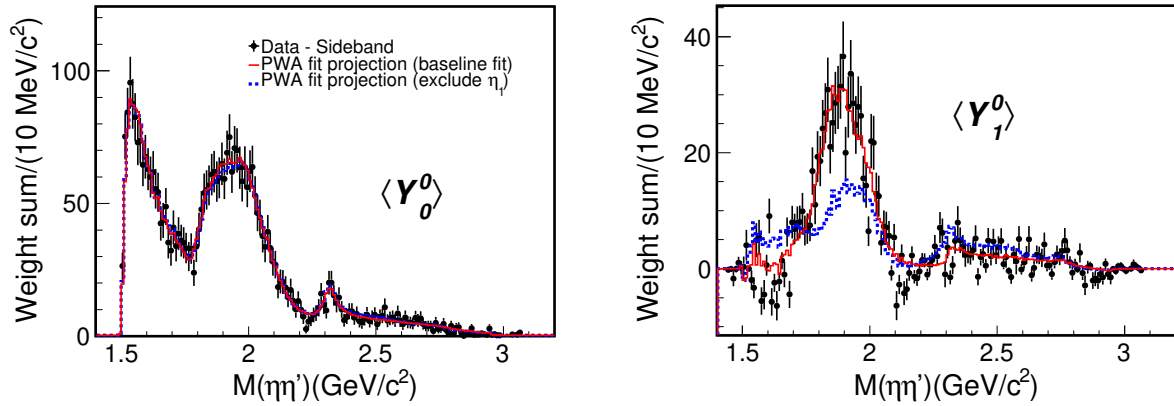


Figure 1.7: Partial wave analysis results of $J/\psi \rightarrow \gamma\eta\eta'$ from the BESIII Collaboration [12]. $\langle Y_l^0 \rangle$ corresponds to the parent particle with spin l .

a supernumeracy of f_0 states and an expected scalar glueball with similar mass has led to a great deal of speculation as to the nature of these states. Establishing the structure of the observed states has been very difficult in part because the $q\bar{q}$ states of the CQM and the glueball can mix and therefore one has to properly account for this mixing when interpreting the data. Historically, two pieces of information are used to establish the nature of the f_0 states: cross section in different production mechanisms and decay rates. Production mechanisms that generate the most interest are divided into “glue rich” (e.g. J/ψ radiative decays) and “glue poor” (e.g. $\gamma\gamma$ collisions). If one of the observed scalar states is produced copiously in J/ψ radiative decays but little in $\gamma\gamma$ collisions then that state is expected to either be a glueball or at least have a large glueball component in the wave function. Decay rates are an important piece of information because glueballs and the $q\bar{q}$ states of the CQM should have different decay patterns. For the CQM the decay rates depend on the quark content of the meson while glueballs are expected to have flavor-symmetric coupling to final state hadrons [45]. Glueball decays to two pseudoscalars are expected to follow the pattern

$$\Gamma(G \rightarrow \pi\pi : K\bar{K} : \eta\eta : \eta\eta' : \eta'\eta') = 3 : 4 : 1 : 0 : 1 \quad (1.4)$$

with some corrections due to phase space effects. Despite all the effort that has been put into understanding the structure of scalar mesons there is still no consensus. Different models that have been developed have led to different and sometimes contradictory conclusions about the structure of these states. Photoproduction is neither a glue-rich nor a glue-poor environment, however, the two pseudoscalar final states of Eq. 1.4 can be studied at GlueX. Therefore, we may be able to study the decay pattern of scalar mesons.

1.7 Scattering Experiments and Regge Phenomenology

Scattering experiments are an approach to studying the hadron spectrum. These types of experiments can be divided into fixed target experiments, where a beam of particles is incident on a stationary target, and collider experiments, where two beams intersect at some point. For example, in a fixed target experiment one can have a photon beam incident on a stationary proton to study reactions of the type

$$\gamma p \rightarrow X p$$

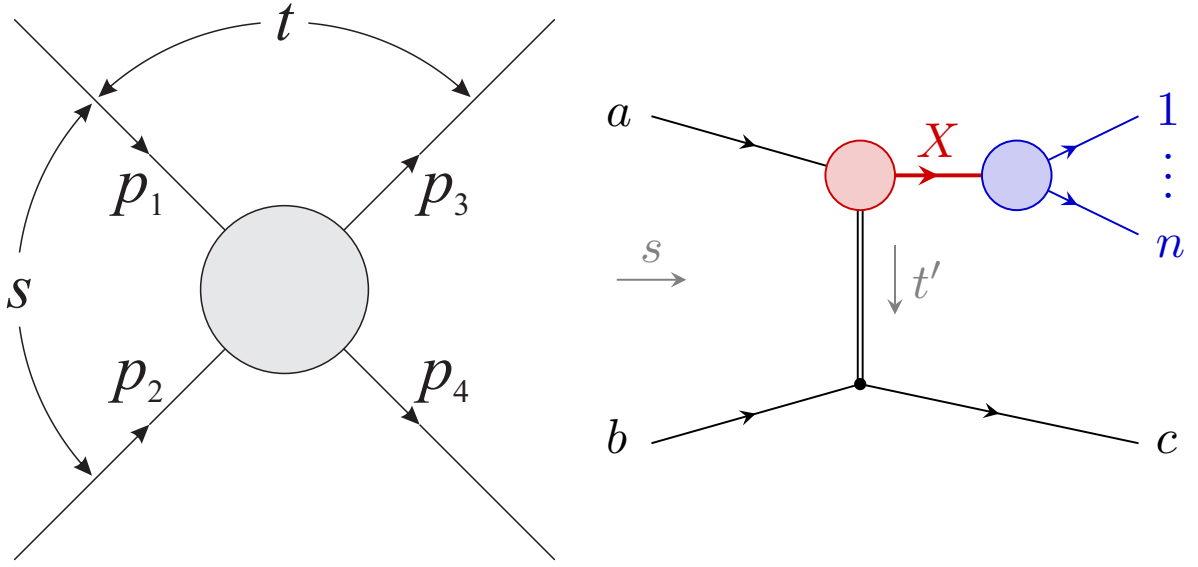


Figure 1.8: (Left) Diagram of a two body scattering process $1 + 2 \rightarrow 3 + 4$. (Right) Production of an intermediate state X in a t -channel exchange process followed by an n body decay of state X . Both figures have been taken from Ref. [7].

where X is a meson (e. g. one of the hybrid mesons or glueballs we have discussed) that has been produced through the interaction of the photon and the proton. For a $2 \rightarrow 2$ scattering process, it is common to define the Mandelstam- s , t and u variables as

$$\begin{aligned}
 s &= (p_1 + p_2)^2 = (p_3 + p_4)^2 = m_1^2 + m_2^2 + 2(E_1 E_2 - \mathbf{p}_1 \cdot \mathbf{p}_2) \\
 t &= (p_1 - p_3)^2 = (p_2 - p_4)^2 = m_1^2 + m_3^2 - 2(E_1 E_3 - \mathbf{p}_1 \cdot \mathbf{p}_3) \\
 u &= (p_1 - p_4)^2 = (p_2 - p_3)^2 = m_1^2 + m_4^2 - 2(E_1 E_4 - \mathbf{p}_1 \cdot \mathbf{p}_4)
 \end{aligned} \tag{1.5}$$

where m_i are the masses of the final state particles and $p_i = (E_i, \mathbf{p}_i)$ are the four-momenta, see Figure 1.8. The three Mandelstam variables satisfy the relation

$$s + t + u = \sum_i m_i^2 \tag{1.6}$$

i.e. two independent variables are necessary to fully characterize the scattering process for given masses m_i . Typically one chooses s and t which are, respectively, the total center of mass energy squared and momentum transferred squared.

It was observed by Chew and Frautschi [46] that hadrons fall in nearly linear trajectories in the $J - M^2$ plane, see Figure 1.9. This relation is parameterized as

$$J(M) = \alpha(0) + \alpha' M^2 \quad (1.7)$$

where $\alpha(0)$ is the y-axis intercept and α' is the Regge trajectory. Mesons are grouped based on their isospin I , spin S , parity P , and total spin J with all but the total spin J being the same. All mesons fall in two Regge trajectories. The blue trajectory in Figure 1.9 is characterized by $S = 1$ and natural parity. The green trajectory is characterized by $S = 0$ and unnatural parity. The red trajectory is called the Pomeron trajectory and, unlike the other trajectories, is not associated with any known meson. A special feature of the Pomeron trajectory is that it is the only trajectory with an intercept greater than 1, which is necessary for the total hadronic cross section to rise at high energies, see Figure 1.9.

At high energy, Regge theory predicts that meson photoproduction occurs through t -channel exchange, see Figure 1.8. However, in Regge theory the object that is exchanged is not a specific particle but a family of resonances on a given Regge trajectory [7]. Still, the convention is to speak of Reggion exchange where each Reggion is associated with a particular Regge trajectory. For example, in Regge theory one speaks of π and ρ exchange when referring to the exchange of the family of π and ρ resonances.

1.8 The $K\bar{K}$ Spectrum

In Figure 1.3 the pseudoscalar kaons are K^+ , K^- , K^0 and \bar{K}^0 . However, throughout this dissertation we will discuss the $K_S K_S$ and $K_S K_L$ final states. This is because, although K^0 and \bar{K}^0 are eigenstates of the strong interaction, the states observed in nature are the K-short (K_S) and the K-long (K_L). The names correspond to the difference in their mean lifetime (τ) which are [3]

$$\tau(K_L) = (5.116 \pm 0.021) \times 10^{-8} \text{s}$$

and

$$\tau(K_S) = (8.954 \pm 0.004) \times 10^{-11} \text{s}.$$

Since K^0 and \bar{K}^0 are the lightest mesons with a strange quark, they can only decay through the weak interaction, see Figure 1.10. Consequently, if a K^0 is produced, it will develop a \bar{K}^0 component

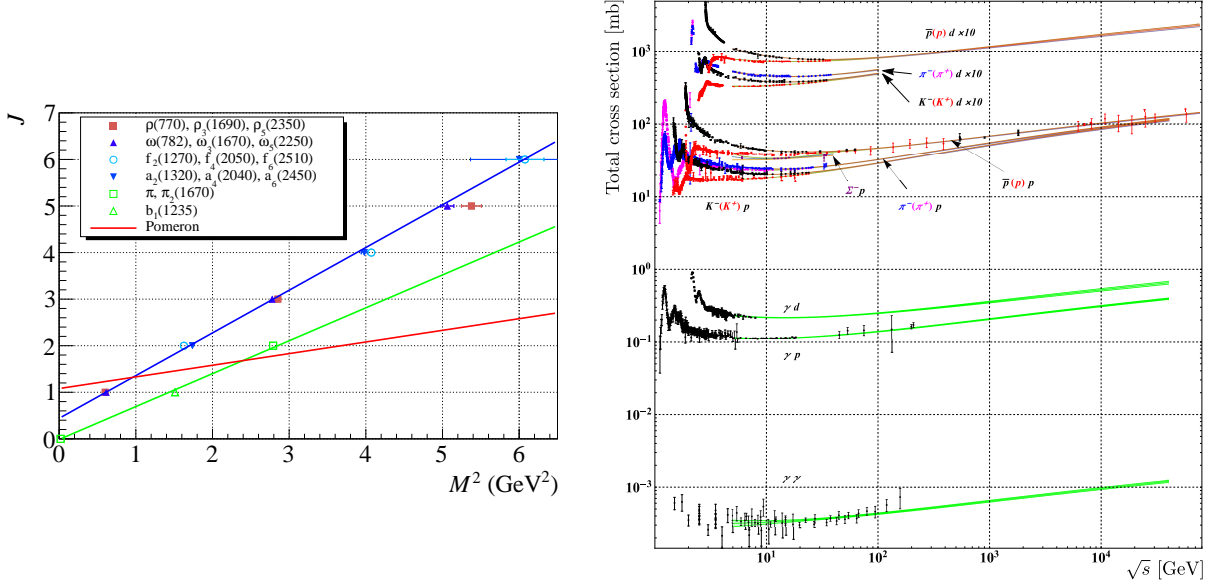


Figure 1.9: (Left) Chew-Frautschi plot for ground state mesons and the Pomeron [7]. (Right) The total cross section for hadronic, γp and $\gamma\gamma$ processes as a function of \sqrt{s} [3].

(visa versa for producing a \bar{K}^0) and therefore one cannot observe a pure K^0 (or \bar{K}^0) in nature. The relations between K^0/\bar{K}^0 and K_S/K_L are

$$|K_L\rangle = \frac{1}{\sqrt{1+\epsilon^2}} \frac{(1+\epsilon)|K^0\rangle - (1-\epsilon)|\bar{K}^0\rangle}{\sqrt{2}}$$

and

$$|K_S\rangle = \frac{1}{\sqrt{1+\epsilon^2}} \frac{(1+\epsilon)|K^0\rangle + (1-\epsilon)|\bar{K}^0\rangle}{\sqrt{2}}$$

where the term ϵ is small and arises due to CP violation in weak decays [47].

The fact that K^0 and \bar{K}^0 are eigenstates of the strong interaction but not the physically observed states has important consequences for the $K\bar{K}$ spectrum. When we say $K\bar{K}$ then we mean both K^+K^- and $K^0\bar{K}^0$ but since K^0 and \bar{K}^0 are not the physical states, $K^0\bar{K}^0$ physically manifests as $K_S K_S$, $K_L K_L$ or $K_S K_L$. Because of Bose symmetry, the spin of the $K_S K_S$ (and $K_L K_L$) system must be even and the spin of the $K_S K_L$ system must be odd. Therefore, even⁺⁺ mesons may decay to $K_S K_S$ (and $K_L K_L$) but not $K_S K_L$ while odd⁻⁻ mesons decay to $K_S K_L$ but not $K_S K_S$. Since K^+ and K^- are the physically observed states there is no analogous separation for the K^+K^- system and all mesons that may decay to $K\bar{K}$ decay to K^+K^- . Therefore, the $K_S K_S$ and $K_S K_L$

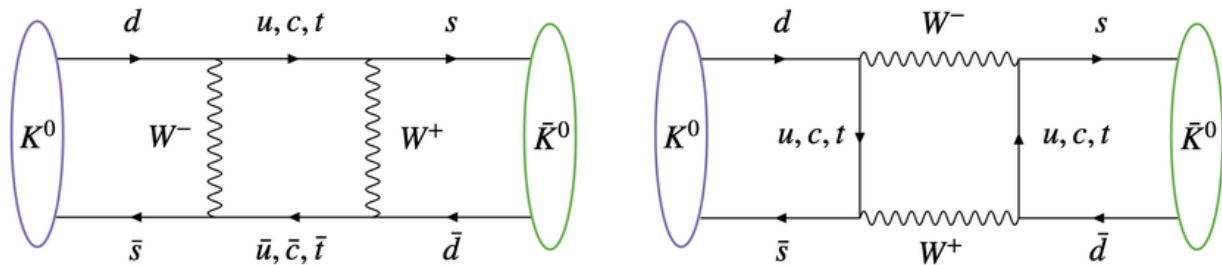


Figure 1.10: $K^0 - \bar{K}^0$ mixing due to the weak interaction [13].

final states act as a filter for the spin of the parent particle. Figure 1.11 gives an illustration of this discussion.

Another important difference when studying K^+K^- and $K^0\bar{K}^0$ is due to isospin. The neutral $K\bar{K}$ isospin states are given by [48]

$$\begin{aligned}
 |K\bar{K}, I = 0\rangle &= -\frac{1}{\sqrt{2}} (|K^+K^- \rangle + |K^0\bar{K}^0 \rangle) \\
 |K\bar{K}, I = 1, I_3 = 0\rangle &= -\frac{1}{\sqrt{2}} (|K^+K^- \rangle - |K^0\bar{K}^0 \rangle).
 \end{aligned}
 \tag{1.8}$$

These isospin relations imply that overlapping isovector and isoscalar neutral mesons destructively interfere in decays to $K^0\bar{K}^0$. For example, based on isospin we would expect that $f_2(1270)/a_2(1320) \rightarrow K_S\bar{K}_S$ will destructively interfere with each other. In practice, these two states are unlikely to completely cancel each other out due to differences in cross sections and mass. Additionally, if the production phases differ then the destructive interference may become constructive.

1.9 Photoproduction and the GlueX Experiment

The GlueX Experiment is a photoproduction experiment with the goal to map the meson spectrum including hybrid mesons. A linearly polarized photon beam, with energy up to ~ 12 GeV, is incident on a proton target (γp) which is surrounded by a nearly 4π hermetic detector. The experimental setup will be discussed in detail in Chapter 3. There is little available experimental data on photoproduction in the range 6 – 12 GeV, especially for the $K\bar{K}$ system. Relevant experimental evidence and theoretical predictions will be discussed in Chapter 2. All mesons shown in Figure 1.11 can be produced in photoproduction which, in most cases, leads to overlapping states. Isolated states can be studied in greater detail since it is not necessary to separate the complicated

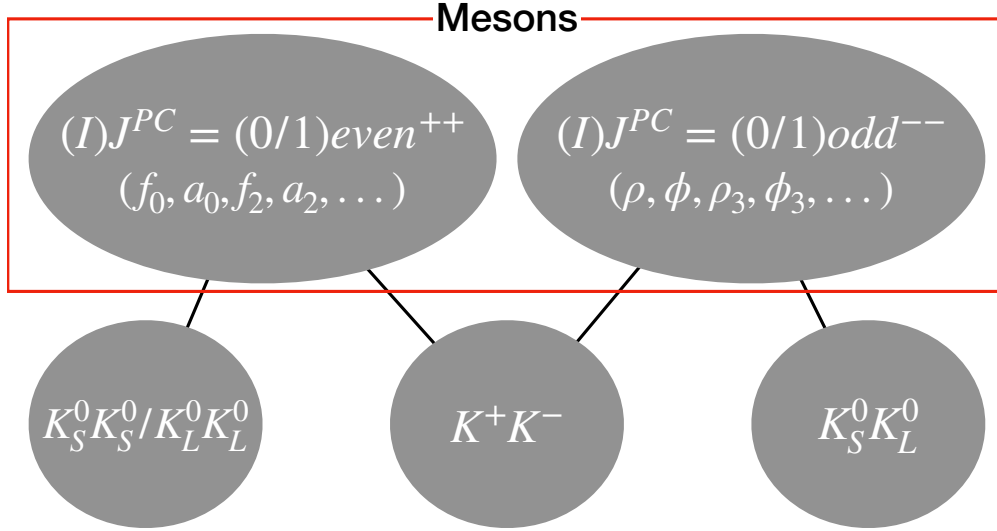


Figure 1.11: Allowed meson decays to $K\bar{K}$ divided by $(I)J^{PC}$ and final state kaon pairs.

dynamics of overlapping states. A common technique (and the one used in this dissertation) used to study overlapping states is to perform a spin decomposition of the invariant mass spectrum before modeling the dynamics of the reaction. The formalisms necessary to perform these analyses are discussed in Chapter 5. The linear polarization of the photon beam is a feature we exploit in this dissertation to provide important information about the production mechanism of meson photoproduction. The data samples used in this dissertation are discussed in Chapter 4. $\phi(1020) \rightarrow K_S K_L$ is an isolated reaction that we study in detail in Chapter 6. The rest of the $K_S K_L$ spectrum is expounded upon in Chapter 7. The $K_S K_S$ spectrum is studied in Chapter 8.

CHAPTER 2

PREVIOUS MEASUREMENTS AND THEORETICAL PREDICTIONS

In this chapter, we review the available experimental and theoretical literature. Section 2.1 reviews several photoproduction measurements of $\phi(1020)$ and a theoretical prediction of the $\phi(1020)$ spin-density matrix elements at $E_\gamma \sim 8.5$ GeV. The photoproduction $K_S K_L$ spectrum is expected to be dominated by vector mesons but there are no measurements in the literature aside from $\phi(1020) \rightarrow K_S K_L$ measurements. In Section 2.2 we discussed the excited vector meson spectrum, $e^+ e^- \rightarrow K_S K_L$ measurements, and photoproduction of $K^+ K^-$. Finally, in Section 2.3 we review the measurements of the $K_S K_S$ spectrum in various production mechanisms.

2.1 $\phi(1020)$ Photoproduction

$\phi(1020)$ photoproduction has been studied by various experiments with polarized and unpolarized photon beams. The observables of interest are the spin-density matrix elements (SDMEs) and cross section (σ). The measured cross section can be expressed as the product of an angular part $W(\theta, \phi, \Phi)$ and a normalization factor A

$$\sigma = A \cdot W(\theta, \phi, \Phi) \tag{2.1}$$

where θ and ϕ are, respectively, the polar and azimuthal angles in a certain frame, Φ is the angle between the polarization and reaction planes. The angular part of the cross section for vector meson photoproduction with a linearly polarized photon beam is

$$W(\cos\theta, \phi, \Phi) = W^0(\cos\theta, \phi) - P_\gamma \cos(2\Phi) W^1(\cos\theta, \phi) - P_\gamma \sin(2\Phi) W^2(\cos\theta, \phi). \tag{2.2}$$

where

$$\begin{aligned} W^0(\cos\theta, \phi) &= \frac{3}{4\pi} \left(\frac{1}{2}(1 - \rho_{00}^0) + \frac{1}{2}(3\rho_{00}^0 - 1)\cos^2\theta - \sqrt{2}\text{Re}\rho_{10}^0\sin 2\theta\cos\phi - \rho_{1-1}^0\sin^2\theta\cos 2\phi \right) \\ W^1(\cos\theta, \phi) &= \frac{3}{4\pi} \left(\rho_{11}^1\sin^2\theta + \rho_{00}^1\cos^2\theta - \sqrt{2}\text{Re}\rho_{10}^1\sin 2\theta\cos\phi - \rho_{1-1}^1\sin^2\theta\cos 2\phi \right) \\ W^2(\cos\theta, \phi) &= \frac{3}{4\pi} \left(\sqrt{2}\text{Im}\rho_{10}^2\sin 2\theta\sin\phi + \text{Im}\rho_{1-1}^2\sin^2\theta\sin 2\phi \right). \end{aligned} \tag{2.3}$$

For an unpolarized photon beam only W^0 contributes. If the production process conserves helicity, i. e. the helicity of the incident photon and the produced vector meson are the same, then we say the production process satisfies s-channel helicity conservation (SCHC). SCHC has the consequence that the only non-zero SDMEs are $\rho_{1-1}^1 = -\text{Im}(\rho_{1-1}^2) = 1/2$. Ballam et al. [1], Omega Photon [2], LEPS [15, 14, 49] and CLAS [16] have measured the cross section and SDMEs of the $\phi(1020)$ with a linearly polarized photon beam. Unpolarized photoproduction was studied by CLAS [50]. Except for the LEPS analysis [15] all publications discussed here use the same formalism.

2.1.1 High Energy Photoproduction

Ballam et al. measured the $\phi(1020)$ SDMEs in one bin of $-t$ and two bins of beam energies [1]. The experiment exposed a hydrogen bubble chamber to a linearly polarized photon beam from the Stanford Linear Accelerator Center (SLAC). Table 2.1 shows the numerical values measured by Ballam et al. Due to large uncertainties they were only able to conclude that $\phi(1020)$ production is consistent with SCHC. Ballam et al. also measured the total and differential cross section of the $\phi(1020)$ in three bins on beam energy. It is worth noting that, at $E_\gamma = 9.3$ GeV, the exponential slope of the differential cross section was determined to be 4.6 ± 0.6 GeV².

The Omega Photon Collaboration measured SDMEs and differential cross section of $\phi(1020)$ at 20–40 GeV beam energy [2]. Similar to SLAC low statistics limited the precision of their measurement determining only one set of SDMEs values, see Table 2.1. Again, it was found that $\phi(1020)$ production is consistent with SCHC. They also measured the exponential slope of the differential cross section to be 5.26 ± 0.3 at 20–27 GeV beam energy and 5.02 ± 0.26 GeV² at 27–40 GeV beam energy. This is consistent with an older measurement at CERN, which determined the exponential slope to be 4.9 ± 0.9 GeV² in the same beam energy range [51].

2.1.2 Low Energy Photoproduction

The LEPS Collaboration measured SDMEs and cross sections in the beam energy range 1.5 – 2.9 GeV [15, 14, 49]. To measure the $\phi(1020)$ SDMEs the LEPS Collaboration took a different approach than SLAC and the Omega Photon Collaboration. Rather than fitting the three-dimensional distribution to determine all nine SDMEs, LEPS used the following set of integrated one-dimensional decay distributions

$$W(\cos\theta) = \frac{3}{2} \left(\frac{1}{2} (1 - \rho_{00}^0) \sin^2\theta + \rho_{00}^0 \cos^2\theta \right) \quad (2.4)$$

Table 2.1: $\phi(1020)$ SDME measurements by SLAC [1] and the Omega Photon Collaboration [2].

Experiment	SLAC		Omega Photon
$-t$ range (GeV ²)	0.02 – 0.80		–
Beam energy (GeV)	2.8 & 4.7	9.3	20–40
ρ_{00}^0	-0.04 ± 0.06	0.00 ± 0.07	0.0332 ± 0.0357
$\text{Re}(\rho_{10}^0)$	-0.00 ± 0.06	-0.01 ± 0.06	-0.0169 ± 0.0204
ρ_{1-1}^0	-0.04 ± 0.10	-0.14 ± 0.06	0.0214 ± 0.0319
ρ_{00}^1	-0.13 ± 0.09	0.08 ± 0.12	0.0253 ± 0.0931
ρ_{11}^1	-0.06 ± 0.11	-0.18 ± 0.13	0.0207 ± 0.1093
$\text{Re}(\rho_{10}^1)$	0.00 ± 0.09	-0.20 ± 0.11	0.1275 ± 0.10
ρ_{1-1}^1	0.18 ± 0.13	0.44 ± 0.15	0.4838 ± 0.1648
$\text{Im}(\rho_{10}^2)$	-0.02 ± 0.10	-0.14 ± 0.09	0.1410 ± 0.0928
$\text{Im}(\rho_{1-1}^2)$	-0.51 ± 0.16	-0.73 ± 0.17	0.5708 ± 0.18
P_σ	0.50 ± 0.28	0.80 ± 0.32	0.94 ± 0.34
Number of events	~ 200	~ 200	1135

$$W(\phi) = \frac{1}{2\pi} (1 - 2\text{Re}\rho_{1-1}^0 \cos 2\phi) \quad (2.5)$$

$$W(\phi - \Phi) = \frac{1}{2\pi} (1 + 2P_\gamma \bar{\rho}_{1-1}^1 \cos [2(\phi - \Phi)]) \quad (2.6)$$

$$W(\phi + \Phi) = \frac{1}{2\pi} (1 + 2P_\gamma \Delta_{1-1} \cos [2(\phi + \Phi)]) \quad (2.7)$$

$$W(\Phi) = 1 - P_\gamma (2\rho_{11}^1 + \rho_{00}^1) \cos 2\Phi. \quad (2.8)$$

This integration reduces the number of SDMEs which can be determined from nine to two plus three combinations and separates a single three-dimensional distribution into five independent distributions. SDMEs extracted in the most recent LEPS publication [15] are shown in Figure 2.1. Above 2.37 GeV the LEPS data is well described by t-channel production with Pomeron and pseudoscalar (π and η) exchange. Below 2.37 GeV and down to threshold at 1.57 GeV, the agreement breaks down suggesting other production mechanisms contribute.

CLAS measured SDMEs of $\phi(1020)$ with a linearly polarized photon beam of $E_\gamma = 1.5 - 2.1$ GeV [16]. The SDMEs were measured as a function of $\cos(\theta)$ in the $\phi(1020)$ center-of-mass frame in three bins of beam energy. Figure 2.2 shows the CLAS measurement at 2 GeV beam energy compared to a measurement by LEPS [14]. In the small region where they overlap both measurements agree and are inconsistent with SCHC indicating a more complicated production mechanism than simple Pomeron exchange.

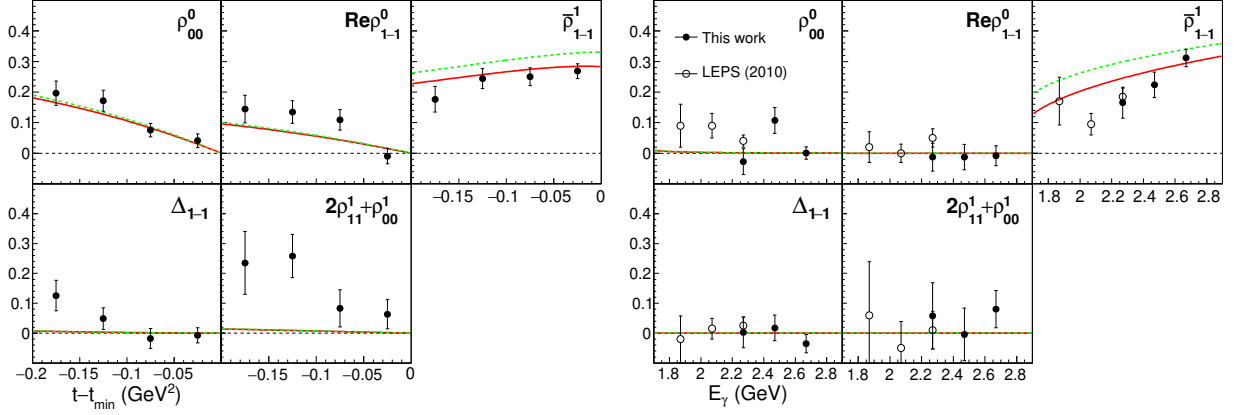


Figure 2.1: (Left) $\phi(1020)$ SDMEs as a function of $t - t_{min}$ in the Gottfried-Jackson frame. The beam energy range is $2.37 < E_\gamma < 2.77$ GeV. (Right) SDMEs as a function of beam energy in the Gottfried-Jackson frame with $t - t_{min} < -0.05$ GeV². Data in open circles comes from a previous LEPS measurement [14]. In both cases the red and green curves are model calculations which included Pomeron, π and η exchange [15]. The difference between the two curves is the strength of the Pomeron coupling.

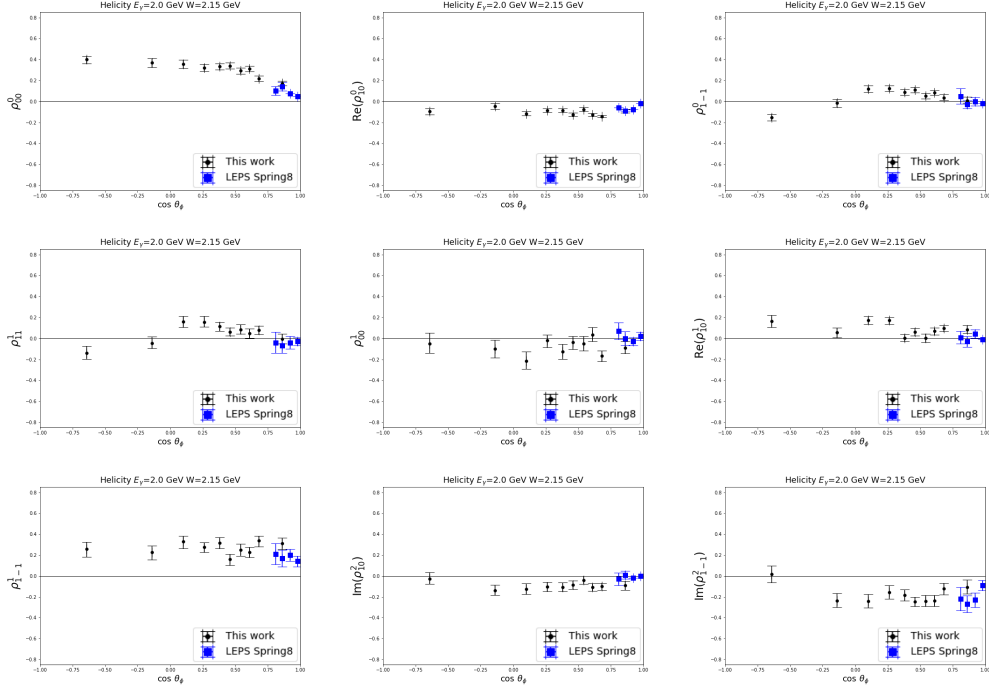


Figure 2.2: $\phi(1020)$ SDMEs measured by CLAS [16] (black points) and LEPS [14] (blue points) at 2 GeV beam energy in the Helicity frame.

Finally, we mention a paper by CLAS [50] which measured both differential cross section and SDMEs of $\phi(1020)$ in decays to K^+K^- and $K_S K_L$. This time, however, the photon beam was unpolarized reducing the number of SDMEs which can be measured and the incident photon energies range from 1.97 GeV to 2.84 GeV. Consistent with the previous low energy photoproduction studies we have discussed, this CLAS paper found that $\phi(1020)$ photoproduction did not obey SCHC at these energies.

2.1.3 Theoretical Prediction at $E_\gamma \sim 8.5$ GeV

A Regge theory based model has been developed by the Joint Physics Analysis Center (JPAC) for photoproduction of light vector mesons [35]. This model was used to predict the Spin Density Matrix Elements (SDMEs) of the $\rho(770)$, $\omega(782)$ and $\phi(1020)$ mesons in photoproduction at $E_\gamma \sim 8.5$ GeV, see Figure 2.3. JPAC models vector meson production as a t -channel exchange of Reggeons. The Reggeons included in the model are the natural parity Pomeron, f_2 and a_2 , as well as the unnatural parity π and η . For $\phi(1020)$ production only Pomeron, π and η exchange are expected to contribute. An f'_2 exchange can be included for $\phi(1020)$ production but is assumed to be a small contribution. Pomeron exchange is assumed to be purely helicity conserving, i. e. the only non-zero SDMEs are $\rho_{1-1}^1 = -\text{Im}(\rho_{1-1}^2) = 1/2$. The Pomeron coupling was determined from the available γp and γd total cross section for $E_\gamma > 2$ GeV. The strength of pseudoscalar (π and η) exchange were determined from measurements of vector meson radiative decays¹, and from the π -nucleon and η -nucleon couplings available in the literature. These predictions can help clarify the production mechanism of light vector mesons. Which is an important step before searching for and understanding the production of excited vector mesons and perhaps hybrid vector mesons.

2.1.4 Summary

In summary, the available high energy data (above 8 GeV beam energy) is consistent with SCHC but is limited by low statistical precision. This can be well described by t -channel process where the exchange of a Pomeron dominates. Low energy data, on the other hand, is abundant and inconsistent with SCHC suggesting a more complicated production mechanism. The LEPS data suggests that $\phi(1020)$ production can be well modelled by Pomeron, π and η exchange starting around 2.37 GeV, well below the beam energy of interest in this dissertation of 8.2 – 8.8 GeV.

¹Radiative decays refers to reactions reactions such as $\phi(1020) \rightarrow \gamma\pi$ or $\phi(1020) \rightarrow \gamma\eta$.

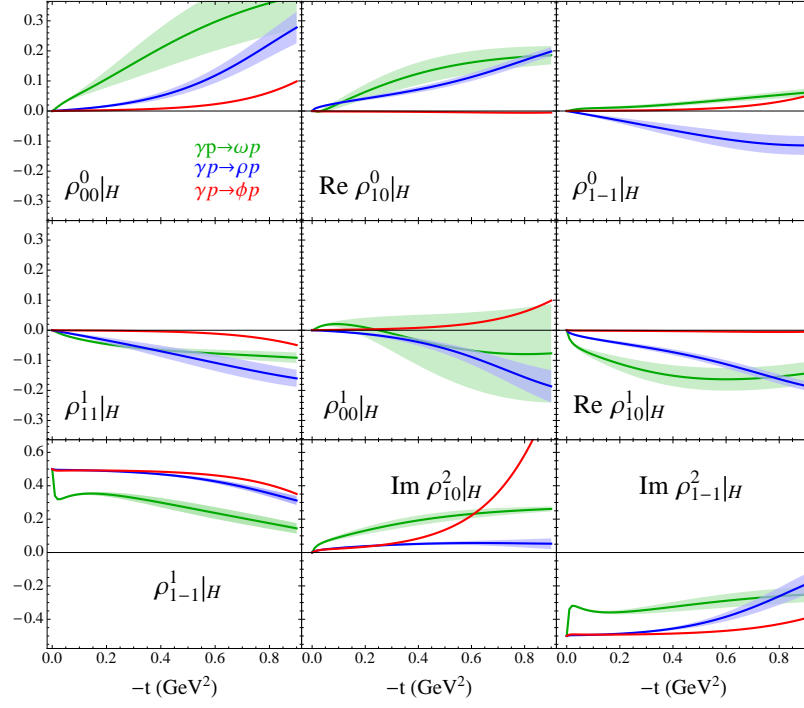


Figure 2.3: JPAC model for Spin Density Matrix Elements of $\rho(770)$, $\omega(782)$, and $\phi(1020)$ photo-production at $E_\gamma = 8.5$ GeV.

Additionally, by comparing to theoretical predictions by JPAC we can better understand light vector meson photoproduction.

2.2 $K_S K_L$ Final State

2.2.1 Established Excited Vector Meson

Below 2 GeV eight vector mesons, see Table 2.2, are considered well established by the PDG [3]. The $K\bar{K}$ final state is an open-strangeness final state. Therefore, in principle the $K\bar{K}$ final state may couple, with varying degrees of strength, to ρ -, ω - and ϕ -states. In the literature the $\omega(1450)$ and $\omega(1650)$ have not been observed to decay to $K\bar{K}$. Therefore, the coupling of the $\omega(1450/1650)$ to $K\bar{K}$ is expected to be weak. Although, $\rho(1450)$ and $\rho(1700)$ are considered well established states their properties (i.e. mass and width) are not well constrained. In the PDG the mass and width for $\rho(1450)$ are determined to be 1.465 ± 0.025 GeV and 400 ± 60 GeV respectively. However, the PDG states these estimates are "an educated guess" [3]. This is likely because the parameters determined by measuring the $\rho(1450)$ parameters in different final states and in different reactions vary wildly. Parameters for $\rho(1700)$ are in a similar state with a mass and width of 1.720 ± 0.020 GeV and 0.250 ± 0.100 GeV, respectively. The last meson to discuss in Table 2.2 is $\phi(1680)$. The PDG estimate the $\phi(1680)$ mass and width are 1.680 ± 0.020 GeV and 0.150 ± 0.050 GeV, respectively, and state that these parameters are "an educated guess".

Table 2.2: Established vector mesons below 2 GeV [3].

I = 1	$\rho(770)$	$\rho(1450)$	$\rho(1700)$
I = 0 ($n\bar{n}$)	$\omega(782)$	$\omega(1420)$	$\omega(1650)$
I = 0 ($s\bar{s}$)	$\phi(1020)$	$\phi(1680)$	

2.2.2 $K_S K_L$ in e^+e^- Collisions

The CMD-2 [52], SND [53], DM1 [54], OLYA [55] and BaBar [17] experiments have all studied the $K_S K_L$ final state in e^+e^- collisions at different center of mass energies. Figure 2.4 shows the measured cross section for each experiment covering $\sim 1.1 - 2.2$ GeV in the center of mass energy. The most precise measurement is presented by the BaBar Collaboration. Figure 2.4 shows $K_S K_L$ events as a function of invariant mass distribution after event selections and background subtraction,

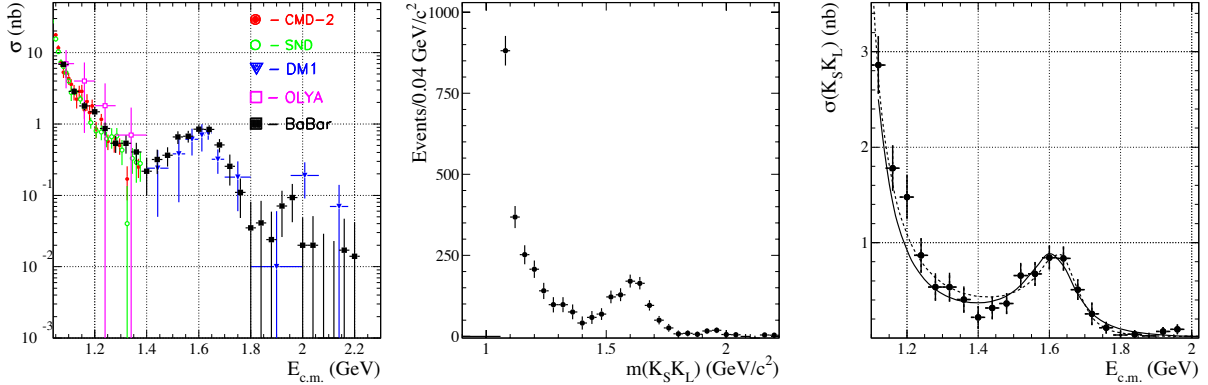


Figure 2.4: (Left) The $e^+e^- \rightarrow K_S K_L$ cross section measured by various experiments. (Middle) $e^+e^- \rightarrow K_S K_L$ events after event selections and background subtraction, BaBar data. (Right) Fitted cross sections measured by the BaBar Collaboration [17].

and the fitted cross section. The first model that was considered contained two resonances and gave a reasonable description of the data with a $\chi^2/\text{ndf} = 30/25 = 1.2$. A second model added a non-resonant background term to the fit which gave an improved $\chi^2/\text{ndf} = 21/23 = 0.91$. The mass and width parameters of the higher mass resonance were determined to be 1.674 ± 0.013 GeV and 0.165 ± 0.080 MeV.

2.2.3 $K\bar{K}$ Photoproduction

There is no available $K_S K_L$ photoproduction data above the $\phi(1020)$. However, $K^+ K^-$ photoproduction has been studied by the Omega Photon Collaboration [2], E401 experiment [18] and FOCUS Collaboration [19]. The three analysis consistently found an enhancement in the $K^+ K^-$ invariant mass distribution around 1.75 GeV. We will discuss each of these experiments.

The $K^+ K^-$ invariant mass spectrum measured by the Omega Photon Collaboration [2] is shown in Figure 2.5. The mass distribution was fitted with a Breit-Wigner for the signal and a third order polynomial for the background. The Breit-Wigner parameters from the fit are

$$M = 1.76 \pm 0.02 \text{ GeV}$$

$$\Gamma = 0.08 \pm 0.04 \text{ GeV.}$$

An attempt was made to measure the spin of the resonance by fitting the polar angle distribution with the function

$$W(\cos\theta) = A [(1 - B)\cos^2\theta + (1 + B)\cos^2\theta.] \quad (2.9)$$

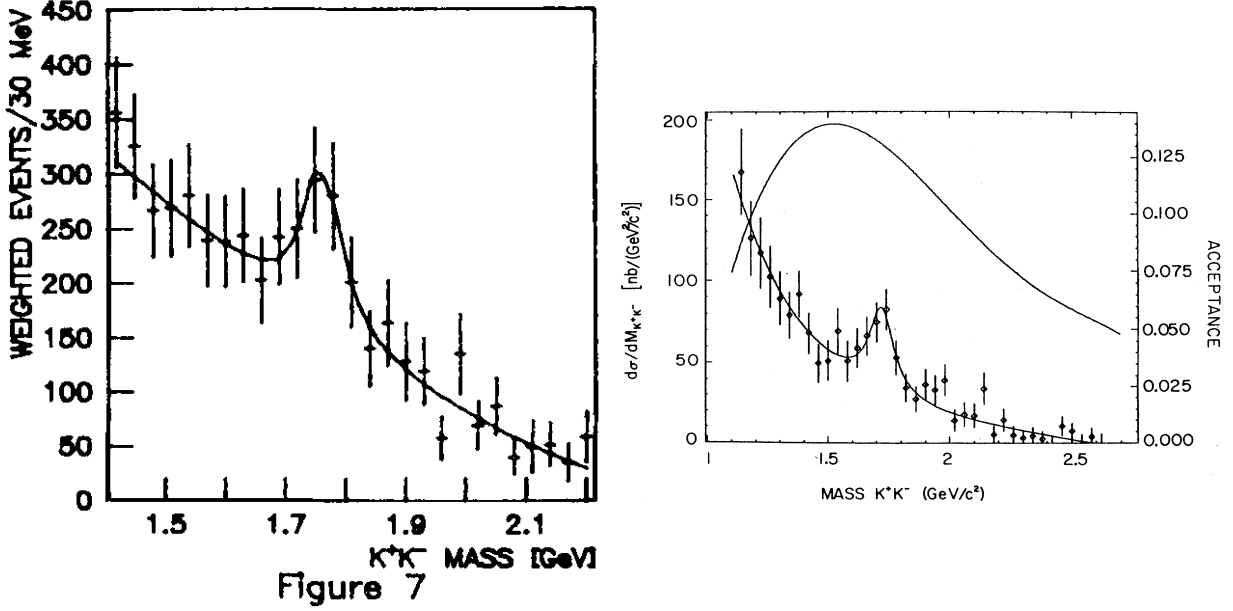


Figure 2.5: (Left) Photoproduction of K^+K^- at measured by the Omega Photo Collaboration [2]. (Right) Photoproduction of K^+K^- measured by the E401 Experiment [18].

The results however, were inconclusive. They proposed that the simplest interpretation is that the enhancement is due to $\phi(1680)$, the radial excitation of $\phi(1020)$. However, no sign of the $X(1750)$ was observed in the $\gamma p \rightarrow K^*K$ data [56] which is inconsistent with the large $\phi(1680)$ signal observed in e^+e^- experiments. The Omega Photon analysis was ultimately inconclusive.

The E401 Experiment [18] also observed the $X(1750)$ in K^+K^- photoproduction, see Figure 2.5. The mass distribution was fitted with a Breit-Wigner, and an exponential plus linear polynomial. The Breit-Wigner parameters from the fit are

$$M = 1.726 \pm 0.022 \text{ GeV}$$

$$\Gamma = 0.121 \pm 0.047 \text{ GeV}$$

with a yield of 123 ± 41 events. The paper concluded that the most likely interpretation of the enhancement was the $\phi(1680)$ and argued that the difference in the Breit-Wigner parameters in photoproduction and e^+e^- experiments are due to interference effects.

The FOCUS Collaboration [19] has the highest statistics K^+K^- photoproduction data from the three experiments, see Figure 2.6. The Breit-Wigner parameters for the $X(1750)$ they found

are

$$M = 1.7535 \pm 0.0015 \pm 0.0023 \text{ GeV}$$

$$\Gamma = 0.1222 \pm 0.0062 \pm 0.0080 \text{ GeV}$$

which are consistent with measurements by the Omega Photon and E401 experiments but inconsistent with e^+e^- measurements. FOCUS also investigated the K^*K final state since evidence from e^+e^- colliders showed that $\phi(1680)$ had a much larger branching fraction to K^*K compared to $K\bar{K}$. However, no structure around 1.7 GeV was observed in the K^*K photoproduction data, see Figure 2.7. Next, they studied the relative cross section of $\phi(1020)$ to $X(1750)$. At high energy, the photoproduction cross section of light vector mesons is known to be similar. Therefore, one would expect the relative cross section of $\phi(1020)$ to $X(1750)$ to be flat if the $X(1750)$ is also a vector meson. The FOCUS data, see Figure 2.7, shows a clear linear dependence as a function of beam energy. Finally, an angular analysis of the data suggested that $X(1750)$ is 2^{++} rather than a 1^{--} state. Because of the difference in mass and branching fraction, as well as the difference in relative cross section and angular distributions. The FOCUS analysis strongly disfavors the interpretation of $X(1750)$ as $\phi(1680)$. However, they do not make a definitive statement as to the nature of $X(1750)$, concluding the paper with the statement "the interpretation of the $X(1750)$ remains uncertain" [19].

2.2.4 The $\phi(2170)$

The $\phi(2170)$ state, formerly known as $Y(2175)$, is considered established by the PDG [3] with mass 2.163 ± 0.007 GeV and width $0.103_{-0.021}^{+0.028}$ GeV. Many interpretations of the nature of $\phi(2170)$ have been proposed in the literature, such as: a conventional $s\bar{s}$ state [57, 58], tetraquark [59], hybrid [60], baryonic $\Lambda\bar{\Lambda}$ state [61], or mesonic $\phi(1020)f_0(980)$ molecule [62]. Although the $\phi(2170)$ has been observed in the multiple decay modes, such as: $\phi(1020)\pi^+\pi^-$, $\phi(1020)\eta$, $\phi(1020)\eta'$, $\omega\eta$, K^+K^- , and $K_S K_L$ [3], it has only been observed in e^+e^- colliders. An analysis of the photoproduction of $\phi(1020)\pi^+\pi^-$ with the GlueX-I data set, see Figure 2.8, shows an enhancement which is consistent with the $\phi(2170)$ [21]. However, the interpretation of the GlueX data is still under discussion.

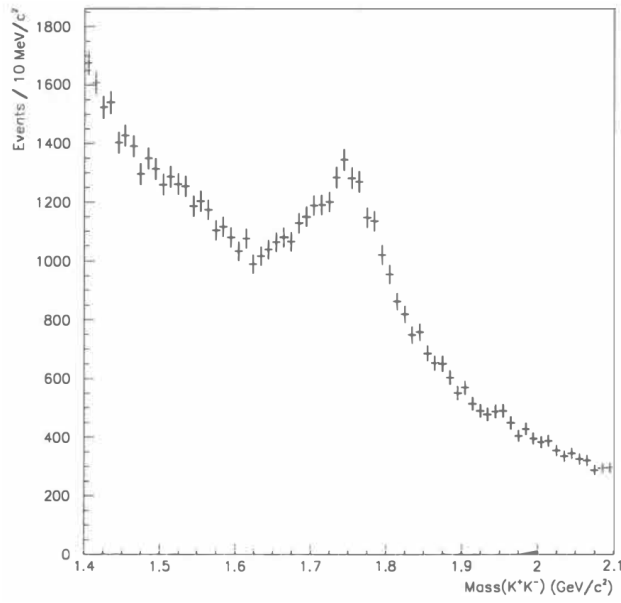


Figure 2.6: K^+K^- invariant mass distribution measure by the FOCUS Collaboration [19].

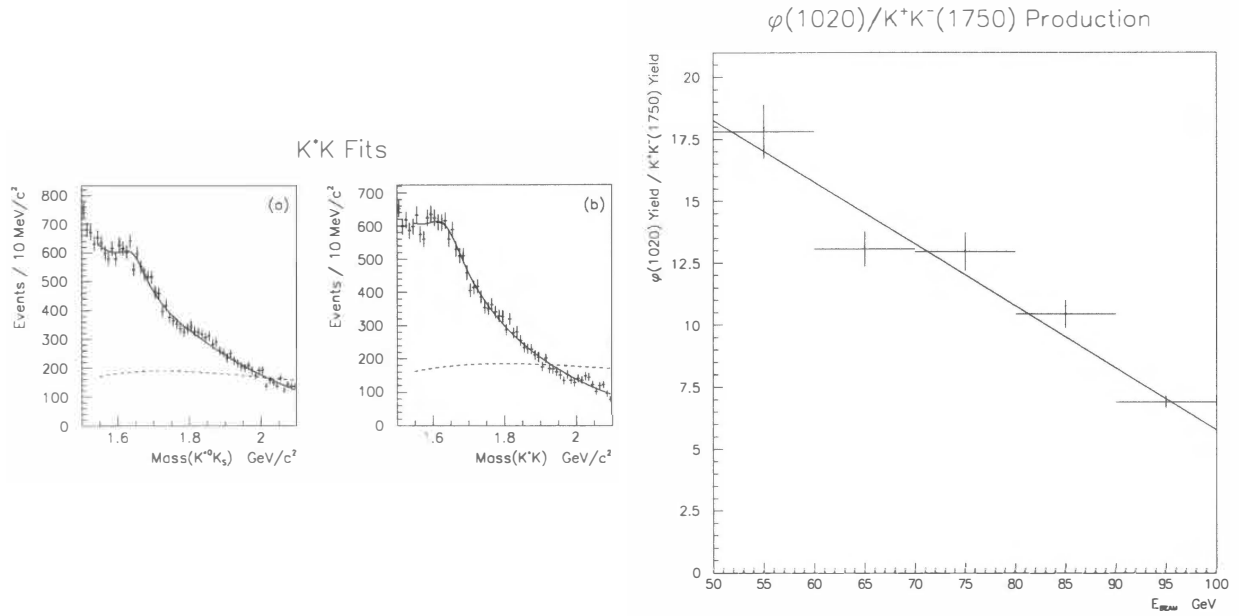


Figure 2.7: (Left) $K^{*0}K_S$ and K^*K mass distributions measured by FOCUS. No evidence for a resonance around 1.7 GeV was found [19]. (Right) Relative cross section of $\phi(1020)$ to $K^+K^-(1750)$ (referred to as $X(1750)$ in the text).

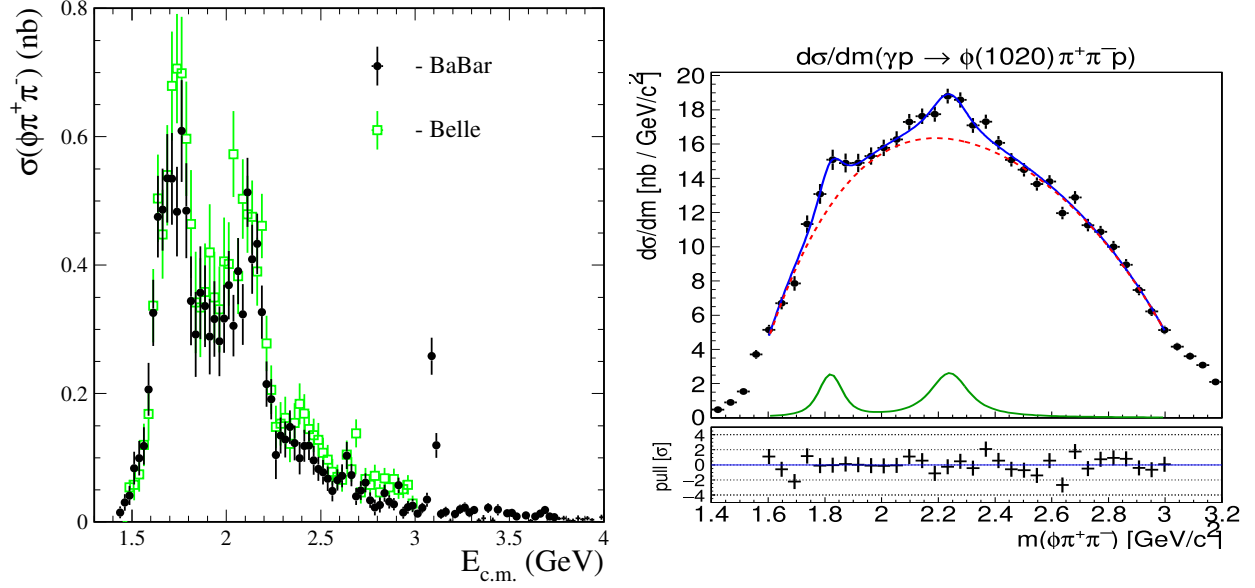


Figure 2.8: (Left) $e^+e^- \rightarrow \phi(1020)\pi^+\pi^-$ cross section as a function of center of mass energy measured by (black) Belle and (green) Babar [20]. (Right) The $\phi(1020)\pi^+\pi^-$ differential cross section measured by GlueX [21].

2.3 $K_S K_S$ Measurements

$K_S K_S$ production has been by CLAS [22], ZEUS [23] and BESIII [24] in different production mechanisms. Figure 2.9 shows the different production mechanisms that have been investigated by these experiments. In this section we review the finding of each experiment. Afterwards, we will review an analysis published by the Joint Physics Analysis Center [25] (JPAC) which used data collected by the BESIII Collaboration.

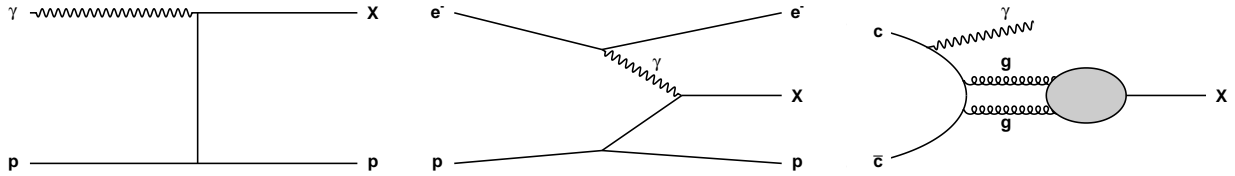


Figure 2.9: (Left) Photoproduction of a hadron X produced in a t-channel exchange as could be seen by GlueX and CLAS. (Middle) Production of a hadron X in ep collider via a virtual photon as could be seen by ZEUS. (Right) Radiative decay of J/ψ as could be seen by BESIII.

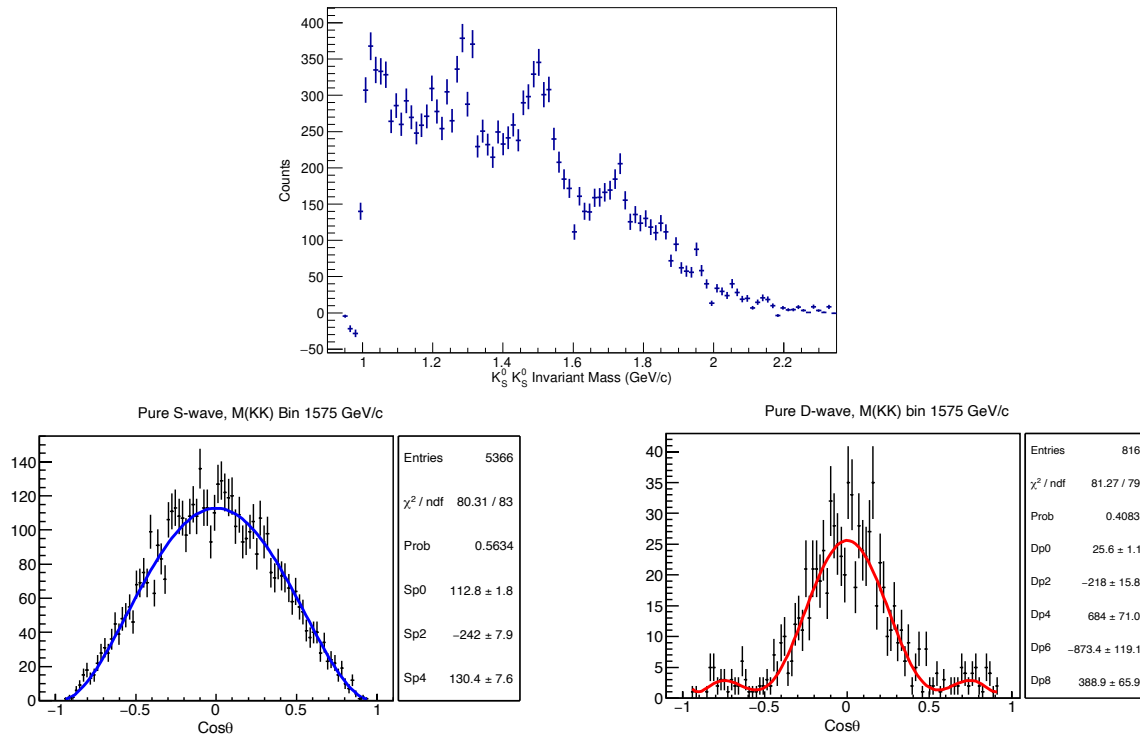


Figure 2.10: (Top) Invariant mass spectrum of $K_S K_S$ published by CLAS[22]. (Bottom) Monte Carlo simulation of pure S-wave (right) and D-wave (left) with the CLAS detector.

2.3.1 CLAS Collaboration

CLAS studied the photoproduction of $K_S K_S$ with an unpolarized beam of energy $E_\gamma = 1.1 - 5.5$ GeV. The K_S particles are determined by their decay to $\pi^+ \pi^-$ pairs while the recoil proton is not detector. The $K_S K_S$ mass spectra measured by CLAS can be seen in Fig. 2.10 after a mass sideband subtraction. Their analysis focused on an enhancement near 1.5 GeV. Examining the behavior of this enhancement as a function of the Mandelstam-t variable showed it is consistent with a resonance produced via a t-channel process. An angular analysis indicated the data in the between 1.4–1.6 GeV in the $K_S K_S$ invariant mass is predominantly S-wave in nature suggestion the enhancement is due to a spin-0 state. However, as can be seen from their Monte Carlo simulations of pure S- and D-wave, see Figure 2.10, the CLAS detector has poor acceptance at extreme angles where the S- and D-waves are most distinct making any angular analysis difficult.

2.3.2 ZEUS Collaboration

An analysis of inclusive $K_S K_S$ production in electron-proton collisions at the Hadron-Electron Ring Accelerator (HERA) was published by the ZEUS Collaboration[23]. The data set was restricted to a kinematical region dominated by photoproduction with small exchange photon virtuality, $Q^2 < 1 \text{ GeV}^2$ and (after event selections) included a sample of 1.3 million K_S candidates with an estimated 8% background contribution. Figure 2.11 shows the $M(K_S K_S)$ distribution fitted with the function:

$$F(m) = a|5BW(f_2(1270) - 3BW(a_2^0(1320)) + 2BW(f_2'(1525)))|^2 + b|BW(f_0(1710))|^2 + cU(m) \quad (2.10)$$

where $BW(R)$ is a Breit-Wigner function defined as

$$BW(R) = \frac{M_R \sqrt{\Gamma_R}}{M_R^2 - m^2 - iM_R \Gamma_R} \quad (2.11)$$

R is the indicated resonance and the background function is

$$U(m) = m^A \exp(-Bm). \quad (2.12)$$

As indicated in Fig. 2.11 the enhancement near 1.3 GeV is identified as due to interference between $f_2(1270)$ and $a_2(1320)$ while enhancements near 1.5 and 1.7 GeV are due to the $f_2'(1525)$ and $f_0(1710)$ respectively.

2.3.3 BESIII Collaboration

The BESIII Collaboration published a paper on $J/\psi \rightarrow \gamma K_S K_S$ with a sample of 1.3 billion J/ψ events[24]. A mass dependent (MD) and mass independent (MI) analysis were carried out in parallel. In the MD analysis the $\gamma K_S K_S$ system was modeled as a coherent sum of resonances. This analysis lead them to identify six 0^{++} and three 2^{++} resonances as well as the intermediate states $K^*(892)$ and $K_1(1270)$. In the MI analysis, the $K_S K_S$ mass is divided into 15 MeV bins and the amplitudes (which are functions of the angles) are extracted independently for each bin. Consistent with the MD analysis, only 0^{++} and 2^{++} amplitudes were found to be significant in the MI analysis. The $K^*(892)$ and $K_1(1270)$ were found to be spread over a wide range of the $K_S K_S$ mass and contribute little to any individual bin. In many bins two sets of distinct but ambiguous solutions were found. In Ref. [26] these ambiguities are attributed to rescattering effects and cannot

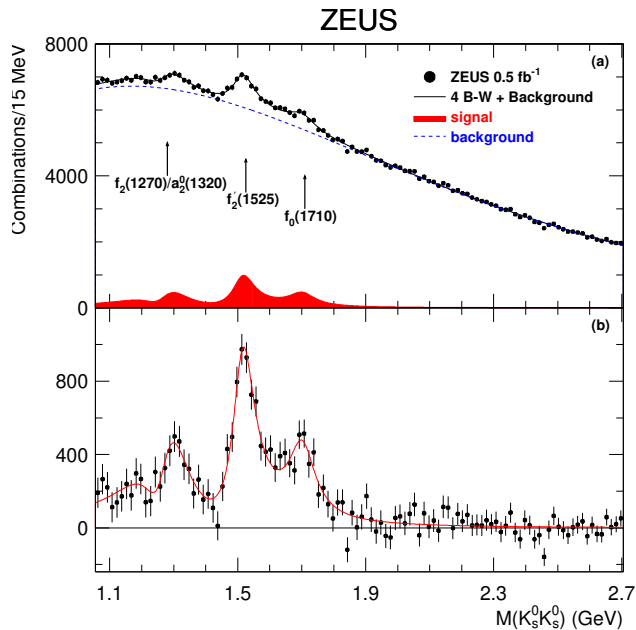


Figure 2.11: Invariant mass distribution of $K_S K_S$ published by ZEUS [23].

be resolved in a model independent way. Figure 2.12 shows a comparison between the MD and MI fits and show good overall agreement between the two approaches. The full list of resonances is provided in Table 2.3.

2.3.4 JPAC Collaboration

Using the Partial Wave Analysis performed by BESIII in $J/\psi \rightarrow \gamma K_S K_S$ [24] and $J/\psi \rightarrow \gamma \pi^0 \pi^0$ [26], JPAC conducted a coupled channel analysis[25]. Their analysis stressed the importance of satisfying (as much as possible) S-matrix principles such as unitarity and analyticity. One limitation to fully satisfy the properties of the S-matrix is the number of open channels that are available to resonances, for example the $f_2(1270)$ is known to decay to $\pi\pi$, $K\bar{K}$, $\eta\eta$ and 4π and all four channels would be required to fully satisfy the S-matrix principles. The available BESIII data for these other channels were deemed to be of lower quality and were excluded. However, fits with only the $\gamma\pi^0\pi^0$ and $\gamma K_S K_S$ data failed to reproduce some of the details of the resonant peaks. This led JPAC to include a third channel which is interpreted as a $\rho\rho$ channel and is not constrained by any data. The results of their analysis can be seen in Figure 2.13 and the resonances they identify are included in Table 2.3.

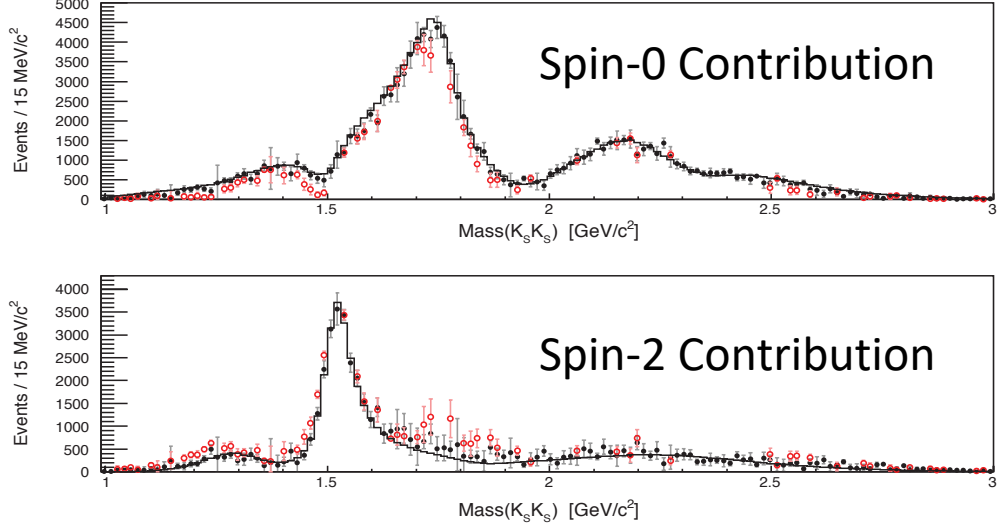


Figure 2.12: Comparison of mass dependent (MD) and mass independent (MI) analysis by the BESIII Collaboration[24]. The MD results are shown in solid black line while solid black markers and open red markers are ambiguous solutions for the MI analysis.

Table 2.3: Resonances identified in J/ψ decays by the analysis of BESIII and JPAC.

J^{PC}	BESIII[24]	JPAC[25]
0^{++}	$f_0(1370), f_0(1500), f_0(1710)$ $f_0(1790), f_0(2200), f_0(2330)$	$f_0(1500), f_0(1710), f_0(2020)$ $f_0(2330)$
2^{++}	$f_2(1290), f_2'(1525), f_2(2340)$	$f_2(1270), f_2'(1525), f_2(1950)$
others	$K^*(892), K_1(1270)$	—

The BESIII and JPAC analysis led a to qualitatively different picture of the resonance contents in these reactions. While BESIII identified 6 f_0 and 3 f_2 resonances in the $\gamma K_S K_S$ final state JPAC identified only 4 f_0 and 3 f_2 resonances when simultaneously analyzing the $\gamma K_S K_S$ and $\gamma \pi^0 \pi^0$ final states. Additionally, while BESIII observed the $f_2(2340)$ JPAC observed the $f_2(1950)$. This is a clear case of different models leading to different qualitative pictures of the resonance content in these reactions and in particular the difficulty in describing the spectrum of f_0 mesons.

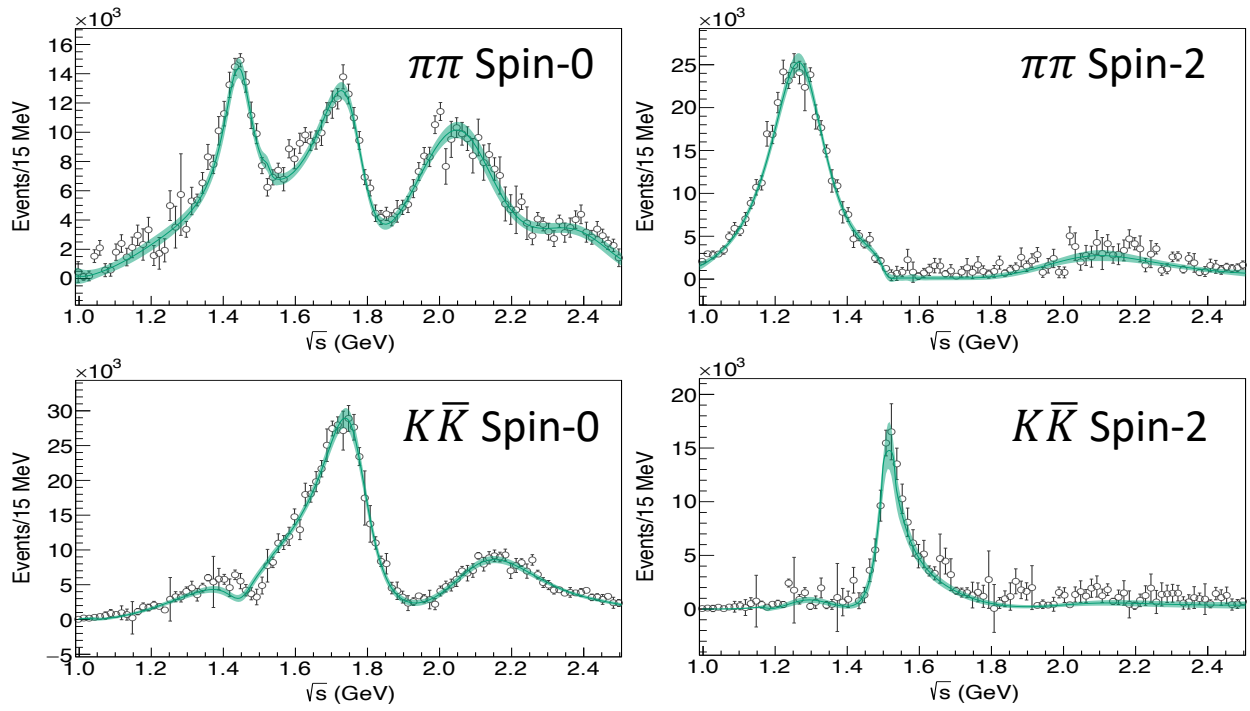


Figure 2.13: Coupled-channel fit by JPAC[25] to $J/\psi \rightarrow \gamma\pi^0\pi^0/\gamma K_S K_S$ BESIII [26, 24] data.

CHAPTER 3

THE GLUEX EXPERIMENT

The GlueX Experiment is housed in Hall D at the Thomas Jefferson National Accelerator Facility (JLab). A beam of energetic electrons is used to produce a tagged high energy linearly polarized photon beam incident on a liquid hydrogen target. The target is surrounded by a nearly hermetic detector capable of measuring both charged and neutral particles. In this chapter we describe the experimental setup from how we convert the electron beam to a photon beam with known energy and polarization to the detector system used to reconstruct a wide array of particles. The most complete description of the beamline and detector instrumentation is found in Ref. [33].

3.1 The Photon Beam

JLab houses the Continuous Electron Beam Accelerator Facility (CEBAF). CEBAF, see Figure 3.1, has the shape of a race track with two long linear accelerators (called North and South Linac) and two arcs. Electron bunches are produced by shining a laser onto a gallium-arsenide wafer. Magnets then direct these electrons into the North Linac. In the linacs, Radio Frequency (RF) cavities accelerate the electrons to higher energies. For Halls A, B and C the electrons can complete up to 5 turns before being redirected into the halls. For Hall D (where the GlueX Experiment is housed) electrons can complete another half turn before entering the hall. CEBAF is capable of supplying beam to all four halls simultaneously and electrons can reach energies up to 12 GeV.

Electron beam bunches are directed toward Hall D in 4 ns intervals. The electron beam is passed through a radiator in order to produce a photon beam, see Figure 3.2. Using a diamond radiator produces a linearly polarized photon beam while an aluminum radiator is used to produce an unpolarized photon beam. In both cases electrons emit photons through bremsstrahlung radiation by interacting with the radiator. After passing the radiator these electrons traverse a dipole magnet causing their trajectory to bend onto the tagger subsystems which determine the energy of the produced photons. The photon beam travels 75m reaching the collimator which focuses the beam. After being collimated the beam passes the Triplet Polarimeter (TPOL) and Pair Spectrometer

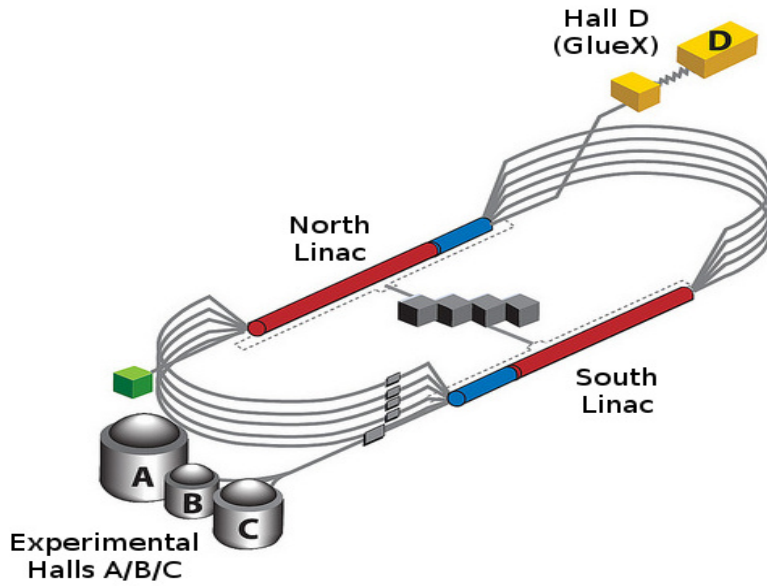


Figure 3.1: Schematic image of CEBAF and the four halls housed at Jefferson Lab.

(PS) where the degree of linear polarization and flux of the photon beam are determined. Finally the beam will either interact with the Liquid Hydrogen target, producing a reaction, or continue until it reaches the photon beam bump.

3.1.1 Producing a tagged photon beam

High energy electrons passing through a 20–60 μm thick diamond crystal radiator produce a linearly polarized photon beam through a process called coherent bremsstrahlung radiation. The

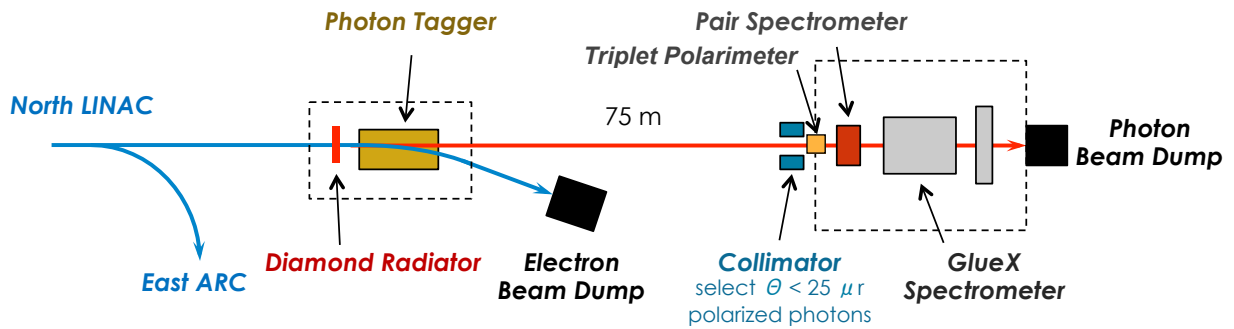


Figure 3.2: Diagram of the Hall D photon production beamline.

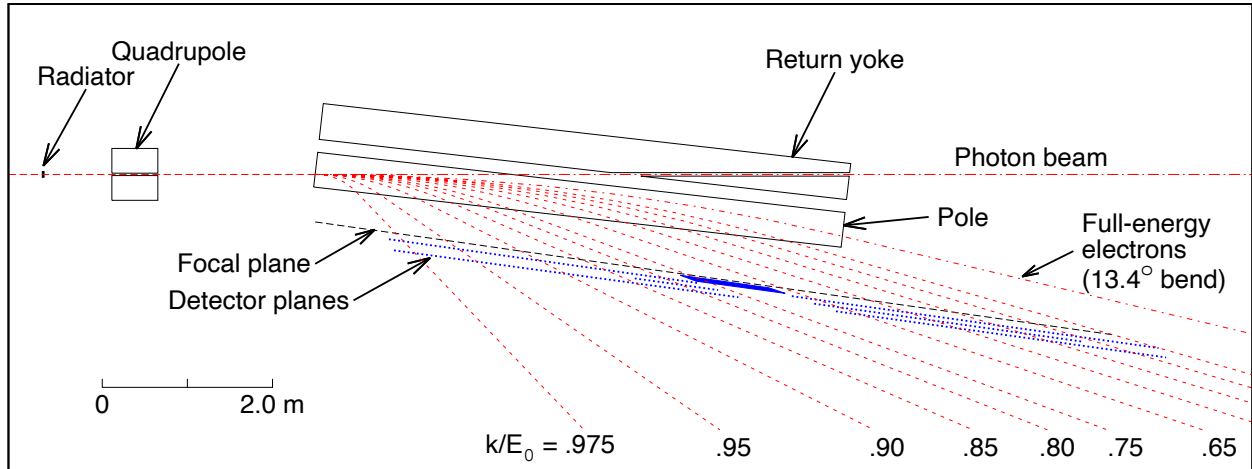


Figure 3.3: Schematic diagram of the tagger system.

angle between the linear polarization of the photons and the floor can be controlled by orienting the diamond radiator. When collecting data the diamond is cycled through four orientations: 0° , 45° , 90° and 135° (or -45°). If the diamond is oriented at $0/90^\circ$ we say it is in the PARA orientation while $-45/45^\circ$ is referred to as PERP orientation. By collecting data with different diamond orientations systematic effects may cancel out.

The aluminum radiator produces an unpolarized photon beam. After cycling through each diamond orientation data is collected with the aluminum radiator. Data taken with the aluminum radiator is useful when investigating if systematic effects are due to effects of the polarized beam.

Tagged photons. After passing through the radiator, electrons traverse a dipole magnet field causing their trajectory to bend onto the Tagger Hodoscope, Tagger Microscope or the electron beam dump. Electrons that emit a high (enough) energy photon are bent into the Tagger Hodoscope (TAGH) and Tagger Microscope (TAGM) to determine the energy of the produced photon, see Figure 3.3. While electrons that do not emit photons are directed towards the beam dump. The tagger system is divided into the TAGH and TAGM. Both taggers consist of arrays of scintillators that differ in resolution and cover different beam energy ranges. The TAGM is a high resolution hodoscope that covers a narrower photon energy range, for GlueX-I it covers $8.2 - 8.8$ GeV. This range corresponds to the *coherent peak*, where the degree of linear polarization and flux is highest, see Figure 3.4. The microscope is segmented into 102 energy columns of approximately equal width.

The TAGH covers 25% to 97% of the electron beam energy, approximately 3 to 12 GeV¹. Consisting of 222 scintillator counters distributed over 9.25 m the TAGH covers a larger area than the TAGM but with less precision.

3.1.2 Beam polarization and flux

Collimating the beam. The photon beam produced by the diamond radiator is a mixture of incoherent and coherent bremsstrahlung radiation. In the beam energy range where the polarization fraction is at its maximum the spread of coherent bremsstrahlung photons is less than that of incoherent bremsstrahlung. Collimating the beam before it enters the hall therefore blocks a larger portion of the unpolarized photons from entering the hall increasing the polarization fraction of the beam. The collimator used while collecting data had a 5 mm diameter aperture.

Measuring photon polarization. Photon polarization is measured via triplet photoproduction ($\gamma e^- \rightarrow e^- e^+ e^-$) of a beryllium foil. Triplet photoproduction occurs when the polarized photons interact with the electric field of an atomic electron in a beryllium target foil producing a high energy $e^+ e^-$ pair. The cross section for polarized triplet photoproduction is

$$\sigma_{triplet} = \sigma_0 [1 - P \Sigma \cos(2\phi)] \quad (3.1)$$

where σ_0 is the unpolarized triplet cross section, P the photon beam polarization fraction, Σ the beam asymmetry for the process², and ϕ the azimuthal angle of the recoil electron trajectory with respect to the plane of polarization for the incident photon beam. The polarization fraction can then be determined by measuring the final state electrons.

The polarization fraction is determined by combining information from the TPOL and PS detectors. The TPOL consists of a converter tray and positioning assembly which holds the beryllium foil in place. When triplet photoproduction occurs the recoiling electron is detected by a silicon strip detector (SSD) providing energy and azimuthal angle information for the (slow) recoiling electron. The high energy electron pair are steered toward the PS by a 1.8 T dipole magnet. This detector is composed of two arms each with two layers, see Figure 3.5. The first layer is formed by two high resolution hodoscopes called PS-A and PS-B. Each hodoscope consist of 145 stacked scintillator tiles that are read out by silicon photomultipliers. The second layer is formed by the PS

¹Excluding the range covered by the TAGM.

²At 9 GeV Σ has been measured to be 0.1990 ± 0.0008 for the GlueX beamline using a 75 μm beryllium foil[63].

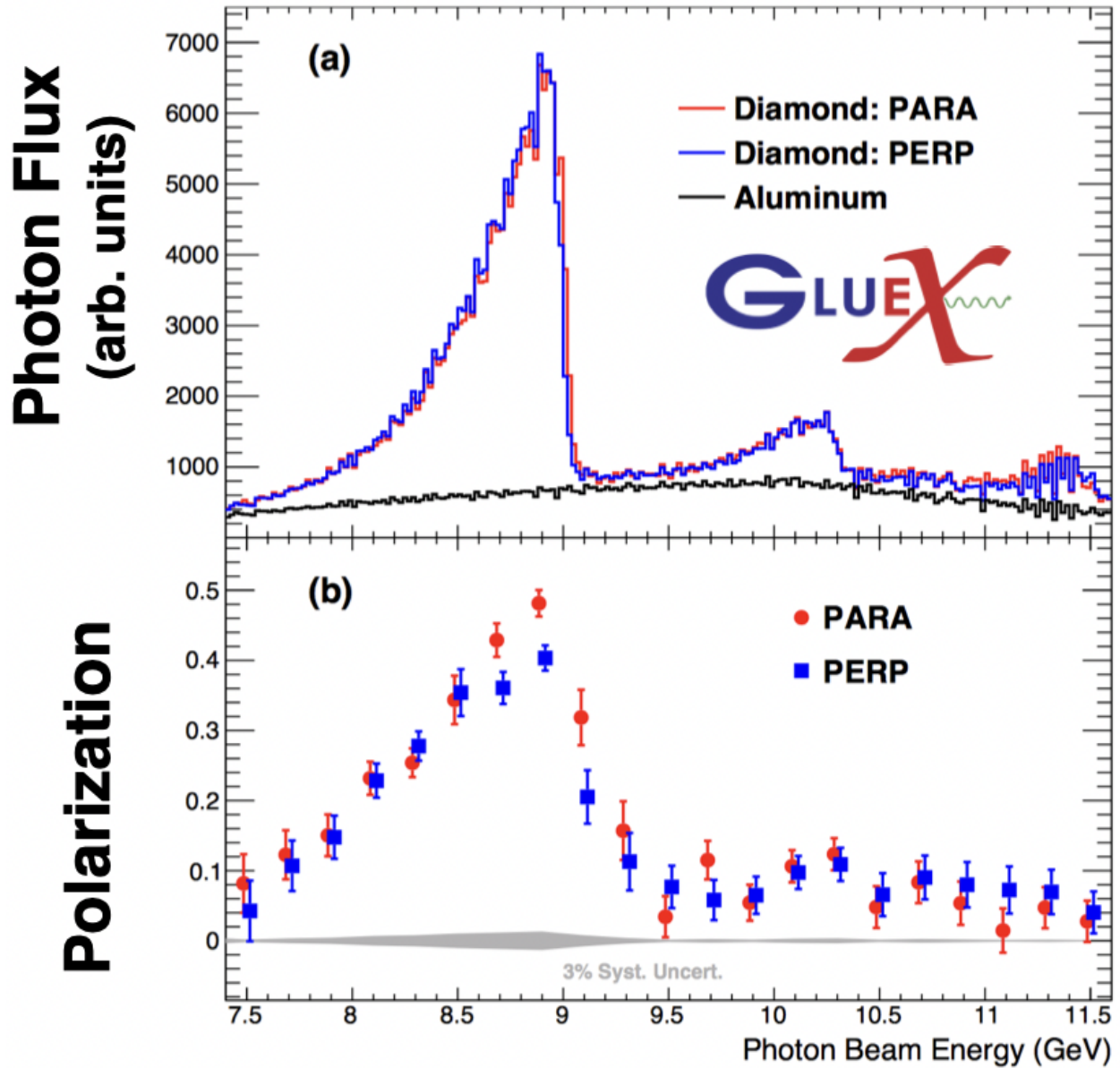


Figure 3.4: (Top) Photon flux as a function of beam energy for PARA ($0/90^\circ$) and PERP ($-45/45^\circ$) diamond orientations and for the aluminum radiator. (Bottom) Polarization fraction as a function of beam energy for PARA and PERP diamond orientations, the aluminum radiator produces an unpolarized photon beam. An increase in the photon flux is seen where the polarization fraction is enhanced. We refer to the beam energy range between 8.2–8.8 GeV as the coherent peak.

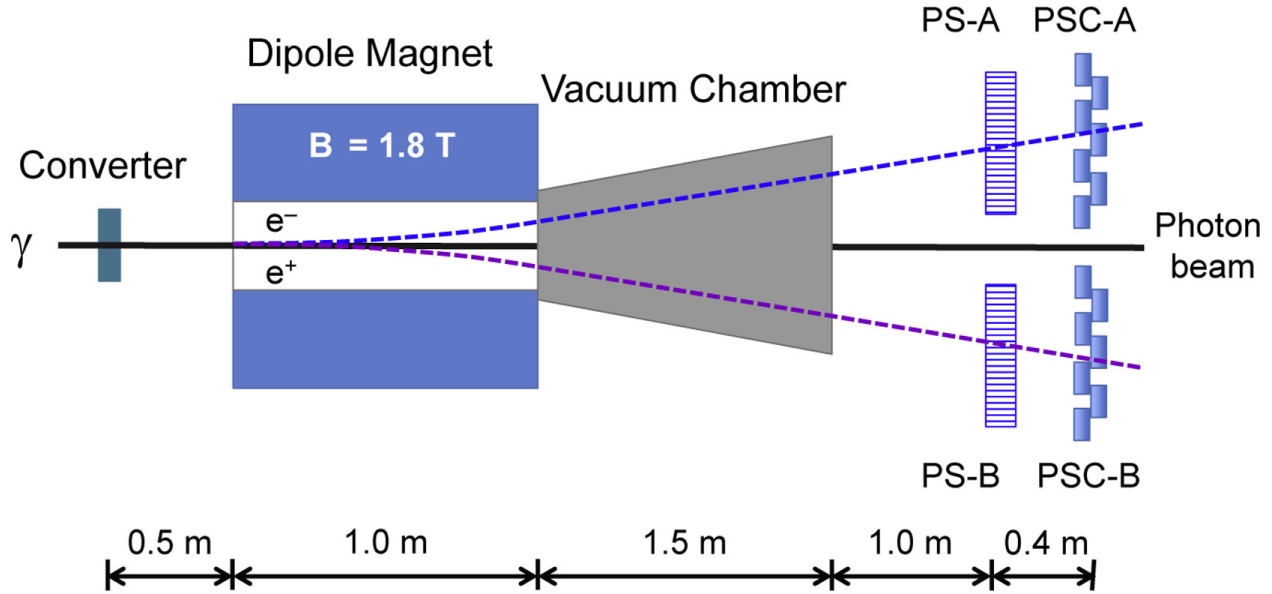


Figure 3.5: Schematic of the Pair Spectrometer. Figure taken from Ref. [27].

coarse counters called PSC-A and PSC-B. Each PSC consists of 16 scintillating counters used to trigger on e^+e^- pairs. When a trigger occurs, data is recorded from the PS hodoscopes and TPOL and used to measure the polarization fraction of the beam.

Measuring the photon flux. The photon flux is determined by converting a known fraction of the photon beam to e^+e^- pairs and counting them in the PS as a function of energy. The total number of beam photons is determined by the TAGH and TAGM systems described previously. The PS is able to reconstruct photon energies from 6–12.4 GeV.

3.2 GlueX Detector

In the path of the photon beam is a stationary liquid hydrogen (LH_2) target enclosed in a chamber. The target is surrounded by the Start Counter (SC), Central Drift Chamber (CDC), Barrel Calorimeter (BCAL), and a superconducting solenoid magnet, See Figure 3.6. Down stream of the target are the Forward Drift Chamber (FDC), DIRC, Time of Flight (TOF) and Forward Calorimeter (FCAL). Next we describe the target, solenoid and each detector that forms the GlueX Spectrometer.

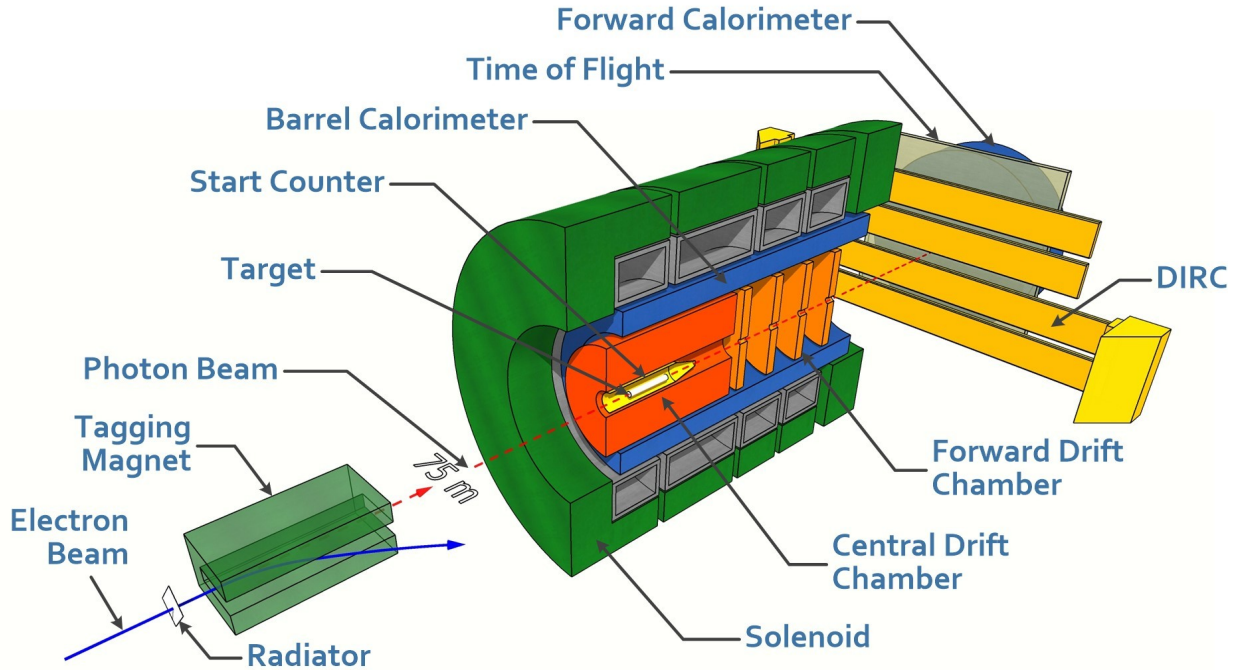


Figure 3.6: Schematic of the GlueX beamline and spectrometer.

3.2.1 Solenoid Magnet

The target, SC, CDC, FDC and BCAL are surrounded by a superconducting solenoid magnet with a inner diameter of 1.85 m and length 4.8 m in length, see Figure 3.6. During nominal running conditions a 1350 A current runs through the solenoid producing a ~ 2 T magnetic field along the axis central of the solenoid. The photon beam passes through the central axis of the solenoid.

The magnet consists of four superconducting coils which produce the magnetic field and four cryostats which maintain the coils at 4.5 K during nominal running conditions. Calculations of the expected magnetic field have been compared to measurements. Along the central axis the maximum deviation of the measured magnetic field (compare to the calculated magnetic field) is 0.2%. The largest deviation is 1.5% and is seen downstream at large radii. These deviations do not noticeably affect the charged particle track momentum resolution since the resolution of the GlueX Spectrometer is larger than 1%.

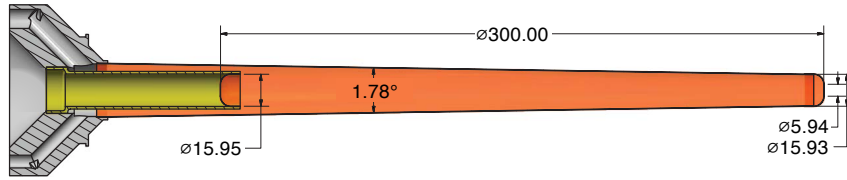


Figure 3.7: Liquid hydrogen target cell. Dimensions are in mm.

3.2.2 Target and Start Counter

The Target is made of liquid hydrogen (LH_2) and is positioned along the path of the photon beam. The target cell is 30 cm long, see Figure 3.7, and contained within a vacuum chamber. In nominal run conditions the target operates around 18° K and 18 psi. The walls where the photon beam enters and leaves the target chamber are made of polyimide foils which are $100 \mu\text{m}$ thick.

3.2.3 Charged Particle Reconstruction

The Central Drift Chamber is a cylindrical straw-tube drift chamber which provides information on position, timing and energy loss for charged particles. The CDC is situated between the SC and BCAL, see Figure 3.6, covering 6° to 168° in the polar angle. It consists of 28 layers of straw tubes, 12 of which are placed parallel to the beam and 16 are at stereo angles of $\pm 6^\circ$, see Figure [28]. Each straw tube has a $20 \mu\text{m}$ diameter wire running down the middle and filled with a 50:50 admixture of Argon to carbon dioxide gas. During nominal run conditions the wires are held at ~ 2100 V. When charged particles pass through a straw tube the gas is ionized. These ionized particles are attracted toward the charged wire producing a pulse which is read out. The spacial resolution of the CDC is $130 \mu\text{m}$ if the particle passes within 4 mm of the wired held inside the tube. The reconstruction efficiency is 98%.

The Forward Drift Chamber is located downstream of the target but still enclosed by the solenoid magnet, see Figure 3.6. It consists of 24 disc shaped planar drift chambers of 1 m diameter which are grouped into 4 packages. Each chamber contains a wire plane and cathode planes on each side separated by 5 mm from the wire plane. The wire plane has two types of wires: a sense wire ($20 \mu\text{m}$ diameter) kept at ~ 2200 V and a field wire ($80 \mu\text{m}$ diameter) at -500 V which are separated by 5 mm. The cathodes are made of $2 \mu\text{m}$ copper strips on Kapton foil and is grounded.

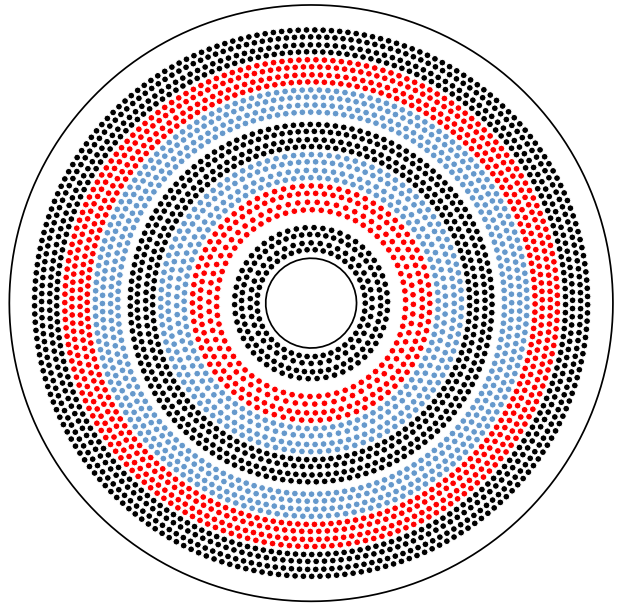


Figure 3.8: (Left) Picture of CDC before completion. (Right) Diagram of each CDC layer, straws parallel to the beam line are shown in black, straws with $+6^\circ$ stereo angle are shown in red and straws with -6° stereo angle are shown in blue. Figures taken from Ref.[28].

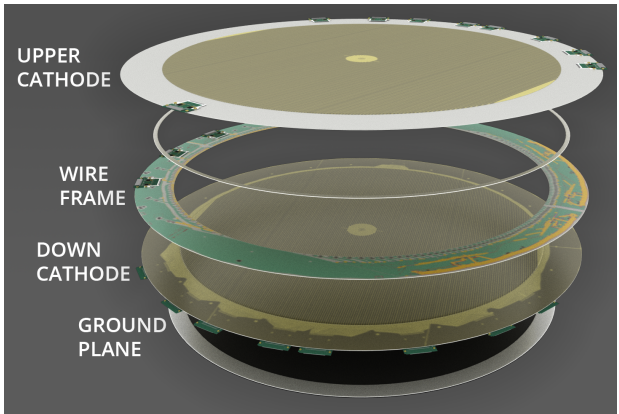


Figure 3.9: (Left) Picture of the fully assembled FDC. (Right) Rendition of one FDC chamber. From top to bottom: upstream cathode, wire frame, downstream cathode and ground plane that separates the chambers.

The two strips are arranged at 75° and 105° angles with respect to the wires. Within a group each chamber is rotated relative to the previous one by 60° . Each chamber is also filled with a mixture of 40% Ar and 60% CO_2 . The full detector covers from 1° to 10° and partial coverage up to 20° in the polar angle. The position resolution is between $140\text{--}240\ \mu\text{m}$ depending on where the hit occurs inside the chamber.

Track Reconstruction takes place in three stages. In the first stage, hits recorded in adjacent layers in the FDC are formed into track segments. These segments are then linked together with a helical model to form track candidates. Similarly, hits in adjacent rings in the CDC are formed into segments and multiple segments are connected to form track candidates. Candidates that originate from the target with $5^\circ - 20^\circ$ degrees are linked together using both the FDC and CDC.

In the second stage, a Kalman filter is used to estimate charged track parameters at the position of closest approach of the track to the beam line. The Kalman filter starts with the hit which is farthest from the beam line and proceeds step by step toward to the closest hit. During this process energy loss and multiple scattering are taken into account according to a map of the magnetic field. Each track is assumed to occur due to a pion unless the track has less than 0.9 GeV momentum in which case it is attributed to a proton.

The final stage matches the fitted tracks obtained in stage two with the Start Counter, Time-of-Flight, Barrel Calorimeter or Forward Calorimeter to determine the start time of a given track. With this the drift time can be determined for each wire that has been associated with the track. Incorporating the drift time each track is refitted using the Kalman filter but this time the hypothesis for e^\pm , π^\pm , K^\pm , p and \bar{p} are all considered.

3.2.4 Neutral Particle Reconstruction

The Barrel Calorimeter envelops the central and forward drift chambers and is surrounded by the solenoid magnet. It has the shape of an open cylinder and was constructed as a lead and scintillating-fiber matrix, see Figure 3.10. The detector is 390 cm long with an inner radius of 65 cm and outer radius of 180 cm. In the azimuthal angle it is segmented into 48 modules and each module is divided 10 times in the radial direction. The target is placed in the backward part of the cylinder covering $11^\circ - 126^\circ$ in the polar angle and complete coverage in the azimuthal angle. This electromagnetic calorimeter can detect photon showers with energies between 0.005 GeV and a few GeV. The resolution of this detector was determined by studying π^0 and η production and

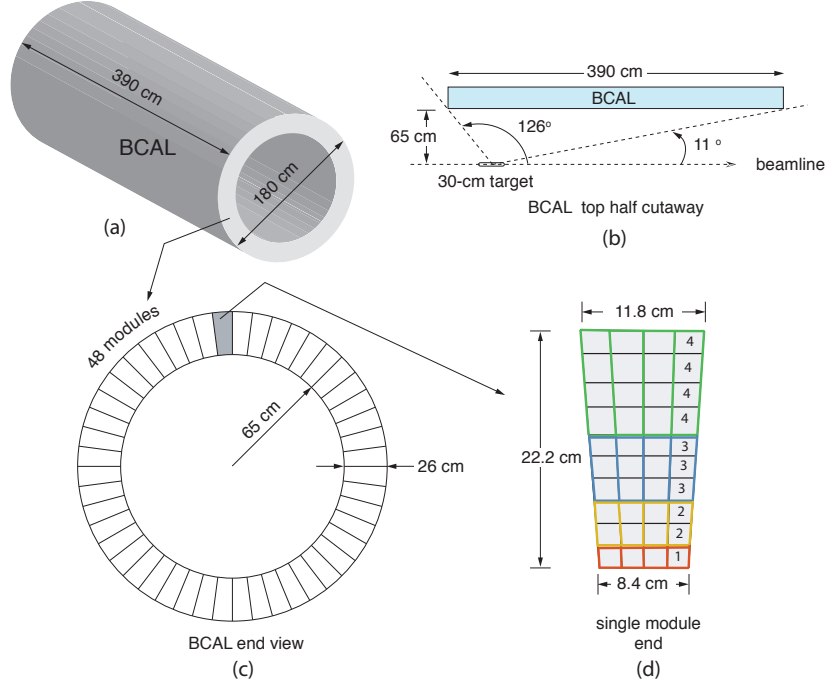


Figure 3.10: Three dimensional rendition of the BCAL. Figure taken from Ref. [29].

was determined to have an energy and spatial resolution of $\sigma_E/E < 10\%$ and 150 ps at 1 GeV respectively.

The Forward Calorimeter is located 5.6 m downstream from the center of the target and stands outside of the solenoid. It is a circular array of 2800 stacked lead glass blocks with a hole in the center to allow the photon beam to pass, see Figure 3.11. Each lead glass has a cross sectional area of 4×4 cm and are 45 cm in length. For each lead block a photo-multiplier tube (PMT) is connected in the back, see Figure 3.11. The FCAL can detect photons energies ranging from 0.1 GeV to several GeV and covers $1^\circ - 11^\circ$ in polar angle.

3.2.5 Particle Identification

The Start Counter envelopes the target and covers $\sim 90\%$ of the solid angle for particles originating from the center of the target, see Figure 3.12. This system consists of 30 scintillator paddles arranged in a cylinder shape with a radius of 7.8 cm, at the downstream end the SC radius shrinks to 2.0 cm. The SC is used for two purposes. The main purpose of this detector is to select the beam bunch that generated the tagged photon which induced the reaction of interest. The

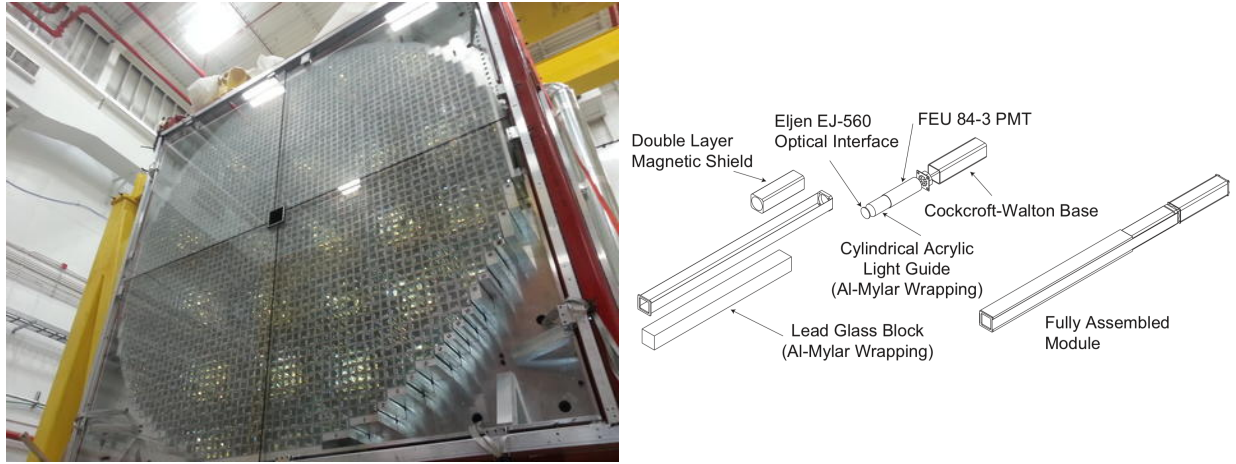


Figure 3.11: (Left) Picture of the FCAL inside Hall D. (Right) Components of an FCAL block.

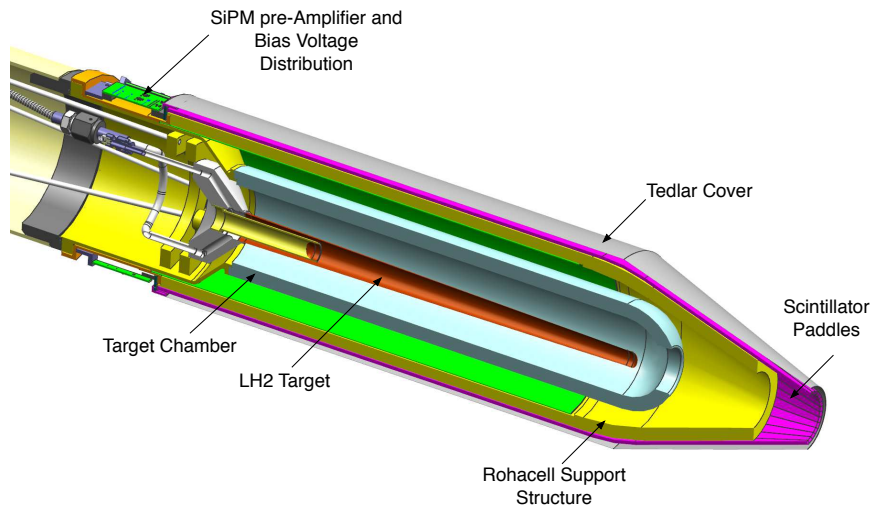


Figure 3.12: Start Counter and target. The photon beam exits through the conically shaped end of the SC, see Ref. [30].

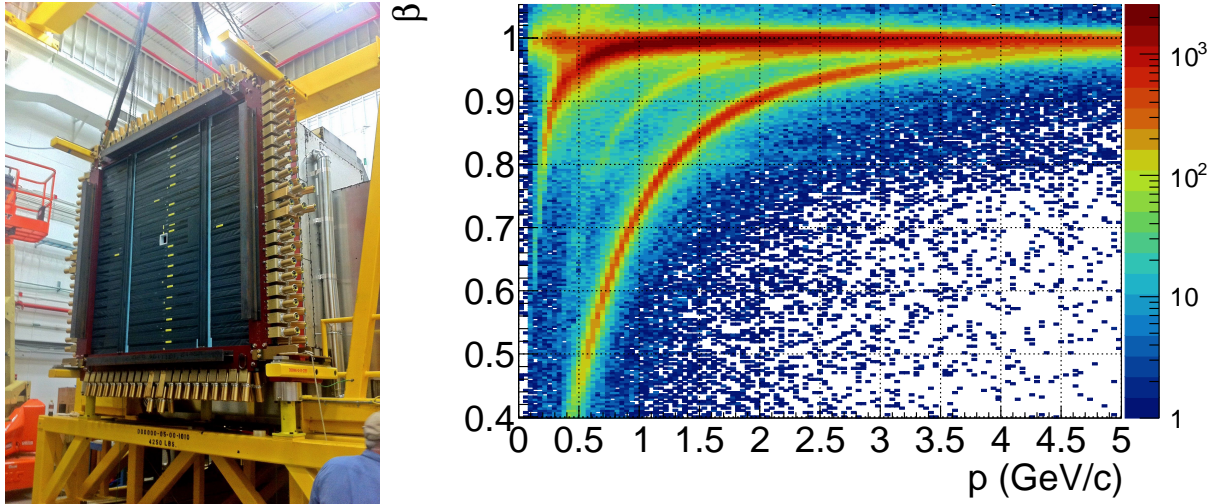


Figure 3.13: (Left) Picture of TOF being lifted into place. (Right) Velocity vs. momentum of positively charged tracks. Bands correspond to e^+ , π^+ , K^+ and p for the TOF detector.

average time resolution is about 234 ps. The secondary use of the SC is to identify protons with momentum of up to 0.9 GeV.

The Time of Flight is located ~ 5.5 m downstream of the target between the DIRC and FCAL. It is a wall formed by two layers of scintillators with a 12×12 cm² aperture at the center, see Figure 3.13. Each layer is made of a plane of stacked scintillator paddles with one being oriented horizontally and the other vertically. In the center region (where the aperture is located) the paddles are 120 cm long, 6 cm wide and 2.54 cm thick. A PMT is attached at the outer end for read out. Paddles outside the beam hole are longer at 252 cm but have the same width and thickness at 6 cm and 2.54 cm respectively. These paddles have PMTs connected at each end of the paddle. This detector covers 0.6° to 13° in the polar angle and has a timing resolution of ~ 100 ps. Figure 3.13 shows a plot of velocity vs. momentum for positively charged tracks detected by the TOF. Starting at the top left these bands are due to positrons, pions, kaons and protons. Kaons and protons can be identified with high certainty up to 2 and 4 GeV in momentum respectively.

3.2.6 The DIRC detector

In 2019 the GlueX detector was upgraded with the DIRC (Detection of Internally Reflected Cherenkov radiation) detector, shown in Figure 3.14, in order to improve charged π/K separation

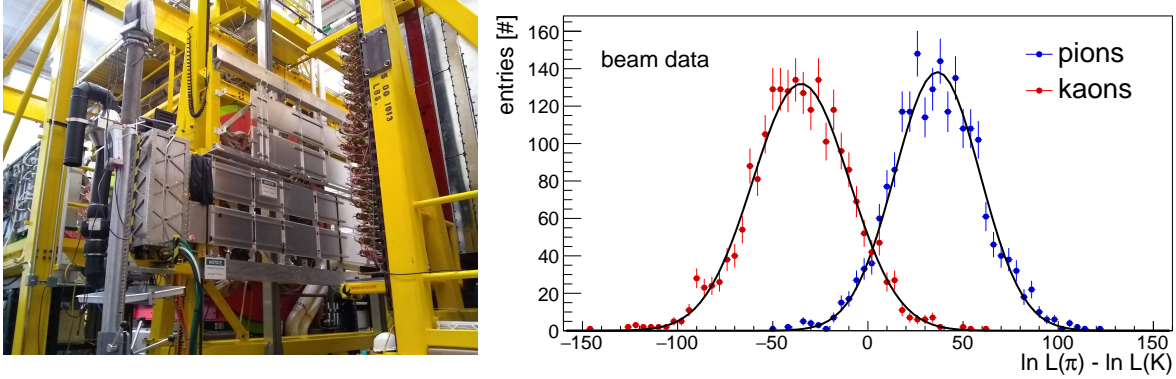


Figure 3.14: (Left) Picture of the installed DIRC detector, figure taken from Ref. [31]. (Right) Log-likelihood difference distribution for 4000 π/K events with 3.5 GeV momentum. The π/K separation is at a 3σ level. Figure taken from Ref. [32].

with momentum up to ~ 4 GeV. This upgrade marks the end of the Phase-I and begin of Phase-II of data collection by the GlueX Experiment. The first batch of Phase-II data has been collected and is approximately the same size as all of Phase-I.

The GlueX DIRC consists of four unmodified bar boxes originally used by the BaBar Experiment at SLAC[64]. Each box contains twelve 4.9 m long fused silica radiator bars attached to two newly constructed compact photon expansion volumes which are filled with distilled water. When charged particles travel through a dielectric material, like water, they emit photons. Mirrors focus these photons on an array of Multi-Anode Photomultipliers (MaPMTs). Each MaPMT has 64 pixels and each pixel has 6×6 mm² area. The total number of readout channels is 11520. The photon timing resolution is ~ 0.8 ns. As seen in Figure 3.14, when including the DIRC for 3.5 GeV momentum pions and kaons can be identified with 3σ confidence.

3.2.7 Trigger and Data Acquisition

When the experiment runs data is collected when a set of trigger conditions are satisfied. There are two main triggers. The first is the PS trigger which was discussed earlier. The second main trigger is called the physics trigger which required that the energy deposited in the FCAL and BCAL satisfy one of the following conditions:

- $2 \times E_{FCAL} + E_{BCAL} > 1$ GeV, $E_{FCAL} > 0$ GeV
- $E_{BCAL} > 1.2$ GeV.

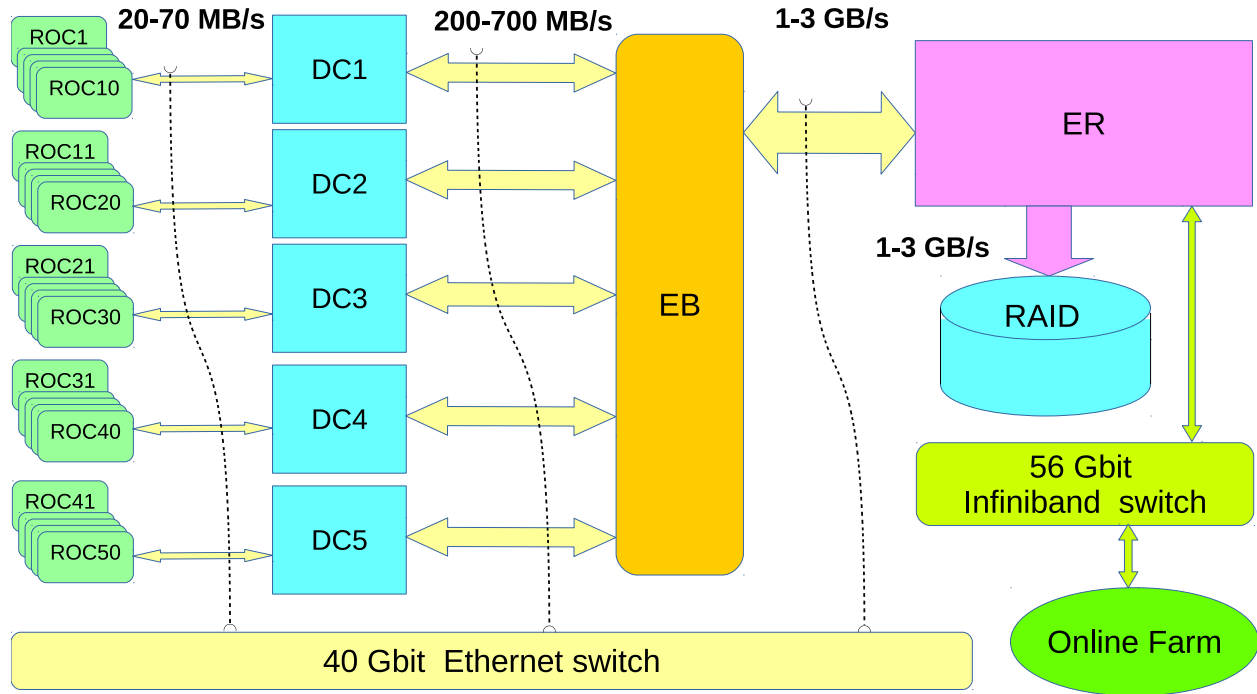


Figure 3.15: Schematic data acquisition system for GlueX [33].

The first condition is motivated by the fact that most events produce forward going energy. The second trigger type is important for accepting events with large transverse energy deposited in the BCAL. Other trigger conditions were also implemented for the purpose of efficiency studies and detector calibration.

Events that satisfy the trigger conditions enter the data acquisition system (DAQ), see Figure 3.15. First they enter the readout controller (ROC) which transfers data to the Data Concentrators (DC) at a rate of 20–70 MB/s. DC are programs that build partial events received from several crates. These partially reconstructed events are routed to the Event Builder (EB) at a rate of 200–700 MB/s to build complete events. The Event Recorder (ER) writes data to local data storage. All nodes are connected to a 40 Gb Ethernet switch and a 56 Gb Infiniband switch. The ethernet switch is exclusively used to the DAQ while the Infiniband switch is used for online data quality monitoring.

CHAPTER 4

DATA ANALYSIS

4.1 Overview

In this work, we have two final states of interest

$$\gamma p \rightarrow K_S K_S p \rightarrow \pi^+ \pi^- \pi^+ \pi^- p$$

and

$$\gamma p \rightarrow K_S K_L p \rightarrow \pi^+ \pi^- (K_L) p.$$

Each reactions are depicted in Figure 4.1. In both cases charged pions and a recoil proton are detected by the spectrometer. K_S particles are identified via their decay to a $\pi^+ \pi^-$ pair, while K_L particles are treated as missing particles since they mostly decay outside the detector¹. Since the identification of $K_S \rightarrow \pi^+ \pi^-$ decays is crucial for both final states, the event selection criteria for both reactions share numerous similarities. For this reason we first describe and motivate event selections that will be used and later discuss the specific choices made for each reaction. To avoid repetition we will first discuss aspects of data analysis that are common to both reactions. Additionally, data selection for the $K_S K_L p$ final state will be divided into two parts:

1. $\phi(1020) \rightarrow K_S K_L$: this resonance is well separated from others leading to a cleaner experimental signature and will be studied in isolation.
2. The $K_S K_L$ mass spectrum above 1.10 GeV: above the $\phi(1020)$, background events are larger requiring stricter event selections and more care in dealing with background contributions.

4.1.1 Datasets and Simulation

Data collected by the GlueX Collaboration is scheduled to be taken in two phases referred to as GlueX-I and GlueX-II. The first phase of data collection was divided into three run periods which took place during Spring 2017, Spring 2018, and Fall 2018. The integrated luminosity for each run

¹The mean life of the K_L is $5.1 \cdot 10^{-8}$ s which gives a $c\tau \sim 15$ m. The detector BCAL is 1.85 m in diameter and the distance between the back of the BCAL and the end of the FCAL is ~ 6.50 m.

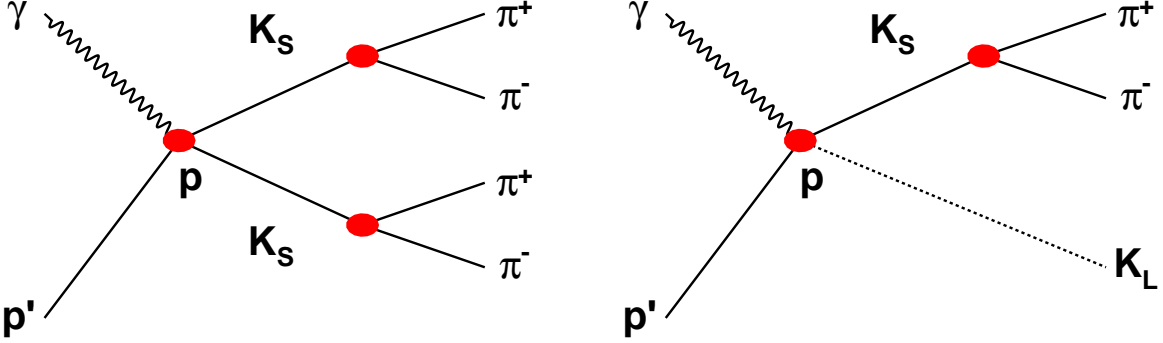


Figure 4.1: Diagram of reactions of interest. (Left) A photon incident on a stationary proton (p) interact producing a recoil proton (p') and two K_S particles at the production vertex (red circle). K_S particles travel some distance before decaying to a $\pi^+\pi^-$ pair, producing a detached vertex. (Right) A photon incident on a stationary proton produces a recoil proton, a K_S and a K_L at the production vertex. The K_L is not detected and the K_S again decays to a $\pi^+\pi^-$ pair.

in the coherent peak is 21.8, 63.0, and 40.1 pb^{-1} , respectively, which corresponds roughly to a ratio of 1:3:2. GlueX-II data is also planned to be collected in three run periods, two of which have been completed and the third is scheduled to start late 2024. Of the two completed run periods only the first is considered in this work which corresponds to an integrated luminosity of 132 pb^{-1} in the coherent peak. Roughly equivalent to the GlueX-I dataset in terms of integrated luminosity. Data collected for GlueX-I produced ~ 3 PB of raw data. The GlueX Collaboration centrally managed the process of turning raw data into Reconstructed Event Storage (REST) files, over 500 TB of data. A typical analysis reconstructs a reaction of interest from REST files based on a set of standardized criteria for particle identification. To facilitate this step the GlueX Collaboration centrally manages Analysis Launches to reconstruct reactions that members of the collaboration are interested in. Table 4.1 shows the Analysis Launch version for each data set that will be used in this work.

4.1.2 Beam energy and Mandelstam- t

The cross-section for a $2 \rightarrow 2$ process, such as $\gamma p \rightarrow Xp$, may be expressed as a function of the Mandelstam variables s and t . The Mandelstam s is the total center of mass energy, which for a

Table 4.1: Summary of datasets used for each analysis.

Run Period	REST Version	Analysis Launch	REST Version	Analysis Launch
Reaction	$\gamma p \rightarrow K_S K_{LP}$		$\gamma p \rightarrow K_S K_{Sp}$	
2017-01	3	Version 60	3	Version 55
2018-01	2	Version 22	2	Version 22
2018-08	2	Version 20	2	Version 19
2019-11	1	Version 9	1	Version 4

Table 4.2: Summary of simulation samples. More details of the MCWrapper configuration can be found on the MCWrapper Records webpage.

Run Period	MCWrapper Project IDs	Software Version XML
	$\gamma p \rightarrow \phi(1020)p$	
2017-01	3406	recon-2017_01-ver03_35.xml
2018-01	3407	recon-2018_01-ver02_28.xml
2018-08	3408	recon-2018_08-ver02_27.xml
	$\gamma p \rightarrow K_S K_{LP}$	
2017-01	3480	recon-2017_01-ver03_35.xml
2018-01	3124	recon-2018_01-ver02_26.xml
2018-08	3136	recon-2018_08-ver02_25.xml
	$\gamma p \rightarrow K_S K_{Sp}$	
2017-01	2609	recon-2017_01-ver03_35.xml
2018-01	1923	recon-2018_01-ver02_28.xml
2018-08	1922	recon-2018_08-ver02_27.xml

photon beam incident on a stationary proton target is²

$$s = (p_\gamma + p_{proton})^2 = 2E_\gamma m_p + m_p^2 \quad (4.1)$$

where p_γ is the photon 4-momentum, p_{proton} is the target proton 4-momentum, E_γ is the photon energy and m_p is the proton mass³. The analysis of this dissertation requires a linearly polarized photon beam. As seen in Figure 3.4, the degree of linear polarization is maximum in the coherent peak ($E_\gamma = 8.2 - 8.8$ GeV). Therefore, we only consider data in this beam energy range. This fixes the Mandelstam s variable.

²In natural units $c = 1$.

³The mass of the proton is 0.938 GeV.

Since the cross-section is a function of s and t it is now natural to study the production of mesons as a function of t . We define t as

$$t = (p_{recoil} - p_{target})^2 \quad (4.2)$$

where p_{recoil} is recoiling proton 4-momentum and p_{target} is the target proton 4-momentum. At 8.5 GeV, beam energy meson production is dominated by t-channel exchange. The momentum transfer for processes that occur through t-channel exchange is empirically known to follow an exponential decay. For the $\phi(1020)$, we will see that the exponential slope is $\sim 4.4 \text{ GeV}^2$. Additionally, baryon production tends to occur at high momentum transfer. Because of this, our analysis will focus up to $\sim 1 \text{ GeV}^2$ in momentum transfer. At very low t there is not enough momentum transferred to the recoiling proton and typically does not reach the drift chambers. We will see that this causes a sharp drop in acceptance typically around $-t \lesssim 0.1 \text{ GeV}^2$.

4.1.3 Accidental Subtraction

The electron beam enters Hall D in a beam bunch every 4 ns and tagged photons can be correctly matched to the beam bunch that produced it. However, multiple photons can be produced by a single beam bunch. If more than one photon is produced with similar energy then it may not be possible to determine which photon produced the event (even after event selections). Photons that are consistent with an event but did not produce the event are called accidentals. Since all photons are produced independently there is no difference between accidental photons produced by the same beam bunch (called in-time) and those produced in a different beam bunch (called out-of-time). We can estimate the amount of accidentals by purposely matching an event detected by the spectrometer with out-of-time photons. If all electron bunches that enter the hall are identical then the number of accidentals events that are in-time is the same as out-of-time events. However, not all electron beam bunches are identical and an additional scale factor must be applied to out-of-time events to correctly subtract accidental events. This run-dependent scale factor was determined in Ref. [65].

4.1.4 Missing Mass

Consider the reaction

$$\gamma p_{target} \rightarrow \pi^+ \pi^- p_{recoil} X_{miss} \quad (4.3)$$

where the initial state photon and proton and the final state π^\pm and recoil proton are all detected. Conservation of four-momentum dictates that the four-momentum of particle X_{miss} is

$$p_{miss} = p_\gamma + p_{target} - (p_{\pi^+} + p_{\pi^-} + p_{recoil}) \quad (4.4)$$

and the missing mass squared (MMS) is

$$MMS = |p_\gamma + p_{target} - (p_{\pi^+} + p_{\pi^-} + p_{recoil})|^2. \quad (4.5)$$

If there is no missing particle then $MMS \approx 0 \text{ GeV}^2$ indicates that we have fully reconstructed all final state particles in the reaction. In the case of a missing particle, it is more convenient to calculate the missing mass of the reaction which will peak at the mass of the particle of interest, if it is present.

Studying a reaction with a missing particle one needs to take great care that other final states are not contributing⁴. Two aspects of photoproduction help us in our studies of $K_S K_L$. First, the initial state (γp) has zero strangeness which is a conserved quantity in strong decays. Since K_S has a strange quark, detecting a K_S requires the production of a partner state with a strange quark. Second, aside from the K_S , the next lightest neutral kaon is $\sim 400 \text{ MeV}$ higher in mass than the K_L ⁵. The nearly identical mass of K_S and K_L means we cannot distinguish them via the missing mass. However, we can search for signs of a second K_S in the final state by looking for extra tracks (from a second $K_S \rightarrow \pi^+ \pi^-$) or extra showers (from $K_S \rightarrow \pi^0 \pi^0$) in the detector to exclude $K_S K_S p$ events when studying $K_S K_L p$.

4.1.5 Kinematic Fitting

Kinematic fitting is a technique that allows us to take the reconstructed 4-vectors of particles and construct new 4-vectors which incorporate our knowledge of the experimental apparatus and physical properties of the reaction, such as 4-momentum conservation. Working with the kinematically fitted 4-vectors has two main advantages. First, the new 4-vectors have improved resolution compared to the measured 4-vectors. Second, one obtains a χ^2 for each combination. If we try to reconstruct an event different from our hypothesis then the event will likely have a large χ^2 value or not converge at all. Reconstructing an event that matches our hypothesis would give a reasonable

⁴This is also true when all particles are reconstructed but typically having a missing particle carries more dangers and pitfalls.

⁵The three lightest neutral kaons are $K_S/K_L(497)$, $K^{*0}(892)$ and $K_1^0(1270)$ [3].

χ^2 value. Figure 4.2 shows the χ^2/ndf distribution for events with and without a K_S using bggen data for the $K_S K_L p$ final state. Events with a K_S have a small χ^2/ndf while events without a K_S follow a flat distribution going up to much larger χ^2/ndf .

For a given combination of an event let \mathbf{y}_0 be the four-momentum measured by the spectrometer, \mathbf{y} the fitted four-momentum, \mathbf{V} the covariance matrix that encodes the detector resolution, and \mathbf{F} the physical constraints imposed on the data. Then we can define a metric to minimize as

$$\chi^2 = (\mathbf{y} - \mathbf{y}_0)^T \mathbf{V}^{-1} (\mathbf{y} - \mathbf{y}_0) + 2\lambda^T \mathbf{F}. \quad (4.6)$$

For uncorrelated variables with Gaussian uncertainties, the χ^2 values will be distributed as

$$f_{\text{NDF}}(x) = \frac{x^{(\text{NDF}/2-1)}}{2^{(\text{NDF}/2)} \Gamma(\text{NDF}/2)} e^{-x/2} \quad (4.7)$$

where Γ is the Gamma function and NDF is the number of degrees of freedom. Because particles are experimentally defined by their 3-momentum vector a final state with N particles will be defined by $3N$ quantities. If we called N_m the number of measured momentum and N_C the number of constraints on the fit, then

$$\text{NDF} = N_C + N_m - 3N. \quad (4.8)$$

Introducing the number of unknowns $N_u = 3N - N_m$, Eq. 4.8 can be rewritten as

$$\text{NDF} = N_C - N_u. \quad (4.9)$$

In the case of the $K_S K_S p$ final state, the reaction is fully reconstructed ($N_u = 0$) and constraints include 4-momentum conservation and three vertices, see Figure 4.1, which give $\text{NDF} = 7$. In the case of the $K_S K_L p$ final state, we do not measure the 3-momentum of the K_L ($N_u = 3$) and constraints include 4-momentum conservation, two vertices, and the mass of the missing particle to be the K_L mass, this gives $\text{NDF} = 3$. For more details on kinematic fitting see Ref [66].

4.1.6 Flight Significance

Although much smaller than the K_L the K_S lifetime is large enough to travel a few centimeters producing a detached vertex⁶. We define the Flight Significance (FS) as

$$FS = \frac{|\vec{x}_{\text{proton}} - \vec{x}_{K_S^0}|}{\sigma_{K_S}} \quad (4.10)$$

⁶The K_S mean life is $\tau = 8.95 \cdot 10^{-11}$ s which gives a $c\tau \sim 0.00716$ m = 7.16 cm.

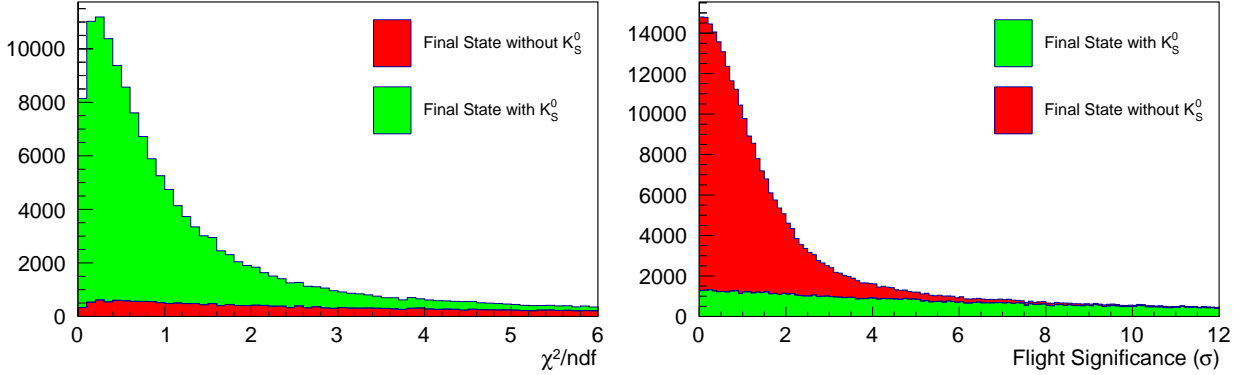


Figure 4.2: (Left) Kinematic fit χ^2 distribution for simulated channels with and without a K_S in the final state. (Right) Flight Significance for simulated data with and without a K_S in the final state.

where $\vec{x}_{\text{proton}}, K_S^0$ and $\sigma_{K_S^0}$ are, respectively, the vertex position 3-vector and vertex uncertainty of the indicated particle. Figure 4.2 shows the FS for events with and without a K_S using bggen data for the $K_S K_L p$ final state. Events without a K_S tend to have small FS while events with a K_S follow a slightly inclined distribution reaching much higher values.

4.1.7 Understanding Backgrounds with Monte Carlo

The photoproduction of hadrons at GlueX energies in most cases is not known well enough to produce realistic simulations of different final states. However, simulations can still be useful and instructive in understanding broad features of backgrounds that may contribute to our final state of interest. For this purpose, a PYTHIA [67] based generator, called bggen, was developed by the collaboration. For each reaction of interest, large simulated data samples generated with bggen will be used to identify background topologies that may contribute to our reaction of interest.

4.2 $\phi \rightarrow K_S K_L$ Event Selections

Here we describe the event selections used to isolate the reaction $\gamma p \rightarrow \phi(1020)p$. As we are only interested in studying the $\phi(1020)$ only events with $M(K_S K_L) < 1.1$ GeV will be considered. Throughout this section, we will compare data and MC for each variable discussed. Unless stated otherwise these comparison plots will have all final event selections, excluding the variable that is plotted. A green-shaded region will indicate the selection that will be placed on the data.

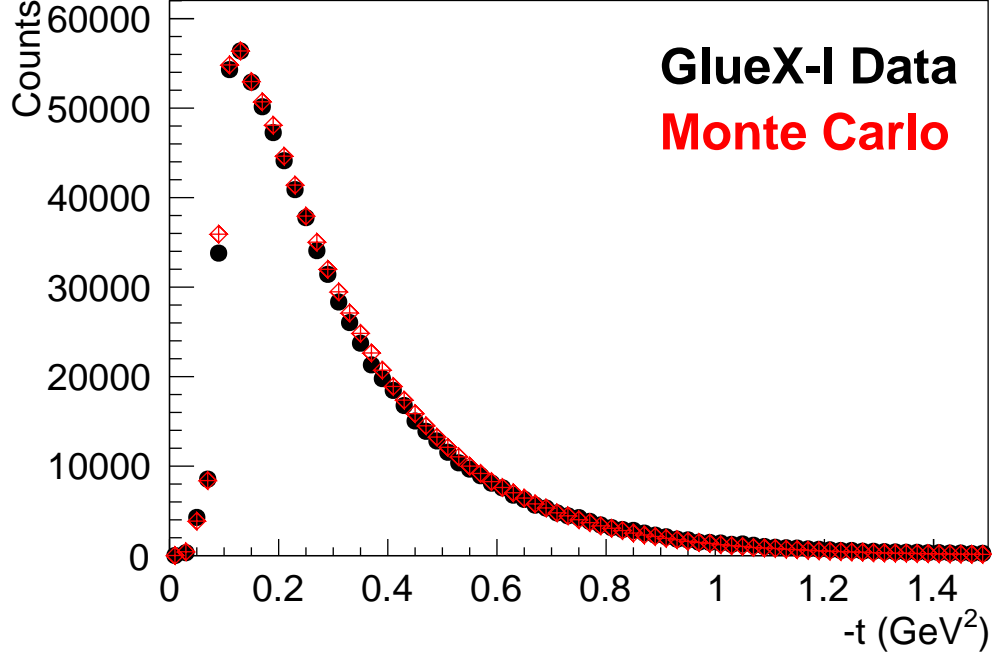


Figure 4.3: Mandelstam- t distribution for data (black) and scaled Monte Carlo (red) after all event selections. The Mandelstam- t distribution was modeled as e^{-bt} with $b = 4.4 \text{ GeV}^{-2}$.

4.2.1 Mandelstam- t

Figure 4.3 shows the Mandelstam- t distribution for data and MC. The MC is modeled as an exponential decay (e^{-bt}) with exponential slope $b = 4.4 \text{ GeV}^{-2}$. As mentioned in the previous section the distributions quickly drop to zero near $-t \sim 0.1 \text{ GeV}^2$ due to a sharp drop in acceptance.

4.2.2 Extra Tracks and Showers

Due to the nearly identical K_S and K_L masses the $K_S K_L$ and $K_S K_S$ final states are kinetically similar and cannot be distinguished by detecting a $K_S \rightarrow \pi^+ \pi^-$ decay and a missing particle with the K_L mass. The main decay modes of K_S are $\pi^+ \pi^-$ (69%) and $\pi^0 \pi^0$ (30%)⁷. Therefore, the two largest decay modes of $K_S K_S$ are $\pi^+ \pi^- \pi^+ \pi^-$ (48%) and $\pi^+ \pi^- \pi^0 \pi^0$ (41%). This leads to an 89% probability of $K_S K_S$ decaying to a final state compatible with our topology of interest.

To study $K_S K_S$ backgrounds we simulated the production of the $K_S K_L p$ and $K_S K_S p$ final states and reconstructed both the same way. The $K_S K_L$ MC used in this study is the Spring 2017

⁷Since the $\pi^0 \rightarrow \gamma \gamma$ branching fraction is 99% most $K_S \rightarrow \pi^0 \pi^0$ decays will produce ~ 4 showers.

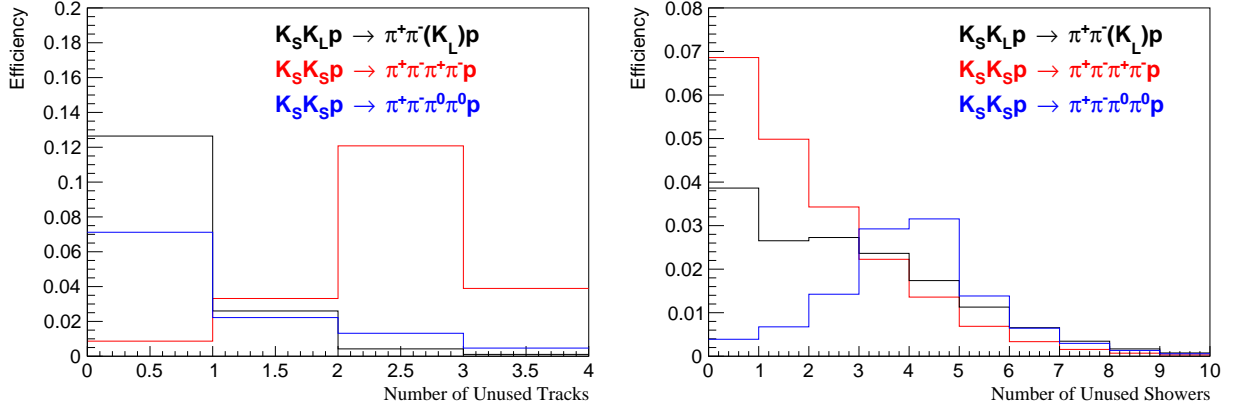


Figure 4.4: (Left) Number of unused charged tracks and (right) number of unused neutral showers for simulated $K_S K_L p$ and $K_S K_S p$ events.

simulation described in Table 4.2. Figure 4.4 shows the reconstruction efficiency as a function of number of unused tracks and neutral showers for reconstructed MC of $K_S K_L p$ and $K_S K_S p$. Decays from $K_S K_S$ to four charged pions tend to have 1–3 extra charged tracks. While decays with two π^0 in the final state tend to have 3 or more unused showers. Removing all unused charged tracks eliminates the $K_S K_S \rightarrow \pi^+ \pi^- \pi^+ \pi^-$ background. While keeping up to 2 unused showers largely removes the $K_S K_S \rightarrow \pi^+ \pi^- \pi^0 \pi^0$ background. This cut does not completely remove the $K_S K_S$ background, however, the $K_S K_L$ cross section is much larger than that of the $K_S K_S$ near the $\phi(1020)$. Figure 4.5 again shows the reconstruction efficiency as a function of number of unused tracks and showers but now with a selection no extra tracks or at most two extra showers as appropriate. Finally, Figure 4.6 compares the number of unused tracks and showers for data and MC. A good agreement between data and MC is seen for the number of unused tracks. Agreement for the number of unused showers distributions is not as good but we will see evidence that this disagreement does not significantly affect the angular distributions.

4.2.3 Missing Mass

As discussed previously, the final state K_L is treated as a missing particle and is indirectly identified via the missing mass. The missing 4-vector is defined as in Eq. 4.4 and the missing mass is $|p_{miss}|$. Figure 4.7 shows the missing mass in data and MC are in good agreement. We apply a

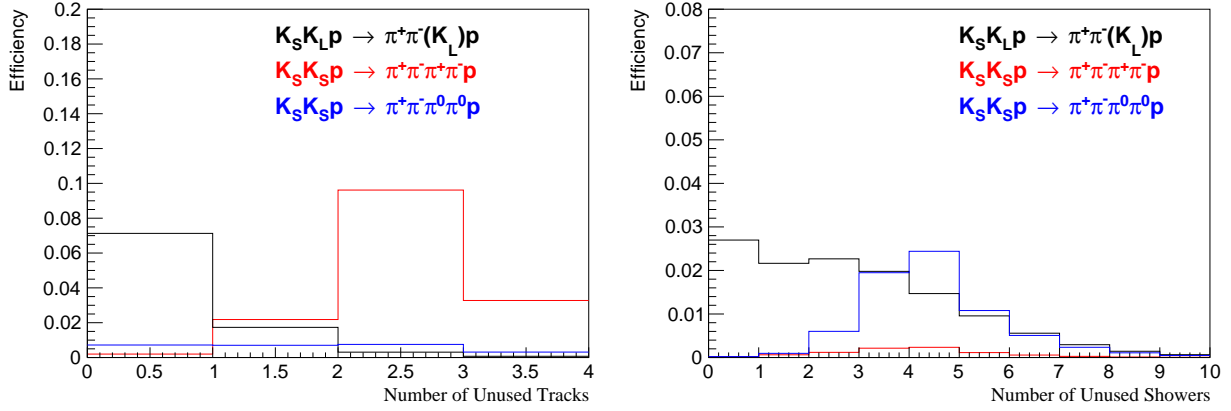


Figure 4.5: Same as Figure 4.4 with (left) at most two unused neutral showers and (right) zero extra charged tracks.

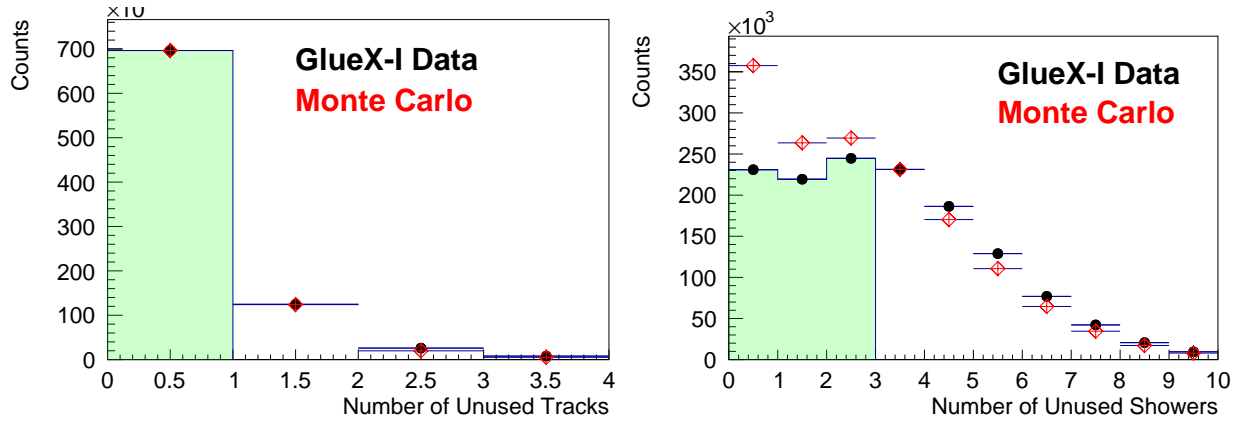


Figure 4.6: (Left) Number of unused tracks for data (black) and MC (red) are in good agreement after event selections. (Right) Number of unused showers for data (black) and MC (red) after event selections. This variable is not well modeled in MC but we will see evidence that this does not strongly affect the angular distributions. In both cases, the shaded green area indicates the selection that will be placed on the data.

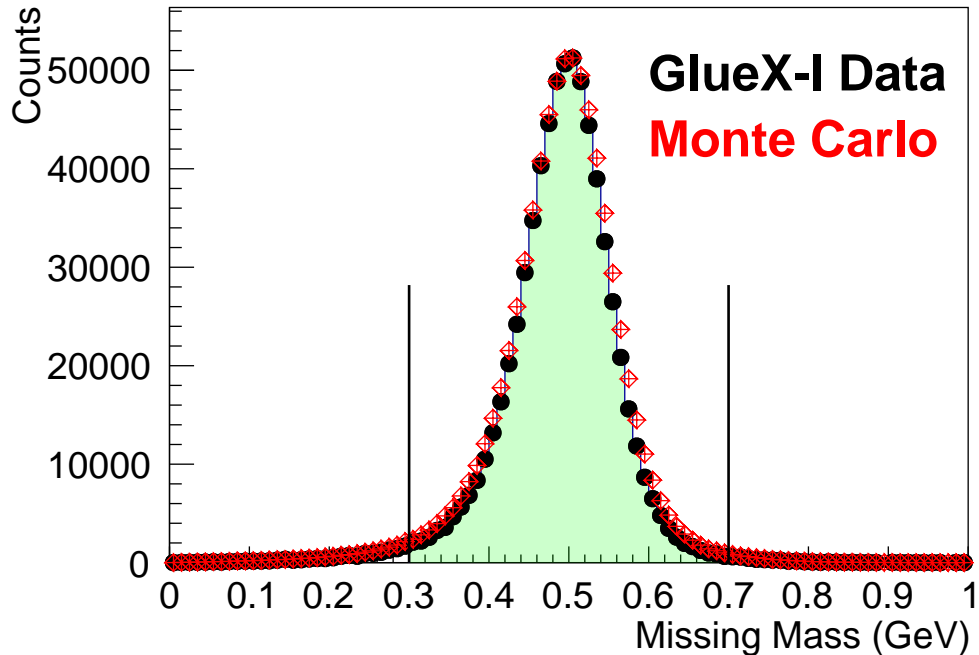


Figure 4.7: Missing mass for GLUEX-I data (black) compared to Monte Carlo (red) after all event selections. Vertical lines indicate the selection placed on this variable which removes 6.5% of the data.

loose selection on this variable and only consider events in the range

$$0.30 < |p_{miss}| < 0.70 \text{ GeV.}$$

4.2.4 Flight Significance and χ^2/ndf

As shown in Figure 4.2 events with no K_S in the final state concentrate at low FS. However, these types of events also have large χ^2 since they are more likely to be kinematically fitted with the wrong hypothesis. Due to this correlation between low FS and large χ^2 we choose to simultaneously optimize the placement of these event selections. Figure 4.8 shows the FS and χ^2/ndf distributions for data and MC with nominal event selections. The procedure we use to determine the FS and χ^2/ndf selection is as follows. We determine the signal (S) and background (B) in our data set⁸ by modeling the $\pi^+\pi^-$ invariant mass distribution as a sum of two normalized Gaussian functions

⁸Here we only discuss backgrounds from non- K_S events.

(for the signal) plus a 2^{nd} order polynomial (for the background). Explicitly

$$F(x) = \frac{N_1}{\sqrt{2\pi}\sigma_1} \exp\left\{-\frac{1}{2} \frac{(x - \mu_1)^2}{\sigma_1^2}\right\} + \frac{N_2}{\sqrt{2\pi}\sigma_2} \exp\left\{-\frac{1}{2} \frac{(x - \mu_2)^2}{\sigma_2^2}\right\} + a_0 + a_1x + a_2x^2 \quad (4.11)$$

where N_i , μ_i and σ_i are, respectively, the normalization, mean, and width of the i^{th} Gaussian and a_0 , a_1 and a_2 are the coefficients of the polynomial. In total, the fit has 9 parameters which are all allowed to vary freely. The mean and width of the signal distribution are calculated as a weighted average

$$x = \frac{N_1x_1 + N_2x_2}{N_1 + N_2} \quad (4.12)$$

where x is either the mean (μ) or width (σ). The amount of signal and background is determined by integrating the Gaussian and polynomial components of the fit in a 2σ window around the mean. Figure 4.9 shows an example fit to the $\pi^+\pi^-$ invariant mass distribution and a comparison between data and MC.

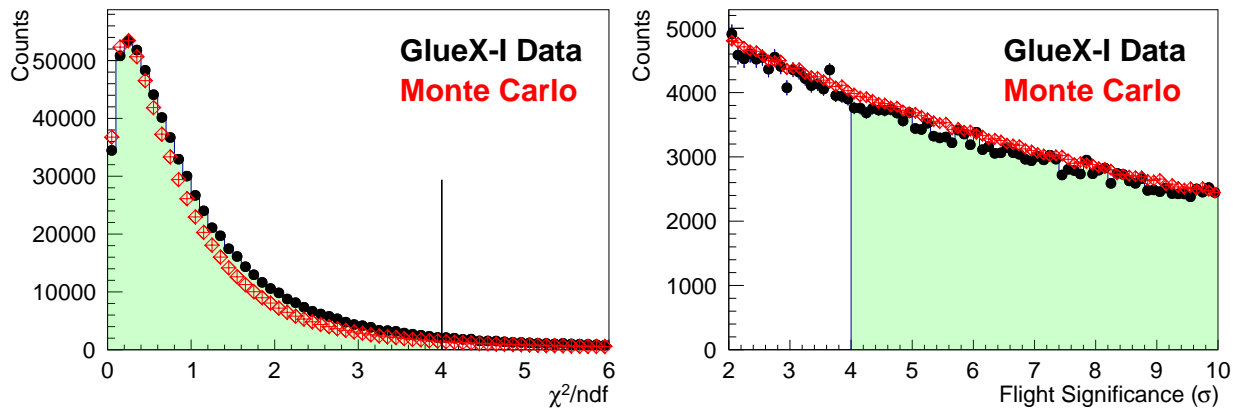


Figure 4.8: (Left) χ^2/ndf distribution for GlueX-I data (black) and Monte Carlo data (red). A vertical line indicates the selection that will be placed on the data. (Right) Flight Significance distribution for GlueX-I (black) and Monte Carlo (red). The shaded green area indicates the selection that will be placed on the data.

For each FS and χ^2/ndf selection, we calculate the signal-to-background ratio, significance ($S/\sqrt{S+B}$), and purity ($S/S+B$). Figure 4.10 shows the results of this analysis. The yield, signal to background, and significance all show a monotonic behavior. The purity on the other hand begins to flatten around a FS of 3.5σ . Choosing a FS greater than 4σ and a χ^2/ndf less than 4 gives a 98% purity while maximizing the yield.

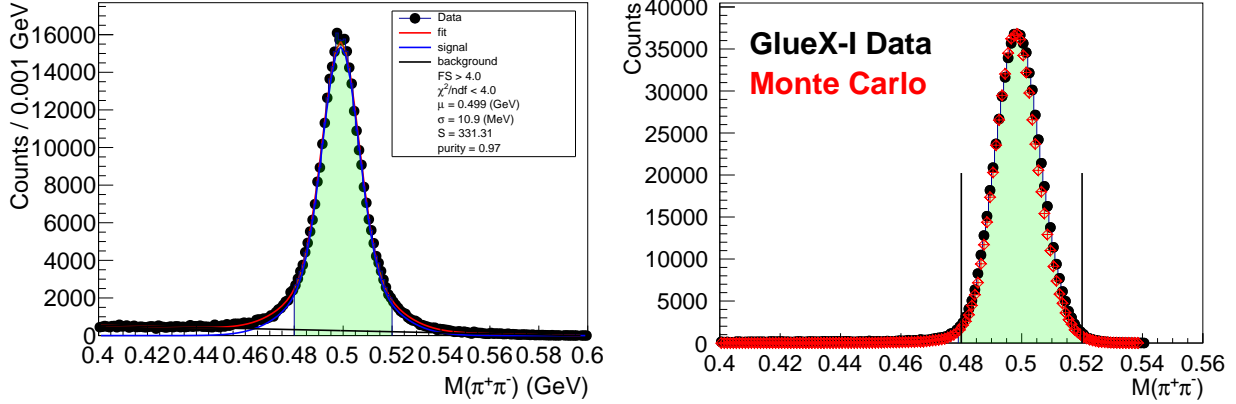


Figure 4.9: (Left) Fit to the $\pi^+\pi^-$ invariant mass spectrum with Eq. 4.11. The shaded green area indicated a 2σ window around the mean. This plot includes events with $M(K_S K_L) < 1.1 \text{ GeV}$. (Right) $\pi^+\pi^-$ invariant mass for GlueX-I data (black) and Monte Carlo (red) after cuts. This plot includes the event selection $1.005 < M(K_S K_L) < 1.04 \text{ GeV}$ and shows that background is negligible inside the $\phi(1020)$ region.

Table 4.3: Fraction of bggen events after nominal event selections in the range $0.99 < M(K_S K_L) < 1.075 \text{ GeV}$.

Topology	Fraction [%]
$\pi^+\pi^- K_L^0 p [K_S^0, \phi]$	97.14
$2\gamma\pi^+\pi^- p [\pi^0, \omega]$	0.98
$\pi^+\pi^- K_L^0 p [K_S^0]$	0.65
$\pi^+\pi^- p$	0.57
All others	0.66

4.2.5 Background Studies with bggen

In Section 4.2.2 we studied specifically the reconstruction of $K_S K_{SP}$ events as $K_S K_L p$. To study a broader spectrum of background channels we have used a sample generated with the bggen generator. The bggen simulations are a useful tool to identify other background channels. Figure 4.11 shows the $K_S K_L$ mass spectrum after applying nominal event selections, see Table 4.4. The total number of events is 39,505 of which 97.14% is the channel of interest, 2.21% are non- $K_S K_L$ events and 0.65% are $K_S K_L$ events that do not come from $\phi(1020)$ decays, see Table 4.3.

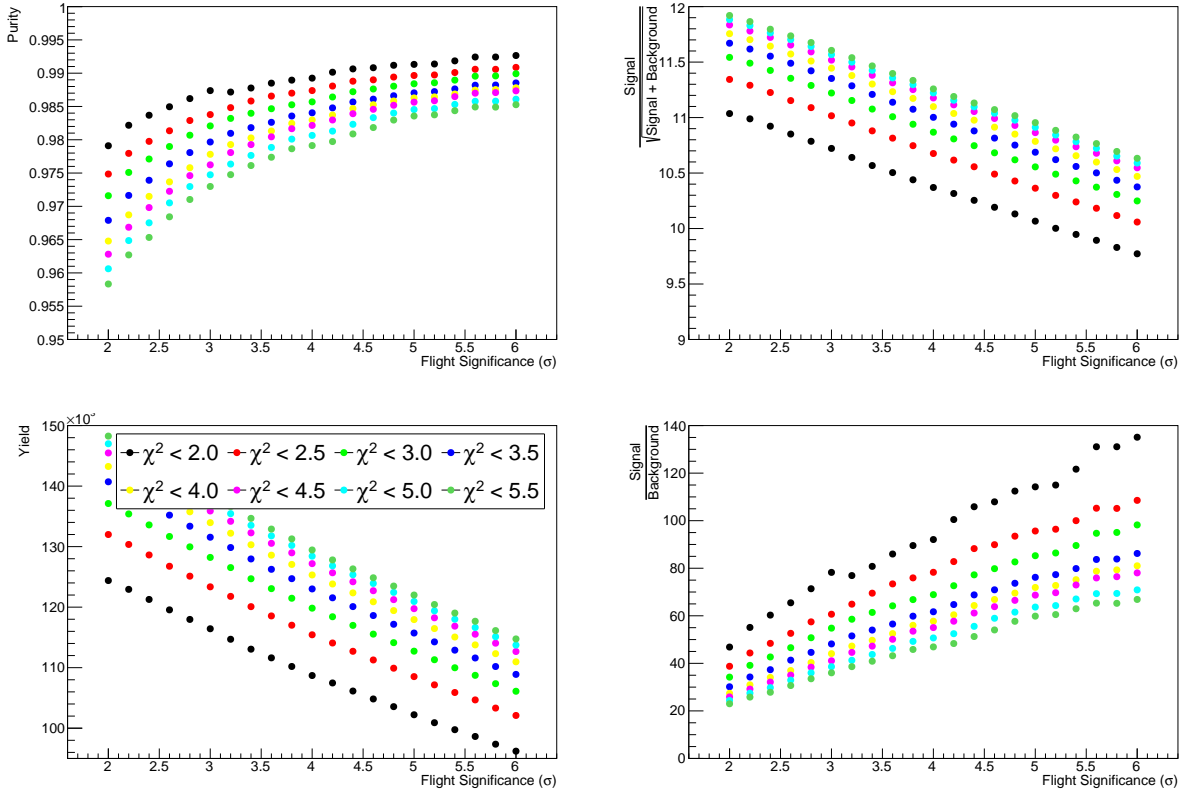


Figure 4.10: Purity, yield, statistical significance and signal-to-background as a function of selecting on Flight Significance for various χ^2/ndf selections.

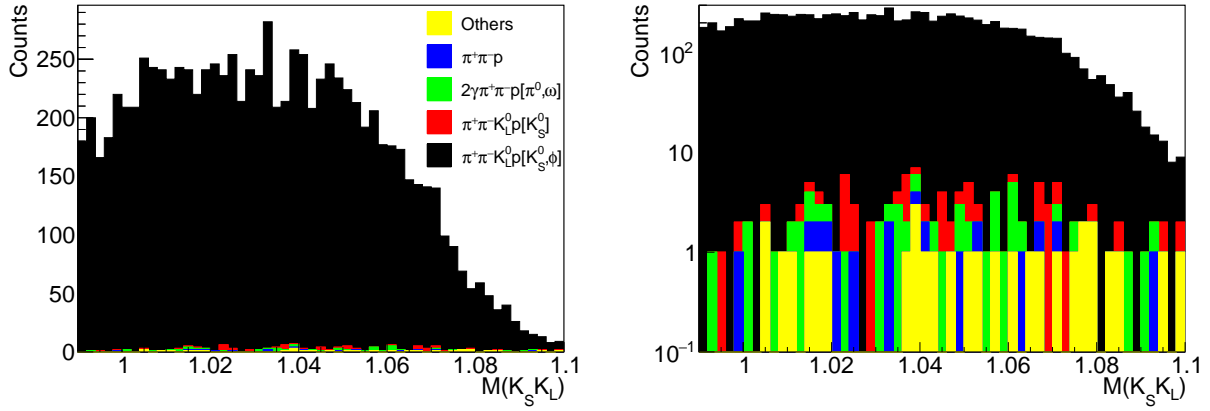


Figure 4.11: Stacked histogram of invariant mass for all topologies after relevant event selections in Table 4.4. The left plot is in a linear scale while the right plot is in a log-y scale.

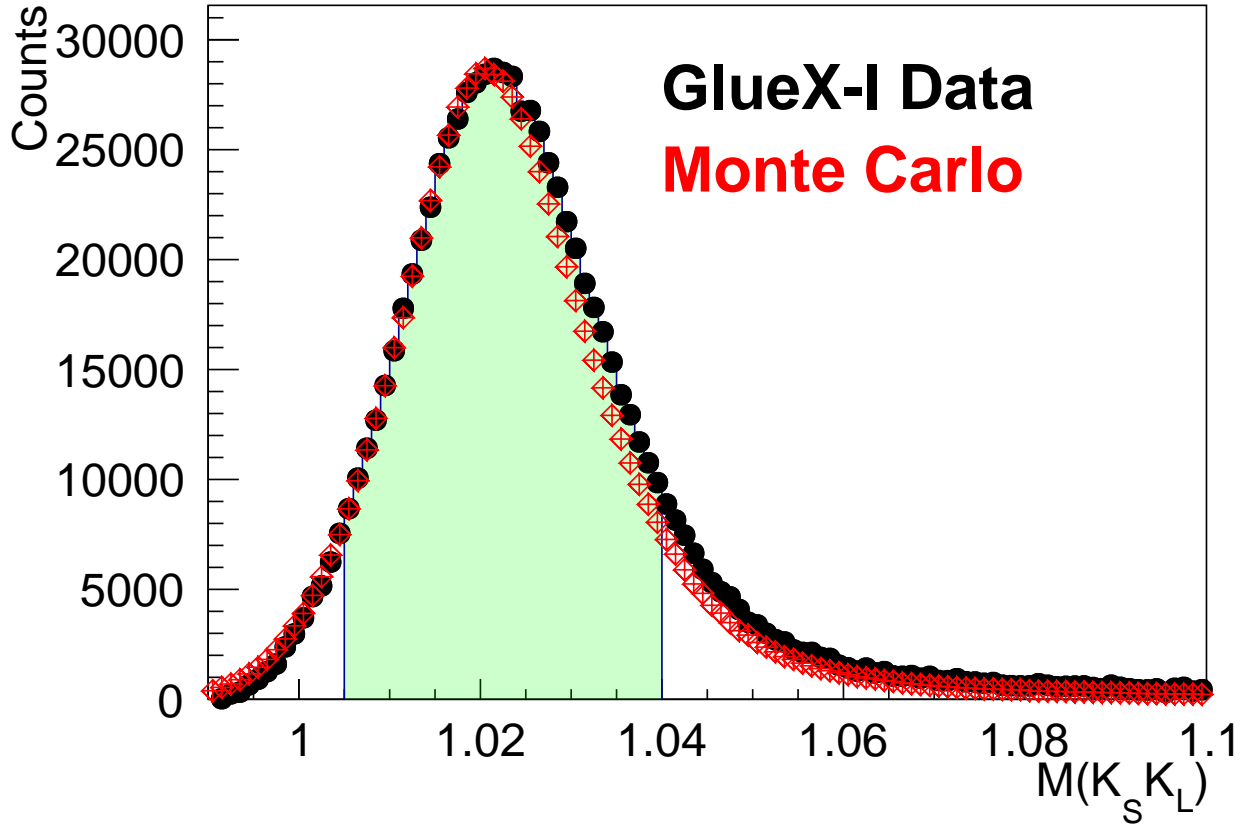


Figure 4.12: $K_S K_L$ invariant mass distribution after nominal events selections for GlueX-I (black points) and Monte Carlo (red points). The shaded green area indicates the nominal selection for measuring the Spin Density Matrix Elements.

4.2.6 $\phi(1020)$ Data Sample

In this section, we have discussed the dataset that will be used to measure the Spin Density Matrix Elements of the $\phi(1020)$. Table 4.4 lists all event selections that will be applied. Figure 4.12 illustrates the $K_S K_L$ invariant mass distribution after nominal event selections.

4.3 High Mass $K_S K_L$ Event Selections

Now we turn our attention to the $M(K_S K_L)$ region above 1.1 GeV. As can be seen in Figure 4.13, two peaks are visible above the $\phi(1020)$. However, backgrounds are much larger relative to the signal and tighter event selections are required. Next, we will go through all event selections and discuss which ones need to be tightened. We will continue to compare data and MC for each

Table 4.4: List of nominal event selections for $\phi(1020) \rightarrow K_S K_L$.

Beam energy	8.2–8.8 GeV
Mandelstam-t	0.15–1.0 GeV ²
Accidental Photon Weight	in time +1 out of time $-1/4$ -scale
Recoil proton z vertex	52 < z < 78 cm
Extra charged tracks	0
Extra neutral showers	< 3
Flight Significance	> 4σ
χ^2/ndf	< 4
Missing Mass	0.3–0.7 GeV
M($\pi^+\pi^-$)	0.480–0.520 GeV
M($K_S K_L$)	1.005–1.04 GeV

event selection and use a green shaded area to indicate the selection that will be placed on the data.

4.3.1 Recoil Proton Vertex and RF-Time

For completeness, we show the RF-Time and recoil proton z-vertex distributions in Figure 4.14. Only events with a recoil proton vertex along the length of the target chamber, 52 – 78 cm, are considered. We skip the first out-of-time peak to avoid tails from in-time events from leaking into the out-of-time peaks.

4.3.2 Mandelstam-t

As seen in Figure 4.15, the $\pi^+\pi^-$ invariant mass sideband is very large at low- t . These events are associated with non- K_S backgrounds since their invariant mass is inconsistent with a K_S . This is confirmed by bggen MC which shows a large background for $t \lesssim 0.2$ GeV² is due to topologies without a K_S . Figure 4.15 also shows the Mandelstam-t distribution for data and MC. The MC was generated with a t -slope of 6 GeV⁻².

4.3.3 Extra Tracks and Showers

The number of unused tracks for bggen data and data/MC is shown in Figure 4.16. The bggen data indicated that events with one or more charged tracks are dominated by background from other topologies. We note that the ratio of events with zero and two unused tracks in bggen data

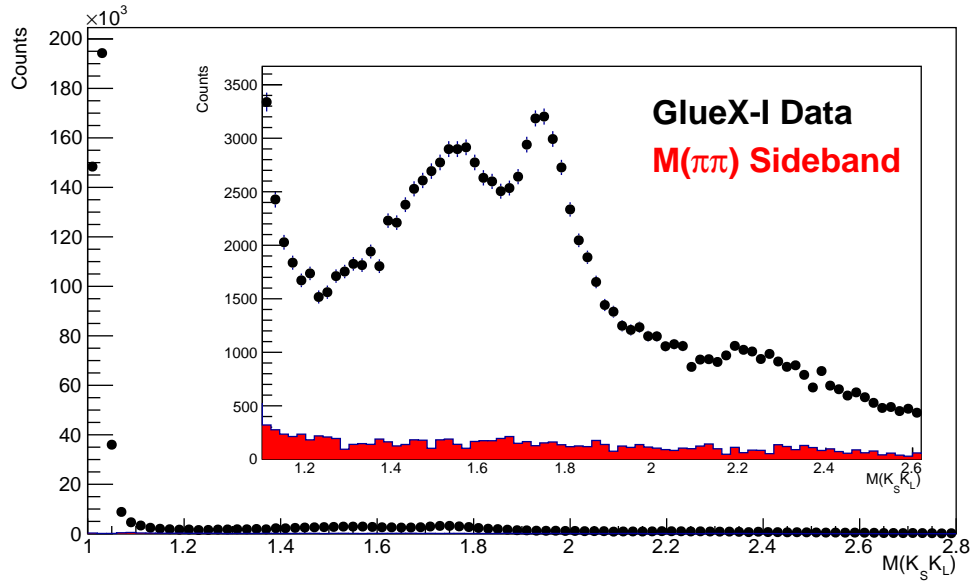


Figure 4.13: $K_S K_L$ invariant mass distribution with the event selections listed in Table 4.4.

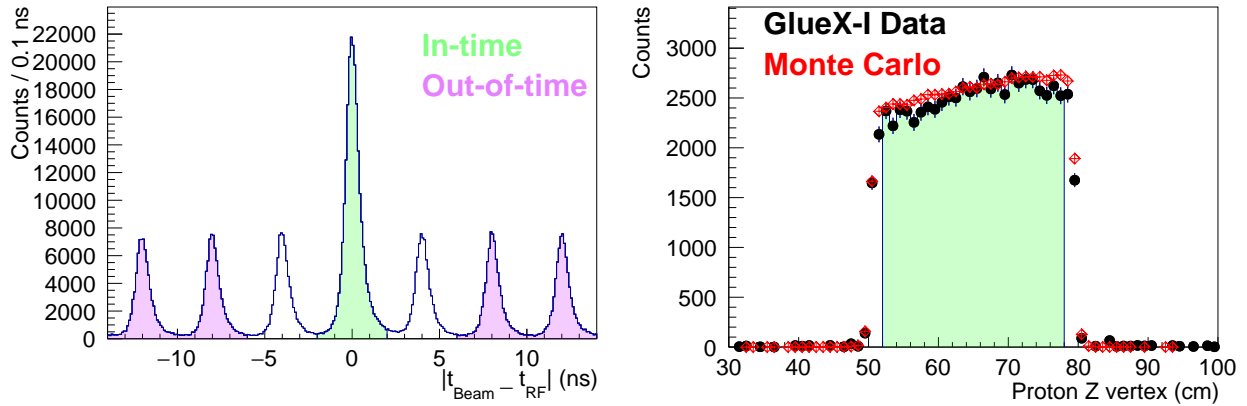


Figure 4.14: (Left) The RF time spectrum. The green shaded area are in-time events and the violet shaded area are out-of-time events which are used for accidental subtraction. (Right) Recoil proton z-vertex.

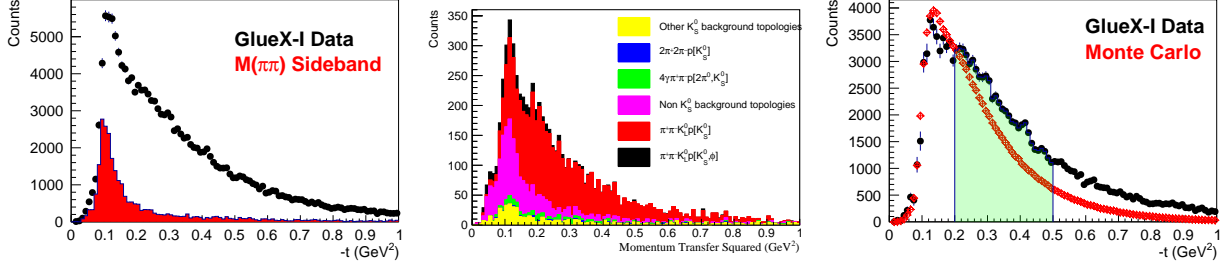


Figure 4.15: (Left) $-t$ distribution for signal events (black points) and $\pi\pi$ sideband events (shaded red). Below the dashed vertical line at 0.2 GeV^2 the data is dominated by background events. (Middle) $-t$ distribution for bggen data divided by topology. Low $-t$ events are dominated by topologies with no K_S in the topology. (Right) $-t$ distribution for data and MC.

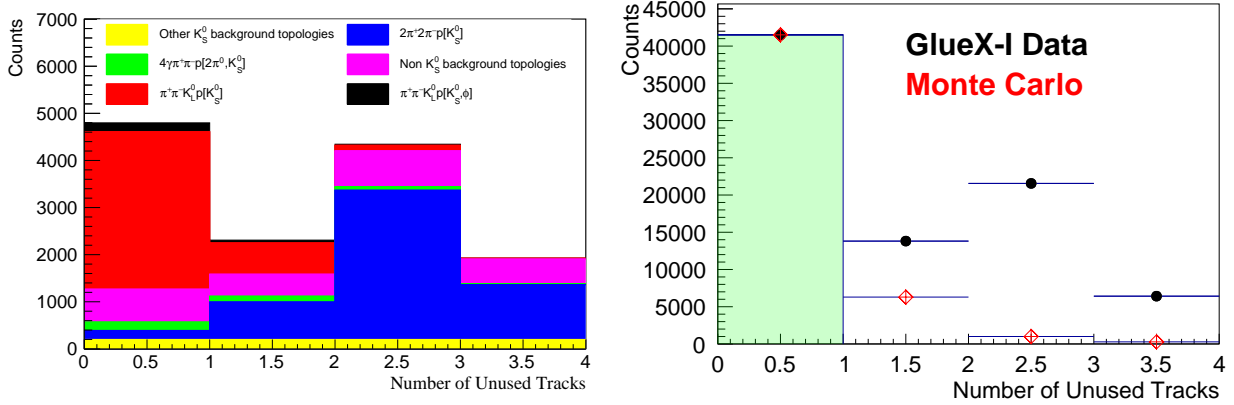


Figure 4.16: Number of unused tracks for (left) bggen data separated by topology and (right) data/MC comparison.

is nearly one-to-one while the same ratio in data is approximately one-to-two. This may indicate that the $K_S K_L$ cross section relative to other channels is larger in data than in bggen. If this is true, then the backgrounds contribution is overestimated in bggen. Distributions of the number of unused showers for bggen and data/MC are shown in Figure 4.17. The bggen data indicates that events with two extra showers are still mostly signal. Since removing events with two extra showers also removes a large amount of signal we will not tighten this event selection.

4.3.4 Flight Significance and χ^2/ndf

Distributions of the flight significance and χ^2/ndf are shown in Figure 4.18. Both distributions are well modeled by MC. We follow the same procedure used for the $\phi(1020)$ analysis to deter-

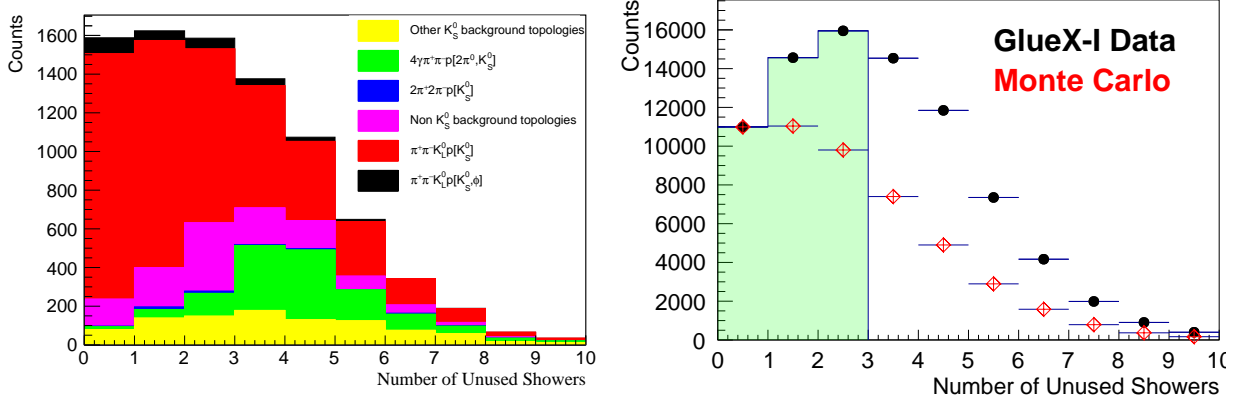


Figure 4.17: Number of unused showers for (left) bkggen data separated by topology and (right) data/MC comparison.

mine these event selections. Figure 4.19 shows the yield, signal to background ratio, significance ($S/\sqrt{S+B}$), and purity ($S/S+B$). The significance is found to be nearly degenerate with little discriminating power. The signal to background ratio shows a monotonic rise and thus does not pick out any individual combination of FS and χ^2/ndf . We choose a FS $> 6\sigma$ and $\chi^2/ndf < 2$ which give a 90% purity.

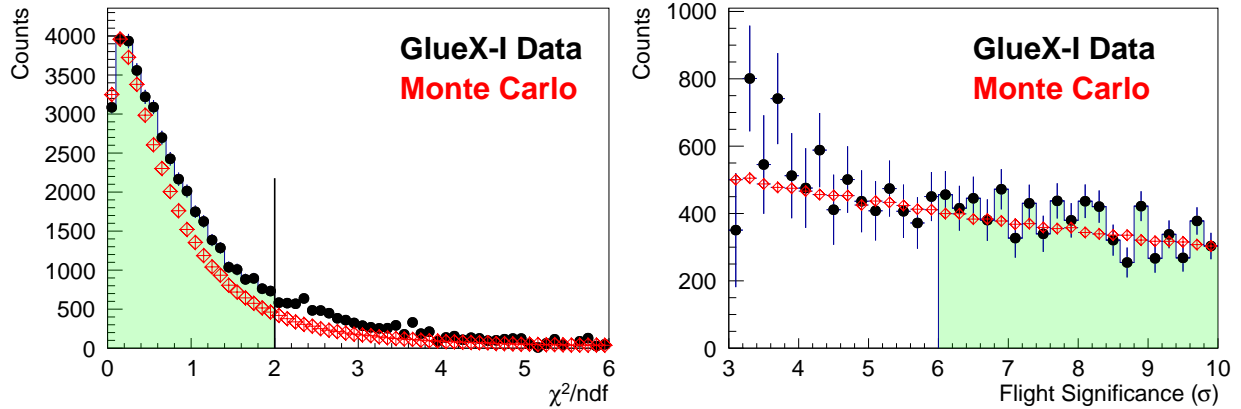


Figure 4.18: (Left) χ^2/ndf distribution for GLUEX-I data (black) and Monte Carlo data (red). A vertical line indicates the selection that will be placed on the data. (Right) Flight Significance distribution for GLUEX-I (black) and Monte Carlo (red). The shaded green area indicates the selection that will be placed on the data.

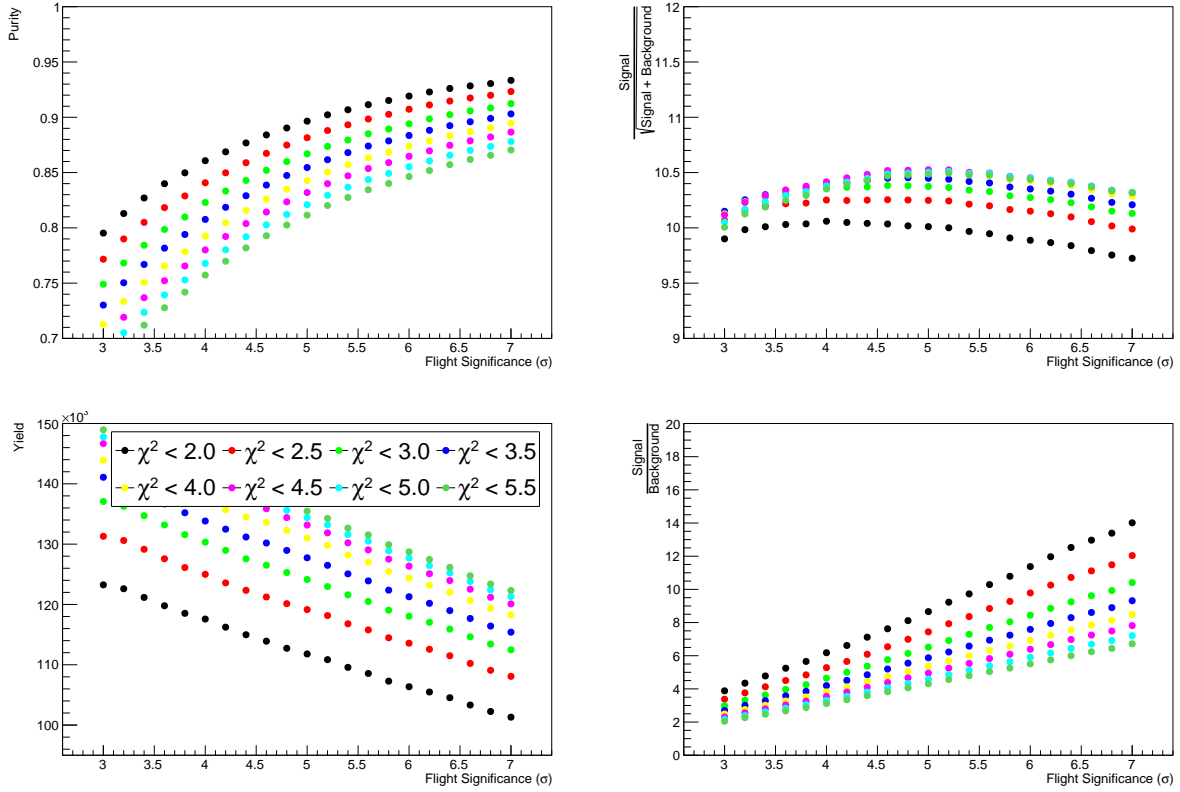


Figure 4.19: Purity, yield, statistical significance and signal to background as a function of selecting on Flight Significance for various χ^2/ndf selections.

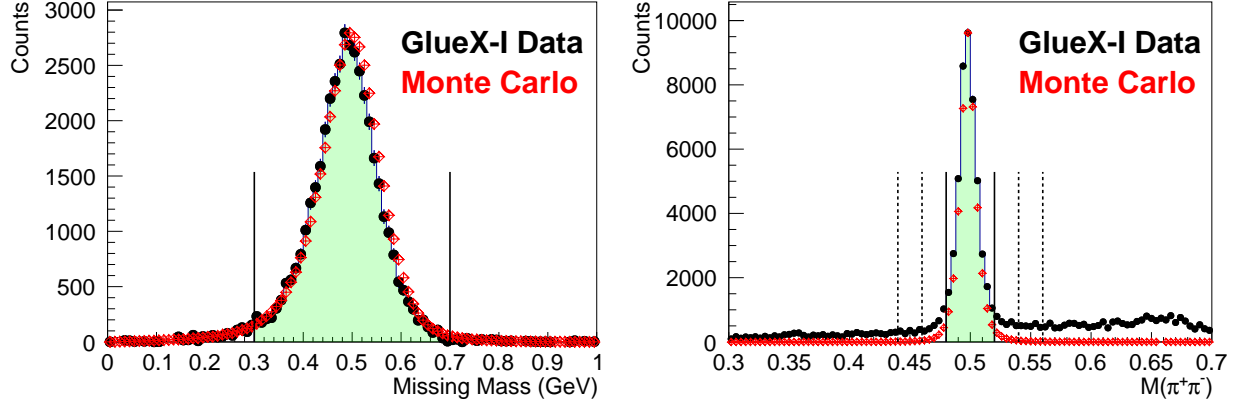


Figure 4.20: (Left) Data and scaled MC for the missing mass distribution. Vertical lines and green shaded area indicate the selection of the data. (Right) Data and scaled MC for the $\pi^+\pi^-$ invariant mass distribution. Solid vertical lines indicate the signal region and dashed vertical lines indicate the sideband regions.

4.3.5 Missing and $\pi^+\pi^-$ Mass Distributions

Figure 4.20 shows data and MC for the missing mass and $\pi^+\pi^-$ invariant mass distributions. The same mass range used for the $\phi(1020)$ analysis will be used.

4.3.6 Background Studies with bggen

With the new set of event selections we calculate the contribution from all backgrounds, see Table 4.5. Figure 4.21 shows the $K_S K_L$ invariant mass distribution for different topologies. $K_S K_L$ signal events are 74% of the data set with the $\phi(1020)$ tail contributing 3%. Backgrounds with a K_S in the topology contribute 12% of the total event with $K_S K_S \rightarrow \pi^+\pi^-\pi^+\pi^-$ contributing 0.5% and $K_S K_S \rightarrow \pi^+\pi^-\pi^0\pi^0$ contributing almost 4%. The remaining 7.5% is due to main topologies each contributing a small amount. The final 14% of the sample is due to events with no K_S in the final state topology. We reiterate that bggen MC is not an accurate estimate of background contributions in real data since the cross sections and angular distributions of most resonances are not known in photoproduction. However, bggen shows that $K_S K_S$ is the largest background contribution and we can effectively reject such events giving us confidence that our data set is predominantly $K_S K_L p$ signal events.

Table 4.5: Fraction of bggen events after nominal event selections in the range $1.1 < M(K_S K_L) < 2.0$ GeV.

Topology	Fraction [%]
$\pi^+\pi^-K_L^0p[K_S^0, \phi]$	3.53
$\pi^+\pi^-K_L^0p[K_S^0]$	70.48
$2\pi^+2\pi^-p[K_S^0]$	0.56
$4\gamma\pi^+\pi^-p[2\pi^0, K_S^0]$	3.74
Other K_S^0 topologies	7.52
Non- K_S^0 topologies	14.17

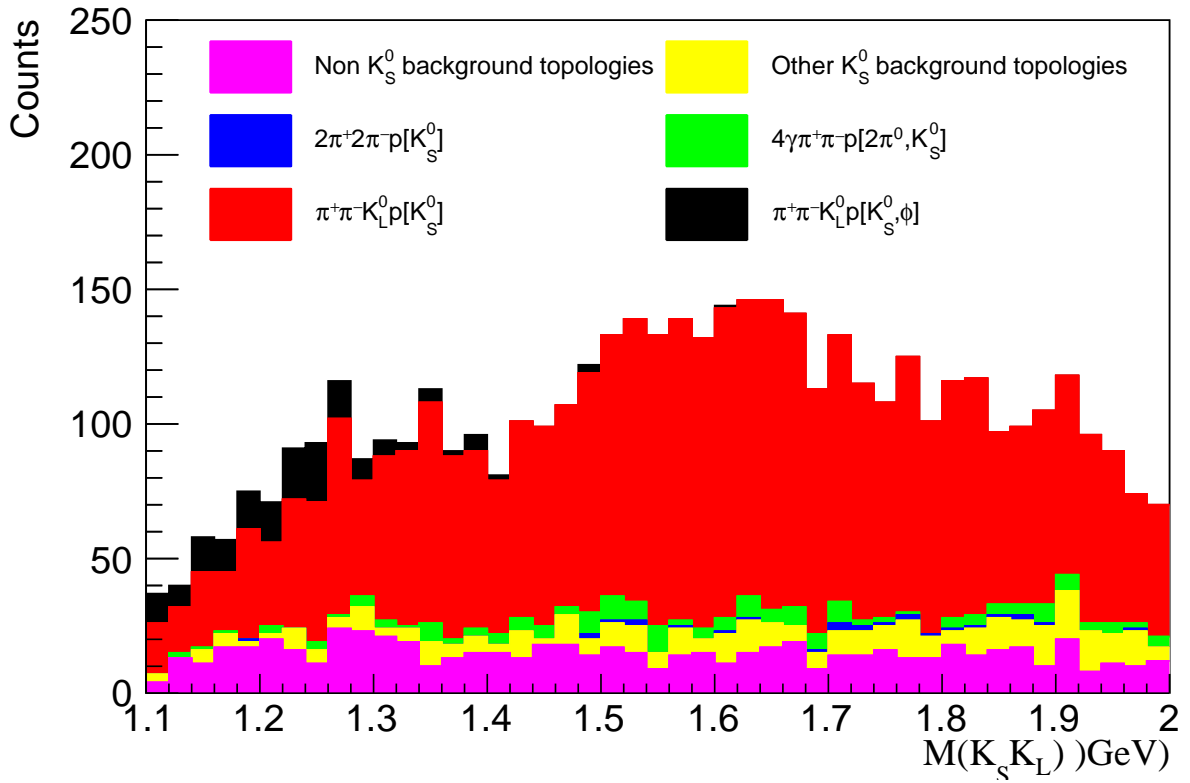


Figure 4.21: $K_S K_L$ invariant mass distribution from bggen MC divided by topology.

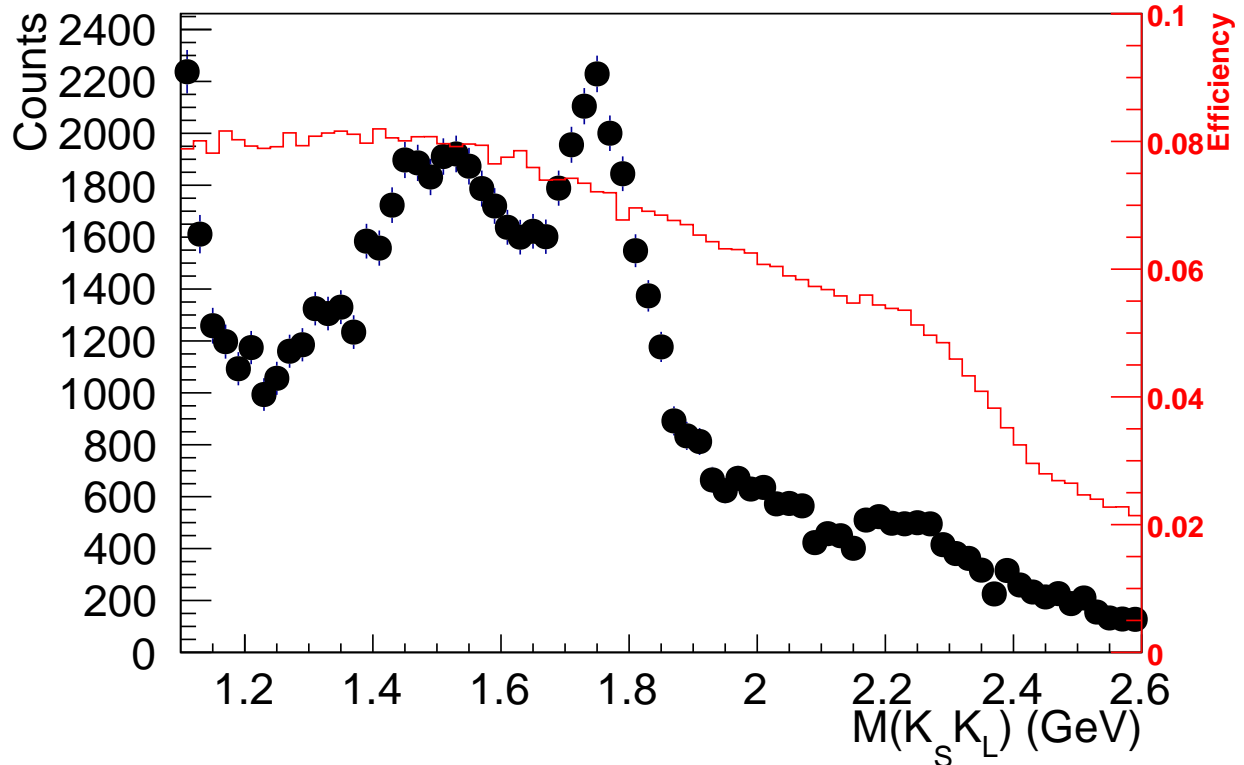


Figure 4.22: (Black) $K_S K_L$ invariant mass distribution after all event selections and sideband subtraction. (Red) Reconstruction efficiency as a function of $K_S K_L$ invariant mass.

4.3.7 $K_S K_L$ Data Sample

In this section, we discussed the data set that will be used for Partial Wave Analysis of $K_S K_L$ above the $\phi(1020)$. All event selections are listed in Table 4.6. Figure 4.22 shows the $K_S K_L$ invariant mass distribution after cuts together with the estimated reconstruction efficiency. Two structures are observed around 1.5 and 1.75 GeV. Understanding these structures will be the focus of Chapter 7.

4.4 $K_S K_S$ Event Selections

4.4.1 Fiducial Event Selections

Figure 4.23 shows the RF-Time, recoil proton z-vertex, and missing mass squared. For this data set, we include four out-of-time beam bunches but skip the first to avoid the possibility of in-time events leaking to the out-of-time region. A fiducial selection is placed on the recoil proton

Table 4.6: List of event selections for $K_S K_L$ events above $\phi(1020)$.

Beam energy	8.2–8.8 GeV
Mandelstam-t	0.20–1.0 GeV ²
Accidental Photon Weight	in time +1 out of time $-1/4$ -scale
Recoil proton z vertex	52 < z < 78 cm
Extra charged tracks	0
Extra neutral showers	< 3
Flight Significance	> 6σ
χ^2/ndf	< 2
Missing Mass	0.3–0.7 GeV
	Signal : 0.480–0.520 GeV
$M(\pi^+\pi^-)$	Left Sideband : 0.420–0.460 GeV
	Right Sideband : 0.540–0.560 GeV
$M(K_S K_L)$	> 1.1 GeV

z-vertex, 52 – 78 cm, to ensure the event originated inside the target chamber. The missing mass squared is defined as in Eq. 4.5. A fiducial selection is placed on the missing mass squared at

$$-0.04 < \text{MMS} < 0.04.$$

4.4.2 Mandelstam-t Distribution

Figure 4.24 shows the $-t$ distributions for data and MC. There is good agreement between data and MC up to $-t \approx 0.4$ GeV². Around this point, the slope of the distribution changes indicating that the dominant production mechanism may have changed.

4.4.3 Flight Significance and χ^2/ndf

Figure 4.25 shows distributions for FS and χ^2/ndf for data and MC. We use the same approach to choose a FS and χ^2/ndf selection as we did for the $K_S K_L p$ channel. Eq. 4.11 is used to model the $\pi^+\pi^-$ invariant mass distribution and we calculate Yield, signal to background ratio, significance ($S/\sqrt{S+B}$ and signal purity ($S/S+B$). The difference this time is that we have two K_S particles in the final state each with a FS. Therefore, rather than varying two variables (FS and χ^2/ndf) we vary three variables (FS for each K_S and χ^2/ndf). Figure 4.26 shows the relevant quantities as a function of FS with $\chi^2/ndf = 4.2$. These variations are inconclusive because of their monotonic

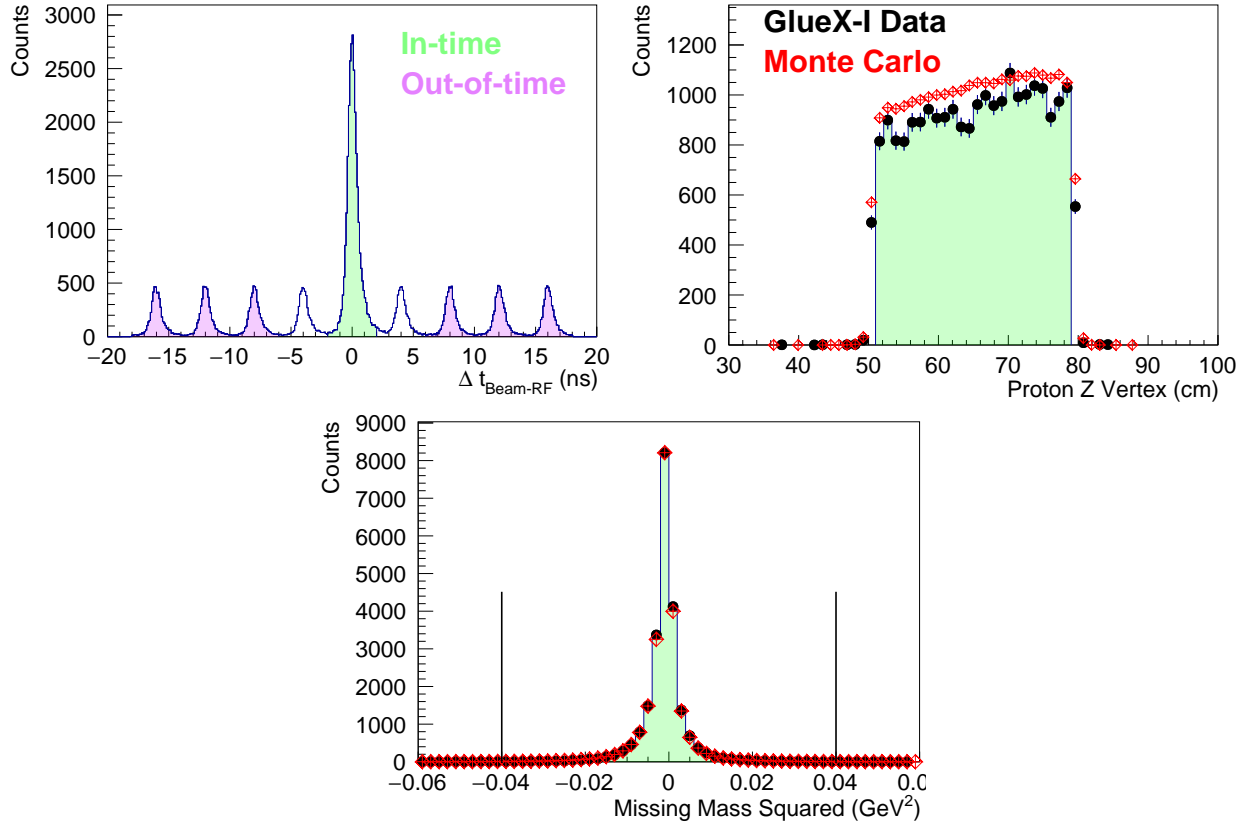


Figure 4.23: (Top left) RF time spectrum. The green shaded area are in-time events and the violet shaded area are out-of-time events. (Top right) Recoil proton z-vertex. (Bottom) Missing mass squared distribution and solid vertical lines indicate the selection of the data.

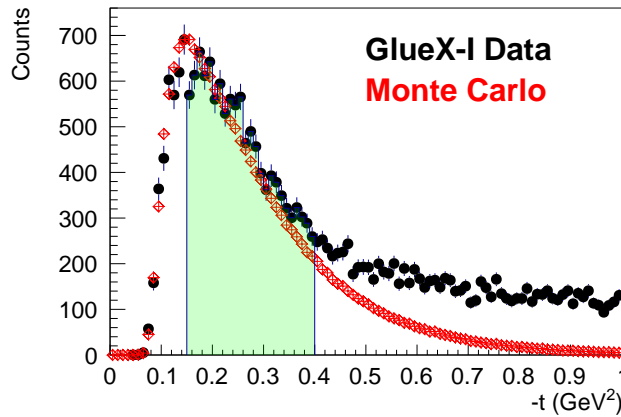


Figure 4.24: Mandelstam- t distribution for data (black) and MC (red). Data shows a change in slope at $-t \approx 0.4 \text{ GeV}^2$ which may indicate a change in the dominant production mechanism.

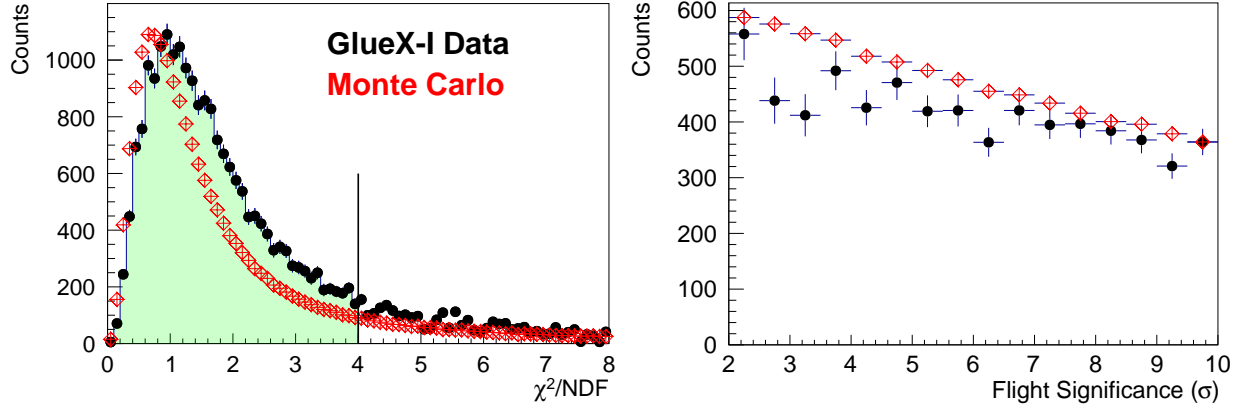


Figure 4.25: (Left) χ^2/ndf distribution for GlueX-I data (black) and Monte Carlo data (red). A vertical line indicates the selection that will be placed on the data. (Right) Flight Significance distribution for GlueX-I (black) and Monte Carlo (red). The shaded green area indicates the selection that will be placed on the data.

behavior. We therefore choose to maximize the yield at 90% purity which occurs at $(\text{FS}^1, \text{FS}^2, \chi^2/\text{ndf}) = (4.2\sigma, 5\sigma, 4.2)$.

4.4.4 $\pi^+\pi^-$ Invariant Mass Distribution

Figure 4.27 shows the $\pi^+\pi^-$ invariant mass distribution. The one-dimensional $\pi^+\pi^-$ invariant mass in the signal region contains 90% K_S events. We place a circular selection, with radius 2σ , on the $\pi_1^+\pi_1^-$ vs. $\pi_2^+\pi_2^-$ distribution. The sideband region is an annulus with an inner radius of 4σ and outer radius $\sqrt{24}\sigma$. The outer radius of the annulus is chosen such that the area of the signal regions and the area of the sideband region are equal.

4.4.5 $K_S K_S$ Data Set

In this section, we have discussed the data set that will be investigated in Chapter 8. All event selections are listed in Table 4.7. Figure 8.1 shows the $K_S K_S$ invariant mass distribution after event selections together with the estimated reconstruction efficiency. Structure is Understanding these structures will be the focus of Chapter 8.

In this section, we discussed the data set that will be used for Partial Wave Analysis of $K_S K_L$ above the $\phi(1020)$. All event selections are listed in Table 4.6. Figure 4.22 shows the $K_S K_L$ invariant mass distribution after cuts together with the estimated reconstruction efficiency. Two

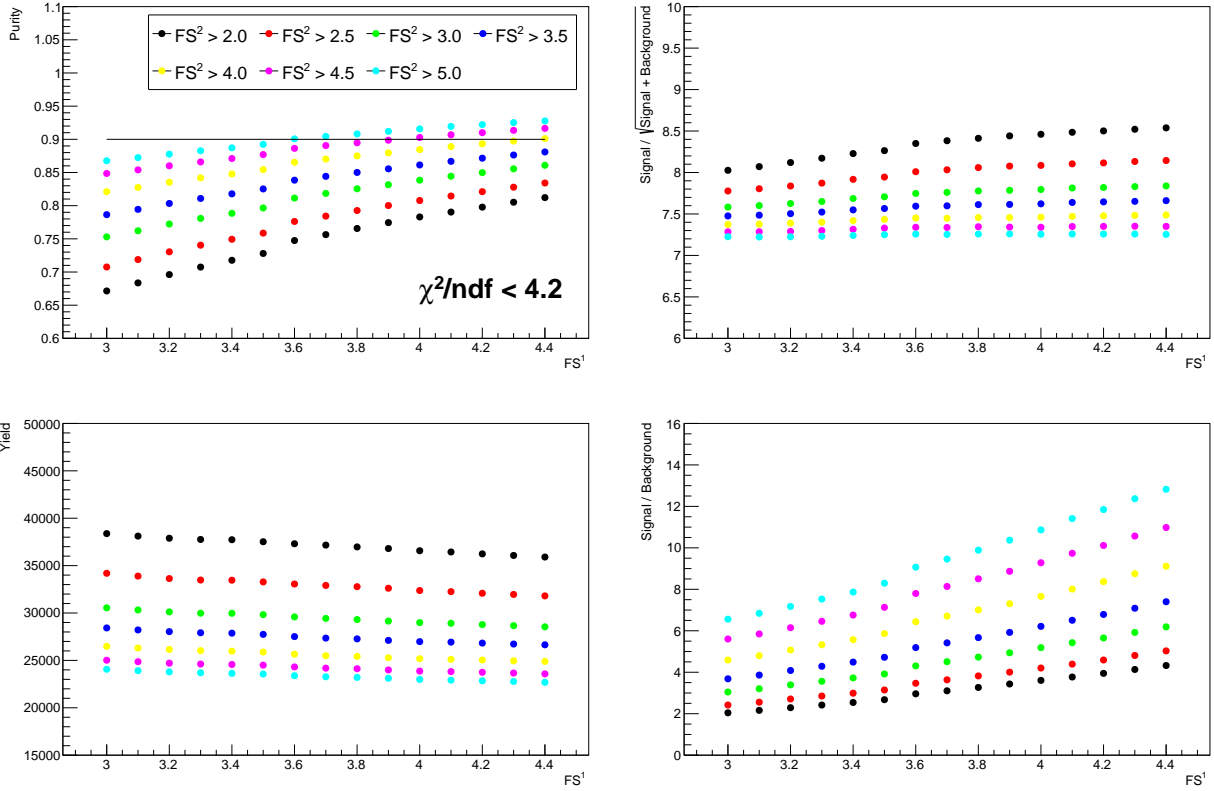


Figure 4.26: Purity, yield, statistical significance and signal to background as a function of selecting on Flight Significance of K_S^1 (FS^1) for various selections on the Flight Significance of K_S^2 (FS^2) selections with $\chi^2/ndf = 4.2$.

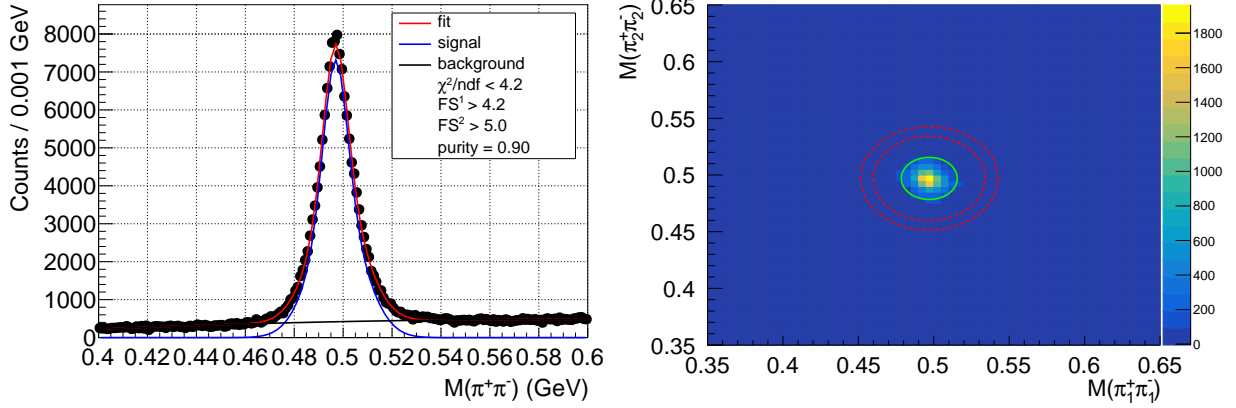


Figure 4.27: (Left) One dimensional $\pi^+\pi^-$ invariant mass distribution fitted with Eq. 4.11. The red line is the total fit while the blue and black lines are the signal and background, respectively. (Right) Two-dimensional $\pi^+\pi^-$ invariant mass distribution. The green circle indicates the signal region and has a radius of 2σ . The red circles indicate the sideband region. The inner red circle has a radius of 4σ and the outer red circle has a radius $\sqrt{24}\sigma$. The radius of the outermost red circle was chosen to make the signal and background areas equal.

structures are observed around 1.5 and 1.75 GeV. Understanding these structures will be the focus of Chapter 7.

Table 4.7: List of event selections for $K_S K_S$ events.

Beam energy	8.2–8.8 GeV
Mandelstam-t	0.15–1.0 GeV ²
Accidental Photon Weight	in time +1 out of time -1/6-scale
Recoil proton z vertex	52 < z < 78 cm
Flight Significance (first K_S)	> 4.2 σ
Flight Significance (second K_S)	> 5 σ
χ^2/ndf	< 4.2
Signal	$M^2(\pi_1^+\pi_1^-) + M^2(\pi_2^+\pi_2^-) < 2\sigma$
Sideband	$4\sigma < M^2(\pi_1^+\pi_1^-) + M^2(\pi_2^+\pi_2^-) < \sqrt{24}\sigma$

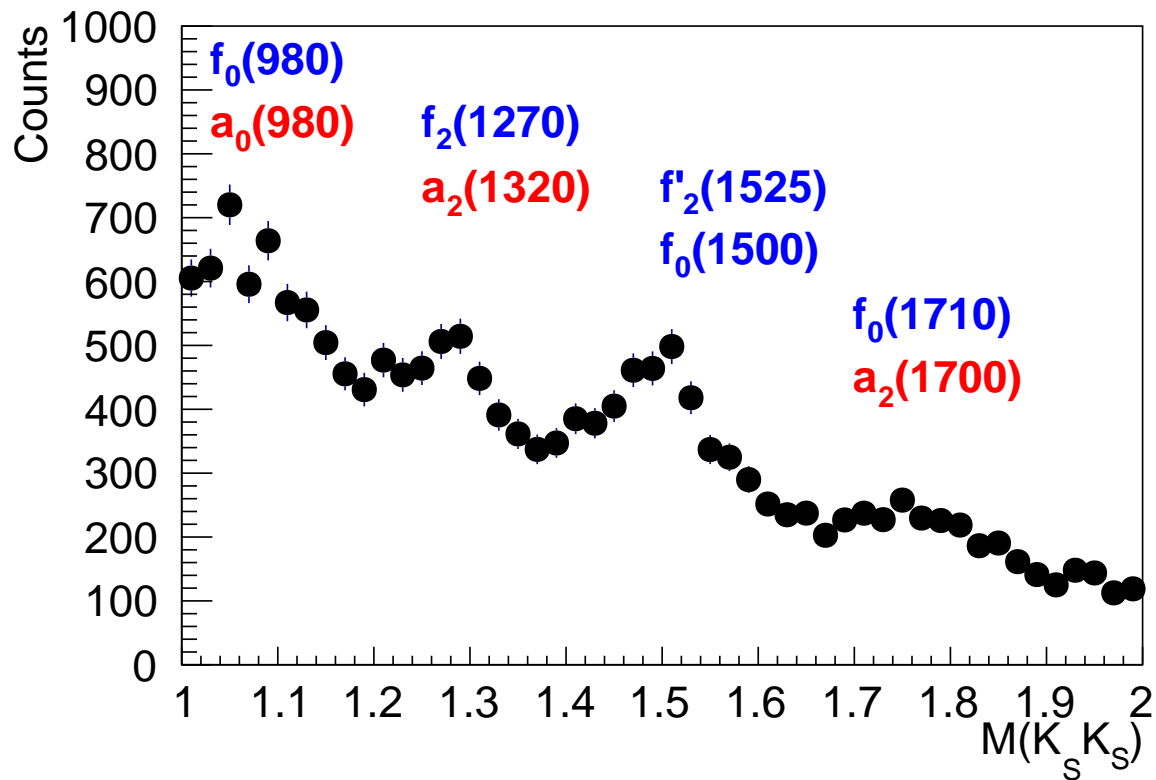


Figure 4.28: $K_S K_S$ invariant mass distribution. Structure is observed at threshold, ~ 1.25 GeV, ~ 1.5 GeV and ~ 1.7 GeV. Known states that may contribute are included with iso-scalars ($f_{0/2}$) in blue and iso-vectors ($a_{0/2}$) in red.

CHAPTER 5

THEORETICAL FORMALISM

In Chapter 4 we showed that we can exclusively reconstruct the $\gamma p \rightarrow K_S K_{SP}$ and $\gamma p \rightarrow K_S K_{LP}$ channels in the GlueX-I data set. We now turn our attention to discussing the theoretical formalism we will use to study the photoproduction of mesons. That is, we wish to understand reactions of the type

$$a + b \rightarrow X + c \rightarrow 1 + 2 + c \quad (5.1)$$

where the meson X decays to two pseudoscalar mesons 1 and 2, i.e. $K_S K_S$ and $K_S K_L$. We assume the production of the meson X occurs through t-channel exchange, see Figure 5.1. Hence, the reaction $a + b \rightarrow 1 + 2 + c$ occurs in a two-step process: (1) a beam of particles a interacts with a target particle b producing a meson X and a recoil particle c (2) the meson X subsequently decays to particle 1 and 2. We also assume that the target is unpolarized and the polarization of the recoil particle is not measured.

In this dissertation, we will employ multiple formalisms. Before describing each formalism we first set up the general problem we wish to solve. Following Ref.[7], the intensity (\mathcal{I}) for a reaction such as Eq. 5.1 is given by

$$\mathcal{I}(s, t, m_X, \Omega, \Phi) = \frac{dN}{ds dt dm_X d\Omega d\Phi} \propto \frac{d\sigma}{ds dt dm_x d\Omega d\Phi} \propto m_X |\mathcal{M}_{fi}|^2 \quad (5.2)$$

where N is the number of observed events, s and t are the Mandelstam-s and t variables, m_X is the mass of the produced meson, Ω is the solid angle of the decay $X \rightarrow 1 + 2$ in the rest frame of the meson X , Φ is the angle between the polarization plane and reaction plane, and \mathcal{M}_{fi} is the amplitude that encodes the whole dynamic content of the reaction [7]. Since the production and decay of the meson X are independent processes, we may factorize the amplitude \mathcal{M}_{fi} as follows

$$\mathcal{M}_{a+b \rightarrow X+c \rightarrow 1+2+c} = \underbrace{\mathcal{P}_{a+b \rightarrow X+c}(s, t, m_X, \Phi)}_{\text{Production Amplitude}} \underbrace{D_X(m_x)}_{\text{Dynamical Amplitude}} \underbrace{\Psi_{X \rightarrow 1+2}(m_X, \Omega)}_{\text{Decay Amplitude}} \quad (5.3)$$

where $\mathcal{P}_{a+b \rightarrow X+c}(s, t, m_X, \Phi)$ describes the production, $D_X(m_x)$ describes the mass dependence of meson X and its decay is described by $\Psi_{X \rightarrow 1+2}(m_X, \Omega)$. Because the types of analysis we are

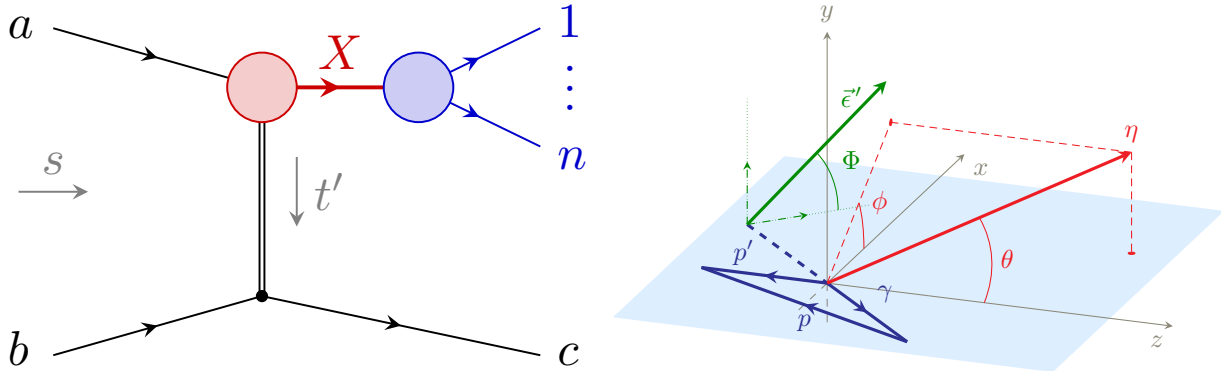


Figure 5.1: (Left) t -channel production of an intermediate state X in a t -channel exchange process followed by an n body decay of state X . This figure has been taken from Ref. [7]. (Right) Definition of the angles in the helicity frame. The reaction plane xz , containing the momenta of the photon beam (γ), the nucleon target (p), and the recoiling nucleon (p'), is in blue. θ and ϕ are the polar and azimuthal angles of the η . The polarization vector of the photon forms an angle Φ with the reaction plane. Figure is taken from Ref. [34].

interested in require a polarized beam, we only consider events in the coherent peak $E_\gamma = 8.2 - 8.8$ GeV. Therefore, we assume that the range of s (see Eq. 4.1) is narrow enough that we may neglect the dependence on s to good approximation.

Now that we have discussed in general terms the quantity we wish to study we will develop different formalisms to describe the data. First, we define the coordinate system that will be used. Then we will develop a formalism to measure the Spin Density Matrix Elements (SDMEs) of a vector meson. Third, we will develop a more general formalism called Partial Wave Analysis (PWA) to study any integer spin meson which decays into two pseudoscalar mesons. The SDME and PWA formalisms describe the angular part of the intensity \mathcal{I} . The dynamical amplitude $D_X(m_X)$ will be developed last. The t dependence of the intensity will not be modeled, instead, we will study the t dependence in data.

5.1 Coordinate System

At GlueX, we study reactions of the type in Eq. 5.1 in the Helicity (\mathcal{H}) or Gottfried-Jackson (GJ) frames [68]. In both cases, we boost into the center-of-mass frame of the reaction followed by a boost into the rest frame of the meson X . For both the \mathcal{H} and GJ frames, the $\hat{y}_{\mathcal{H},GJ}$ -axis is defined to be the normal to the production plane. In terms of the center-of-mass momentum of the

photon and meson X , \vec{p}_γ and \vec{p}_X respectively, we have

$$\hat{y}_{\mathcal{H},GJ} = \frac{\vec{p}_\gamma \times \vec{p}_X}{|\vec{p}_\gamma \times \vec{p}_X|} \quad (5.4)$$

In the helicity frame the $\hat{z}_{\mathcal{H}}$ -axis is defined by the direction of the center-of-mass momentum of X , explicitly we have

$$\hat{z}_{\mathcal{H}} = \frac{\vec{p}_X}{|\vec{p}_X|} \quad (5.5)$$

The \mathcal{H} is chosen to be a right-handed coordinate system by choosing $\hat{x}_{\mathcal{H}}$ to be

$$\hat{x}_{\mathcal{H}} = \hat{y}_{\mathcal{H}} \times \hat{z}_{\mathcal{H}}. \quad (5.6)$$

Figure 5.1 show the definition of the \mathcal{H} for the reaction $\gamma p \rightarrow \pi^0 \eta p$. The GJ frame is defined with the \hat{z}_{GJ} -axis in the direction of the incident photon and is also chosen to be right-handed. We therefore have,

$$\hat{z}_{GJ} = \frac{\vec{p}_\gamma}{|\vec{p}_\gamma|} \quad \hat{x}_{GJ} = \hat{y}_{GJ} \times \hat{z}_{GJ}. \quad (5.7)$$

We will work in the \mathcal{H} system unless otherwise stated.

In the Helicity frame the daughter particle 1 in Eq. 5.1 has momentum $\vec{p}_{\mathcal{H}}^1$, we define the polar and azimuthal angles, $\theta_{\mathcal{H}}$ and $\phi_{\mathcal{H}}$ respectively, as

$$\cos(\theta_{\mathcal{H}}^1) = \frac{(\vec{p}_{\mathcal{H}}^1)_z}{|\vec{p}_{\mathcal{H}}^1|} \quad (5.8)$$

$$\tan(\phi_{a_{\mathcal{H}}}) = \frac{(\vec{p}_{\mathcal{H}}^1)_y}{(\vec{p}_{\mathcal{H}}^1)_x}. \quad (5.9)$$

The analogous angles can be calculated by simply using the momentum of particle 1 in the GJ frame rather than the \mathcal{H} frame.

5.2 Spin Density Matrix Elements

We restrict our discussion of Spin-Density Matrix Elements to the special case of Eq. 5.1

$$\gamma N \rightarrow V N \rightarrow P P' N \quad (5.10)$$

where γ is the initial state photon, N is the same nucleon in the initial and final state, V is a vector meson, and $P^{(\prime)}$ are pseudoscalar mesons that decay from V . The following discussion is based on Ref. [69].

The photoproduction of a vector meson can be described by a production amplitude T , that connects the spin-density matrix $\rho(\gamma)$ of the initial state photon to the spin-density matrix $\rho(V)$ of the vector meson[70], we write

$$\rho(V) = T\rho(\gamma)T^\dagger. \quad (5.11)$$

In the center-of-mass helicity representation Eq. 5.11 can be rewritten as

$$\rho(V)_{\lambda_V \lambda'_V} = \frac{1}{N} \sum_{\lambda_{N'} \lambda_\gamma \lambda_N \lambda'_\gamma} T_{\lambda_V \lambda_{N'}, \lambda_\gamma \lambda_N} \rho(\gamma)_{\lambda_\gamma \lambda'_\gamma} T_{\lambda'_V \lambda_{N'}, \lambda'_\gamma \lambda_N}^* \quad (5.12)$$

where λ 's denote the helicities of the respective particles of reaction 5.34, and N is the normalization factor:

$$N = \frac{1}{2} \sum_{\lambda_{N'} \lambda_\gamma \lambda_N \lambda'_\gamma} |T_{\lambda_V \lambda_{N'}, \lambda_\gamma \lambda_N}|^2 \quad (5.13)$$

Incorporating the polarization of the photon we can express the photon spin-density matrix as

$$\rho(\gamma) = \frac{1}{2}\mathbf{I} + \frac{1}{2}\mathbf{P}_\gamma \cdot \boldsymbol{\sigma} \quad (5.14)$$

where \mathbf{P}_γ depends on the type of polarization, \mathbf{I} is the identity matrix and $\boldsymbol{\sigma}$ are the Pauli matrices. For a linearly polarized beam, we have

$$\mathbf{P}_\gamma = P_\gamma(-\cos 2\Phi, -\sin 2\Phi, 0) \quad (5.15)$$

with $P_\gamma \in [0, 1]$ and Φ is the angle between the polarization vector and the photon. To explicitly show the dependence of $\rho(V)$ on the polarization vector \mathbf{P}_γ , we define

$$(\rho^0, \rho^\alpha) = T \left(\frac{1}{2}\mathbf{I}, \frac{1}{2}\boldsymbol{\sigma}^\alpha \right) T^\dagger. \quad (5.16)$$

where ρ is the spin-density matrix of the vector meson and $\alpha = 1, 2, 3$. Now, we can use Eq. 5.14 and Eq. 5.16 to get

$$\rho(V) = \rho^0 + \sum_{i=1}^3 P_\gamma^\alpha \rho^\alpha \quad (5.17)$$

The relation between ρ^α and T is

$$\begin{aligned}
\rho_{\lambda_V \lambda'_V}^0 &= \frac{1}{2N} \sum_{\lambda'_N \lambda_\gamma \lambda_N} T_{\lambda_V \lambda'_N, \lambda_\gamma \lambda_N} T_{\lambda'_V \lambda'_N, \lambda_\gamma \lambda_N}^* \\
\rho_{\lambda_V \lambda'_V}^1 &= \frac{1}{2N} \sum_{\lambda'_N \lambda_\gamma \lambda_N} T_{\lambda_V \lambda'_N, -\lambda_\gamma \lambda_N} T_{\lambda'_V \lambda'_N, \lambda_\gamma \lambda_N}^* \\
\rho_{\lambda_V \lambda'_V}^2 &= \frac{i}{2N} \sum_{\lambda'_N \lambda_\gamma \lambda_N} \lambda_\gamma T_{\lambda_V \lambda'_N, -\lambda_\gamma \lambda_N} T_{\lambda'_V \lambda'_N, \lambda_\gamma \lambda_N}^* \\
\rho_{\lambda_V \lambda'_V}^3 &= \frac{i}{2N} \sum_{\lambda'_N \lambda_\gamma \lambda_N} \lambda_\gamma T_{\lambda_V \lambda'_N, \lambda_\gamma \lambda_N} T_{\lambda'_V \lambda'_N, \lambda_\gamma \lambda_N}^*
\end{aligned} \tag{5.18}$$

From parity conservation, it can be shown that

$$\rho_{\lambda \lambda'}^\alpha = (-1)^{\lambda - \lambda'} \rho_{-\lambda -\lambda'}^\alpha, \quad \alpha = 0, 1 \tag{5.19}$$

$$\rho_{\lambda \lambda'}^\alpha = -(-1)^{\lambda - \lambda'} \rho_{-\lambda -\lambda'}^\alpha, \quad \alpha = 2, 3 \tag{5.20}$$

The angular distributions of the decaying meson in its rest frame are described by the decay amplitude M , we write

$$\begin{aligned}
\frac{dN}{d \cos\theta d\phi} &= W(\cos\theta, \phi) = M \rho(V) M^\dagger \\
&\sum_{\lambda_V \lambda'_V} \langle \theta, \phi | M | \lambda_V \rangle \rho(V)_{\lambda_V \lambda'_V} \langle \lambda'_V | M^\dagger | \theta, \phi \rangle
\end{aligned} \tag{5.21}$$

where

$$\langle \theta, \phi | M | \lambda_V \rangle = C \sqrt{\frac{3}{4\pi}} D_{\lambda_V 0}^{1*}(\phi, \theta, -\phi) \tag{5.22}$$

and $D_{\lambda 0}^1$ are the Wigner rotation functions. Following the convention of Schilling [69], the Wigner rotations are explicitly given by

$$\begin{aligned}
D_{10}^1(\phi, \theta, -\phi) &= -\frac{1}{\sqrt{2}} \sin\theta e^{-i\phi} \\
D_{00}^1(\phi, \theta, -\phi) &= \cos\theta \\
D_{-10}^1(\phi, \theta, -\phi) &= -\frac{1}{\sqrt{2}} \sin\theta e^{i\phi}.
\end{aligned} \tag{5.23}$$

Using the fact that $\rho(V)$ is hermitian combined with Eq.'s 5.21, 5.22 and 5.23 gives

$$\begin{aligned}
W(\cos\theta, \phi, \rho(V)) &= \frac{3}{4\pi} \left(\frac{1}{2} (\rho_{11} + \rho_{-1-1}) \sin^2\theta + \rho_{00} \cos^2\theta + \frac{1}{\sqrt{2}} (-\text{Re}\rho_{10} + \text{Re}\rho_{-10}) \sin 2\theta \sin\phi \right. \\
&\quad \left. + \frac{1}{\sqrt{2}} (\text{Im}\rho_{10} + \text{Im}\rho_{-10}) \sin 2\theta \sin\phi - \text{Re}\rho_{1-1} \sin^2\theta \cos 2\phi + \text{Im}\rho_{1-1} \sin^2\theta \sin 2\phi \right)
\end{aligned} \tag{5.24}$$

where $\rho_{ij} = \rho(V)_{ij}$ on the right hand side of the equation. Since W is linear in $\rho(V)$ we can use the same decomposition as in Eq. 5.17:

$$W(\cos\theta, \phi, \rho) = W^0(\cos\theta, \phi) + \sum_{i=1}^3 P_\gamma^\alpha W^\alpha(\cos\theta, \phi) \quad (5.25)$$

where $W^\alpha(\cos\theta, \phi) = W(\cos\theta, \phi, \rho^\alpha)$ with $\alpha = 0, 1, 2, 3$. The symmetry properties of ρ^α (Eq.'s 5.19 and 5.20) reduce W^α to

$$\begin{aligned} W^0(\cos\theta, \phi) &= \frac{3}{4\pi} \left(\frac{1}{2}(1 - \rho_{00}^0) + \frac{1}{2}(3\rho_{00}^0 - 1)\cos^2\theta - \sqrt{2}\text{Re}\rho_{10}^0\sin 2\theta\cos\phi - \rho_{1-1}^0\sin^2\theta\cos 2\phi \right) \\ W^1(\cos\theta, \phi) &= \frac{3}{4\pi} \left(\rho_{11}^1\sin^2\theta + \rho_{00}^1\cos^2\theta - \sqrt{2}\text{Re}\rho_{10}^1\sin 2\theta\cos\phi - \rho_{1-1}^1\sin^2\theta\cos 2\phi \right) \\ W^2(\cos\theta, \phi) &= \frac{3}{4\pi} \left(\sqrt{2}\text{Im}\rho_{10}^2\sin 2\theta\sin\phi + \text{Im}\rho_{1-1}^2\sin^2\theta\sin 2\phi \right) \\ W^3(\cos\theta, \phi) &= \frac{3}{4\pi} \left(\sqrt{2}\text{Im}\rho_{10}^3\sin 2\theta\sin\phi + \text{Im}\rho_{1-1}^3\sin^2\theta\sin 2\phi \right). \end{aligned} \quad (5.26)$$

Now we may write the final form of $W(\cos\theta, \phi, \Phi)$ by using the fact that we have a linearly polarized beam (Eq. 5.15):

$$W(\cos\theta, \phi, \Phi) = W^0(\cos\theta, \phi) - P_\gamma\cos(2\Phi)W^1(\cos\theta, \phi) - P_\gamma\sin(2\Phi)W^2(\cos\theta, \phi). \quad (5.27)$$

An important aspect of the SDMEs we have just derived is that, at high energy, special combinations of SDMEs ($\rho_{ik}^{N,U}$) separated contributions from natural ($P = (-1)^J$) and unnatural ($P = -(-1)^J$) t-channel exchange. These combinations are given by

$$\begin{aligned} \rho_{ik}^{N,U} &= \frac{1}{2} (\rho_{ik}^0 \mp (-1)^i \rho_{-ik}^1) \\ &= \frac{1}{2} (\rho_{ik}^0 \mp (-1)^{-k} \rho_{i-k}^1) \end{aligned} \quad (5.28)$$

going from the first to the second line we have used Eq. 5.19. The contribution to the total cross section from natural (σ^N) and unnatural (σ^U) parity exchange may be (and typically are) different. This asymmetry is referred to as the parity asymmetry (P_σ) and is related to the SDMEs as

$$P_\sigma = \frac{\sigma^N - \sigma^U}{\sigma^N + \sigma^U} = 2\rho_{1-1}^1 - \rho_{00}^1 \quad (5.29)$$

In Ref [71] it was shown that several relations among the SDMEs hold under certain conditions. If we assume that the amplitudes that correspond to the helicity double flip, then we find the following relations:

$$\rho_{1-1}^1 = -\text{Im}(\rho_{1-1}^2) \quad (5.30)$$

$$Re(\rho_{10}^1) = -Im(\rho_{10}^2) \quad (5.31)$$

$$\rho_{1-1}^0 = \pm \rho_{11}^1. \quad (5.32)$$

If we assume a single production mechanism, then we find:

$$Re(\rho_{10}^0) = \pm Re(\rho_{10}^1). \quad (5.33)$$

5.3 Partial Wave Analysis

The following discussion is based on Ref. [34]. Consider the reaction Eq 5.1 for photoproduction of any intermediate integer spin meson X which decays to two pseudoscalar mesons

$$\gamma N \rightarrow XN \rightarrow PP'N. \quad (5.34)$$

The angular component of the intensity is given by

$$\mathcal{I}(\Omega, \Phi) = \frac{dN}{d\Omega d\Phi} \propto |\mathcal{M}_{fi}|^2 \quad (5.35)$$

and the matrix element \mathcal{M}_{fi} is

$$\mathcal{M}_{fi} = \langle PP' | M_{X \rightarrow PP'} T_{\gamma N \rightarrow XN} | \gamma N \rangle \quad (5.36)$$

where $T_{\gamma N \rightarrow XN}$ is the production amplitude, $M_{X \rightarrow PP'}$ is the decay amplitude and the final state nucleon is neglected. We now insert a complete set of $|\ell m\rangle$ states to obtain

$$\mathcal{M}_{fi} = \sum_{\ell m}^{\infty} \underbrace{\langle ab | M | \ell m \rangle}_{\text{Decay Amplitude}} \underbrace{\langle \ell m | T | \gamma N \rangle}_{\text{Production Amplitude}} \quad (5.37)$$

where we dropped the subscript for T and M to simplify notation. In the helicity frame $|ab\rangle \rightarrow |\Omega\rangle$ with $\Omega = (\theta, \phi)$. The decay amplitude for spinless particles is

$$\langle \Omega | M | \ell m \rangle = Y_{\ell}^m(\Omega) \quad (5.38)$$

with $\ell = 1, 2, \dots$ and $m = -\ell, \dots, \ell$, and the production amplitude is

$$\langle \ell m | T | \gamma N \rangle = T_{\ell m} \quad (5.39)$$

The intensity can now be written as

$$\begin{aligned}
\mathcal{I} &\propto |\mathcal{M}_{fi}|^2 = \left| \sum_{\ell m} Y_{\ell}^m(\Omega) T_{\ell m} \right|^2 \\
&= \sum_{\ell m \ell' m'} Y_{\ell}^m(\Omega) \underbrace{T_{\ell m} T_{\ell' m'}^*}_{\rho_{mm'}^{\ell \ell'}(X)} A_{\ell m}^*(\Omega) \\
&= \sum_{\lambda_{N'} \lambda_{\gamma} \lambda_N \lambda'_{\gamma}} \sum_{\ell m \ell' m'} Y_{\ell}^m(\Omega) T_{m \lambda_{N'}^J, \lambda_{\gamma} \lambda_N}^{\ell} \rho_{\lambda_{\gamma} \lambda'_{\gamma}}(\gamma) T_{m' \lambda_{N'}, \lambda'_{\gamma} \lambda_N}^{\ell' *} Y_{m'}^{\ell' *}(\Omega). \\
&= \sum_{\lambda_{N'} \lambda_{\gamma} \lambda_N \lambda'_{\gamma}} A_{\lambda_{N'}, \lambda_{\gamma} \lambda_N}(\Omega) \rho_{\lambda_{\gamma} \lambda'_{\gamma}} A_{\lambda_{N'}, \lambda'_{\gamma} \lambda_N}(\Omega)
\end{aligned} \tag{5.40}$$

In the second line, we expand the square of the matrix element and identify $T_{\ell m} T_{\ell' m'}^*$ as the spin-density matrix elements of the intermediate meson X . In the third line, we use Eq 5.12 to connect the photon and meson spin density matrix elements. In the last line, the partial wave amplitudes are defined as

$$A_{\lambda_{N'}, \lambda_{\gamma} \lambda_N}(\Omega) = \sum_{\ell m} Y_{\ell}^m(\Omega) T_{m \lambda_{N'}^J, \lambda_{\gamma} \lambda_N}^{\ell} \tag{5.41}$$

Since the intensity \mathcal{I} is linear in $\rho(\gamma)$ we use the same decomposition as in Eq. 5.27:

$$\mathcal{I}(\Omega, \Phi) = \mathcal{I}^0(\Omega) - P_{\gamma} \mathcal{I}^1(\Omega) \cos 2\Phi - P_{\gamma} \mathcal{I}^2(\Omega) \sin 2\Phi \tag{5.42}$$

with

$$\begin{aligned}
\mathcal{I}^0(\Omega) &= \frac{\kappa}{2} \sum_{\lambda_{\gamma}, \lambda_N \lambda_{N'}} A_{\lambda, \lambda_N \lambda_{N'}}(\Omega) A_{\lambda, \lambda_N \lambda_{N'}}^* \\
\mathcal{I}^1(\Omega) &= \frac{\kappa}{2} \sum_{\lambda_{\gamma}, \lambda_N \lambda_{N'}} A_{-\lambda, \lambda_N \lambda_{N'}}(\Omega) A_{\lambda, \lambda_N \lambda_{N'}}^* \\
\mathcal{I}^2(\Omega) &= i \frac{\kappa}{2} \sum_{\lambda_{\gamma}, \lambda_N \lambda_{N'}} \lambda A_{-\lambda, \lambda_N \lambda_{N'}}(\Omega) A_{\lambda, \lambda_N \lambda_{N'}}^*
\end{aligned} \tag{5.43}$$

where κ is a scale factor that contains all the kinematics. It is convenient to work in the reflectivity basis

$${}^{\epsilon} T_{m, \lambda_N \lambda_{N'}}^{\ell} = \frac{1}{2} \left[T_{+1m, \lambda_N \lambda_{N'}}^{\ell} - \epsilon (-1)^m T_{-1-m, \lambda_N \lambda_{N'}}^{\ell} \right]. \tag{5.44}$$

The advantage of the reflectivity basis is that in the high energy limit the amplitudes with $\epsilon = +1(-1)$ are dominated by natural (unnatural) t -channel exchanges [34]. Parity invariance implies

$${}^{\epsilon} T_{m, -\lambda_N \lambda_{N'}}^{\ell} = \epsilon (-1)^{\lambda_N - \lambda_{N'}} {}^{\epsilon} T_{m, \lambda_N \lambda_{N'}}^{\ell}. \tag{5.45}$$

This allows us to define two sets of partial waves

$$[\ell]_{m,0}^\epsilon = {}^\epsilon T_{m,++}^\ell \quad [\ell]_{m,1}^\epsilon = {}^\epsilon T_{m,+ -}^\ell \quad (5.46)$$

which correspond to the nucleon helicity non-flip and flip, respectively. Inserting Eq.' 5.41, 5.45 and 5.46 into 5.43 we obtain

$$I(\Omega, \Phi) = 2\kappa \sum_k \left\{ (1 - P_\gamma) \left| \sum_{\ell,m} [\ell]_{m;k}^{(-)} \Re \mathfrak{e} [Z_\ell^m(\Omega, \Phi)] \right|^2 + (1 - P_\gamma) \left| \sum_{\ell,m} [\ell]_{m;k}^{(+)} \Im \mathfrak{m} [Z_\ell^m(\Omega, \Phi)] \right|^2 + (1 + P_\gamma) \left| \sum_{\ell,m} [\ell]_{m;k}^{(+)} \Re \mathfrak{e} [Z_\ell^m(\Omega, \Phi)] \right|^2 + (1 + P_\gamma) \left| \sum_{\ell,m} [\ell]_{m;k}^{(-)} \Im \mathfrak{m} [Z_\ell^m(\Omega, \Phi)] \right|^2 \right\} \quad (5.47)$$

$[\ell]_{m,k}^\epsilon$ are complex amplitudes, $Z_\ell^m(\Omega, \Phi) = e^{-i\Phi} Y_\ell^m$, and κ denotes the nucleon helicity spin flip and non-flip amplitudes. For a more detailed derivation of Eq. 5.47 see Ref. [72].

5.4 The Dynamical Amplitude

The dynamical amplitude $D_X(m_X)$ is very complicated to model and approximations are typically used. An isolated resonance far from threshold that decays to a single final state is well modeled by a relativistic Breit-Wigner parameterized as

$$BW(m; m_0, \Gamma_0) = \frac{m_0 \Gamma(m)}{m_0^2 - m^2 + im_0 \Gamma(m)} \quad (5.48)$$

with

$$\Gamma(m) = \Gamma_0 \frac{m_0}{m} \frac{p}{p_0} \frac{F_l^2(p)}{F_l^2(p_0)} \quad (5.49)$$

where m_0 is the mass and Γ_0 is the width of the resonance, and F_l are the barrier factors computed as functions of $z = (p/p_R)^2$ as [41]

$$\begin{aligned} F_0(z) &= 1 \\ F_1(z) &= \sqrt{\frac{2z}{z+1}} \\ F_2(z) &= \sqrt{\frac{13z^2}{(z-3)^2 + 9z}} \\ F_3(z) &= \sqrt{\frac{277z^3}{z(z-15)^2 + 9(2z-5)^2}}. \end{aligned} \quad (5.50)$$

The line shape of the Breit-Wigner amplitude is shown in Figure 5.2

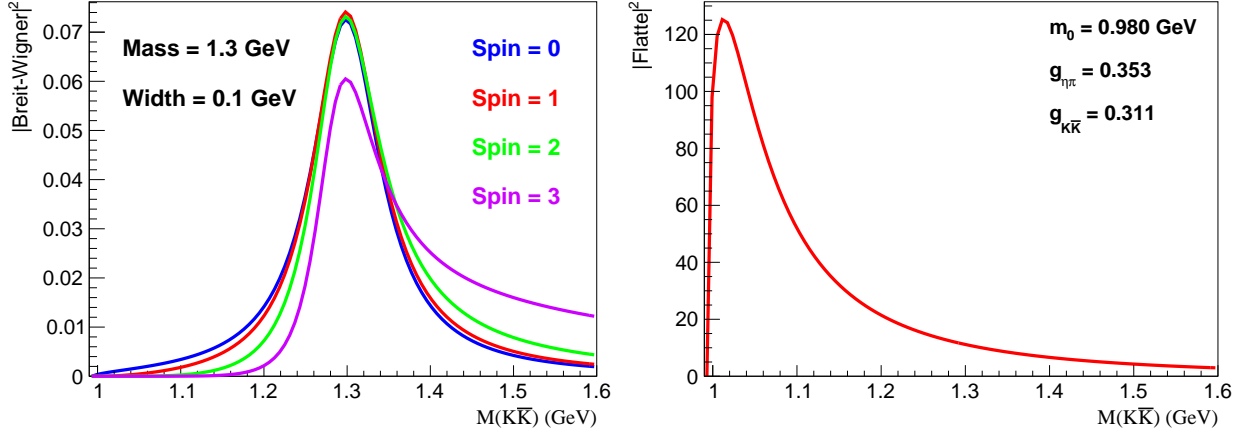


Figure 5.2: (Left) Modulus square of the Breit-Wigner amplitude (Eq. 5.48) for various ℓ , mass $m_0 = 1.3$ GeV, and width $\Gamma_0 = 0.1$ GeV. (Right) Modulus square of Flatté amplitude (Eq. 5.51) with mass $m_0 = 0.980$ GeV, $g_i = g_{\eta\pi} = 0.353$ GeV and $g_i = g_2 = g_{K\bar{K}} = 0.311$ GeV.

If a resonance has a strong coupling to two final states and sits near the threshold of one of the final states. Then it is more appropriate to use a Flatté parameterization [73, 74] which is given by

$$Flatté(m; i, m_{m_0}, g_1, g_2) = \frac{g_i \sqrt{\rho_i}}{m_0^2 - m^2 + i(\rho_1(m)g_1^2 + \rho_2(m)g_2^2)} \quad (5.51)$$

where m_0 is the mass of the resonance, i is the final state to be modeled, $\rho_{1,2}$ are the phase space factors, $g_{1,2}$ are the coupling strength to the indicated channel, and 1/2 represent the first and second two particle final state. If the i 'th final state is composed of particles a and b , then the phase space factor reads:

$$\rho_{ab} = \frac{\sqrt{[m^2 - (m_a - m_b)^2][m^2 - (m_a + m_b)^2]}}{m^2} \quad m > m_a + m_b \quad (5.52)$$

$$\rho_{ab} = 0 \quad m \leq m_a + m_b$$

The line shape of the Flatté amplitude is shown in Figure 5.2 for the case of $a_0(980) \rightarrow K\bar{K}$.

In the case when multiple resonances overlap which decay to multiple channels more refined methods, such as the K-matrix approach, should be used. The K-matrix method is a general construction for coupled-channel scattering amplitudes \mathcal{M}_{f_i} that guarantees two-particle unitarity [3]. There are various ways to parametrize the K-matrix, we will follow the approach of Ref. [75]. For each partial wave, the mass-dependent amplitude $F_i(m)$ is parametrized as

$$F_i(m) = \sum_j (I + K(m)C(m))_{ij}^{-1} \cdot P_j(m) \quad (5.53)$$

where i and j represent the two-body decay channels and m is the invariant mass of the respective two-body sub-channel. The analyticity is taken into account by using the Chew-Mandelstam function $C(m)$ [75]. $P_j(m)$ represents one element of the P-vector, which is given by

$$P_j(s) = \sum_{\alpha} \left(\frac{\beta_{\alpha} g_{\alpha_j}}{m_{\alpha}^2 - m^2} + \sum_k c_{kj} \cdot m^{2k} \right) \cdot B^l(q_j, q_{\alpha_j}) \quad (5.54)$$

where β_{α} is a complex parameter and represents the photoproduction coupling strength of resonance α . g_{α_j} is the coupling strength of resonance α to the decay channel j . m_{α} is the mass of resonance α , and $B^l(q_j, q_{\alpha_j})$ is the barrier factor for decay channel j with orbital angular momentum l , breakup momentum q and the resonance breakup momentum q_{α_j} . The $c_{kj} \cdot m^{2k}$ term describes background contributions for the production.

$$K_{ij}(s) = \sum_{\alpha} B^l(q_i, q_{\alpha_i}) \cdot \left(\frac{g_{\alpha_i}^{bare} g_{\alpha_j}^{bare}}{m_{\alpha}^{bare2} - s} + \tilde{c}_{ij} \right) \cdot B^l(q_j, q_{\alpha_j}) \quad (5.55)$$

CHAPTER 6

$\phi(1020)$ PHOTOPRODUCTION

6.1 Spin Density Matrix Elements at GlueX

6.1.1 Methodology

We use an unbinned extended-maximum likelihood fit to measure the Spin Density Matrix Elements of $\phi(1020)$ using the AmpTools framework. We define the likelihood function as

$$\mathcal{L} = \frac{e^{-\bar{N}} \bar{N}^N}{N!} \prod_{i=1}^N \sigma(\theta_i, \phi_i, \Phi_i) \eta(\theta_i, \phi_i, \Phi_i) \quad (6.1)$$

where N is the total number of events, \bar{N} is the expectation value, $\sigma(\theta, \phi, \Phi)$ is the cross section and $\eta(\theta, \phi, \Phi)$ is the acceptance. Computationally it is more convenient to minimize the negative log-likelihood, so we rewrite Eq. 6.1 as:

$$\ln \mathcal{L} = \sum_{i=1}^N \ln \sigma(\theta_i, \phi_i, \Phi_i) + \sum_{i=1}^N \ln \eta(\theta_i, \phi_i, \Phi_i) - \ln N! - \int d\Omega \sigma(\theta, \phi, \Phi) \eta(\theta, \phi, \Phi) \quad (6.2)$$

the middle term ($\sum \ln \eta - \ln N!$) is omitted from the fit since it is a constant and the absolute value of the likelihood function is not of interest. The measured cross section σ of a reaction can be expressed as a product of the angular distribution $W(\theta, \phi, \Phi)$ and a normalization factor A :

$$\sigma = A \cdot W(\theta, \phi, \Phi). \quad (6.3)$$

The function $W(\theta, \phi, \Phi)$ was derived in Section 5.2 for a linearly polarized photon beam, we write the equation here for convenience:

$$\begin{aligned} W(\cos \theta, \phi, \Phi) &= W^0(\cos \theta, \phi) - P_\gamma \cos(2\Phi) W^1(\cos \theta, \phi) - P_\gamma \sin(2\Phi) W^2(\cos \theta, \phi). \\ W^0(\cos \theta, \phi) &= \frac{3}{4\pi} \left(\frac{1}{2}(1 - \rho_{00}^0) + \frac{1}{2}(3\rho_{00}^0 - 1)\cos^2\theta - \sqrt{2} \text{Re} \rho_{10}^0 \sin 2\theta \cos \phi - \rho_{1-1}^0 \sin^2\theta \cos 2\phi \right) \\ W^1(\cos \theta, \phi) &= \frac{3}{4\pi} \left(\rho_{11}^1 \sin^2\theta + \rho_{00}^1 \cos^2\theta - \sqrt{2} \text{Re} \rho_{10}^1 \sin 2\theta \cos \phi - \rho_{1-1}^1 \sin^2\theta \cos 2\phi \right) \\ W^2(\cos \theta, \phi) &= \frac{3}{4\pi} \left(\sqrt{2} \text{Im} \rho_{10}^2 \sin 2\theta \sin \phi + \text{Im} \rho_{1-1}^2 \sin^2\theta \sin 2\phi \right). \end{aligned} \quad (6.4)$$

The integral in Eq 6.2 can now be written as

$$\int d\Omega \sigma(\theta, \phi, \Phi) \eta(\theta, \phi, \Phi) = A \underbrace{\int d\Omega W(\theta, \phi, \Phi) \eta(\theta, \phi, \Phi)}_{\mathcal{I}}. \quad (6.5)$$

The integral \mathcal{I} is approximated using a Monte Carlo method as

$$\mathcal{I} \approx \frac{4\pi}{N_{MC}} \sum_{j=i}^{N_{MC}^{acc}} W(\theta_j, \phi_j, \Phi_j) \quad (6.6)$$

where N_{MC} is the number of generated MC events and N_{MC}^{acc} is the number of reconstructed MC events that passed our selection criteria. The MC used to evaluate the integral \mathcal{I} is the large phase space MC sample discussed in Chapter 4.

6.1.2 Nominal Measurement

Following the described methodology we analyze 9 bins in $-t$ between 0.15 and 1.0 GeV². The bins follow a logarithmic distribution to more evenly distribute the number of events. Due to the miss-modelling of the $\phi(1020)$ lineshape, see Figure 4.12, the phase space MC is weighed to match the $K_S K_L$ invariant mass distribution in data. A beam energy dependent polarization fraction is used in the fits. The angle of the diamond radiator was determined for each run period in Ref. [76]. We take the luminosity weighted average as the nominal diamond orientation, see Appendix B for more details. The resulting SDMEs are shown in Figure 6.1, with statistical uncertainties provided by MINUIT. We use the mean and variance in each $-t$ bin to plot the results.

6.1.3 Bootstrap Uncertainties

Uncertainties extracted from MINUIT are expected to be underestimated due to the large number of parameters in the fits. A more precise determination of the uncertainties can be obtained by using the bootstrap method. In the bootstrap method, we perform N pseudo-experiments by sampling with replacement the signal and background data while keeping the size of each data set fixed. Here we perform 500 pseudo-experiments to estimate the uncertainty of each SDME. Figure 6.2 shows the distribution of SDMEs for the first bin in $-t$. For each distribution, we calculate the standard deviation and use this as the uncertainty for that SDME in that bin. Uncertainties obtained with the bootstrap method are 20–30% larger than those estimated by MINUIT. SDMEs with uncertainties obtained from MINUIT and the bootstrap method are compared in Figure 6.3.

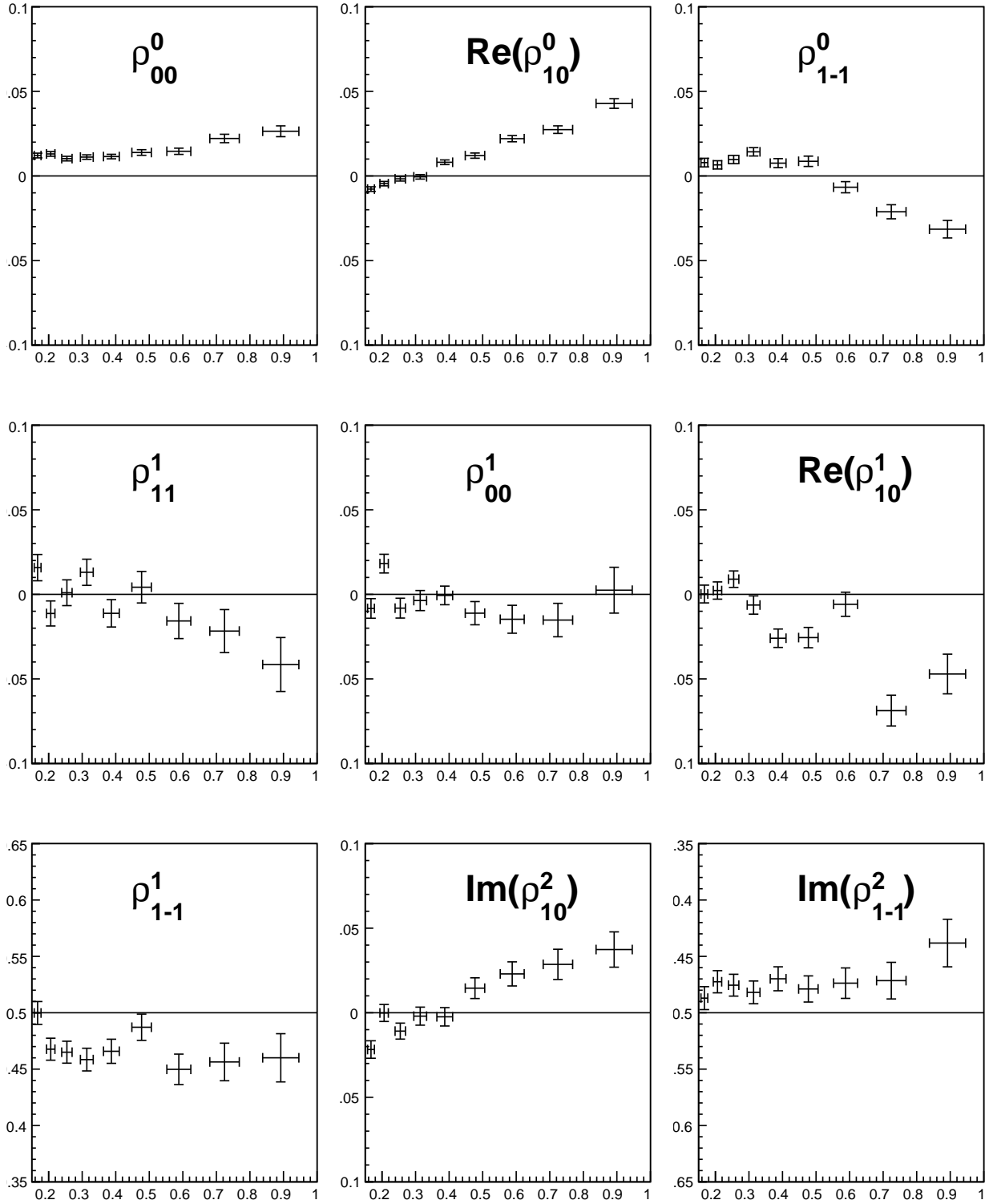


Figure 6.1: Spin Density Matrix Elements for $\phi(1020) \rightarrow K_S K_L$. Only statistical uncertainties obtained from MINUIT are shown.

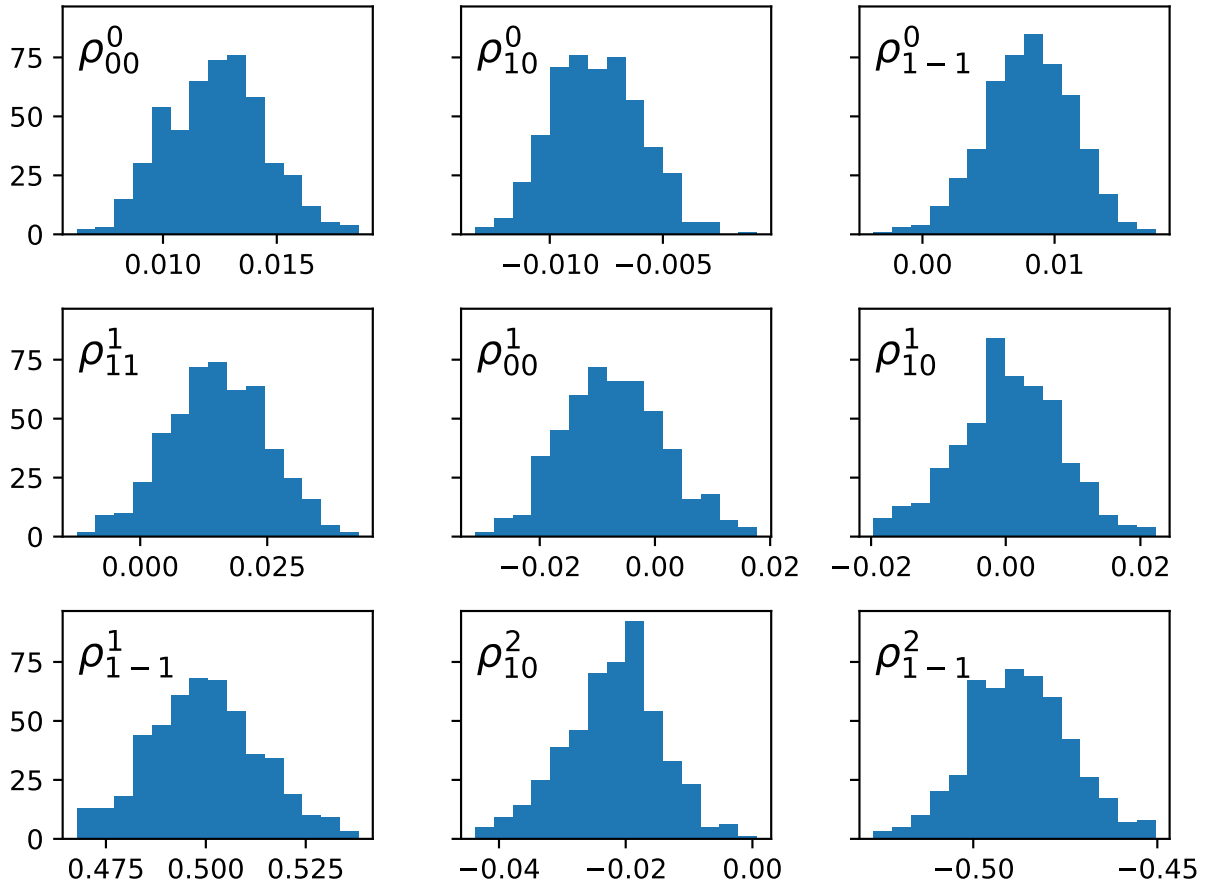


Figure 6.2: Distribution of SDMEs for 500 bootstrap iterations for the first $-t$ bin ($-t \approx 0.15$ GeV²).

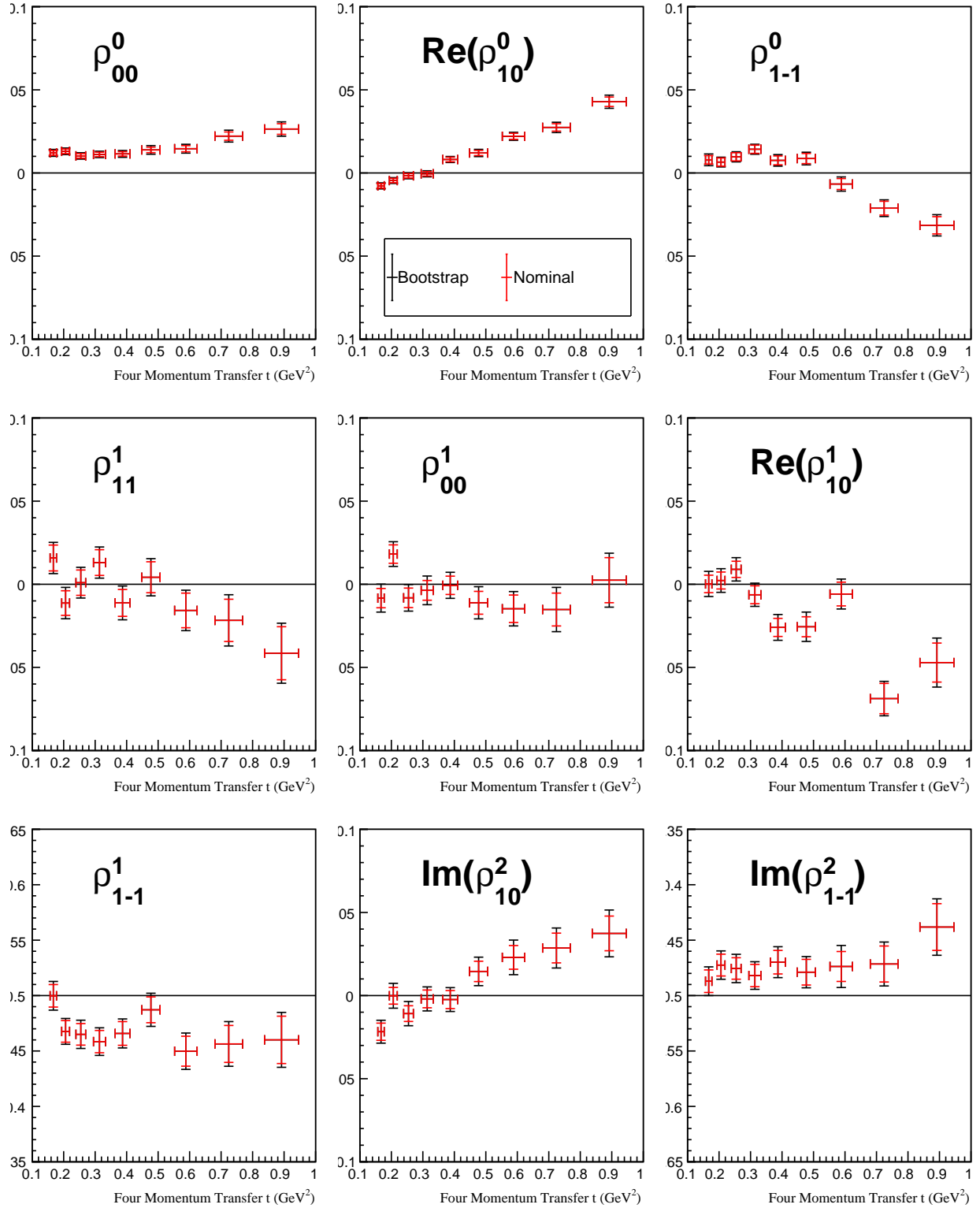


Figure 6.3: SDMEs with uncertainties obtained from MINUIT and using the bootstrap method. The mean value for both distributions is obtained from MINUIT.

6.1.4 Estimating Systematic Uncertainties: Event Selections

We follow the methodology suggested by R. Barlow [77] to gauge the stability of our measurement of $\phi(1020)$ SDMEs due to variations in event selections. For each variation of an event selection, we fit the new data set with starting parameters set to the nominal values, see Figure 6.1. The new converged values of each variation are then compared to the nominal SDMEs by calculating the Barlow criteria

$$\frac{\Delta_B}{\sigma_{Barlow}} = \frac{x_{nominal} - x_{variation}}{\sqrt{|\sigma_{nominal}^2 - \sigma_{variation}^2|}} \quad (6.7)$$

where x_i and σ_i are the SDME values and uncertainties for the nominal and varied data sets, and $\sigma_{Barlow} = \sqrt{|\sigma_{nominal}^2 - \sigma_{variation}^2|}$. The Barlow criteria are calculated using uncertainties obtained from MINUIT. Variations that give a $|\Delta_B| < \sigma_{Barlow}$ are not considered significant. If a variation consistently gives $|\Delta_B| > 4\sigma_{Barlow}$ then it must be included as a systematic uncertainty. Cases that sit in the middle are evaluated more carefully.

Large changes in event selections may cause large differences in the $K_S K_{LP}$ sample size not only in signal events but also in background events. When possible we avoid large changes to the sample size by choosing variations that change the size of the nominal data set by no more than 10%. For most event selections we test three variations typically choosing two stricter and one looser selections. Any change to our selection on number of unused showers and tracks will change the size of the $K_S K_{LP}$ sample by more than 10% and will allow more background events with a second kaon to enter the data set. For extra showers, we test one looser and one stricter selection, and for extra tracks, we test one looser selection. The variations made to each event selection are shown in Figure 6.4.

No systematic uncertainty is attributed to our determination of $\phi(1020)$ SDMEs due to event selections based on the results of the Barlow test. Take for example the results from varying the $\pi^+\pi^-$ invariant mass. Figure 6.5 shows the fit results for each variation together with the nominal SDMEs. For each SDME and each bin, we calculate the Barlow test, see Figure 6.6. A few sporadic points are outside $\pm 4\sigma_{Barlow}$ but these appear as individual ‘‘jumps’’ and the neighboring bins are well within $\pm 4\sigma_{Barlow}$. It is unlikely that a systematic effect will affect one bin but not a neighboring bin. We therefore consider these points outliers and do not attribute a systematic effect due to this event selection. All other tests of event selections show qualitatively similar behavior as the $\pi^+\pi^-$

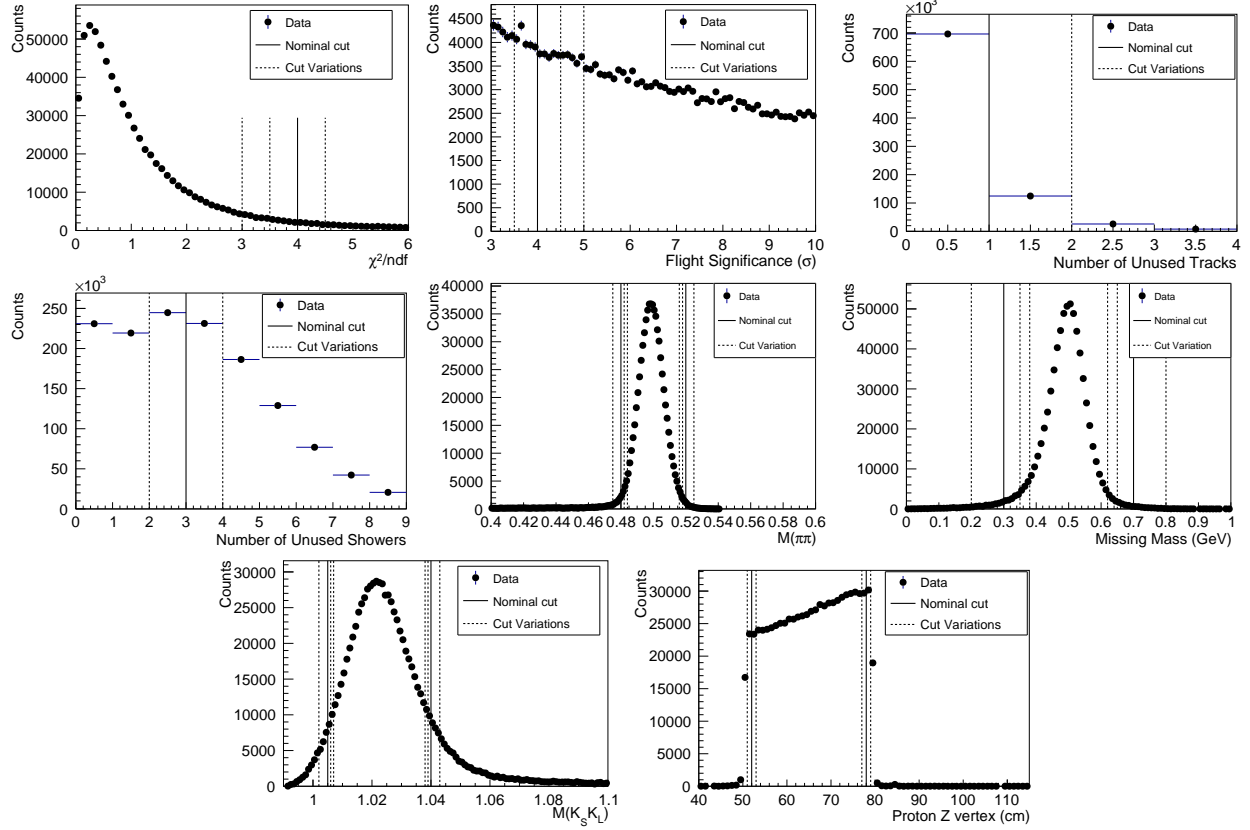


Figure 6.4: Distributions for all event selections after nominal cuts (excluding the plotted variable). Solid vertical lines indicate the nominal selection and dashed vertical lines indicate variations that are tested.

invariant mass test and no systematic effect is attributed to them. The results from all these tests are shown in Appendix C.

6.1.5 Estimating Systematic Uncertainties: Independent Data Sets

When fitting the nominal data set, we assume that all variables are reasonably well modeled and that the physics is the same throughout. We can test these assumptions by subdividing our nominal data set into independent pieces and determine if the $\phi(1020)$ SDMEs obtained from these pieces are statistically compatible. The Barlow test cannot be used for these kinds of tests because the term $\sigma_{Barlow} = \sqrt{|\sigma_1 - \sigma_2|}$ assumes that the two data sets are correlated. A test of statistical compatibility is the *pull*, defined as

$$pull = \frac{x_1 - x_2}{\sqrt{\sigma_1^2 + \sigma_2^2}} \quad (6.8)$$

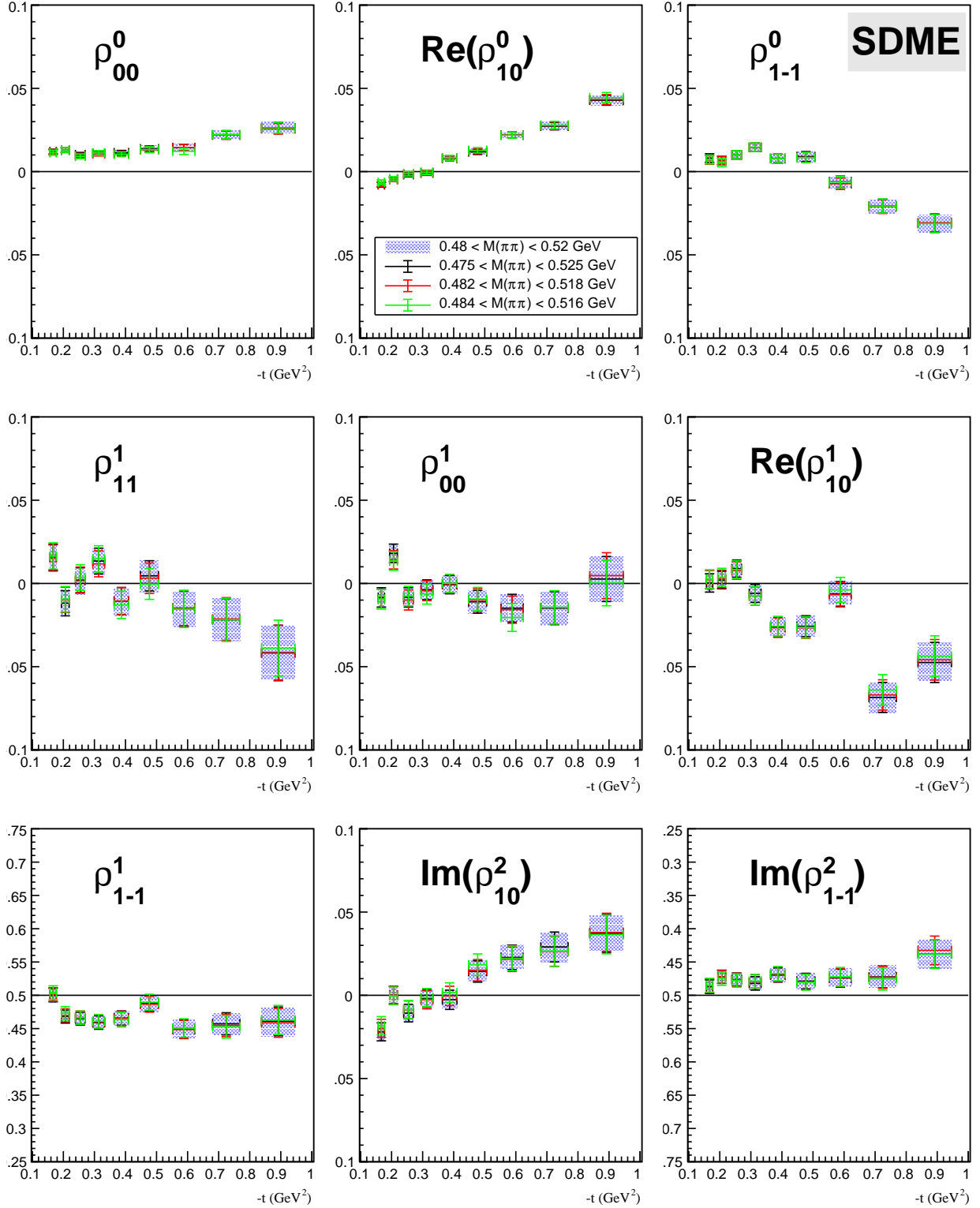


Figure 6.5: Spin-Density Matrix Elements for the nominal data set and three variations on the $\pi^+\pi^-$ invariant mass selection.

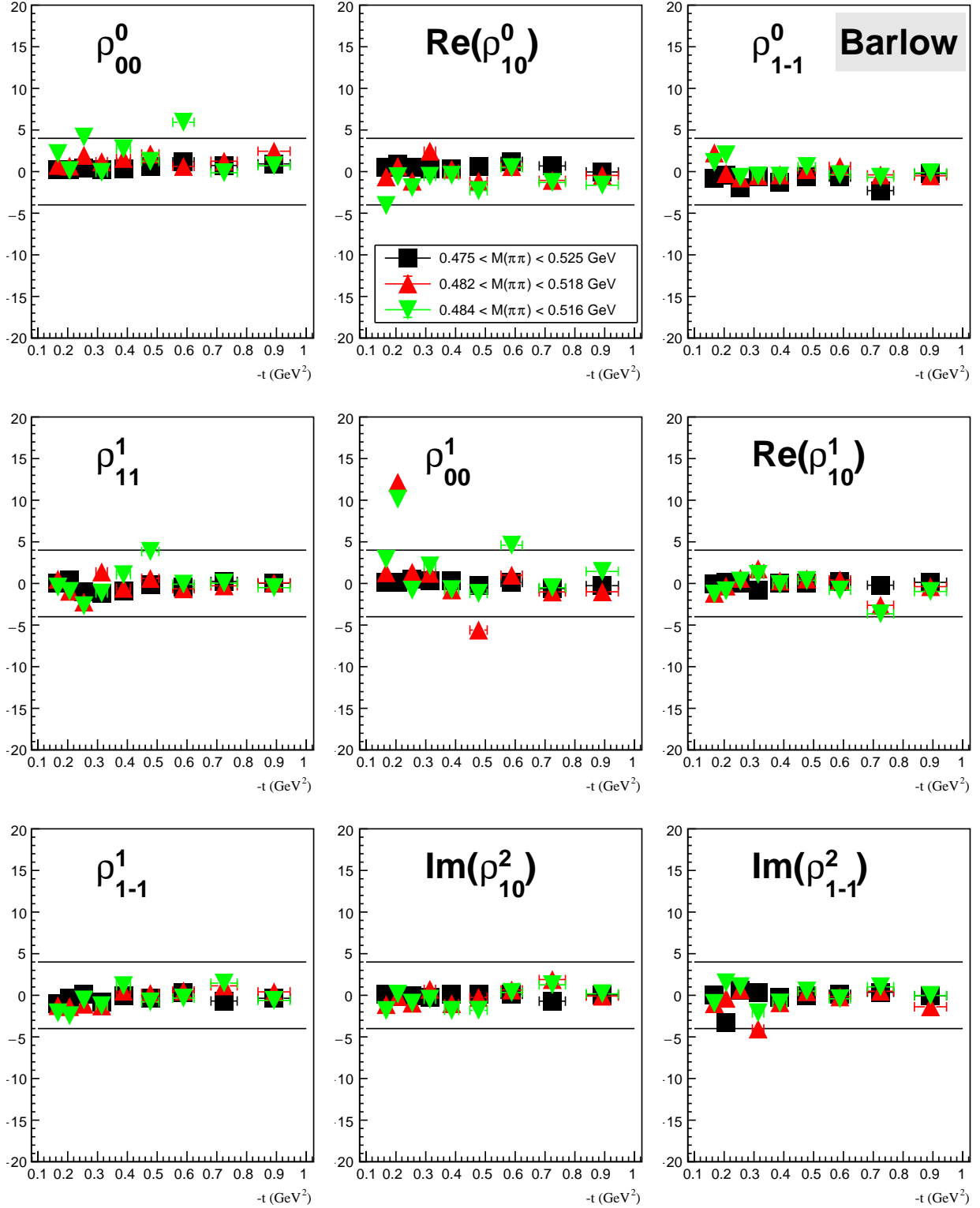


Figure 6.6: Barlow significance test for each $\pi\pi$ invariant mass variation as a function of $-t$. Horizontal lines indicate $\pm 4\sigma_{Barlow}$.

where x_i and σ_i are the SDME values and uncertainties for data sets 1 and 2, respectively.

Above/Below the $\phi(1020)$ Mass The SDME model used in this analysis assumes that the data only contains decays of a vector meson. To test the effect of backgrounds we separate the nominal data set into two bins of $K_S K_L$ invariant mass divide at 1.2 GeV. Figure 6.7 shows the $\phi(1020)$ SDMEs for the nominal selection and upper/lower half of the $K_S K_L$ invariant mass distribution. To evaluate the statistical compatibility of the upper/lower halves, we calculate the pull, see Eq. 6.8, for each SDME as a function of $-t$. For each SDME we calculate the mean (μ) and standard deviation (σ) of the pulls. Assuming that the two data sets are statistically consistent, we expect the pull distributions to be Gaussian distributed with a mean of 0 and a standard deviation of 1. Figure 6.8 shows the pull for each SDME along with their mean and standard deviation. Only $\text{Re}(\rho_{10}^0)$ and ρ_{1-1}^0 show a mean that is inconsistent with 0. For each bin and each SDME, a systematic uncertainty due to $K_S K_L$ invariant mass is estimated for $\text{Re}(\rho_{10}^0)$ by calculating $\text{pull} \cdot \sigma$, as defined in Eq. 6.8. For ρ_{1-1}^0 we use the mean pull, $\mu = 2.8$ as seen in Figure 6.8. Since the pull distribution is fairly flat as a function of $-t$ the mean pull smooths over the fluctuations.

Beam Energy We can estimate if the $\phi(1020)$ SDMEs depend on the beam energy by separating the data into two E_γ bins. Figure 6.9 shows the $\phi(1020)$ SDMEs for the nominal selection and two equally sized bins of beam energy. Figure 6.10 shows the distributions. Only the mean of ρ_{11}^1 is seen to deviate substantially from expectations. We estimate the systematic effect for ρ_{11}^1 by calculating the $\text{pull} \cdot \sigma$ for each bin and each SDME.

Perpendicular Diamond Orientations Figure 6.11 shows the $\phi(1020)$ SDMEs for the nominal selection and two sets of perpendicular (0/90 and 45/-45) diamond orientations. Figure 6.12 shows the pull distributions. All SDMEs are roughly consistent with a mean of 0 and a standard deviation of 1. We do not take a systematic uncertainty due to the different diamond orientations.

2017 and 2018 Run Periods Figure 6.13 shows the $\phi(1020)$ SDMEs for the GlueX-I and each run period. Due to the smaller statistics of each data set, we found it necessary to reduce the binning from nine bins to seven bins. Still, one bin for Spring 2017 and one for Fall 2018 did not properly converge. We ignore this bin when calculating the pulls which are shown in Figure 6.14. Although some SDMEs show relatively large standard deviations no strong bias is seen. We conclude that these data sets are statistically consistent.

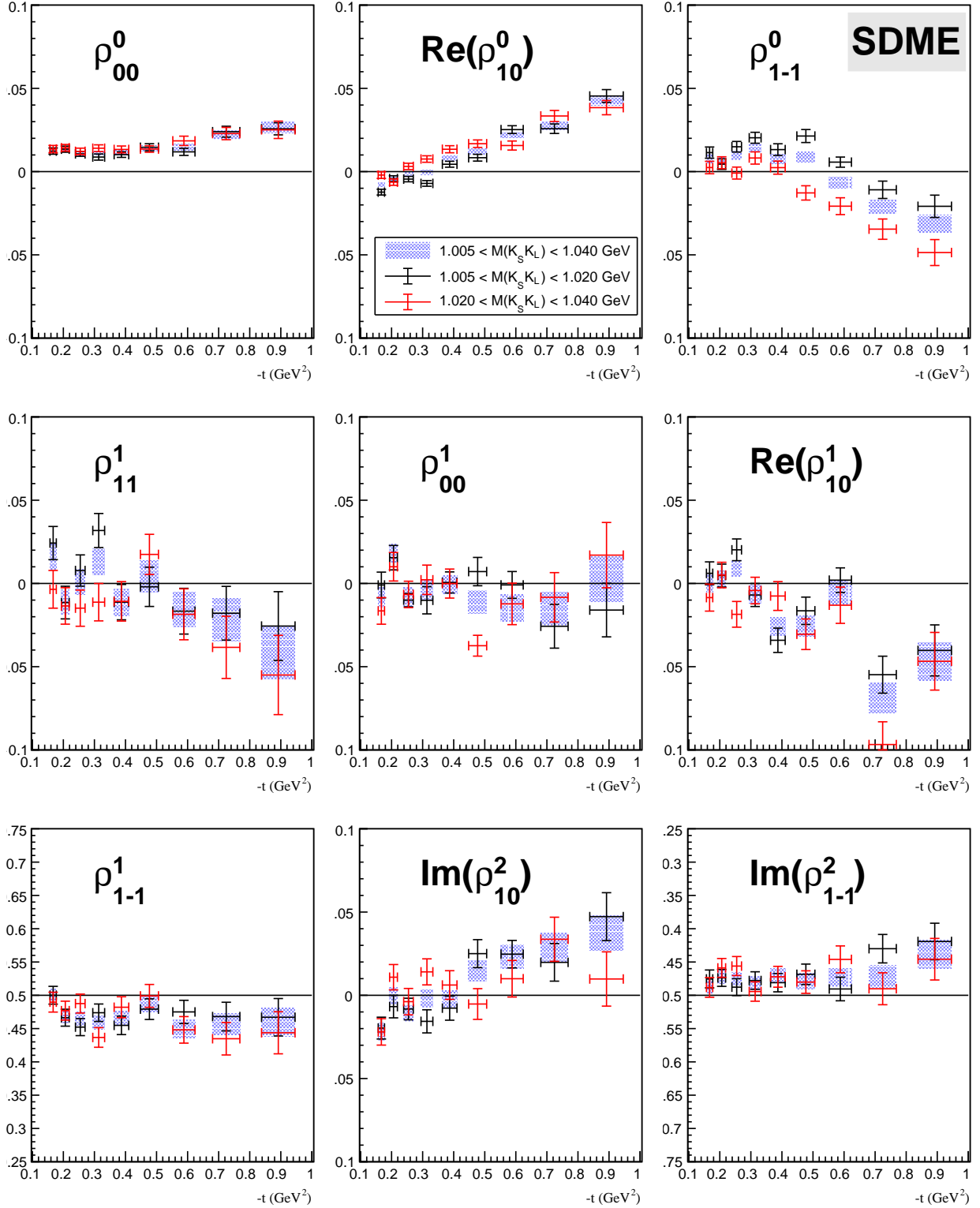


Figure 6.7: Spin-Density Matrix Elements as a function of $-t$ for lower/upper half of the $M(K_S K_L)$ distribution. The nominal results are drawn as a blue box. Only uncertainties from MINUIT are shown.

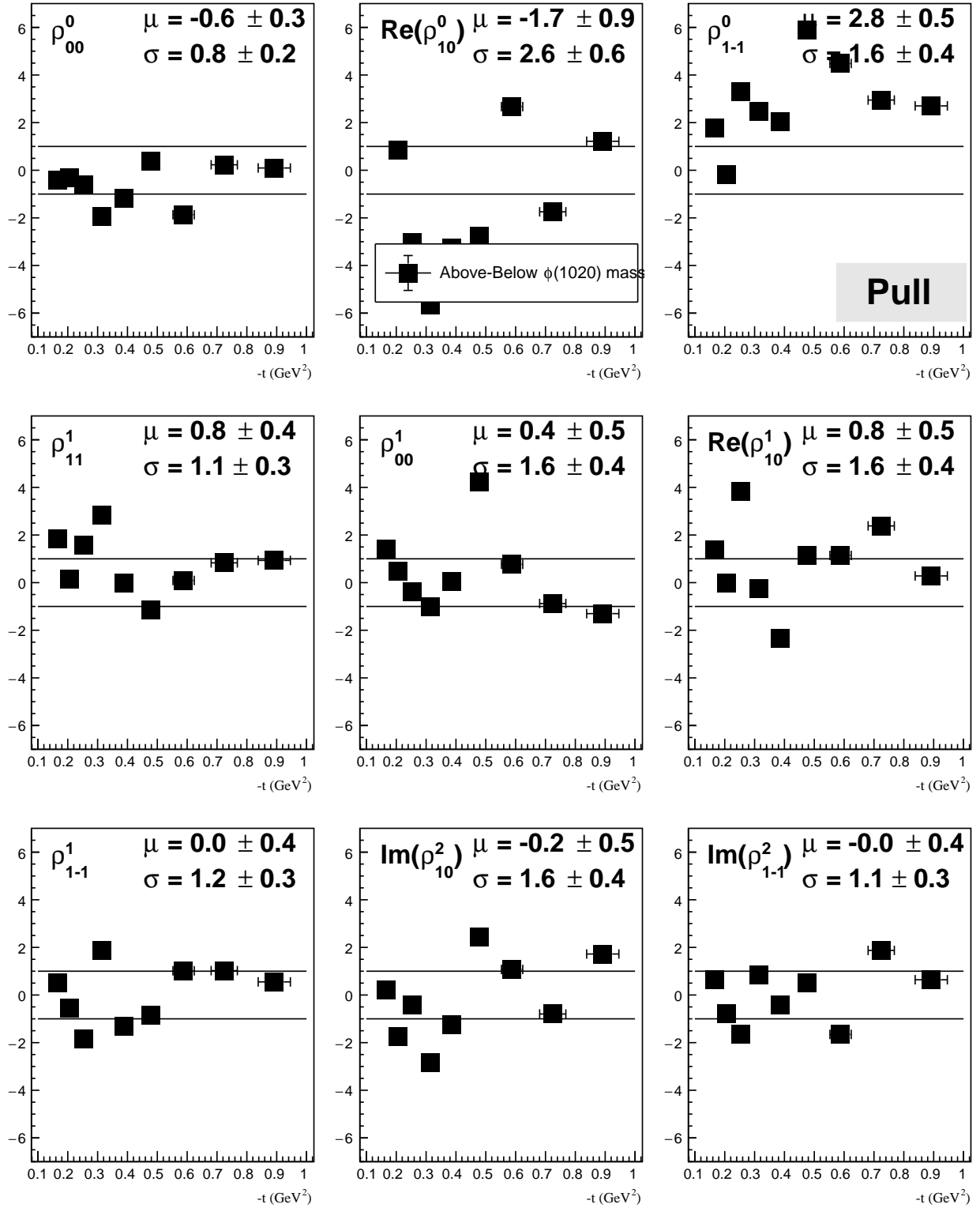


Figure 6.8: Pull for the lower/upper half of the $M(K_S K_L)$ distribution as a function of $-t$. Horizontal lines indicate $\pm 1\sigma$.

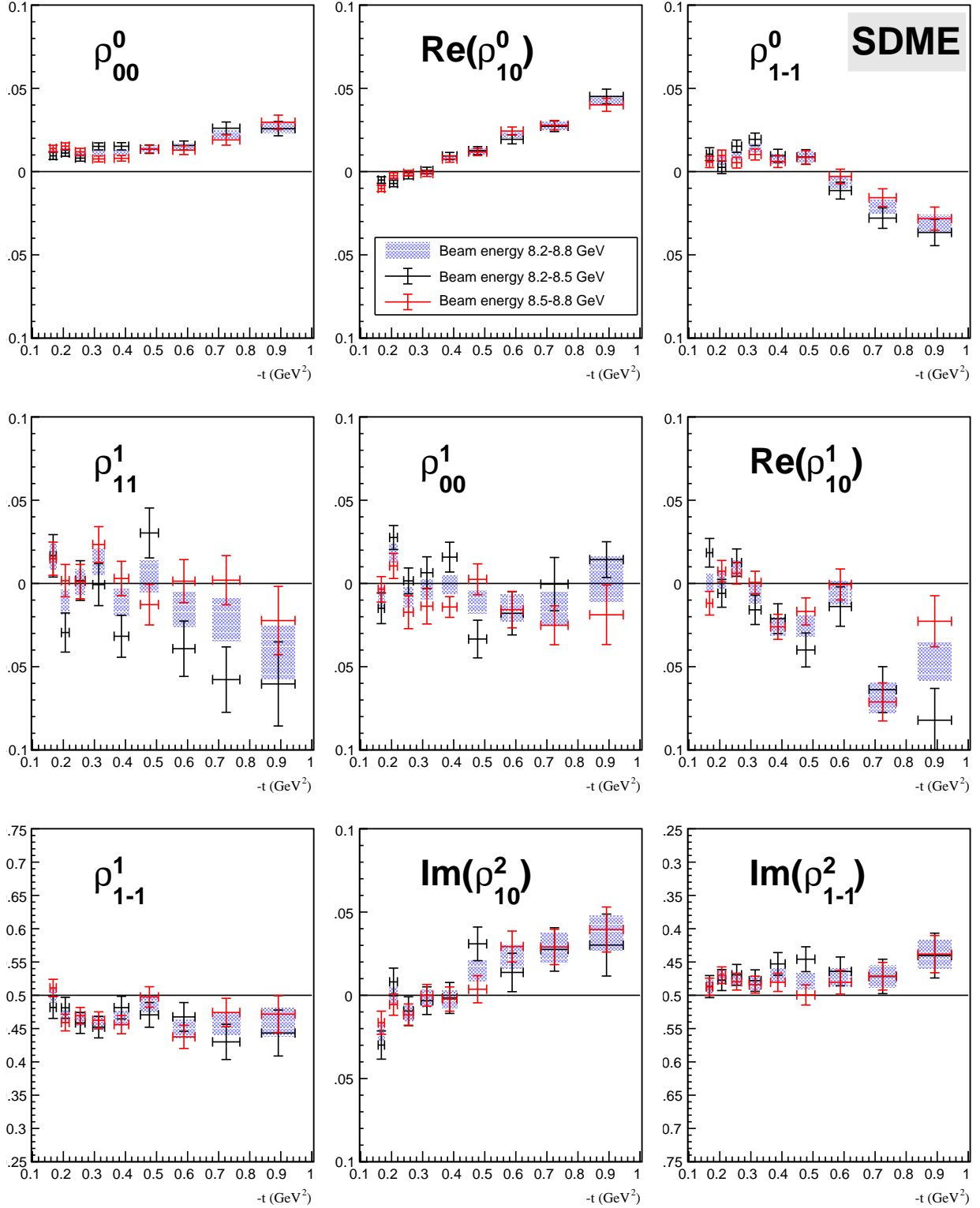


Figure 6.9: Spin-Density Matrix Elements as a function of $-t$ in bins of photon beam energy. The nominal results are drawn as a blue box. Only uncertainties from MINUIT are shown.

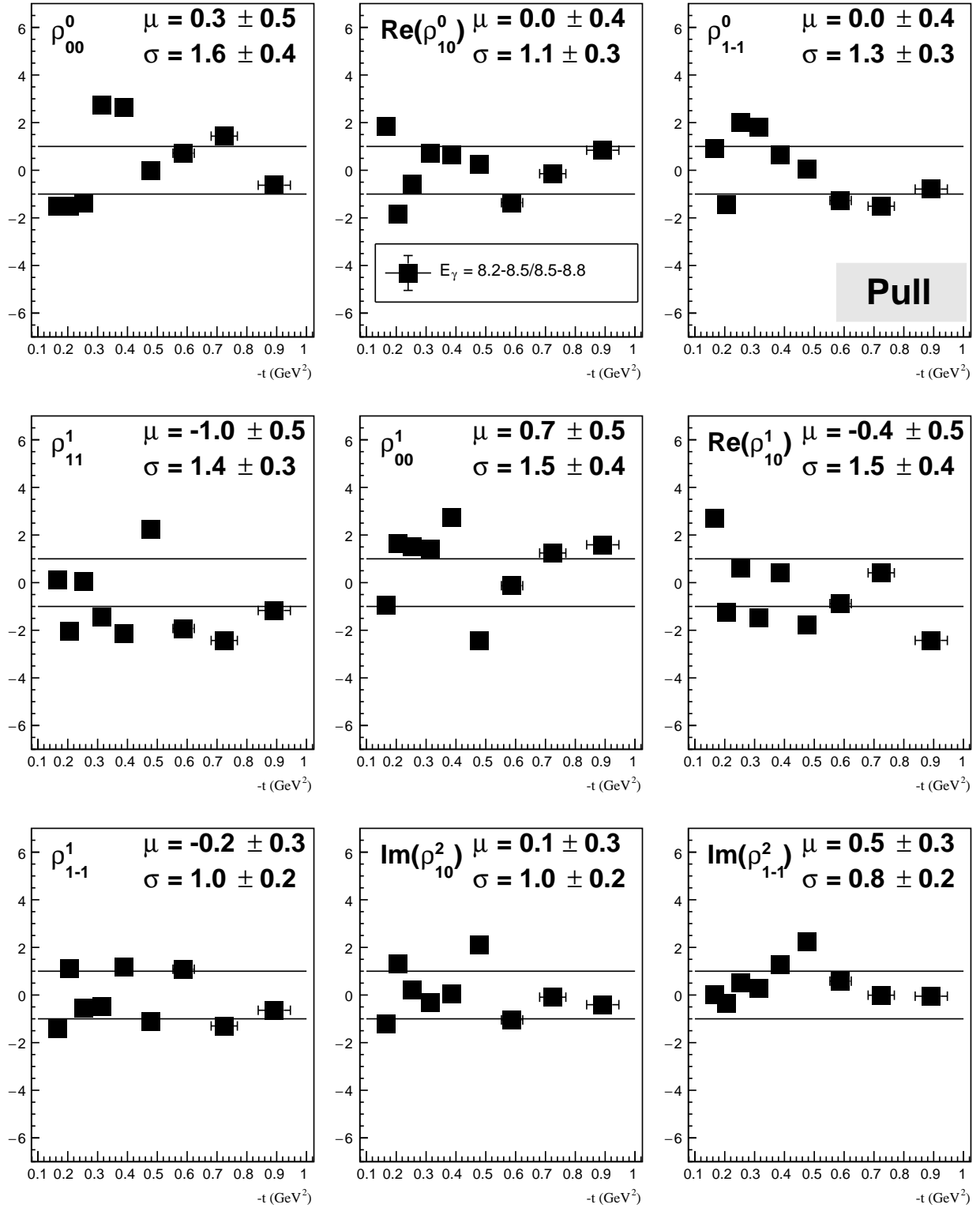


Figure 6.10: Pull for each beam energy bin as a function of $-t$. Horizontal lines indicate $\pm 1\sigma$.

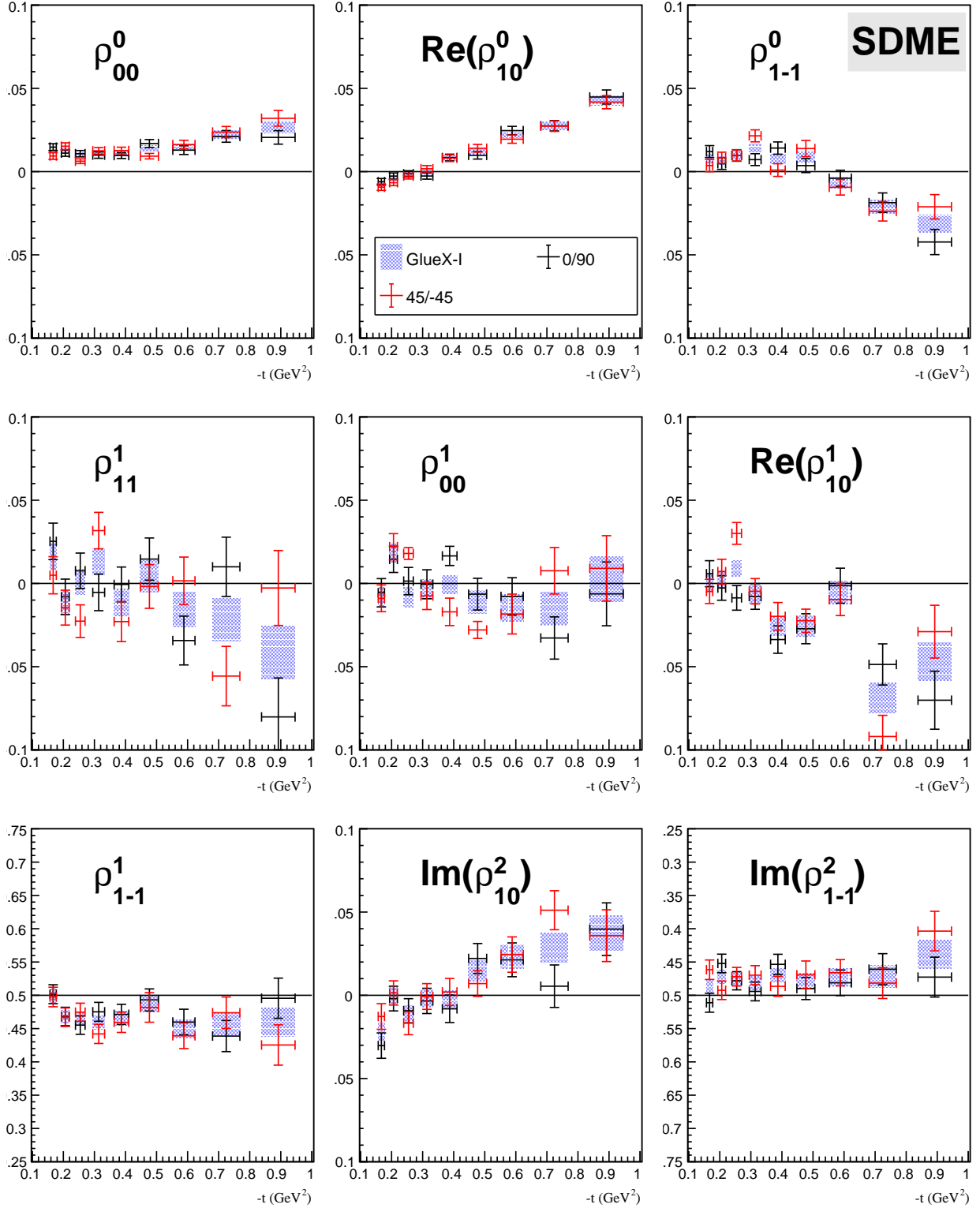


Figure 6.11: Spin-Density Matrix Elements as a function of $-t$ for 0/90 and 45/-45 diamond orientations. The nominal results are drawn as a blue box. Only uncertainties from MINUIT are shown.

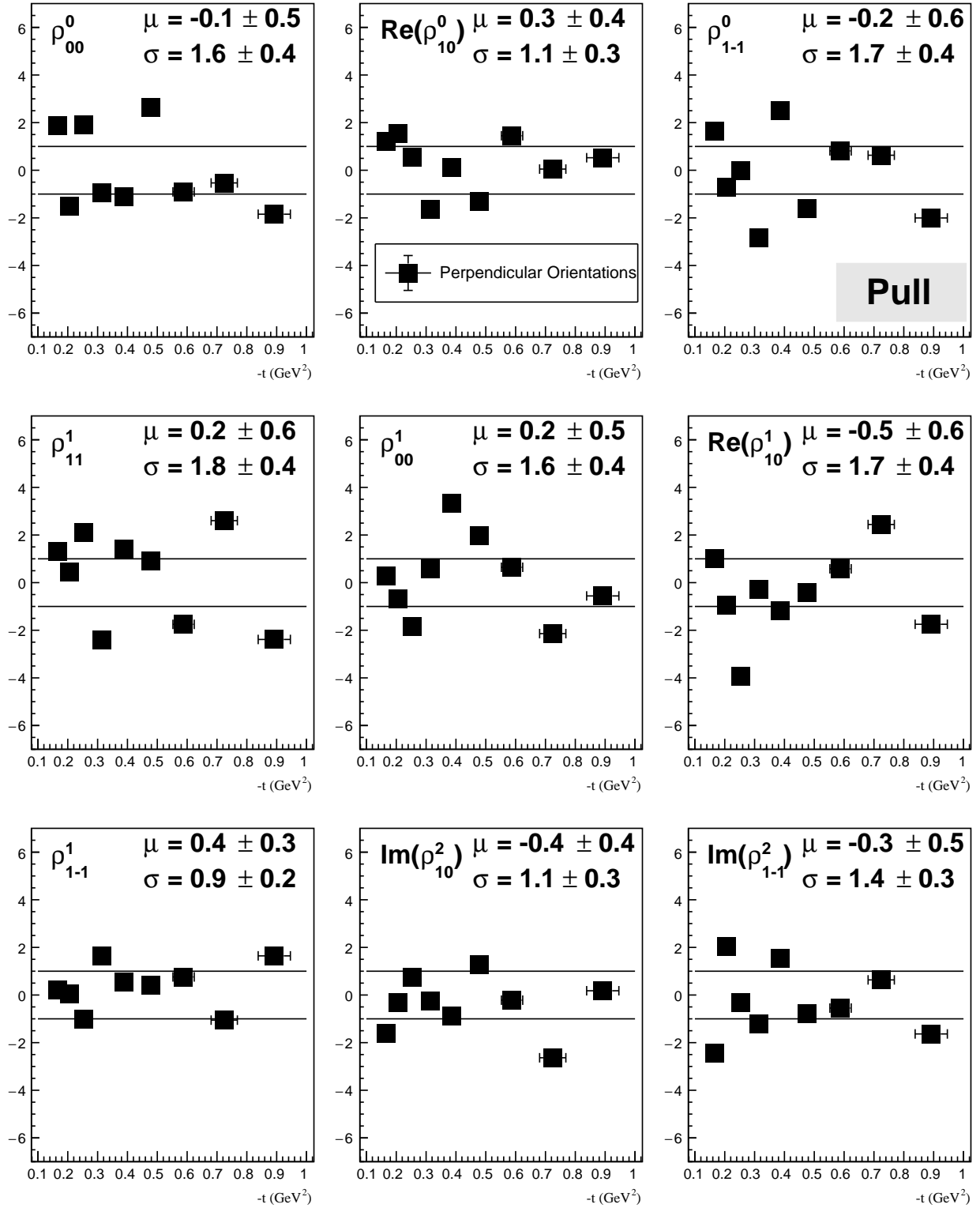


Figure 6.12: Pull distributions for 0/90 and 45/−45 diamond orientations as a function of $-t$. Horizontal lines indicate $\pm 1\sigma$.

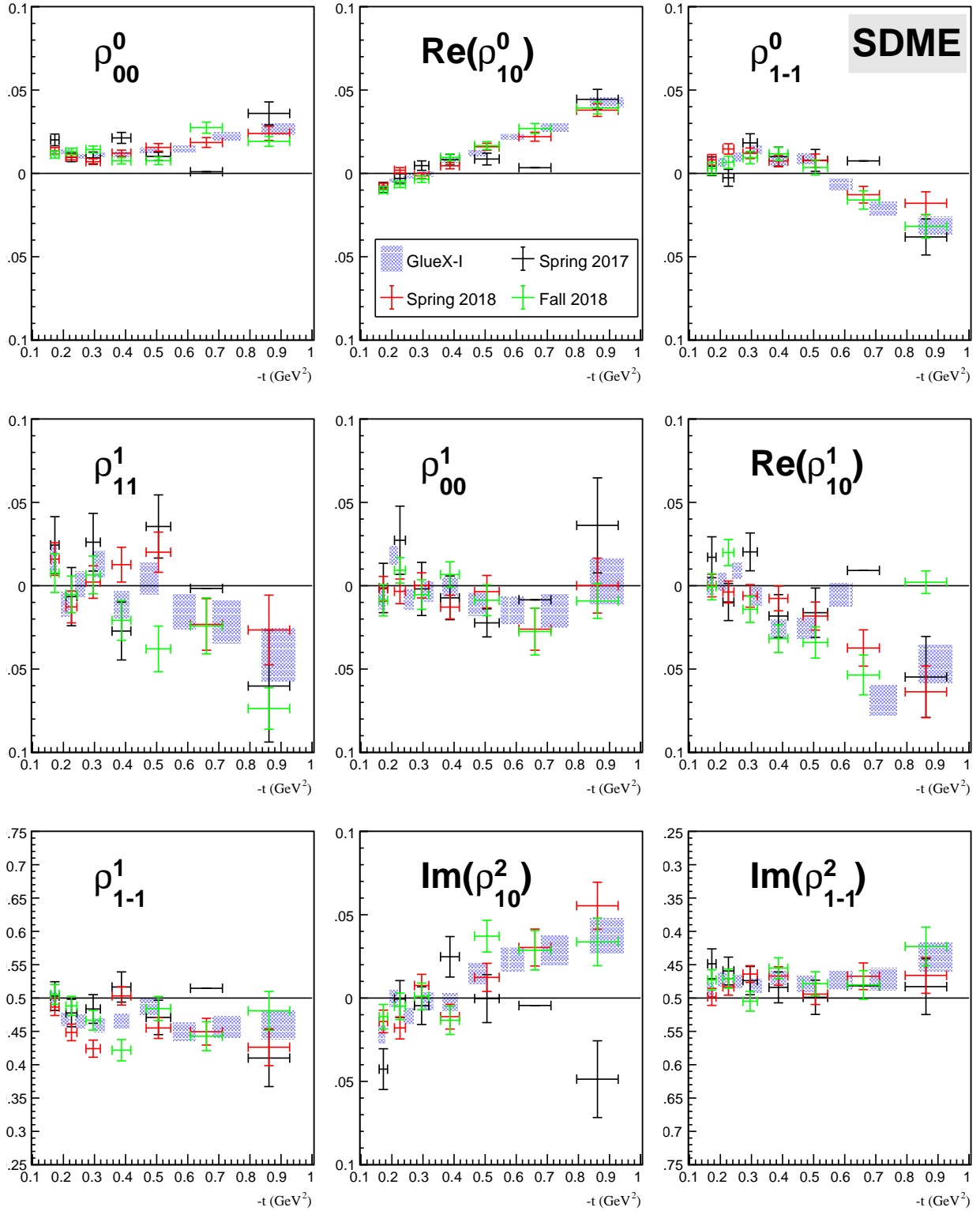


Figure 6.13: Spin-Density Matrix Elements as a function of $-t$ for each run period and full Phase-I data. The nominal results are drawn as a blue box. Only uncertainties from MINUIT are shown.

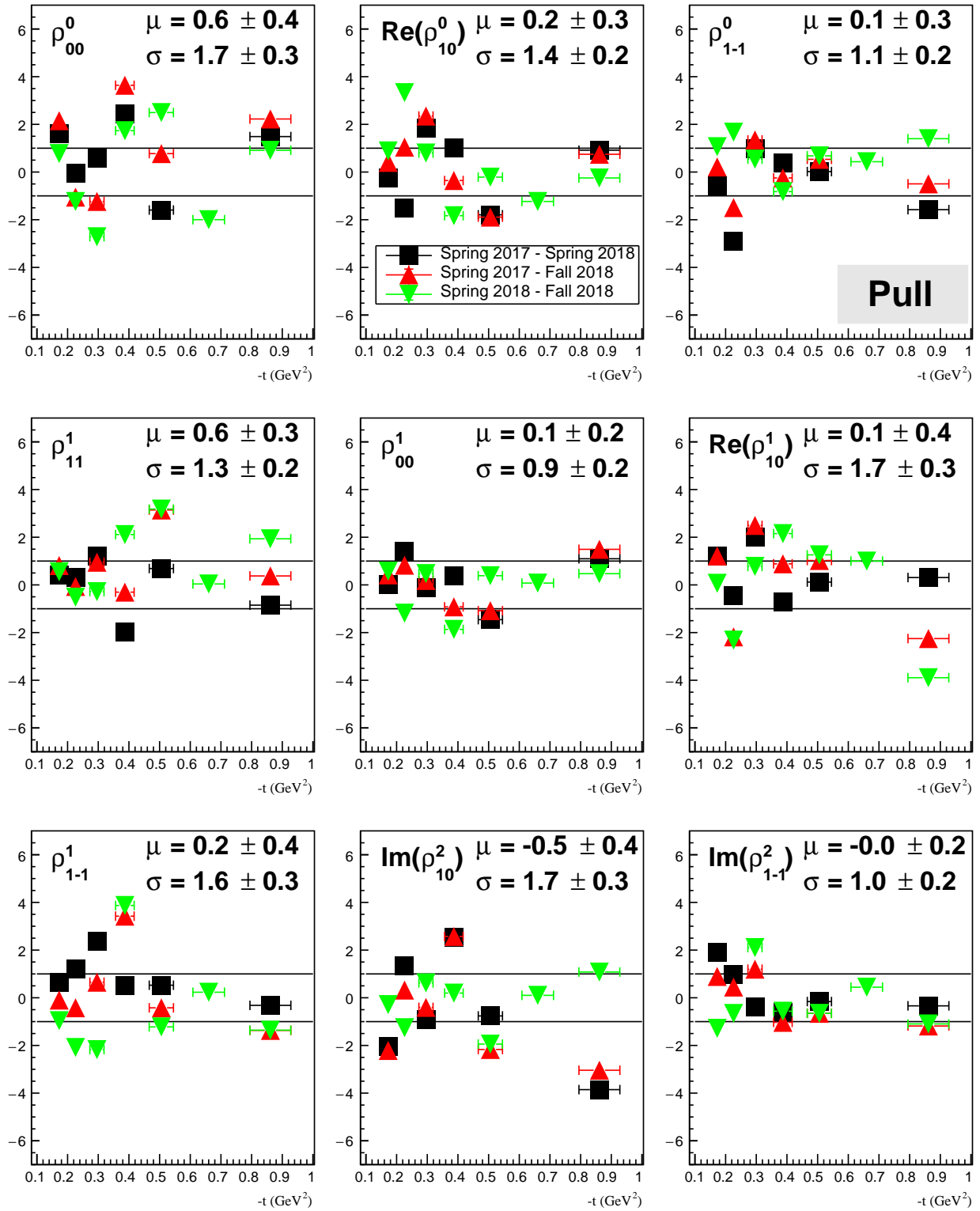


Figure 6.14: Pull for each run period as a function of $-t$. Horizontal lines indicate $\pm\sigma$.

Comparison to Spring 2020 Data is shown in Figure 6.15. Both data sets are similar in size but the MC sample used to estimate the acceptance of the Spring 2020 data is 40 million while 100 million events were generated for GlueX-I. Additionally, the Spring 2020 data has not been studied in detail. Still, comparing the SDMEs extracted from each data set is useful since the same trends should be observed in both data sets. Figure 6.15 shows the SDMEs for GlueX-I and Spring 2020 data and the pull distributions are shown in Figure 6.16. A systematic effect is seen for ρ_{00}^0 , $\text{Re}(\rho_{10}^0)$ and ρ_{11}^1 . However, since the Spring 2020 data has not been investigated closely and the observed trends are consistent between both data sets, we conclude that the level of agreement is satisfactory.

6.1.6 Estimating Systematic Uncertainties: Other Test

Polarization Angle (Φ) is a fixed parameter in the fit which was determined by an external analysis, see Appendix B. The sensitivity to this fixed parameter is determined by varying the value by \pm one standard deviation. Figure 6.17 shows $\phi(1020)$ SDMEs for the nominal polarization angle and the variations. The effect of varying the polarization angle is difficult to see by eye. However, in Figure 6.18 we calculate the percent difference $(1 - x_{\text{variation}}/x_{\text{nominal}})$ and find that some SDMEs have a large percent difference. Since both the polarized ($\rho^{1,2}$) and unpolarized (ρ^0) SDMEs have at least one bin with a larger than one percent difference, we assign a systematic uncertainty to all SDMEs and all bins. The systematic effect is estimated by taking the difference between the nominal and offset values and choosing the larger of the two deviations.

Polarization Fraction (P_γ) is a fixed parameter in the fit and was determined by an independent analysis with a 2.1% uncertainty. The intensity, see Eq. 5.27, is linear in P_γ and affects only the ρ^1 and ρ^2 terms. As a purely external input the uncertainty on P_γ should be uncorrelated to other systematic effects. We quadratically add a 2.1% uncertainty to the ρ^1 and ρ^2 terms.

Input-Output Test We generated 20M events with all SDMEs set to 0 except for ρ_{1-1}^1 and $-\text{Im}(\rho_{1-1}^2)$, which were set to 0.5 and -0.5 , respectively. The polarization angle (Φ) and polarization fraction (P_γ) were set to 0° and 0.36 respectively. The generated sample was analyzed in the same way as the data. After event selections, the MC is about 40% larger than the nominal data set. Figure 6.19 shows the results of the fit. Some bins in ρ_{11}^1 , $\text{Re}(\rho_{10}^1)$ and $\text{Im}(\rho_{10}^2)$ are not consistent with the generated values but appear to be random fluctuations rather than a systematic bias. On the other hand, ρ_{00}^0 shows a clear systematic shift away from the generated value. We

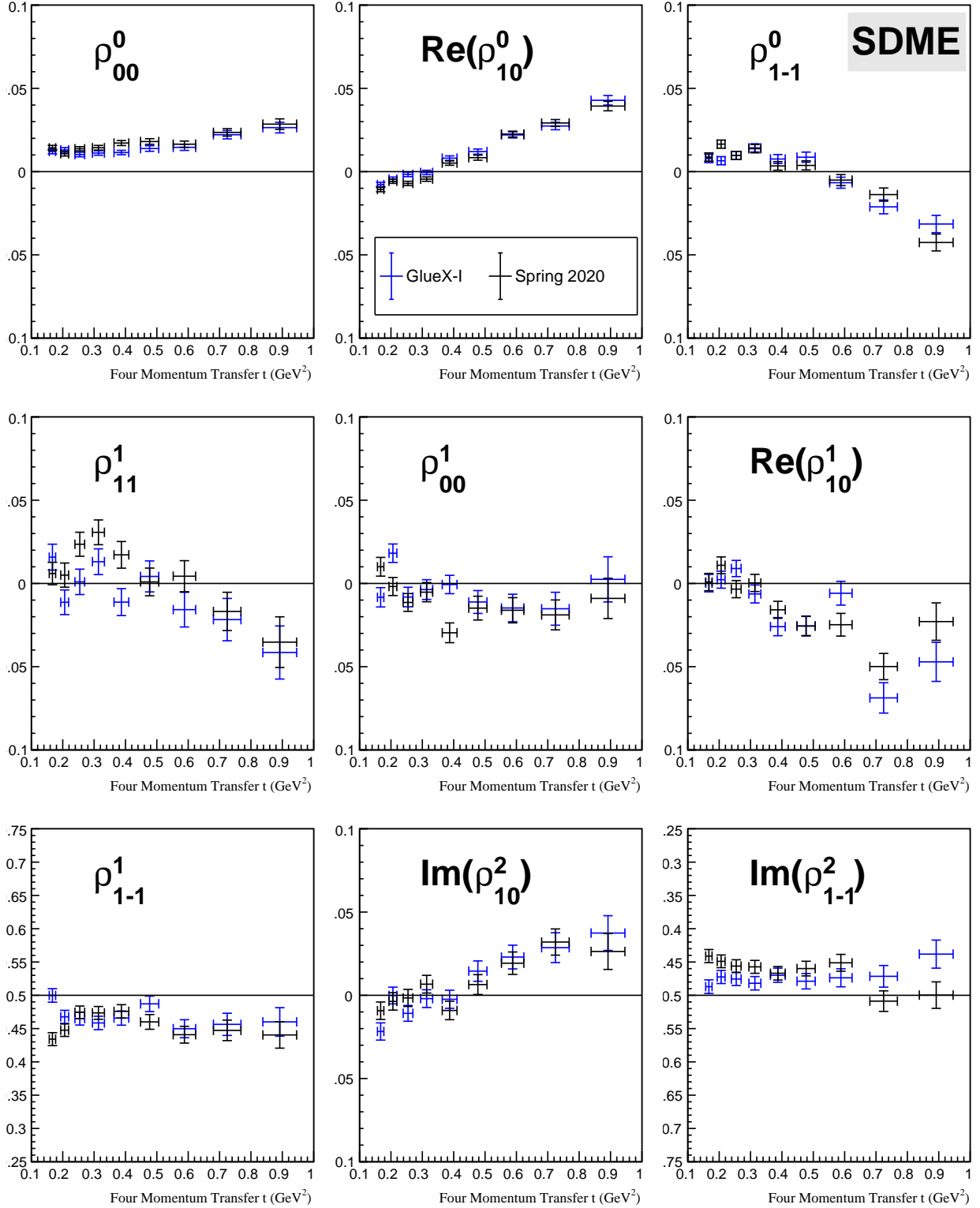


Figure 6.15: Spin-Density Matrix Elements as a function of $-t$ for GlueX-I and Spring 2020 data. The nominal results are drawn as a blue box. Only uncertainties from MINUIT are shown.

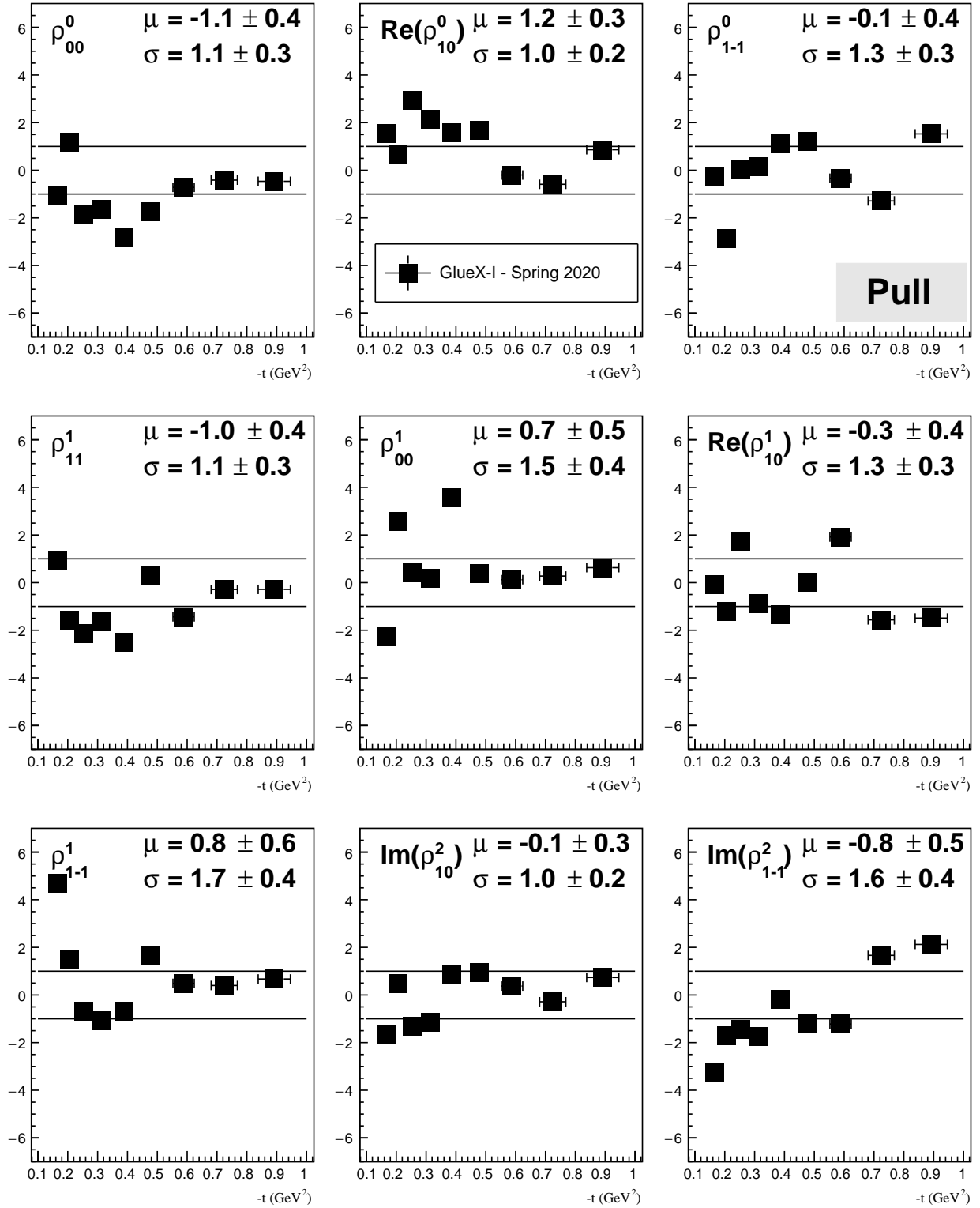


Figure 6.16: Pull for each run period as a function of $-t$. Horizontal lines indicate $\pm 1\sigma$.

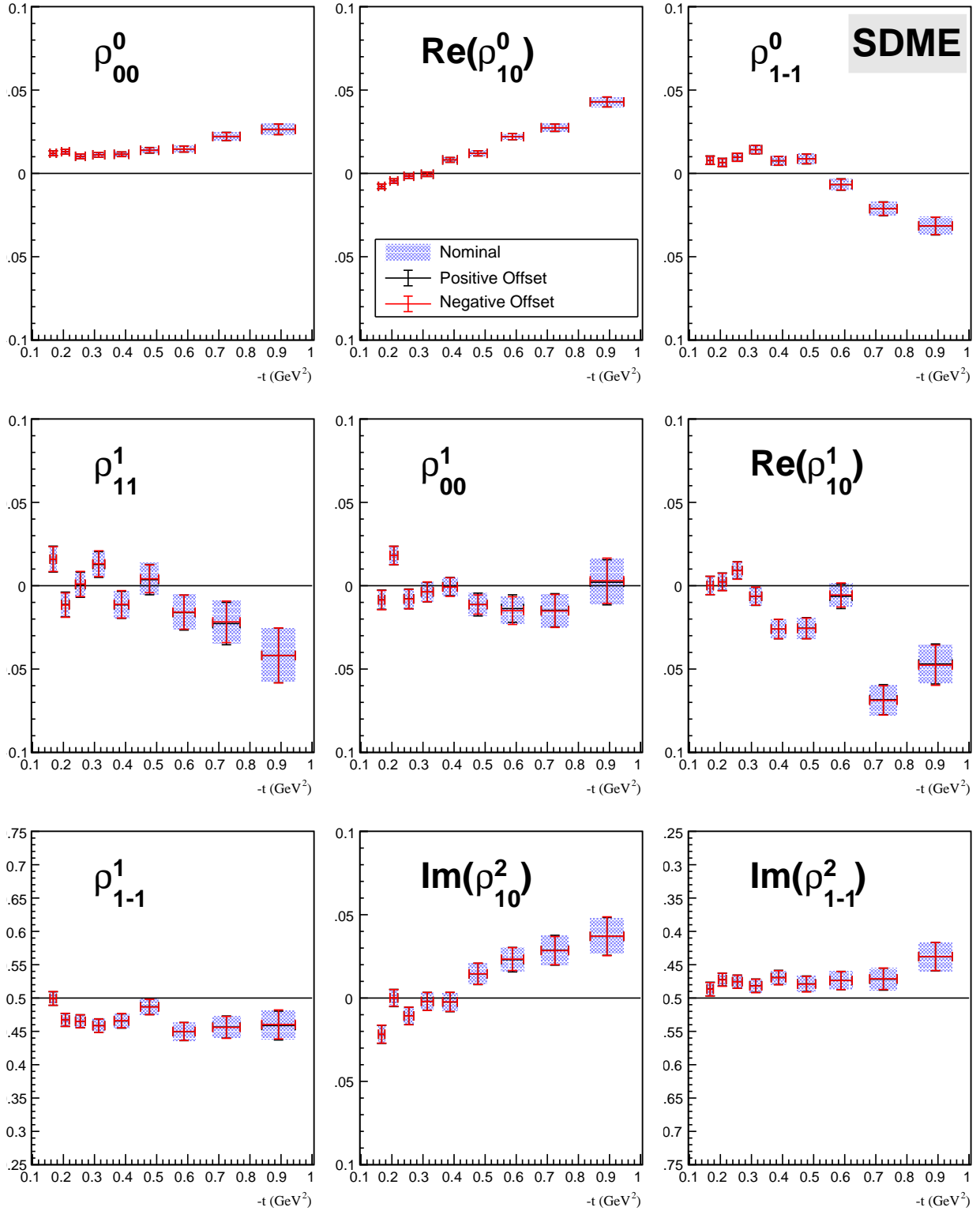


Figure 6.17: Spin-Density Matrix Elements as a function of $-t$ for polarization angle at the nominal value and offset by $\pm 1\sigma$. The nominal results are drawn as a blue box. Only uncertainties from MINUIT are shown.

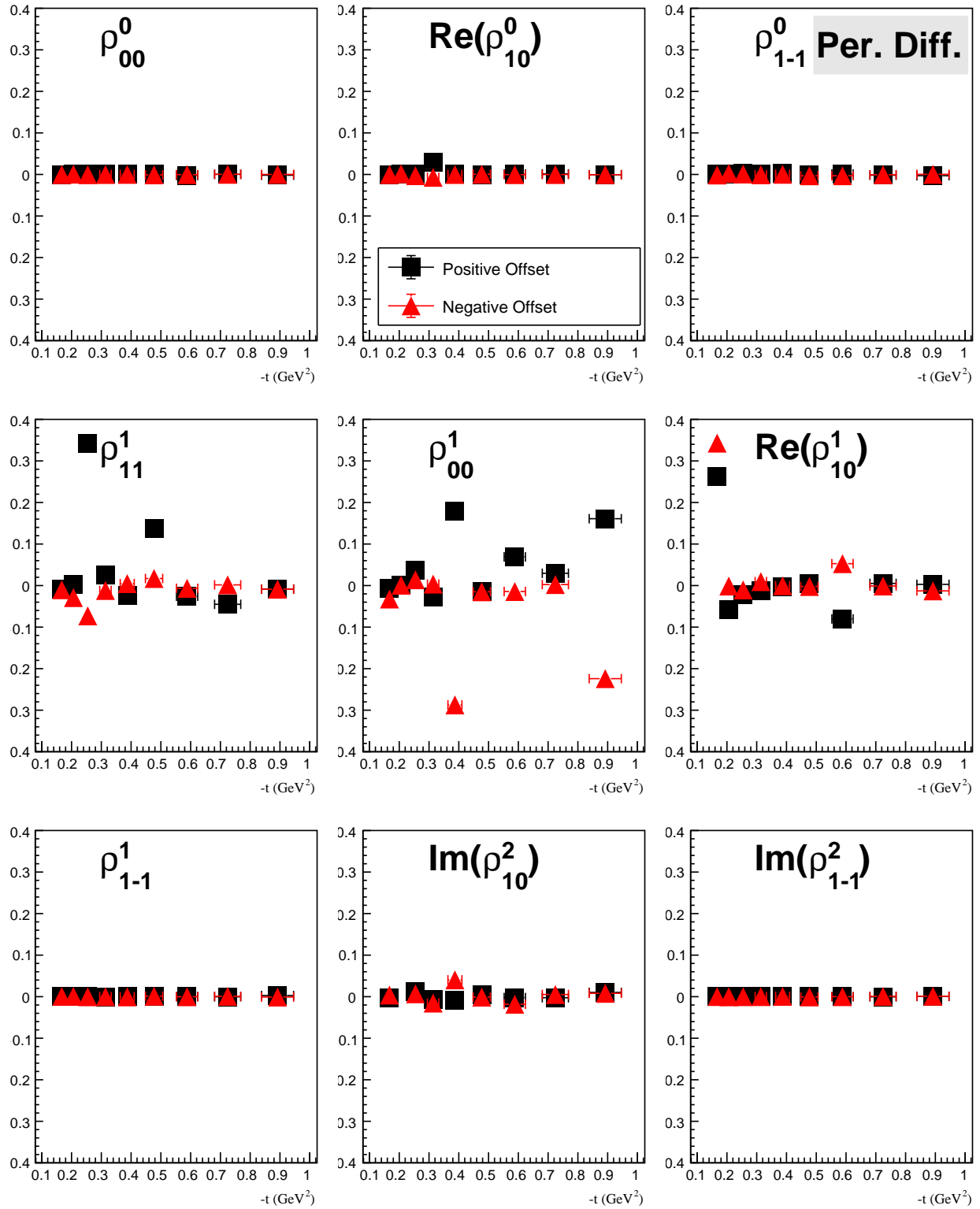


Figure 6.18: Percent difference for polarization angle offset by $\pm 1\sigma$ as a function of $-t$. Horizontal lines indicate $\pm 1\sigma$.

determine the size of the offset by fitting the ρ_{00}^0 points with a constant which was found to be 0.0075 ± 0.0005 . The cause of this offset has not been determined. Conservatively, we assume that the upper bound on the fitted constant (0.008) is a 1σ uncertainty on some unknown source of systematic uncertainty that is uncorrelated to other systematic uncertainties we have explored.

6.1.7 Summary of Systematic Studies

Table 6.1 summarizes all systematic studies for this analysis. No systematic effect is attributed to event selections, diamond orientations, or run periods. We estimated the uncertainty of SDMEs that showed a systematic effect when calculating the pull distributions by calculating $n\sigma$ where n is the pull and σ is the combined standard deviation. The pull distribution for ρ_{1-1}^0 are fairly constant as a function of $-t$, see Figures 6.8. We therefore choose n to be the average pull for each bin. For ρ_{1-1}^0 and ρ_{11}^1 , n is the pull for that bin. A systematic uncertainty is attributed to each SDME in each bin due to the polarization angle (Φ). To estimate this systematic contribution we take the difference between the nominal and offset SDMEs. For each SDME and each bin, we use the larger of the two deviations. For the polarized SDMEs ($\rho^{1,2}$), we add a 2.1% contribution due to the uncertainty on the polarization fraction (P_γ). The input-output MC test suggests there is a bias of 0.008 on our determination of ρ_{00}^0 . We assume that 0.008 is a 1σ uncertainty on some unknown source of systematic uncertainty. We assume all sources of systematic uncertainty are uncorrelated and add them in quadrature to determine the total systematic uncertainty. Figure 6.20 shows the $\phi(1020)$ SDMEs together with the total systematic uncertainty.

6.1.8 Final Result

The $\phi(1020)$ SDMEs with statistical and systematic uncertainties are shown in Figure 6.21 along with the JPAC model and expectations from s-channel helicity conservation¹. We find the $\phi(1020)$ SDMEs are consistent with SCHC at low $-t$. ρ_{1-1}^1 and ρ_{1-1}^2 are constant as a function of $-t$ but systematically shift away from the expected values of ± 0.5 . ρ_{00}^0 is also systematically above 0 and shows a small rise at higher $-t$. A rise in $-t$ is also present in the JPAC model although it is much smaller in data. ρ_{11}^1 and ρ_{10}^2 are consistent with the JPAC model, however, the deviation from SCHC present in the JPAC model is due to unnatural exchange which we will see is inconsistent with the data. The other SDMEs are not well described by the JPAC model at high $-t$.

¹Remember that SCHC implies that the only non-zero SDMEs are $\rho_{1-1}^1 = -Im(\rho_{1-1}^2) = 1/2$.

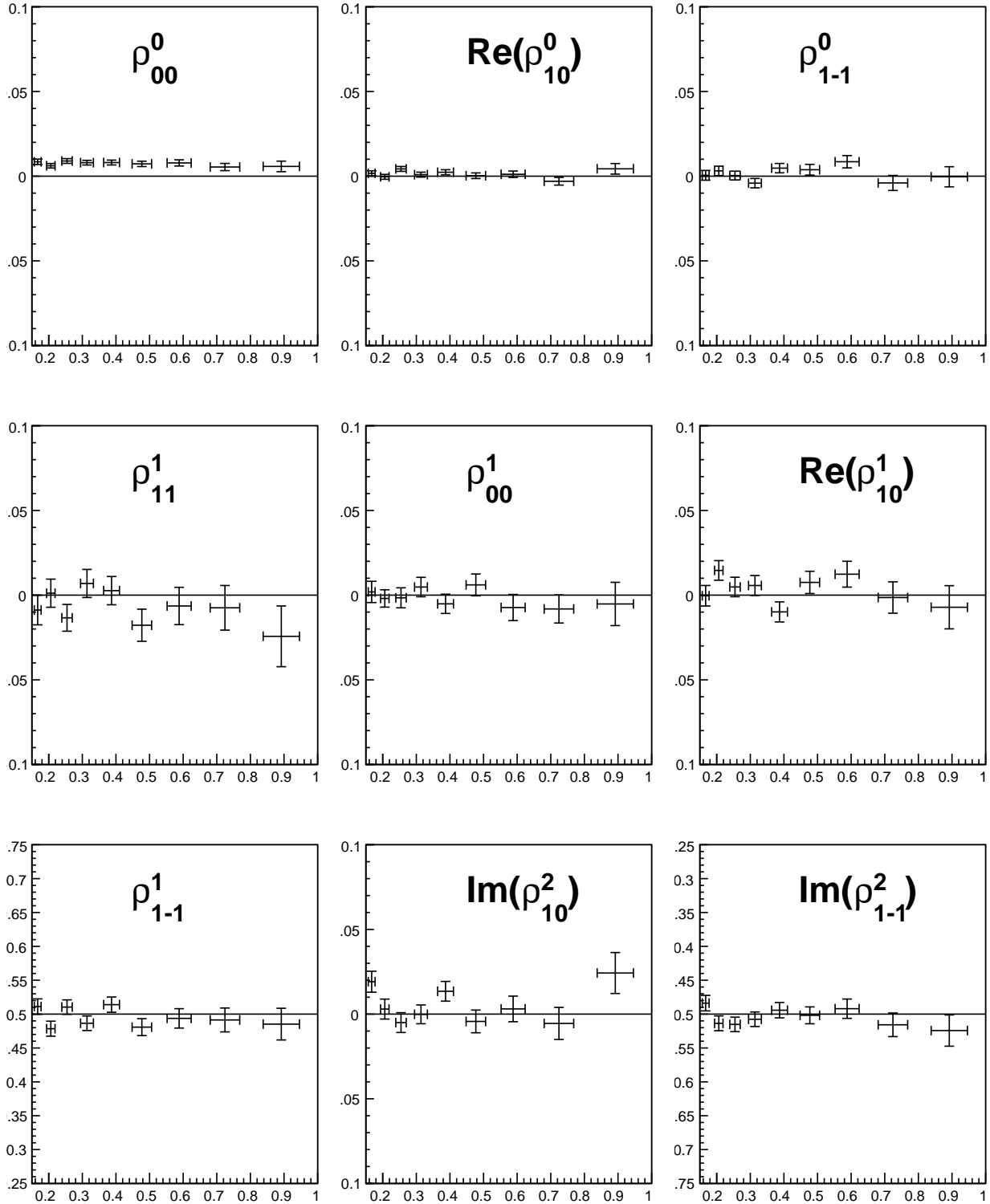


Figure 6.19: Spin-Density Matrix Elements as a function of $-t$ for an MC input-output test. Only uncertainties from MINUIT are shown. The ρ_{00}^0 term is systematically above the generated value. Fitting this term with a constant we find the offset to be 0.0075 ± 0.0005 .

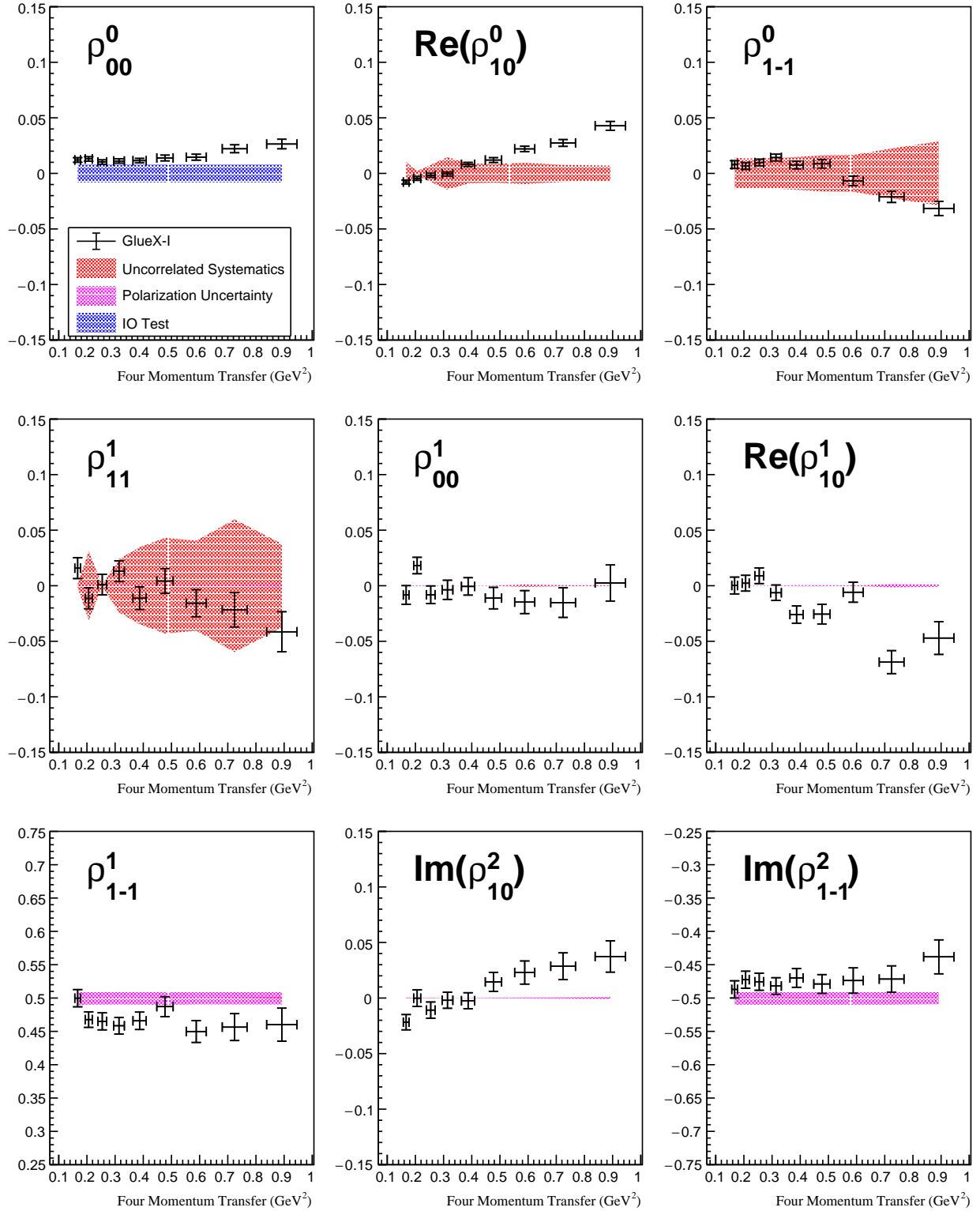


Figure 6.20: (Black) SDMEs with bootstrap uncertainties and (red) total systematic uncertainty.

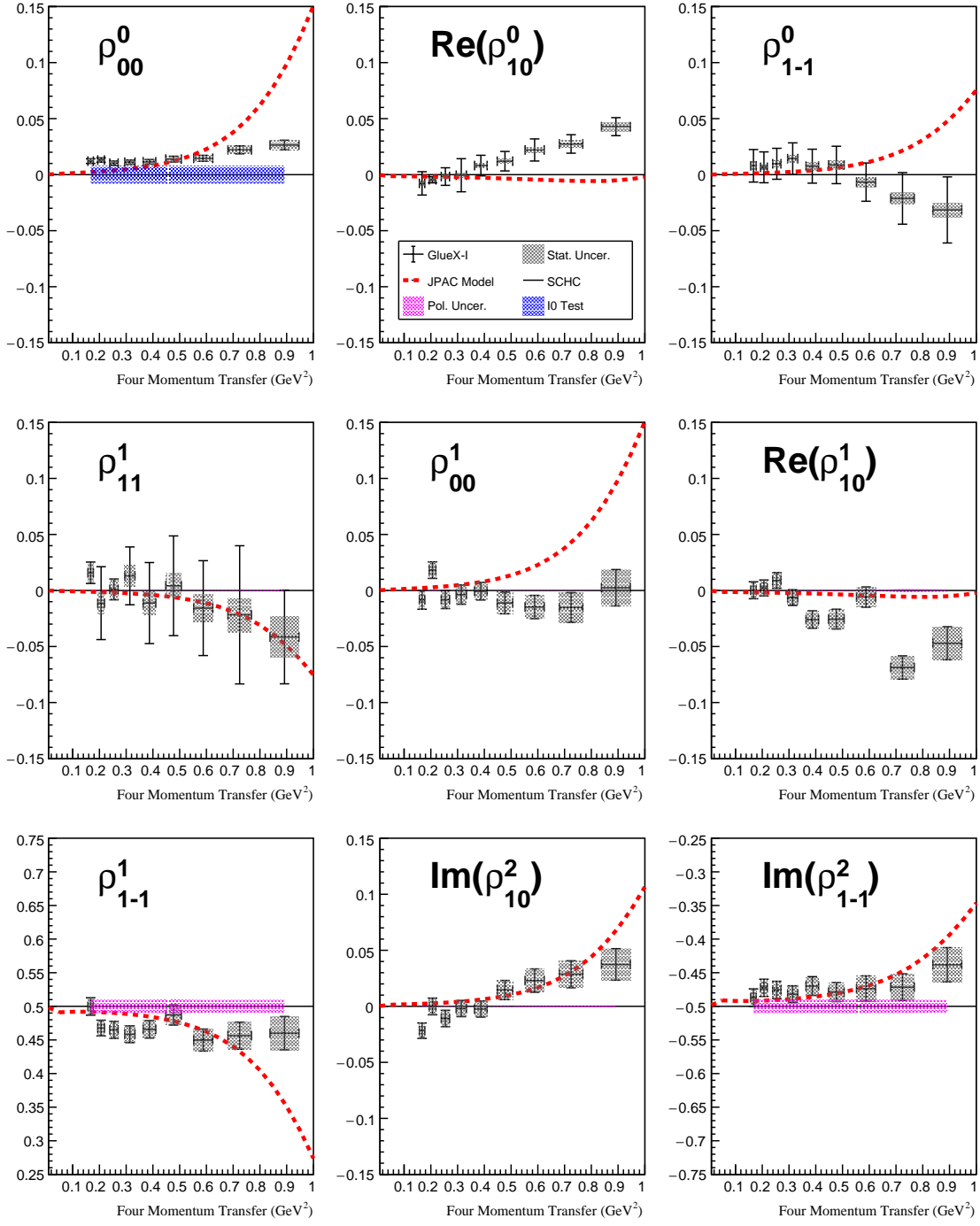


Figure 6.21: Spin-Density Matrix Elements for photoproduction of $\phi(1020) \rightarrow K_S K_L$ at $E_\gamma = 8.2 - 8.8$. The plotted uncertainties correspond to statistical and systematic uncertainties added in quadrature. The JPAC model is shown in dashed blue lines. The solid horizontal indicates s-channel helicity conservation.

Table 6.1: Sources of systematic uncertainty which have been investigated.

Systematic Study	Comments
Event Selections	
M($\pi^+\pi^-$)	No systematic effect, see Figures 6.5 and 6.6
Missing Mass	No systematic effect, see Figures C.1 and C.2
M($K_S K_L$)	No systematic effect, see Figures C.3 and C.4
χ^2/ndf	No systematic effect, see Figures C.5 and C.6
Flight Significance	No systematic effect, see Figures C.7 and C.8
Proton Z-vertex	No systematic effect, see Figures C.9 and C.10
Number of Unused Tracks	No systematic effect, see Figures C.11 and C.12
Number of Unused Showers	No systematic effect, see Figures C.13 and C.14
Independent Data Sets	
Above/Below $\phi(1020)$ Mass	Systematic to $\text{Re}(\rho_{10}^0)$ and ρ_{1-1}^0 , see Figure 6.7 and 6.8
Beam Energy	Systematic to ρ_{11}^1 , see Figure 6.9 and 6.10
Perpendicular Orientations	No systematic effect, see Figure 6.11 and 6.12
2017 and 2018 Run Periods	No systematic effect, see Figure 6.13 and 6.14
Other Tests	
Polarization Angle	Systematic to all SDMEs, see Figure 6.17 6.18
Polarization Fraction	2.1% to polarized SDMEs ($\rho^{1,2}$)
Input-output Test	Systematic uncertainty to ρ_{00}^0 of 0.008, see Figure 6.19

6.1.9 Interpretation of $\phi(1020)$ Spin-Density Matrix Elements

In Chapter 5.2 we discussed several special combinations of SDMEs that, under some assumptions, give information about the production of the vector meson. We will now use these special combinations to better understand $\phi(1020)$ photoproduction.

At high energy special combinations of SDMEs separate the contributions from natural (ρ^N) and unnatural (ρ^U) t-channel exchange. These combinations are given by

$$\rho_{11}^N = \frac{1}{2} (\rho_{11}^0 + \rho_{1-1}^1) \quad \rho_{11}^U = \frac{1}{2} (\rho_{11}^0 - \rho_{1-1}^1) \quad (6.9)$$

$$\rho_{00}^N = \frac{1}{2} (\rho_{00}^0 + \rho_{00}^1) \quad \rho_{11}^U = \frac{1}{2} (\rho_{00}^0 - \rho_{00}^1) \quad (6.10)$$

$$\rho_{1-1}^N = \frac{1}{2} (\rho_{1-1}^0 + \rho_{11}^1) \quad \rho_{1-1}^U = \frac{1}{2} (\rho_{1-1}^0 - \rho_{11}^1) \quad (6.11)$$

$$\rho_{10}^N = \frac{1}{2} (\rho_{10}^0 + \rho_{10}^1) \quad \rho_{10}^U = \frac{1}{2} (\rho_{10}^0 - \rho_{10}^1) \quad (6.12)$$

Figure 6.22 shows each $\rho^{N,U}$ term for data along with the JPAC model and expectations from SCHC. The natural components show more structure than their unnatural partners. The ρ_{11}^N term is flat and consistent with 0.5 throughout the whole $-t$ range. The ρ_{00}^N term is systematically above,

but consistent with, zero throughout the full $-t$ range. Finally, the ρ_{1-1}^N and ρ_{10}^N terms start off at zero at small $-t$ but deviate from SCHC at higher $-t$. However, ρ_{1-1}^N stays consistent with zero throughout the whole $-t$ range due to large uncertainties. This indicates a contribution from a natural parity exchange other than the Pomeron, perhaps a contribution from f_2' exchange which was neglected in the JPAC model.

To leading order, the asymmetry of natural to unnatural contributions is reducible to the parity asymmetry P_σ , which is given by

$$P_\sigma = \frac{\sigma^N - \sigma^U}{\sigma^N + \sigma^U} = 2\rho_{1-1}^1 - \rho_{00}^1 \quad (6.13)$$

Figure 6.23 illustrates our measured parity asymmetry along with the JPAC model and expectations from SCHC. The measured asymmetry is constant and consistent with pure natural exchange but systematically below expectations from SCHC. Given that Figure 6.22 indicates a negligible unnatural parity exchange contribution the systematic shift from $P_\sigma = 1$ seen in data is likely due to a systematic miss-modeling of the acceptance or a background that has not been considered. Looking at Eq. 6.13 and Figure 6.21 the source of the shift can be attributed to ρ_{1-1}^1 since ρ_{00}^1 is consistent with zero throughout the whole $-t$ range.

So far, we have discussed what the SDMEs tell us about the naturality of the exchange particle in $\phi(1020)$ photoproduction. In Chapter 5.2, we also discussed three relations that hold if one assumes that contributions from helicity double flip amplitudes are negligible and one relation assuming a single production mechanism. Based on those relations we define the following four terms

$$\begin{aligned} \delta_1 &= \rho_{1-1}^1 - (-Im(\rho_{1-1}^2)) \\ \delta_2 &= Re(\rho_{10}^1) - (-Im(\rho_{10}^2)) \\ \delta_3 &= Re(\rho_{10}^0) - (-Re(\rho_{10}^1)) \\ \delta_4 &= \rho_{1-1}^0 - \rho_{11}^1 \end{aligned} \quad (6.14)$$

Figure 6.24 shows each δ_i term for data and the JPAC model. All four relations are consistent with zero indicating that the contribution from helicity double-flip amplitudes is negligible and that a single production mechanism dominates. For Eq. 5.33 we find that $Re(\rho_{10}^0) = -Re(\rho_{10}^1)$ and for Eq. 5.32 we find that $\rho_{1-1}^0 = \rho_{11}^1$. It was shown in Ref [71] that the $\rho(770)$ and $\omega(782)$ SDMEs extracted with GlueX data also satisfy Eq. 6.14.

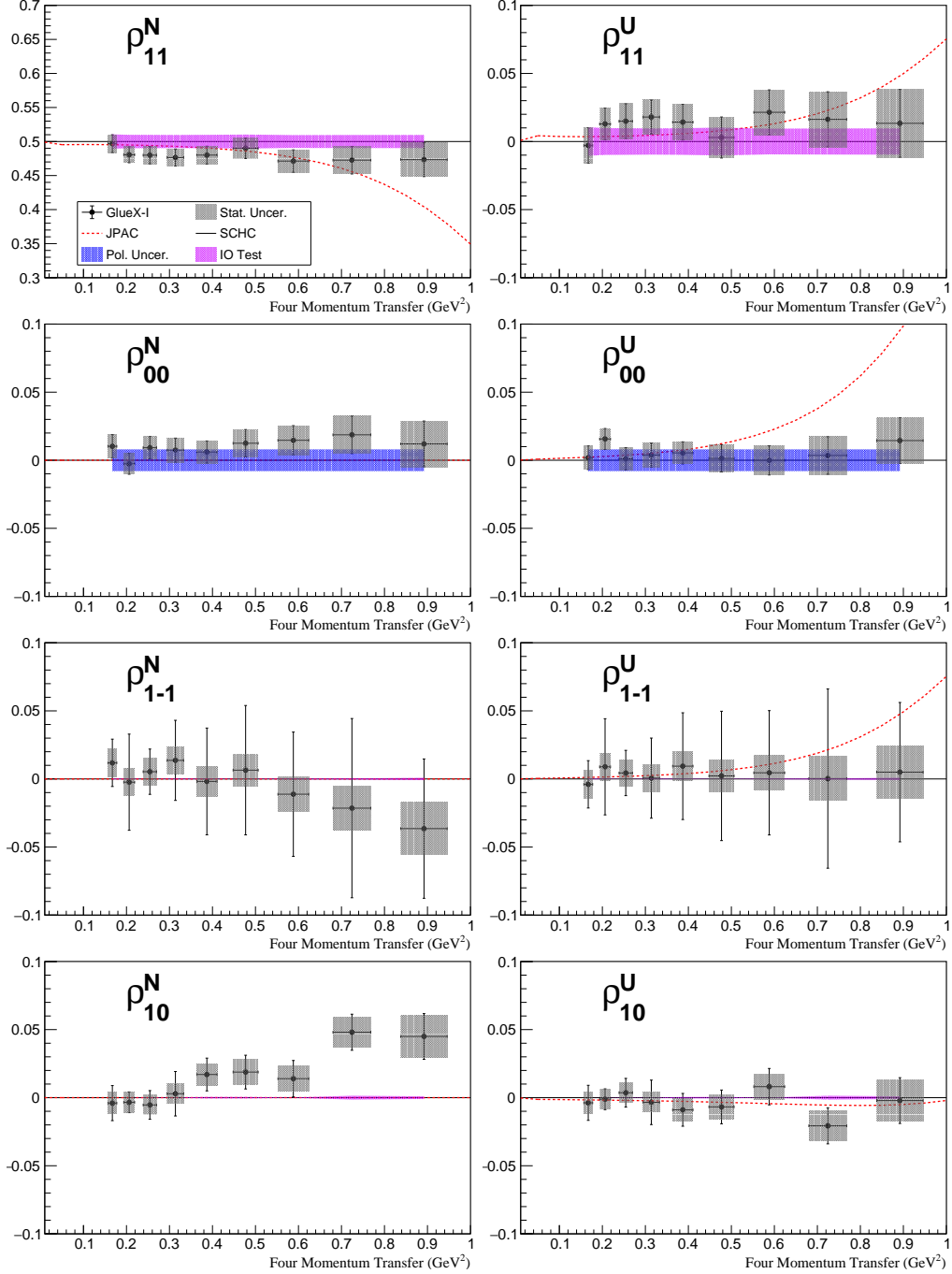


Figure 6.22: Combinations of $\phi(1020)$ SDMEs for (black points) GlueX measurement, (black line) SCHC and, (blue) JPAC model. All ρ^U combinations are consistent with zero indicating a negligible contribution from unnatural parity exchange. The ρ^N terms show some structure: ρ_{11}^N and ρ_{00}^N are consistent with SCHC while ρ_{1-1}^N and ρ_{10}^N deviate from SCHC indicating the contribution of a natural parity exchange other than the Pomeron. The JPAC model deviates from SCHC due to π and η exchange which the data suggests are negligible.

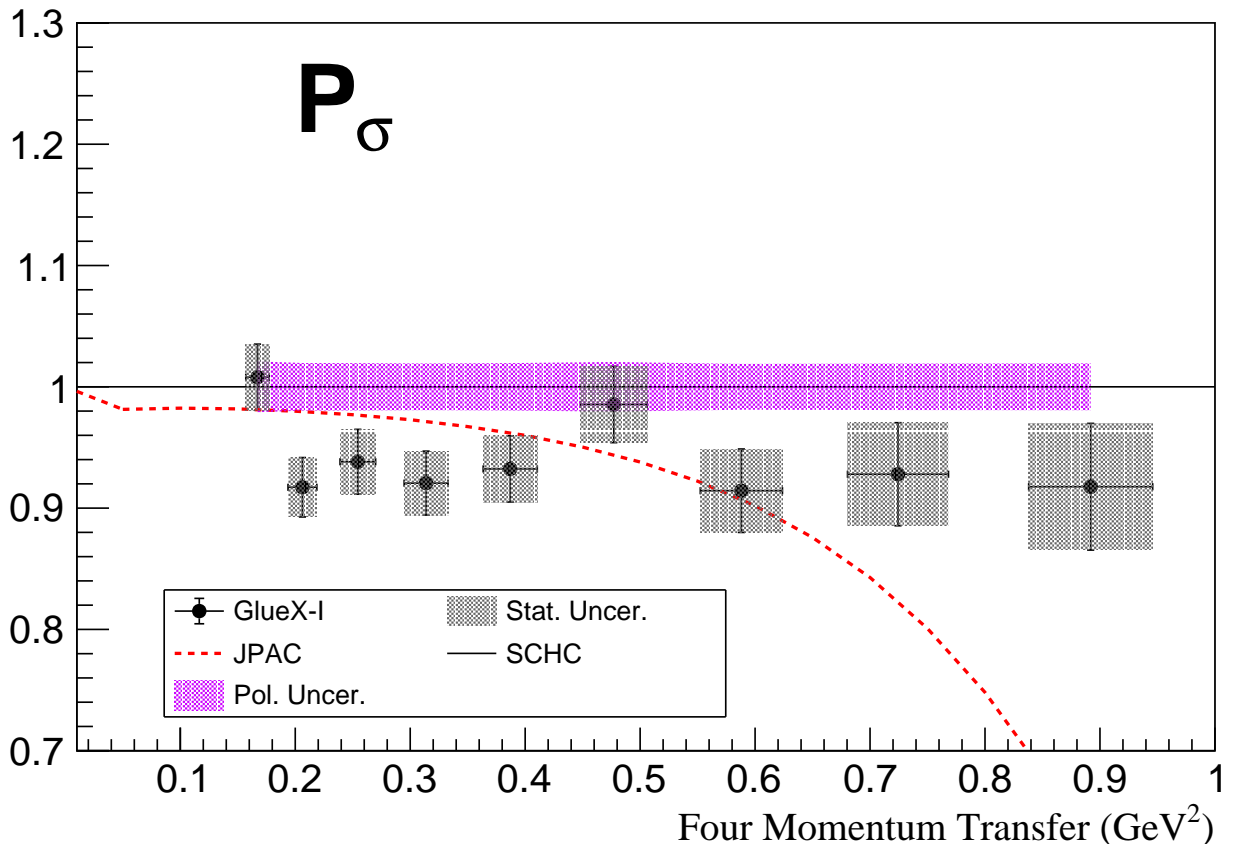


Figure 6.23: Parity asymmetry of $\phi(1020)$ photoproduction for (black points) GlueX measurement, (black line) SCHC and, (blue) JPAC model. The GlueX measurement shows a fairly flat behavior which is systematically below $P_\sigma = 1$.

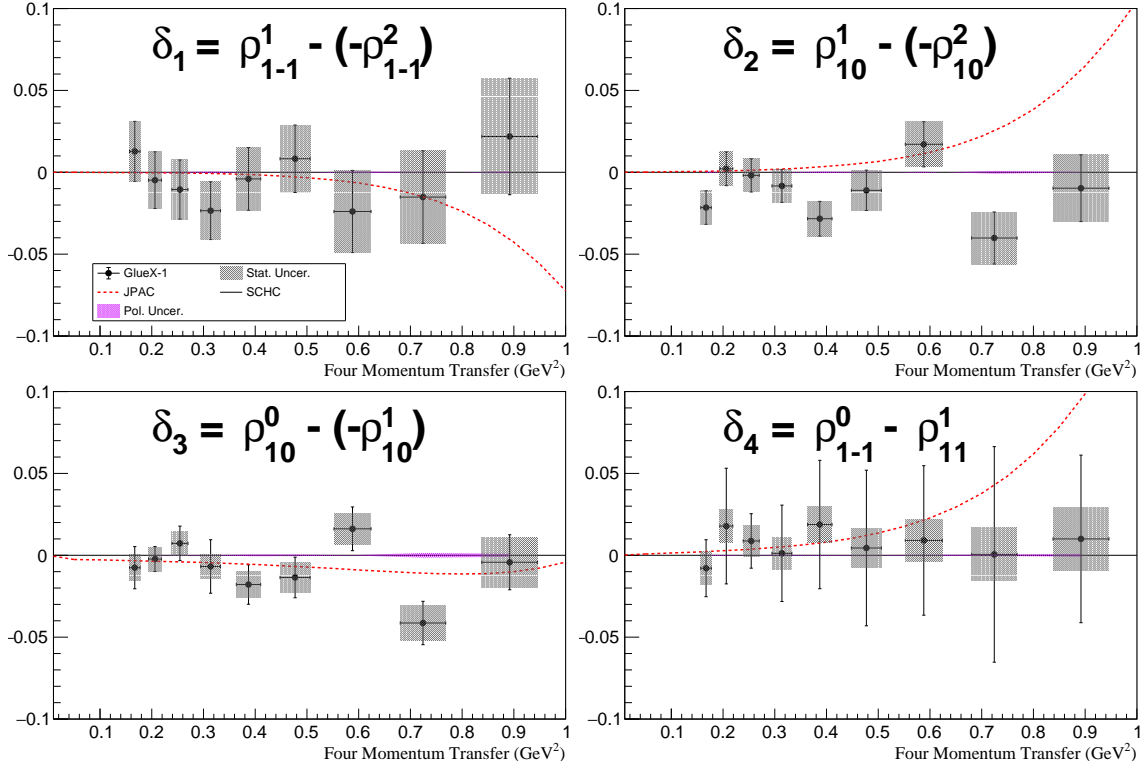


Figure 6.24: Combinations of $\phi(1020)$ SDMEs for (black points) GlueX measurement, (black line) SCHC, and (blue) JPAC model.

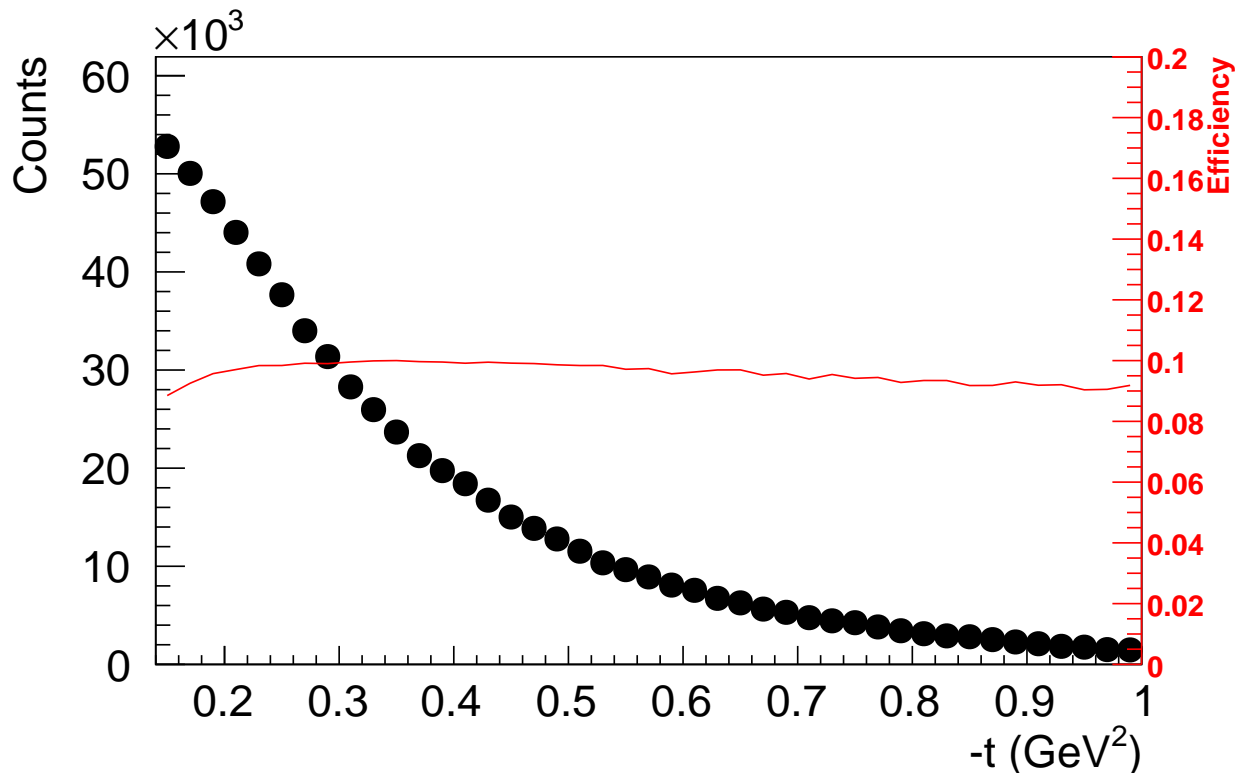


Figure 6.25: Mandelstam- t distribution and reconstruction efficiency.

6.2 Differential Cross Section at $E_\gamma = 8.2 - 8.8$ GeV

So far in this Chapter, we have studied the angular distributions of $\phi(1020) \rightarrow K_S K_L$ as a function of $-t$ but have neglected to discuss the normalization. We measure the differential cross section by calculating

$$\frac{d\sigma}{d(-t)} = \frac{N}{\epsilon \cdot \text{Flux} \cdot \text{Target} \cdot \Delta t \cdot \mathcal{B}(\phi(1020) \rightarrow K_S K_L) \cdot \mathcal{B}(K_S \rightarrow \pi^+ \pi^-)} \quad (6.15)$$

where N is the number of measured events, ϵ is the reconstruction efficiency, Flux is the total polarized tagged flux, Δt is the bin width, and \mathcal{B} is the branching ratio of the decay $\phi(1020) \rightarrow K_S K_L$ (34%) followed by $K_S \rightarrow \pi^+ \pi^-$ (69%) no branching ratio for the K_L decay is needed because we do not select any specific decay channel. Figure 6.25 shows the measured $-t$ distribution and the estimated reconstruction efficiency.

In Chapter 4 we saw that the distribution of number of unused showers, see Figure 4.6, is not well modeled by MC. However, the fact that we did not see a significant effect on the SDMEs

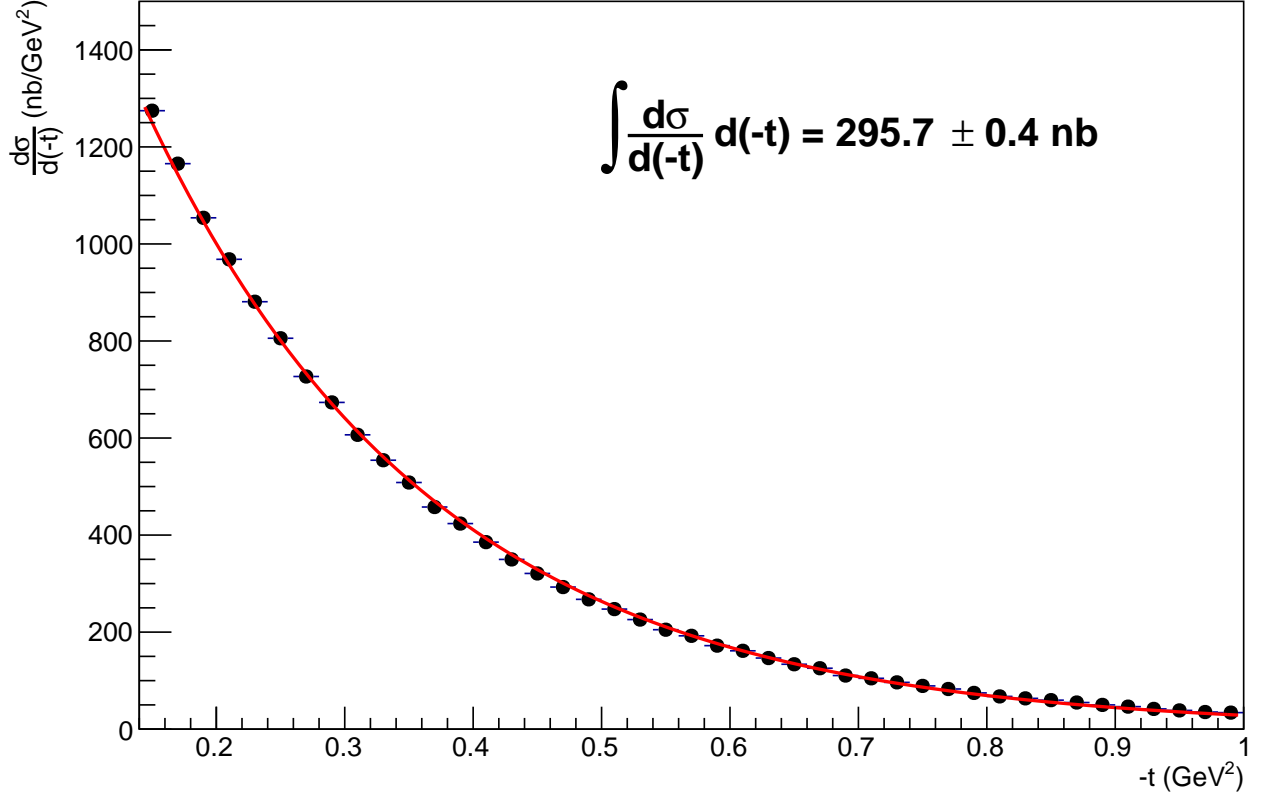


Figure 6.26: (Black) $\phi(1020)$ differential cross section and (red) fit to data with an exponential model. The integrated cross section in the $-t$ range 0.15–1.0 GeV² is estimated to be 295.7 ± 0.4 nb.

when varying the number of unused showers indicates that the miss-modelling affects primarily the normalization of the efficiency. Since we are now interested in the differential cross section the normalization is very important and we therefore exclude the number of unused showers selection from the data set. The measured differential cross section is shown in Figure 6.26 where the data is modeled as an exponential slope (Ae^{Bt}). The exponential slope determined from the fit is -4.44 ± 0.01 GeV⁻². The integrated cross section for $-t \in (0.15, 1.0)$ GeV² is 295.7 ± 0.4 nb. SLAC [1] measurement of the $\phi(1020)$ differential cross section at $E_\gamma = 9.3$ GeV. They obtained an integrated cross section of 212 ± 42 nb for $-t \in (0.2, 0.8)$ GeV². This is in good agreement with our measurement in the same range, which is 209.2 ± 0.3 nb. For the differential slope SLAC found 4.6 ± 0.6 GeV⁻¹, in good agreement with our measurement.

CHAPTER 7

HIGH MASS $K_S K_L$ PHOTOPRODUCTION

In this chapter, we investigate the $K_S K_L$ spectrum above $\phi(1020)$. As can be seen in Figure 7.1, there are two prominent peaks below 2 GeV. Above 2 GeV are no obvious structures, but we will show evidence for a resonance around 2.2 GeV. To extract information on the properties of potential particles, first we will model the dominant features of the $K_S K_L$ invariant mass distribution assuming that the spectrum is dominated by spin-1 resonances. Then, we will perform a Partial Wave Analysis (PWA) to determine the dominant spin contributions.

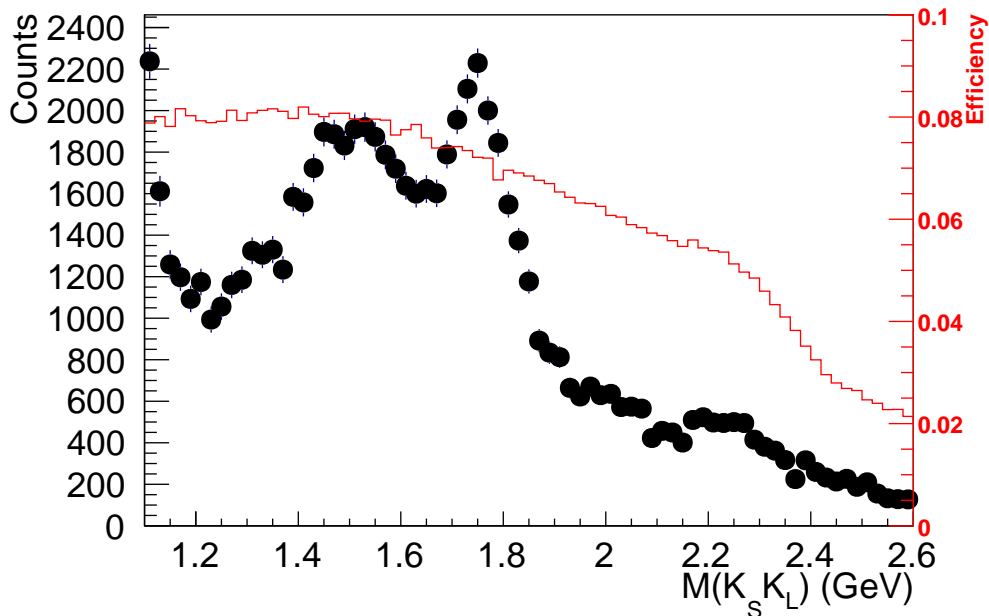


Figure 7.1: (Black) $K_S K_L$ invariant mass spectrum and (red) efficiency.

7.1 The One Dimensional $K_S K_L$ Invariant Mass Distribution

Figure 7.1 suggests that the $K_S K_L$ invariant mass spectrum is dominated by two overlapping resonances below 2 GeV while at higher mass there are no dominant features. However, the reconstruction efficiency dramatically falls going from $\sim 8\%$ at 1.1 GeV to $\sim 2\%$ at 2.6 GeV. Such

a large change in reconstruction efficiency is likely to affect the parameters of the models we use. Therefore, rather than modeling the measured $K_S K_L$ invariant mass distribution, we model the acceptance corrected distribution. First, we model the acceptance corrected $K_S K_L$ invariant mass spectrum as two resonances that sit on top of a smoothly varying background. Both resonances are parameterized as spin-1 Breit-Wigner functions and the background is described using a first order polynomial. Two models are considered, model 1 assumes there is no interference between the resonances or background. Explicitly, model 1 reads

$$F_1(m) = \sum_{i=1}^2 |N_i \cdot BW_{\ell=1}^i(m; M_i, \Gamma_i)|^2 + \sum_{i=0}^1 a_i \cdot m^i \quad (7.1)$$

where N_i , M_i and Γ_i are the yield, mass and width of the i^{th} resonance, and a_i are the coefficients of the polynomial. Model 2 allows for interference between the two resonances but not with the background. Model 2 explicitly reads

$$F_2(m) = \left| \sum_{i=1}^2 N_i \cdot e^{i\Delta\phi_{1i}} \cdot BW_{\ell=1}^i(m; M_i, \Gamma_i) \right|^2 + \sum_{i=0}^1 a_i \cdot m^i \quad (7.2)$$

where $\Delta\phi_{1i} = \phi_1 - \phi_i$ is the phase difference between the first resonance and the i^{th} resonance. The data around 1.1 – 1.15 GeV has a very steep slope, perhaps due to the tail of $\phi(1020)$, we avoid this region of the data and fit the data above 1.15 GeV. Figure 7.2 shows a fit to the $K_S K_L$ invariant mass using models 1 and 2 with all parameters allowed to vary freely in both fits. Both fits describe the data reasonably well below 2 GeV but there appears to be some structure around 2.2 GeV which is not well described by the fit. Therefore, we extend models 1 and 2 to have three Breit-Wigner functions. Explicitly, models 3 and 4 read:

$$F_3(m) = \sum_{i=1}^3 |N_i \cdot BW_{\ell=1}^i(m; M_i, \Gamma_i)|^2 + \sum_{i=0}^1 a_i \cdot m^i \quad (7.3)$$

and

$$F_4(m) = \left| \sum_{i=1}^3 N_i \cdot e^{i\Delta\phi_{1i}} \cdot BW_{\ell=1}^i(m; M_i, \Gamma_i) \right|^2 + \sum_{i=0}^1 a_i \cdot m^i. \quad (7.4)$$

A fit to data with models 3 and 4 is shown in Figure 7.3.

A list of vector mesons with the mass and width together with the resonance parameters obtained from fitting the data with each model is given in Table 7.1. Model 2 gives the worst description of the data between the two peaks. Except for model 2, the mass of the first Breit-Wigner

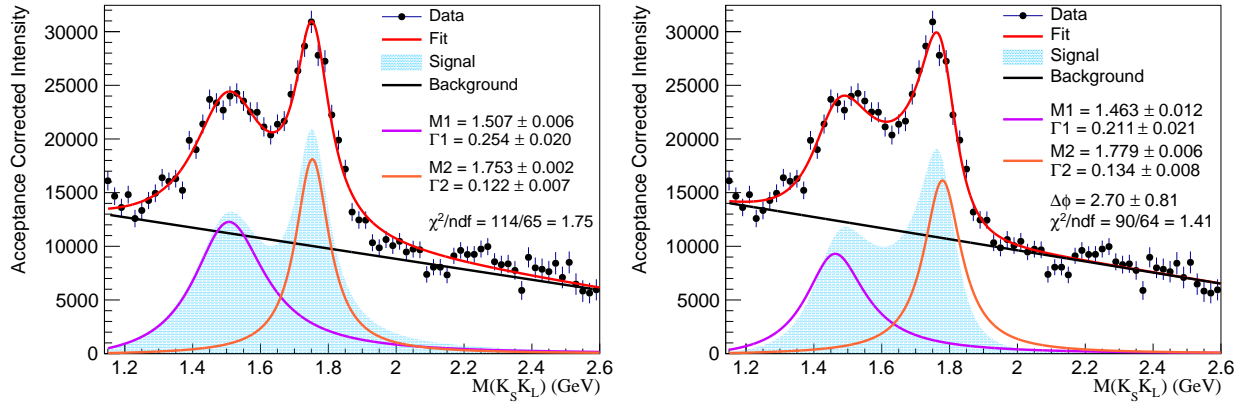


Figure 7.2: (Left) Fit to data using model 1, see Eq 7.1. (Right) Fit to data using model 2, see Eq 7.2.

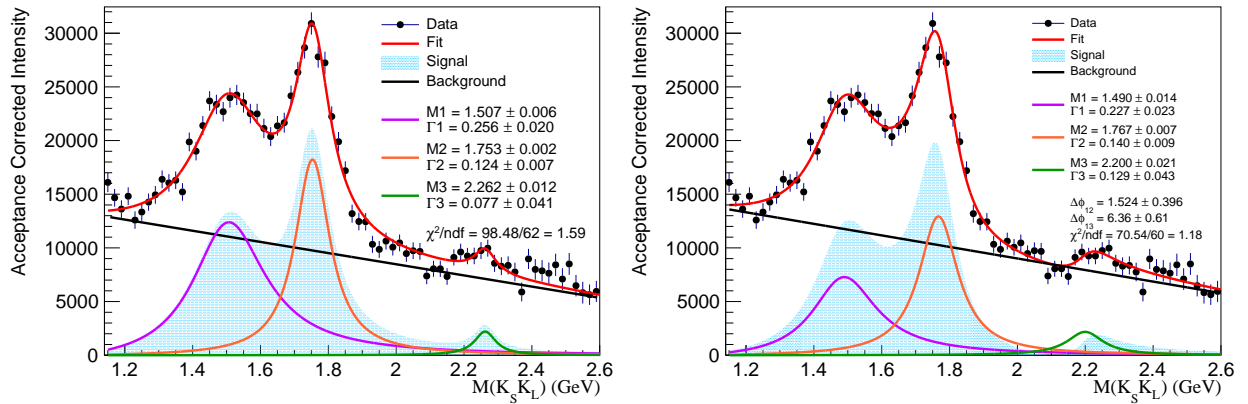


Figure 7.3: (Left) Fit to data using model 3, see Eq 7.3. (Right) Fit to data using model 4, see Eq 7.4.

Table 7.1: (Above) List of well-established vector mesons and the PDG average for their mass and width [3]. (Below) Mass and width parameters were obtained from a fit to data for each model discussed in the text.

Established Vector Mesons					
Resonance	Mass (GeV)	Width (GeV)	Resonance	Mass (GeV)	Width (GeV)
$\omega(1420)$	1.410 ± 0.060	0.290 ± 0.190	$\omega(1650)$	1.670 ± 0.030	0.315 ± 0.035
$\rho(1450)$	1.465 ± 0.025	0.400 ± 0.060	$\phi(1680)$	1.680 ± 0.020	0.150 ± 0.050
			$\rho(1700)$	1.720 ± 0.020	0.250 ± 0.100
			$X(1750)$	1.753 ± 0.003	0.120 ± 0.010

Parameters from Fit to Data					
Model	M_1 (GeV)	Γ_1 (GeV)	Model	M_2 (GeV)	Γ_2 (GeV)
1	1.507 ± 0.006	0.254 ± 0.020	1	1.753 ± 0.002	0.122 ± 0.007
2	1.463 ± 0.012	0.211 ± 0.021	2	1.779 ± 0.006	0.134 ± 0.008
3	1.507 ± 0.006	0.256 ± 0.020	3	1.753 ± 0.002	0.124 ± 0.007
4	1.490 ± 0.014	0.227 ± 0.023	4	1.767 ± 0.007	0.140 ± 0.009

is around 1.5 GeV which is larger than the $\omega(1420)$ or $\rho(1450)$ masses. The width ranges from 0.210 – 0.260 GeV which is consistent with the $\omega(1420)$ width but given the difference in mass and the large uncertainty on the $\omega(1420)$ width, the evidence is too weak to identify this as the $\omega(1420)$. The mass of $\rho(1450)$ is closer to our measured mass but the PDG average for the width is much larger than what we observe. To complicate things further, some papers report very different mass and width parameters for $\rho(1450)$. In principle, both $\omega(1420)$ and $\rho(1450)$ can decay to $K_S K_L$ in which case the observed peak is due to a mixture of both. Adding another Breit-Wigner to the fit, however, is not a fruitful pursuit since the resonance parameters of $\omega(1420)$ and $\rho(1450)$ are not well constrained and we do not know the detailed shape of the background.

For all models, the second Breit-Wigner mass parameter is consistently at or above 1.750 GeV and a width parameter in the range 0.120 – 0.140 GeV. These parameters are inconsistent with $\omega(1650)$. The $\rho(1700)$ mass is a bit low but the width is much larger (albeit with a large uncertainty) than what we observe. That leaves the $\phi(1680)$ and $X(1750)$ which we discussed in Chapter 2. Although, the width is consistent with both resonances the $\phi(1680)$ mass is at least 70 MeV lower than what we find in our models while the $X(1750)$ is a match. This is in line with previous photoproduction data which consistently finds the $X(1750)$ in $K^+ K^-$ decays, see Chapter 2.2.3.

The fit quality, measured by the χ^2/ndf , improves when adding a third Breit-Wigner to the fit. Comparing the no interference models (1 and 3) the χ^2/ndf improves from 1.75 to 1.59 and

Table 7.2: Mass and width for the third Breit-Wigner parameters obtained from fit to data using models 3 and 4 and parameters for $\phi(2170)$. One set of parameters is the PDG average [3] and the other set of parameters are those reported by the BESIII Collaboration in K^+K^- [4] and $K_S K_L$ [5] decays.

Parameters	Model			$\phi(2170)$	
	3	4	PDG	$e^+e^- \rightarrow K^+K^-$	$e^+e^- \rightarrow K_S K_L$
M (GeV)	2.262 ± 0.012	2.200 ± 0.021	2.163 ± 0.007	2.239 ± 0.013	2.274 ± 0.020
Γ (GeV)	0.077 ± 0.041	0.129 ± 0.043	0.103^{+28}_{-21}	0.139 ± 0.024	0.086 ± 0.067

comparing interference models (2 and 4) the χ^2/ndf improves from 1.41 to 1.18. The only well-established vector meson in this mass region is $\phi(2170)$. A list of the model parameters and $\phi(2170)$ measurements reported by the PDG [3] and BESIII Collaboration [4, 5] is given in Table 7.2. The mass and width parameters of the interference model as consistent with the PDG average. The no-interference model is not consistent with the PDG average but is consistent with the measurement by BESIII in K^+K^- [4]. An analysis of the $\phi(1020)\pi^+\pi^-$ spectrum with the GlueX-I data also finds a signal consistent with the $\phi(2170)$. Although the improvement in the fit quality is modest with the GlueX-I data set, including the Phase-II data set will assist in making a more conclusive determination.

7.2 Partial Wave Analysis

7.2.1 Angular Distributions

To better understand resonances above 1.1 GeV in the $K_S K_L$ invariant mass spectrum, we can study the angular distributions in the Helicity frame. Figure 7.5 shows the polar angle for $\ell = 1, 3$ in spectroscopic notation where $\ell_m = 1_m, 3_m = P_m, F_m$. Figure 7.4 shows the polar and azimuthal angles (see Eq. 5.8 and 5.9) of the K_S in the \mathcal{H} frame as a function of the $K_S K_L$ invariant mass. In Chapter 5 we discussed that the polar and azimuthal angles enter the intensity equation through a coherent sum of spherical harmonic $Y_\ell^m(\cos\theta, \phi) = P_\ell(\cos\theta)e^{-im\phi}$ functions. Therefore, an observed azimuthal angle is not flat only if there is interference between multiple resonances. The non-flat behavior of the azimuthal angle, seen in Figure 7.4, is a clear sign of interference between multiple resonances. The polar angle is not as simple to interpret, indicating that there are contributions from multiple partial waves.

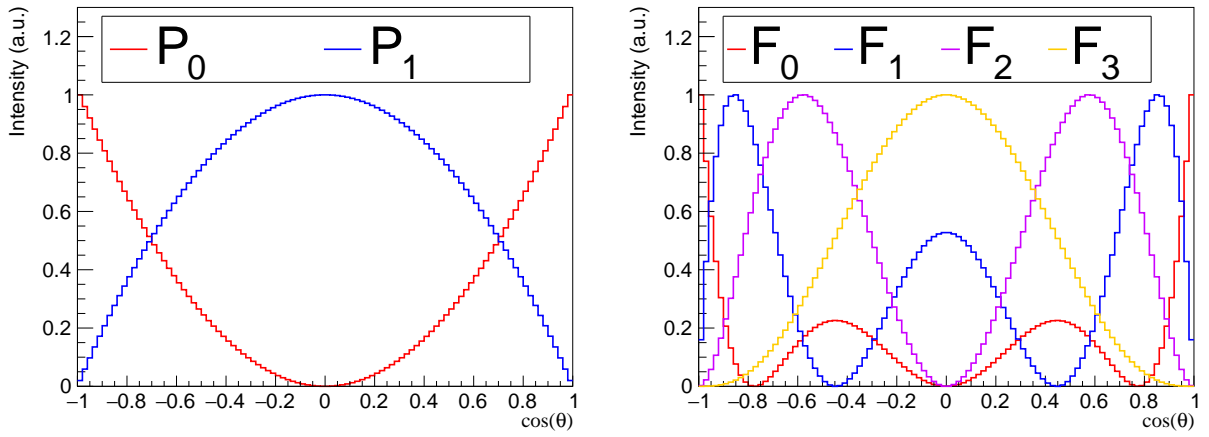


Figure 7.4: Polar angle distributions for (left) $\ell = 1$ amplitudes and (right) $\ell = 3$ amplitudes.

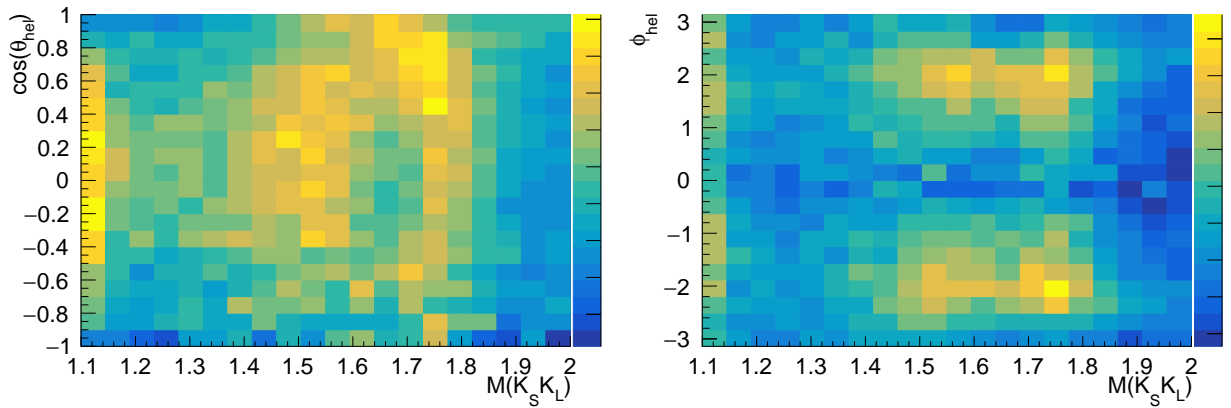


Figure 7.5: Acceptance corrected $K_S K_L$ invariant mass vs. (left) $\cos(\theta)$ and (right) ϕ in the Helicity frame.

7.2.2 Baryon Contributions

So far, we have only considered reactions of the form

$$\gamma p \rightarrow Mp \rightarrow K^0 \bar{K}^0 p$$

where a meson M decays to two kaons. However, we can also produce two kaons and a proton in the following way

$$\gamma p \rightarrow K^0 \Sigma^+ \rightarrow K^0 \bar{K}^0 p$$

where Σ^+ decays to \bar{K}^0 and a proton¹. Figure 7.6 shows the K_{Sp} , $K_L p$, $\pi^+ p$ and $\pi^- p$ invariant mass distributions. The πp distributions show no structure that could suggest a contribution from a Δ^{++} , N^* , or Λ baryons. This is expected since our data is 90% consistent with two kaons and we have applied a mass sideband subtraction to remove the remaining 10%. The $K_L p$ distribution has a narrow peak near 1.75 GeV, possibly due to the known $\Sigma^+(1775)$. The K_{Sp} distribution does not show such a clear feature but some structure is visible below ~ 2.2 GeV. Due to the small size of the $\Sigma^+ \rightarrow K_L p$ we do not remove it.

7.2.3 Methodology

To determine the partial waves from data, we perform an unbinned extended maximum likelihood fit using the AmpTools framework. For N independent observations of \mathbf{x}_i , the extended maximum likelihood can be expressed as a function of the parameters $\boldsymbol{\theta}$ as

$$\mathcal{L}(\boldsymbol{\theta}) = \frac{e^{-\mu} \mu^N}{N!} \prod_{i=1}^N \mathcal{P}(\mathbf{x}_i; \boldsymbol{\theta}) \quad (7.5)$$

where $\mathcal{P}(\mathbf{x}_i; \boldsymbol{\theta})$ is the n -dimensional probability density and μ is the model-predicted number of observed events. Following Ref. [78], $\mathcal{P}(\mathbf{x}_i; \boldsymbol{\theta})$ and μ can be expressed in terms of the intensity $\mathcal{I}(\mathbf{x}; \boldsymbol{\theta})$ and the efficiency $\eta(\mathbf{x})$ as

$$\mu = \int \mathcal{I}(\mathbf{x}; \boldsymbol{\theta}) \eta(\mathbf{x}) d\mathbf{x} \quad (7.6)$$

and

$$\mathcal{P}(\mathbf{x}_i; \boldsymbol{\theta}) = \frac{1}{\mu} \mathcal{I}(\mathbf{x}; \boldsymbol{\theta}) \eta(\mathbf{x}) d\mathbf{x}. \quad (7.7)$$

¹Note that in terms of quark content $K^0 = d\bar{s}$, $\bar{K}^0 = \bar{d}s$, $p = uud$ and $\Sigma = uds$

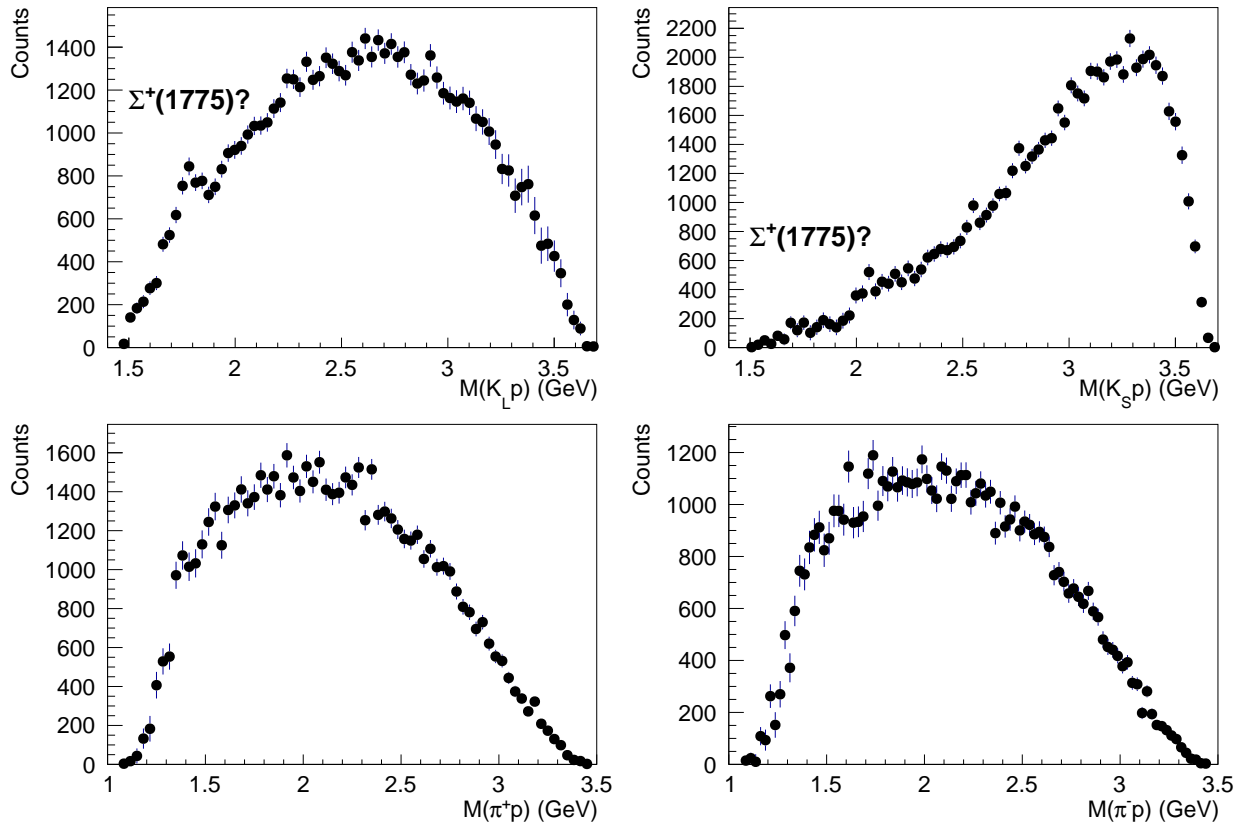


Figure 7.6: (Top left) $K_L p$ invariant mass distribution, the peak near 1.75 GeV is possibly due to the $\Sigma^+(1775)$. (Top right) $K_S p$ invariant mass distribution, there is some structure below ~ 2.2 GeV but no clear sign of a Σ^+ contribution. (Bottom left) $\pi^+ p$ and (bottom right) $\pi^- p$ invariant mass distributions, no sign of a baryon contribution is observed in the mass spectrum.

In practice, rather than maximizing the $\mathcal{L}(\boldsymbol{\theta})$ it is more useful to minimize $-2\ln\mathcal{L}(\boldsymbol{\theta})$. To do so, we rewrite Eq 7.5 as

$$-2\ln\mathcal{L}(\boldsymbol{\theta}) = -2 \left(\sum_{i=1}^N \ln\mathcal{I}(\mathbf{x}_i; \boldsymbol{\theta}) - \int \mathcal{I}(\mathbf{x}; \boldsymbol{\theta})\eta(\mathbf{x})d\mathbf{x} \right) + c_1. \quad (7.8)$$

As discussed in Chapter 5, the intensity for a Partial Wave Analysis is given by

$$I(\Omega, \Phi) = 2\kappa \sum_{k=\substack{\text{spin flip} \\ \text{non-flip}}} \left\{ (1 - P_\gamma) \left| \sum_{\ell, m} [\ell]_{m; k}^{(-)} \Re \mathfrak{e} [Z_\ell^m(\Omega, \Phi)] \right|^2 + (1 - P_\gamma) \left| \sum_{\ell, m} [\ell]_{m; k}^{(+)} \Im \mathfrak{m} [Z_\ell^m(\Omega, \Phi)] \right|^2 + (1 + P_\gamma) \left| \sum_{\ell, m} [\ell]_{m; k}^{(+)} \Re \mathfrak{e} [Z_\ell^m(\Omega, \Phi)] \right|^2 + (1 + P_\gamma) \left| \sum_{\ell, m} [\ell]_{m; k}^{(-)} \Im \mathfrak{m} [Z_\ell^m(\Omega, \Phi)] \right|^2 \right\}. \quad (7.9)$$

In the GlueX data set we have no information about the spin of the recoil proton, and therefore, cannot identify if the proton has undergone a spin flip or not. We assume that one of the two cases is dominant and neglect the sum over k . The sum over ℓ and m has to be truncated at some finite value in order to perform the fit.

Below 2 GeV in mass, there is evidence for three spin-3 states², only one spin-4 state³ and no spin-5 states [3]. Therefore, we assume that the partial wave expansion can be truncated at⁴ $\ell = 3$. We can reduce the wave set further for $K_S K_L$ since only mesons with $J^{PC} = \text{odd}^{--}$ are allowed to decay to this final state.

We perform a mass independent (MI) fit to the data by fitting the angular distributions in small bins of the $K_S K_L$ invariant mass and assume the dynamics can be neglected. This is done for subsequent independent bins (i.e. 1.1 – 1.2 GeV, 1.2 – 1.3 GeV, ...) to produce a partial wave scan as a function of $K_S K_L$ invariant mass. The strength of this methodology is that: (1) it introduces the least amount of model dependence into the fit, and (2) modeling the dynamics is pushed to a later stage of analysis. The weakness of the methodology is that: (1) a large number of free parameters are introduced often producing a substantial amount of statistical fluctuations, and (2) mathematical ambiguities may exist making it impossible to extract the “true” amplitudes without introducing additional model dependence.

²These are $\omega_3(1650)$, $\rho_3(1690)$ and $\phi_3(1850)$.

³The $a_4(1970)$ which has been observed mostly in πp reactions.

⁴This also truncates m since $m = -\ell, \dots, \ell$.

7.2.4 Assuming Only Spin-1 Contributions

For $\ell = 1$, there are three m -projections and for $\ell = 3$, there are seven m -projections, for each m -projection, there are two reflectivities and each amplitude is a complex number. Therefore, a fit with all allowed $\ell = 1$ and 3 partial waves include 20 amplitudes with 38 parameters⁵ making this a prohibitively complicated fit. The photoproduction cross sections of the lightest vector mesons are known to be large compared to other mesons, so we may expect the cross sections of excited vector mesons to be larger than those of the spin-3 states. This assumption should hold at least below 1.6 GeV since the lightest 3^{--} state is ~ 1.650 GeV in mass. Therefore, we first assume that the $K_S K_L$ spectrum is dominated by spin-1 resonances and fit the data with all $\ell = 1$ amplitudes. Explicitly, the intensity model is

$$I(\Omega, \Phi) = \left\{ (1 - P_\gamma) \left| \sum_{\substack{\ell=1 \\ m=-1,0,1}} [\ell]_{m;k}^{(-)} \Re \mathfrak{e} [Z_\ell^m(\Omega, \Phi)] \right|^2 + (1 - P_\gamma) \left| \sum_{\substack{\ell=1 \\ m=-1,0,1}} [\ell]_{m;k}^{(+)} \Im \mathfrak{m} [Z_\ell^m(\Omega, \Phi)] \right|^2 + (1 + P_\gamma) \left| \sum_{\substack{\ell=1 \\ m=-1,0,1}} [\ell]_{m;k}^{(+)} \Re \mathfrak{e} [Z_\ell^m(\Omega, \Phi)] \right|^2 + (1 + P_\gamma) \left| \sum_{\substack{\ell=1 \\ m=-1,0,1}} [\ell]_{m;k}^{(-)} \Im \mathfrak{m} [Z_\ell^m(\Omega, \Phi)] \right|^2 \right\}. \quad (7.10)$$

Figure 7.7 shows the total intensity of each amplitude from fitting the data. The P_1^+ wave has a sharp dip that reaches zero around 1.65 GeV followed by a rise and subsequent fall. This structure can only be produced by destructive interference which, given the location of the dip, is likely due to interference between the resonances producing the first bump and the resonance producing the second bump. The P_1^- wave has most of the intensity around 1.6 – 1.8 GeV, producing a bump-like structure in this range. The P_0^+ wave also appears to have a broad structure around 1.4 – 1.8 GeV, perhaps due to multiple resonances. Other waves have some intensity but do not show any clear structure. Figure 7.8 shows the total positive reflectivity and total negative reflectivity obtained from the fit. Below ~ 1.3 GeV, the spectrum is dominated by positive parity exchange. The two peak structure seen in the total intensity is also present in the positive reflectivity distribution but now with a more pronounced dip between the two peaks compared to the total intensity. This dip is more pronounced in the positive reflectivity waves because a large part of the intensity goes into the negative reflectivity waves, which peak just below 1.7 GeV. Above ~ 1.75 GeV, the positive

⁵We must set one of the amplitudes, for each reflectivity, to be real to measure the phase with respect to that amplitude.

and negative reflectivity contributions appear to alternate in strength. This behavior is unphysical and suggests that the fit cannot distinguish the two reflectivities.

The quality of the fit can be inspected by comparing the angular distributions of the model and data. Four representative bins are used for a discussion here but plots of each angular distribution for each bin can be seen in Appendix D. We compare the $\cos(\theta)$, ϕ , Φ and $\psi = \phi - \Phi$ angles for each bin. Figure 7.9 shows the angular distributions for the first bin and is well described by a dominant P_1 wave. Figure 7.10 shows the angular distributions for the tenth bin, the angular distributions can no longer be described by a P_1 wave but are still well described by P-wave amplitudes. Figure 7.11 shows the angular distributions for the twentieth bin, the angular distributions are well described, and we see strong interference in the ϕ angular distribution. Figure 7.12 shows the angular distributions for the twenty-fourth bin, we see that the P-wave amplitudes cannot describe some features of the angular distributions. This discrepancy could be explained by the presence of an F-wave contribution, miss-modeling of the angular distributions, or background contributions. In the next section, we investigate possible F-wave contributions.

In Chapter 4, we estimated that $\sim 12\%$ of events after event selections are due to a background topology with a second kaon that is not the K_L . This estimate is not reliable since the cross sections of most resonances are not known. Still one might expect a non-negligible contribution from these background topologies. Unlike signal events which are produced by physical processes that can have interference effects, backgrounds from miss-identified two kaon channels are produced by other physical processes and therefore do not interfere with the signal process. The fact that the angular distributions are fairly well described by only P-wave amplitudes suggests that background contributions are small. We tested this hypothesis by adding an incoherent constant term to the intensity function. The intensity of this new background term was found to be consistent with zero in all bins except one. This indicates that if there are backgrounds that have not been considered, then their angular distributions are not isotropic.

7.2.5 Exploring Spin-3 Contributions

In the previous section, we saw that while angular distributions below 1.6 GeV are well described by P-wave amplitudes, some features above this energy cannot be exclusively accounted for by P-wave amplitudes. To investigate the potential influence of F-wave amplitudes, we fit the data with all P-wave amplitudes plus a single F-wave. This is done for every F-wave amplitude, 14

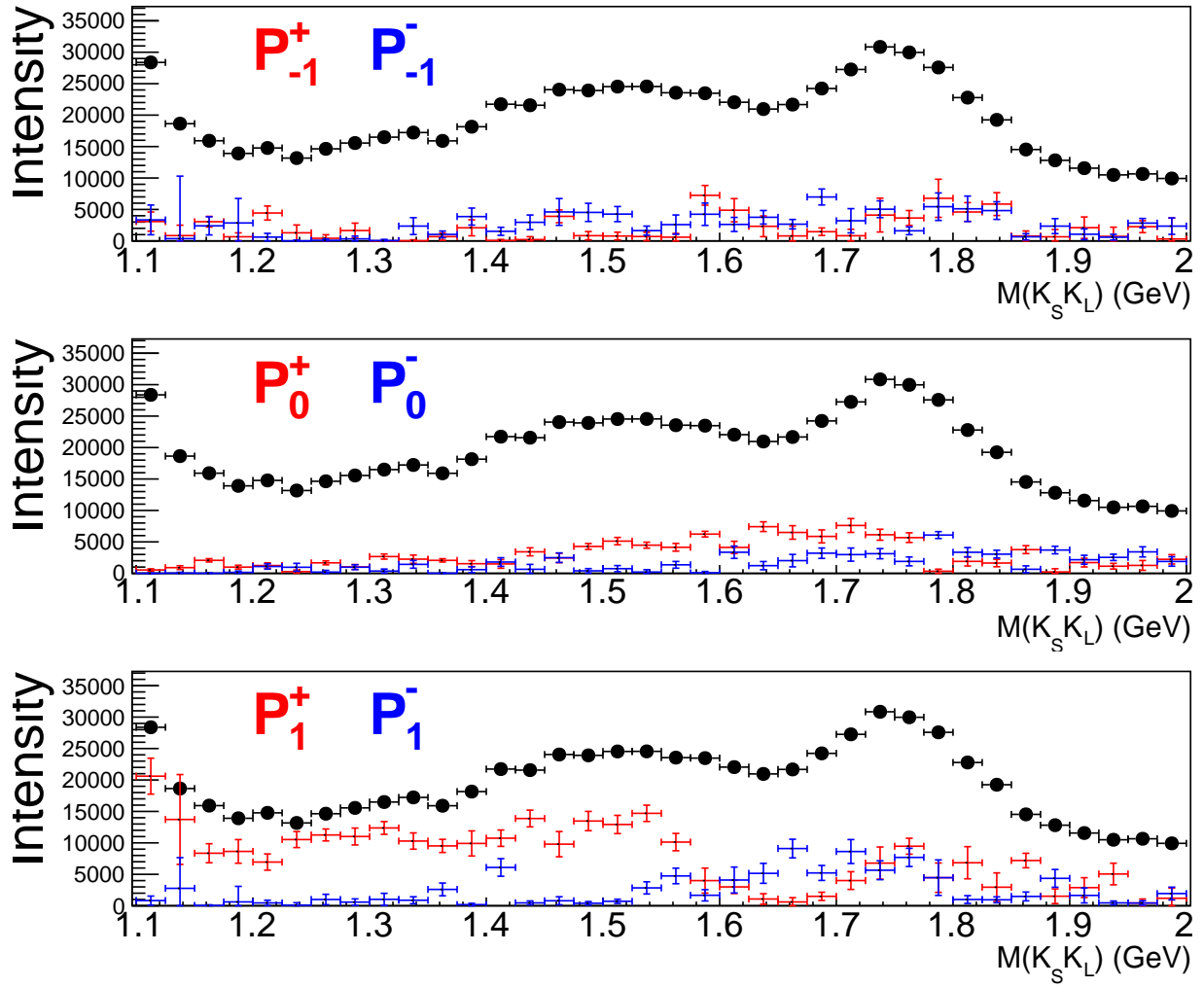


Figure 7.7: Results for Partial Wave Analysis assuming only contributions from spin-1 resonances. Each panel shows the (point) total intensity and (crosses) the intensity of the indicated partial wave.

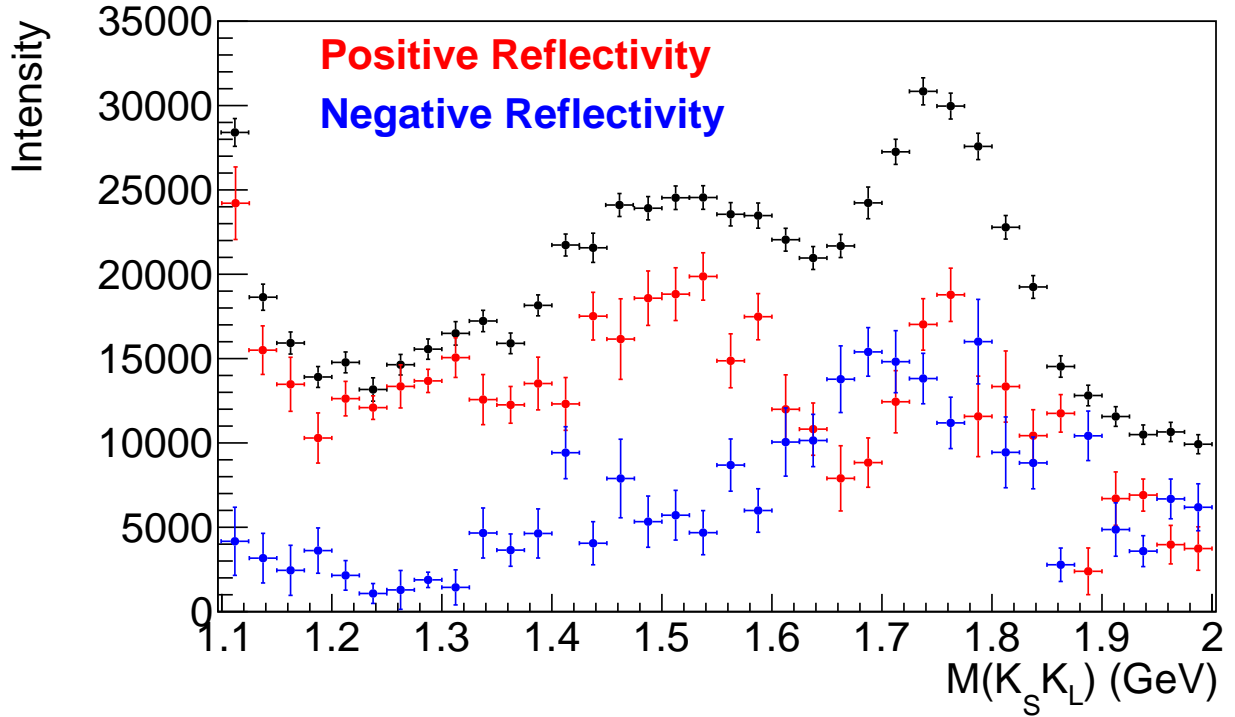


Figure 7.8: (Points) Total intensity, (red) positive reflectivity contribution, and (blue) negative reflectivity contribution for fit with all $\ell = 1$ amplitudes and no $\ell = 3$ amplitude.

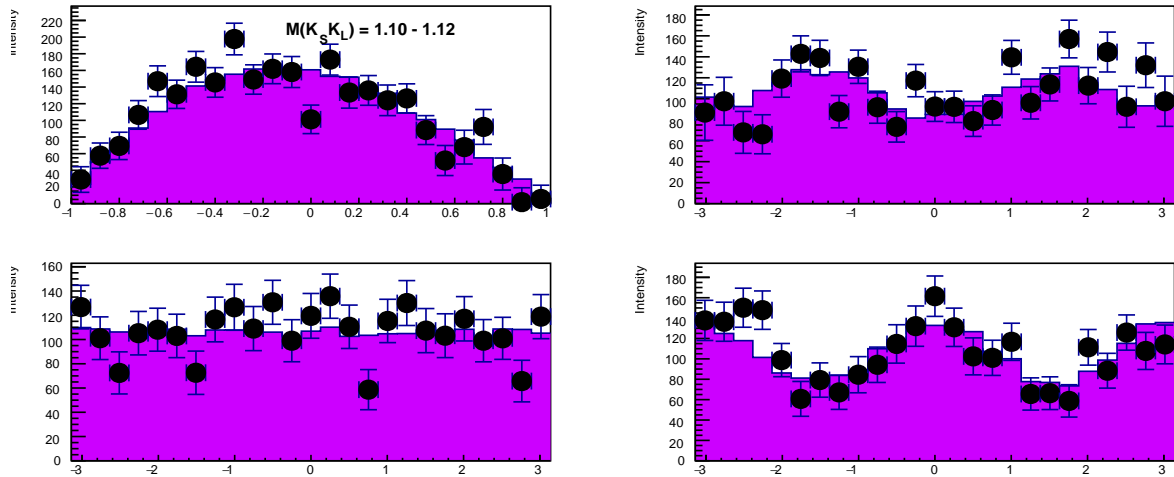


Figure 7.9: (Top left) Polar angle and (top right) azimuthal angle of K_S in the \mathcal{H} frame, (bottom left) polarization angle, and (bottom right) $\psi = \phi - \Phi$ angle. These angular distributions are for the first $K_S K_L$ invariant mass bin.

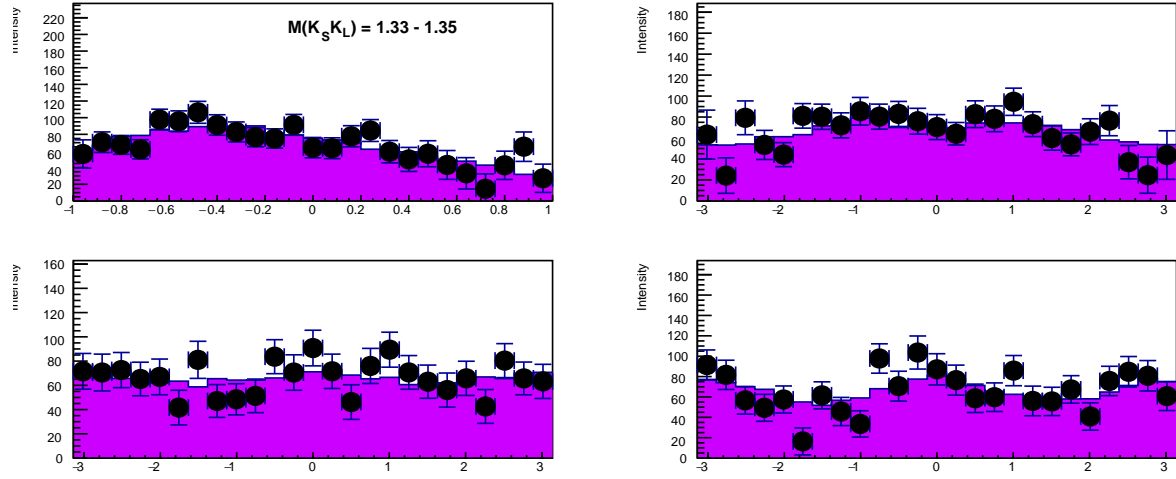


Figure 7.10: (Top left) Polar angle and (top right) azimuthal angle of K_S in the \mathcal{H} frame, (bottom left) polarization angle, and (bottom right) $\psi = \phi - \Phi$ angle. These angular distributions are for the ninth $K_S K_L$ invariant mass bin.

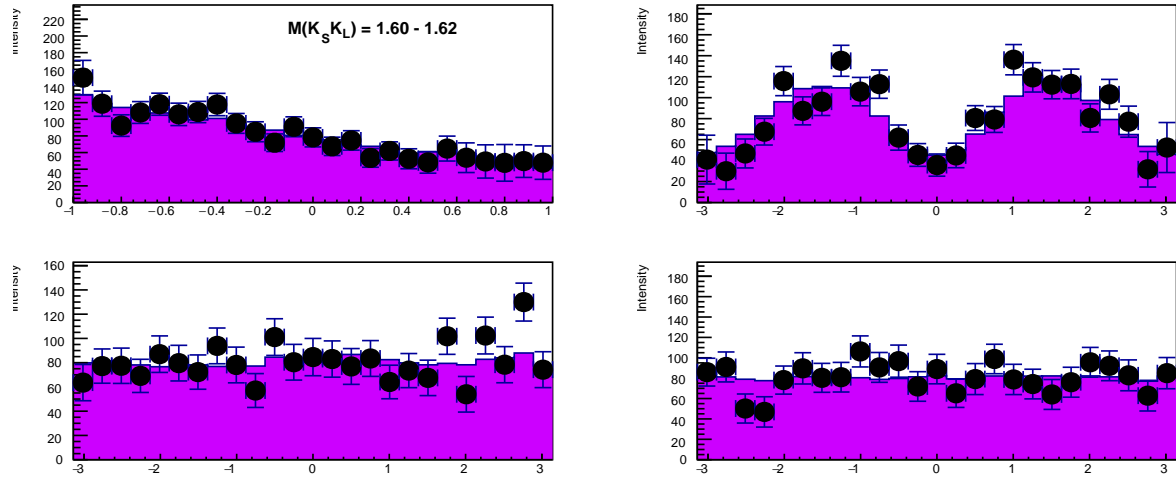


Figure 7.11: (Top left) Polar angle and (top right) azimuthal angle of K_S in the \mathcal{H} frame, (bottom left) polarization angle, and (bottom right) $\psi = \phi - \Phi$ angle. These angular distributions are for the twentieth $K_S K_L$ invariant mass bin.

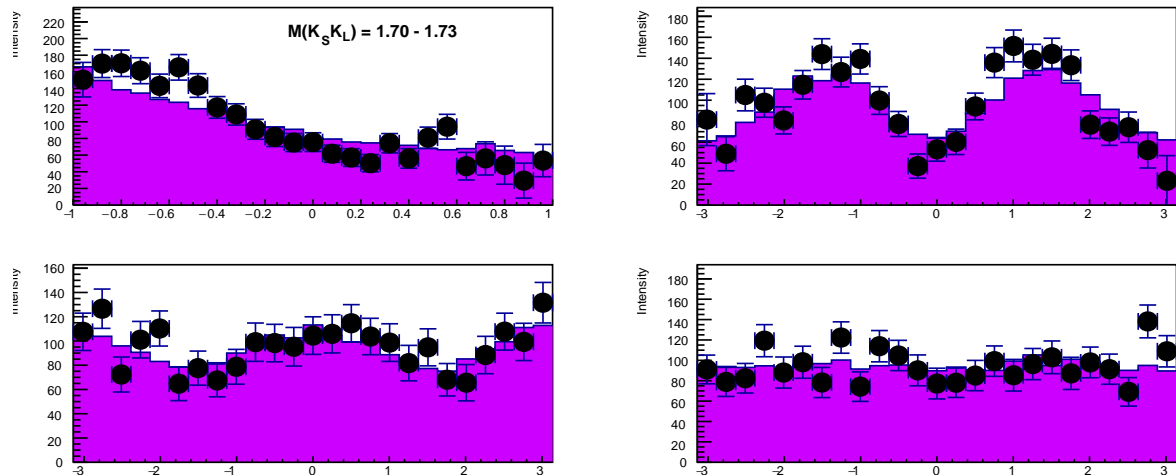


Figure 7.12: (Top left) Polar angle and (top right) azimuthal angle of K_S in the \mathcal{H} frame, (bottom left) polarization angle, and (bottom right) $\psi = \phi - \Phi$ angle. These angular distributions are for the twenty-fourth $K_S K_L$ invariant mass bin.

Table 7.3: Percent contribution from each F-wave m-projection from a fit with all P-waves plus the indicated F-wave m-projection. The largest contributing waves account for 10% of the total intensity.

F-wave m-projection	-3	-2	-1	0	1	2	3
Positive Reflectivity [%]	9	9	7	3	7	9	10
Negative Reflectivity [%]	10	10	6	3	6	10	9

different fits in total. No F-wave amplitude is found to contribute more than 10% of the total intensity, see Table 7.3. The intensities for each fit are shown in Appendix D. However, including an F-wave amplitude does change some qualitative features of the P-wave intensities. Inspecting the angular distributions of the F_0^\pm and F_3^\pm waves for the 1.70 – 1.72 GeV bin, see Figures 7.13 and 7.14, we see little improvement in the modelling the angles. This suggests that the changes in the partial wave intensities are driven by instability in the fit rather than an F-wave contribution. Introducing an F_1^\pm or F_2^\pm , see Figures 7.15 and 7.16 respectively, does improve the description of the angular distributions indicating that the data is consistent with a small spin-3 contribution. However, including different F_1 or F_2 waves affects the P-wave intensities differently, complicating the interpretation of the results. Still, the absence of a large F-wave contribution strengthens the hypothesis that the $K_S K_L$ spectrum is dominated by P-wave amplitudes.

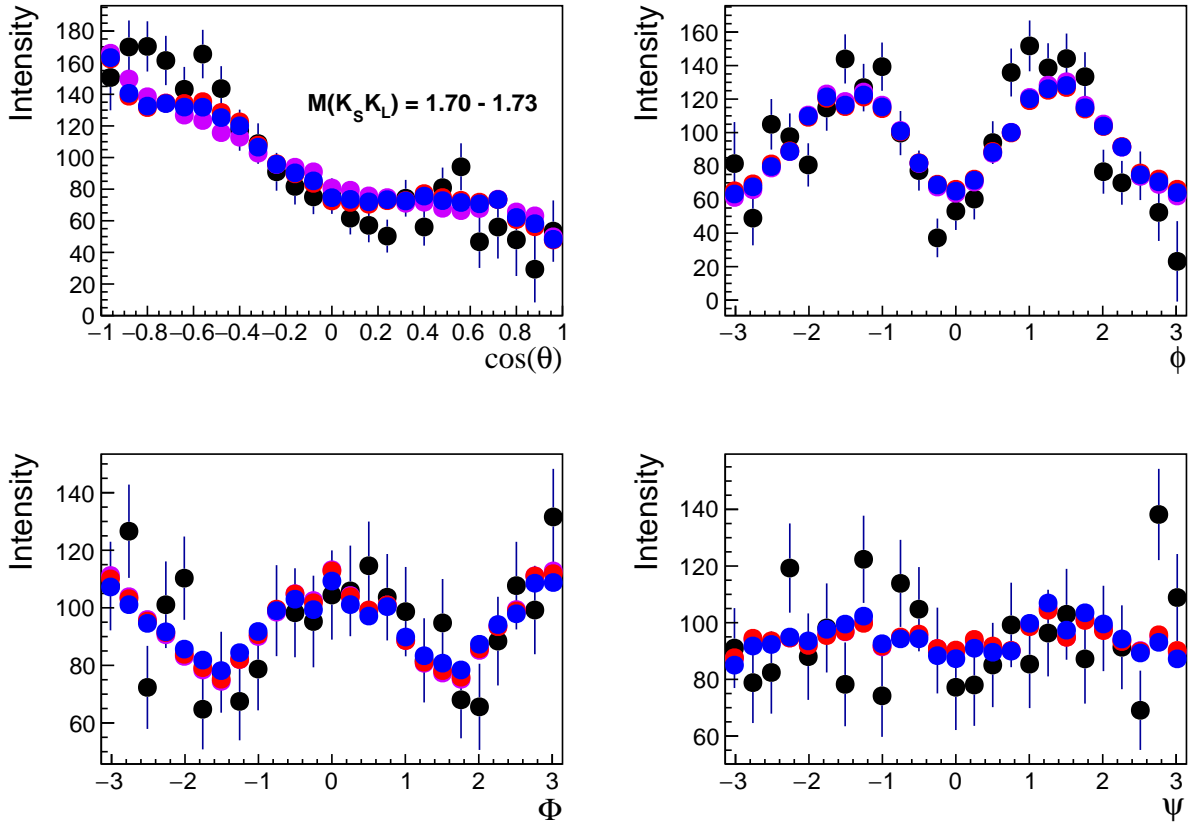


Figure 7.13: (Top left) Polar angle and (top right) azimuthal angle of K_S in the \mathcal{H} frame, (bottom left) polarization angle, and (bottom right) $\psi = \phi - \Phi$ angle. These angular distributions are for the twenty-fourth $K_S K_L$ invariant mass bin. Three fits to data are shown: (violet) all P-wave amplitudes, (red) all P-wave and F_0^+ , and (blue) all P-wave and F_0^- .

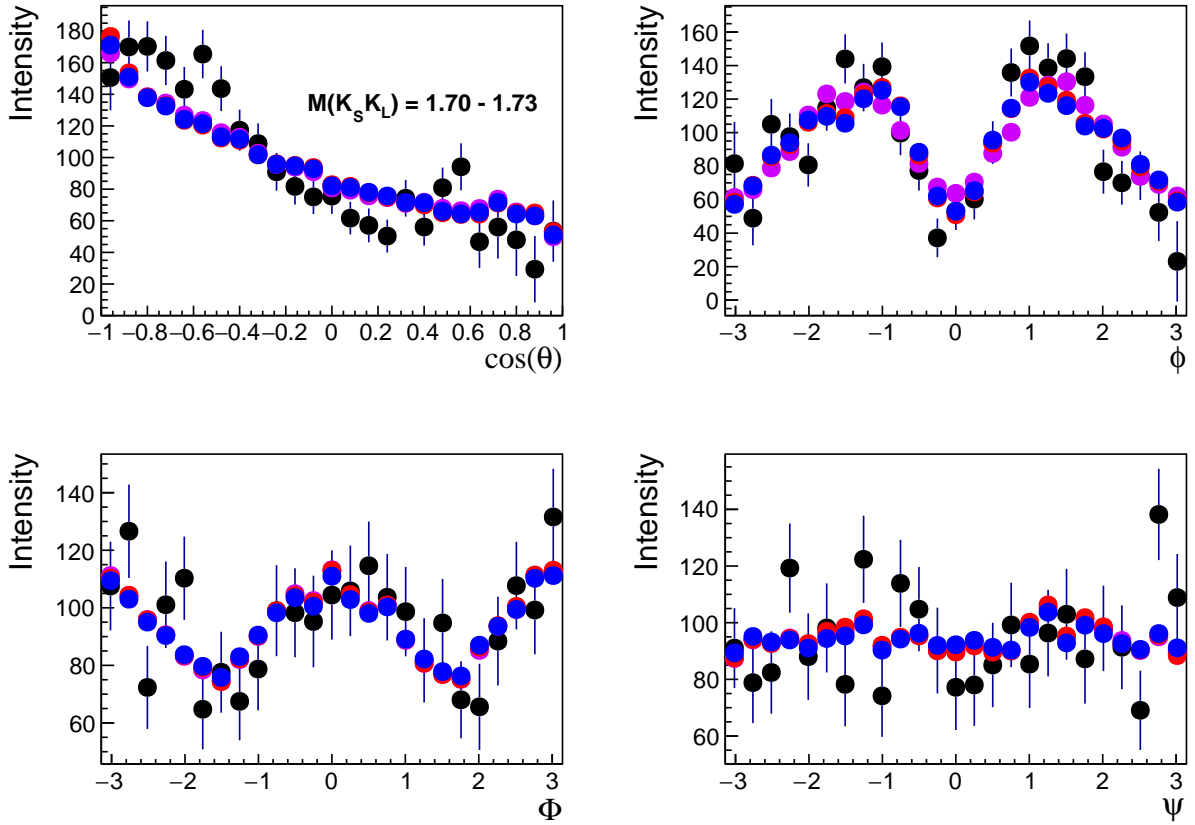


Figure 7.14: (Top left) Polar angle and (top right) azimuthal angle of K_S in the \mathcal{H} frame, (bottom left) polarization angle, and (bottom right) $\psi = \phi - \Phi$ angle. These angular distributions are for the twenty-fourth $K_S K_L$ invariant mass bin. Three fits to data are shown: (violet) all P-wave amplitudes, (red) all P-wave and F_3^+ , and (blue) all P-wave and F_3^- .

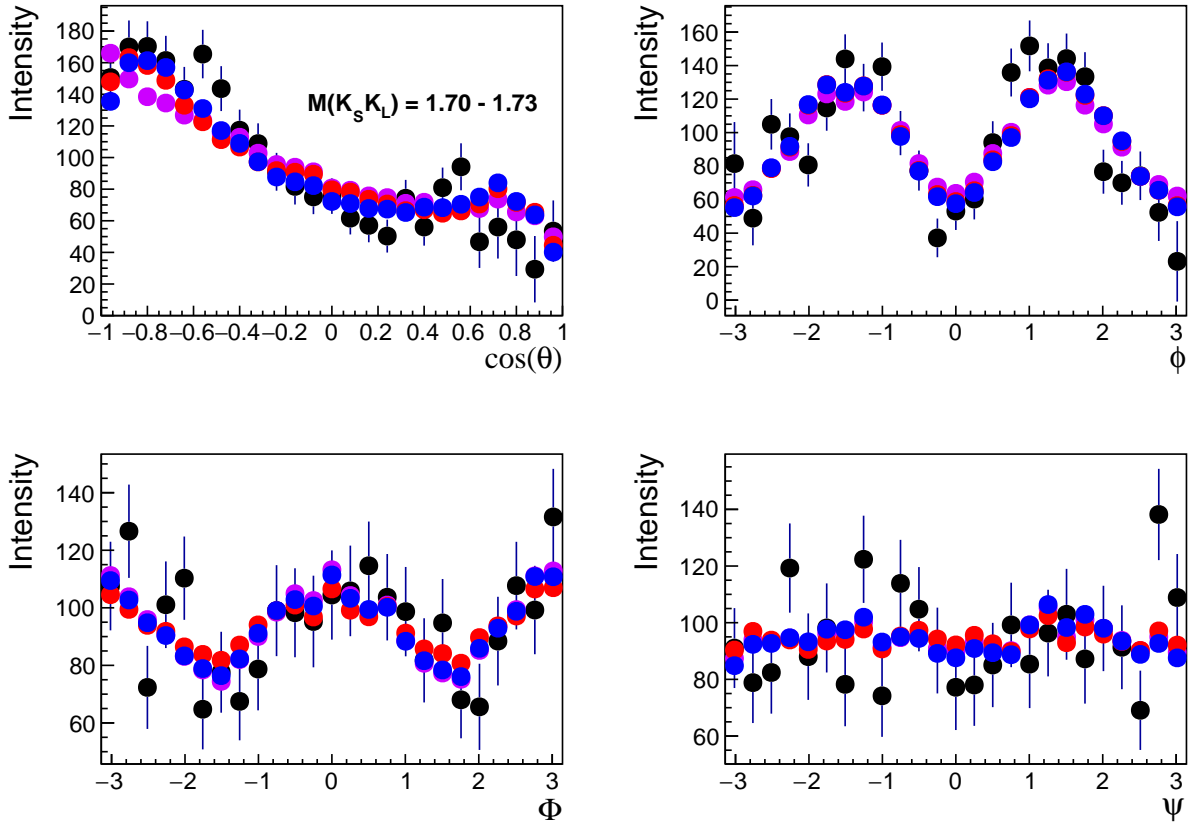


Figure 7.15: (Top left) Polar angle and (top right) azimuthal angle of K_S in the \mathcal{H} frame, (bottom left) polarization angle, and (bottom right) $\psi = \phi - \Phi$ angle. These angular distributions are for the twenty-fourth $K_S K_L$ invariant mass bin. Three fits to data are shown: (violet) all P-wave amplitudes, (red) all P-wave and F_1^+ , and (blue) all P-wave and F_1^- .

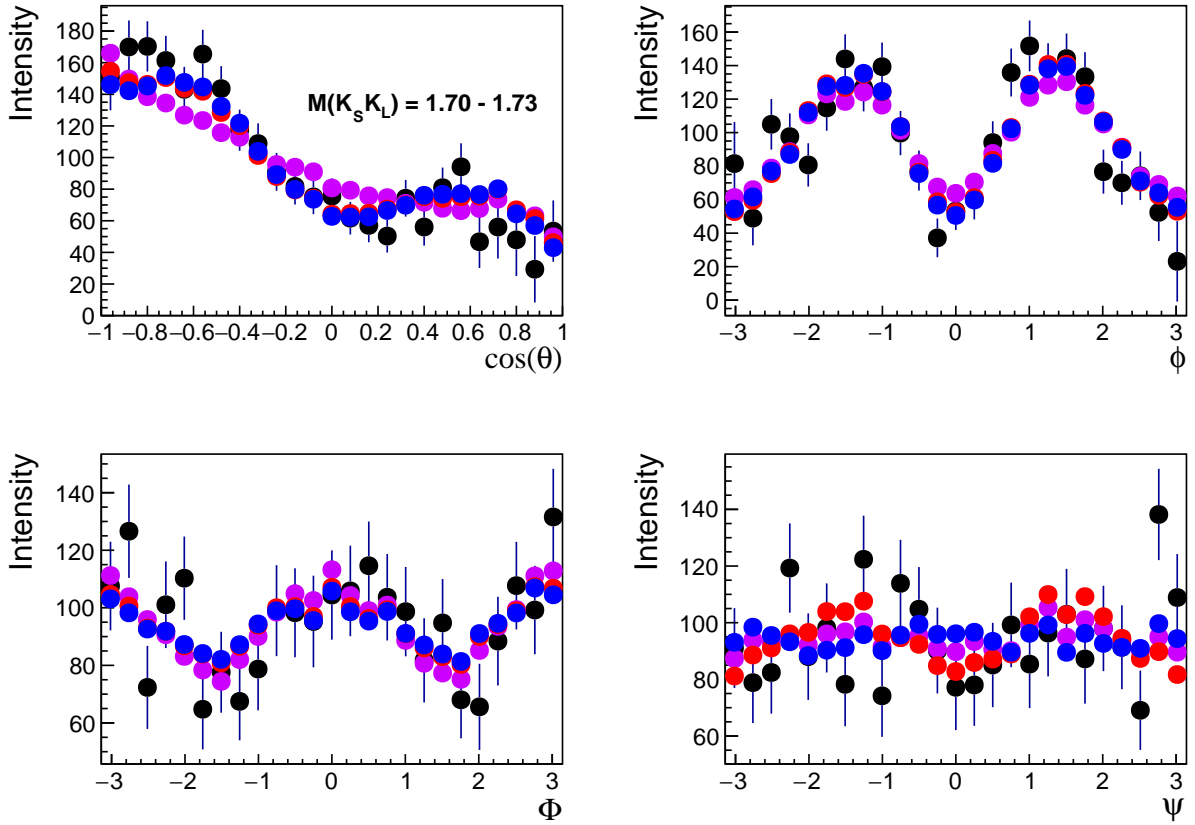


Figure 7.16: (Top left) Polar angle and (top right) azimuthal angle of K_S in the \mathcal{H} frame, (bottom left) polarization angle, and (bottom right) $\psi = \phi - \Phi$ angle. These angular distributions are for the twenty-fourth $K_S K_L$ invariant mass bin. Three fits to data are shown: (violet) all P-wave amplitudes, (red) all P-wave and F_2^+ , and (blue) all P-wave and F_2^- .

CHAPTER 8

$K_S K_S$ PHOTOPRODUCTION

In this chapter, we investigate the $K_S K_S$ spectrum. As can be seen in Figure 8.1, several structures are visible in the spectrum and each can be attributed to more than one known meson. To extract information on the properties of potential particles, first we will model the dominant features of the $K_S K_S$ invariant mass distribution. Then, we will perform a Partial Wave Analysis (PWA) to determine the dominant spin contributions.

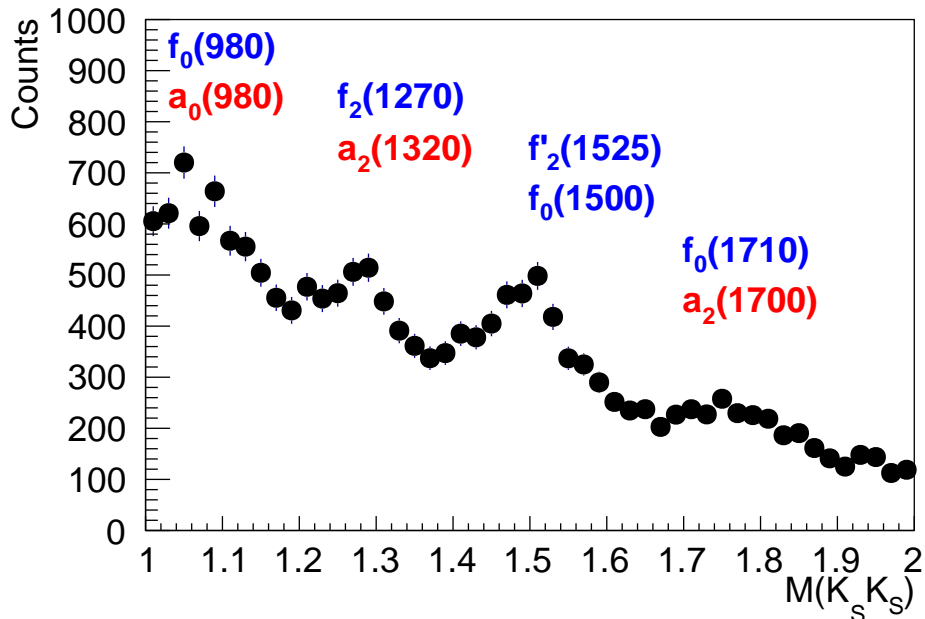


Figure 8.1: $K_S K_S$ invariant mass spectrum in the coherent beam $E_\gamma = 8.2 - 8.8$ GeV and at $-t = 0.1 - 0.4$ GeV. Several well established (blue) iso-vector and (red) iso-scalar mesons that may decay to $K_S K_S$ are shown.

8.1 The $K_S K_S$ Invariant Mass Distribution

Figure 8.1 suggests that modeling the $K_S K_S$ mass spectra is very complicated due to the large number of overlapping resonances. To increase the statistical precision of the data we select $K_S K_S$

events over the full beam energy range. A simple model that incorporates the main feature can provide useful information. For example, how significant is the enhancement seen near 1.7 GeV? To tackle this question, we build a simple model based on Breit-Wigner and Flatté distributions to describe the peak structures in the mass spectrum. The rest of the observed distribution is modeled by a smoothly varying background parametrized by:

$$BG(m; A, B, C) = (m - 0.99)^A \exp(B + Cm) \quad (8.1)$$

where A , B and C are free parameters. The exponential is chosen because of the fast monotonic decay, while the $(m - 0.99)^A$ enforces a rapid drop to zero near threshold. At threshold, we assume that the $a_0(980)$ meson dominates and parameterize it as

$$Flatté(m; m_{a_0}, g_{\eta\pi}, g_{K\bar{K}}) = \left| \frac{g_{K\bar{K}} \sqrt{\rho_{K\bar{K}}}}{m_{a_0}^2 - m^2 + i(\rho_{\eta\pi}(m)g_{\eta\pi}^2 + \rho_{K\bar{K}}(m)g_{K\bar{K}}^2)} \right|^2 \quad (8.2)$$

where m_{a_0} is the mass of the $a_0(980)$, $\rho_{\eta\pi}/\rho_{K\bar{K}}$ are the phase space factors and $g_{\eta\pi}/g_{K\bar{K}}$ are the couplings to the indicated channel. Both coupling $g_{\eta\pi}$ and $g_{K\bar{K}}$ are fixed to 353 MeV and 311 MeV respectively [74].

We build two models, one assuming the $a_0(980)$ and three resonances plus a background

$$F_1(m) = Flatté(a_0) + BW_1^{J=2} + BW_2^{J=0} + BW_3^{J=0} + BG \quad (8.3)$$

and another with the $a_0(980)$ and only two resonances plus a background

$$F_2(m) = Flatté(a_0) + BW_1^{J=2} + BW_2^{J=0} + BG \quad (8.4)$$

where BW are the Breit-Wigner distributions as defined in Eq. 5.48. In both models, we assume no interference between the resonances. Fits to data for both models are shown in Figure 8.2. We calculate the statistical significance of the third Breit-Wigner as $\sqrt{\chi^2(F_2) - \chi^2(F_1)}$. With $\chi^2(F_1) = 207.5$ and $\chi^2(F_2) = 326.8$ this gives evidence is greater than 10σ in favor of a resonances around 1.75 GeV. The mass and width parameters for the third Breit-Wigner, $a_2(1700)$ and $f_0(1710)$ are listed in Table 8.1. The mass of BW_3 is high compared to both resonances while the width is closer to $f_0(1710)$. The difference in the parameters could be due to neglecting interference effects or miss-modeling of the background among other possibilities. Although it is not clear which resonance, there is strong evidence for the presence of at least one state at ~ 1.75 GeV. Our next step is to study the angular distributions to better understand the resonances below 2.0 GeV.

Table 8.1: Parameters of the $a_2(1700)$ and $f_0(1710)$ taken from the PDG [6]. $BW_3^{J=0}$ is a part of the F_1 model.

	Mass (GeV)	Width (GeV)
$f_0(1710)$	1.704 ± 0.012	0.123 ± 0.018
$a_2(1700)$	1.698 ± 0.040	0.265 ± 0.060
$BW_3^{J=0}$	1.770 ± 0.006	0.094 ± 0.012

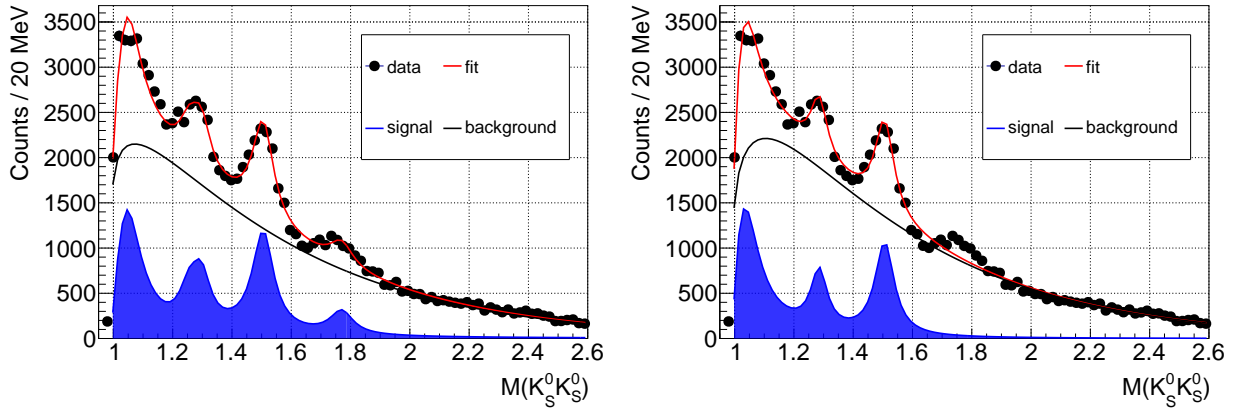


Figure 8.2: (Left) Fit to data with model F_1 . The mass and width of the third Breit-Wigner are 1.770 ± 0.006 GeV and 0.094 ± 0.012 GeV respectively. (Right) Fit to data with model F_2 .

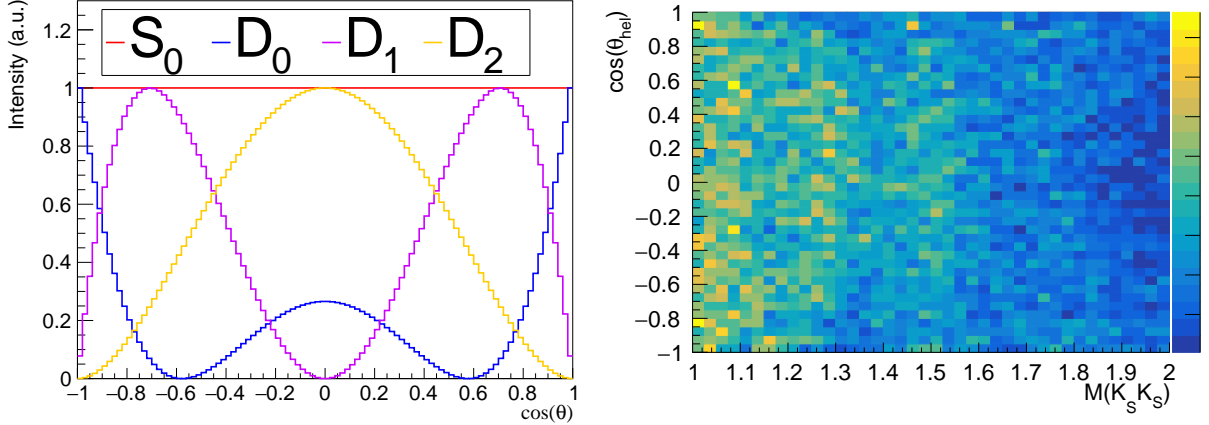


Figure 8.3: (Left) Polar angle distribution for $\ell_m = 0_m = S_m$ and $\ell_m = 2_m = D_m$. (Right) Acceptance corrected distribution of $M(K_S K_S)$ vs. $\cos(\theta)$ in the Helicity system.

8.2 Partial Wave Analysis

8.2.1 Angular Distributions and Baryon Contributions

Analogously to the $K_S K_L$ system we study the angular distributions of the $K_S K_S$ system in the Helicity frame. As discussed in Chapter 1.8, only mesons with $J^{PC} = \text{even}^{++}$ decay to $K_S K_S$. Figure 8.3 shows the polar angle distributions in the Helicity frame for $\ell = 0, 2$ waves and the acceptance corrected $M(K_S K_S)$ vs. $\cos(\theta)$ distribution. A rigorous analysis of the angular distributions will be performed, but at this stage, it is instructive to discuss the angular distributions to understand the broad features of the data. Below 1.1 GeV the angular distributions appear to be flat, consistent with a contribution from $f_0(980)$ and $a_0(980)$ (e. g. S_0) mesons. Around 1.3 GeV a band is visible with less intensity at extreme angles, $\cos(\theta_{\text{hel}}) \approx 1/-1$, consistent with a contribution from $f_2(1270)$ and $a_2(1320)$ decaying in a D_2 wave. At 1.5 GeV a band is also visible, but within the statistical precision of the data, it is difficult to discern any structure. Above 1.6 GeV the statistical precision of the data is small and we do not interpret this part of the data at this stage.

As in the $K_S K_L p$ channel, we observe an enhancement in the $K_S p$ invariant mass distribution, see Figure 8.4, at ~ 1.7 GeV. This enhancement is consistent with the production of a Σ^+ in the reaction

$$\gamma p \rightarrow K_S \Sigma^+ \rightarrow K_S K_S p.$$

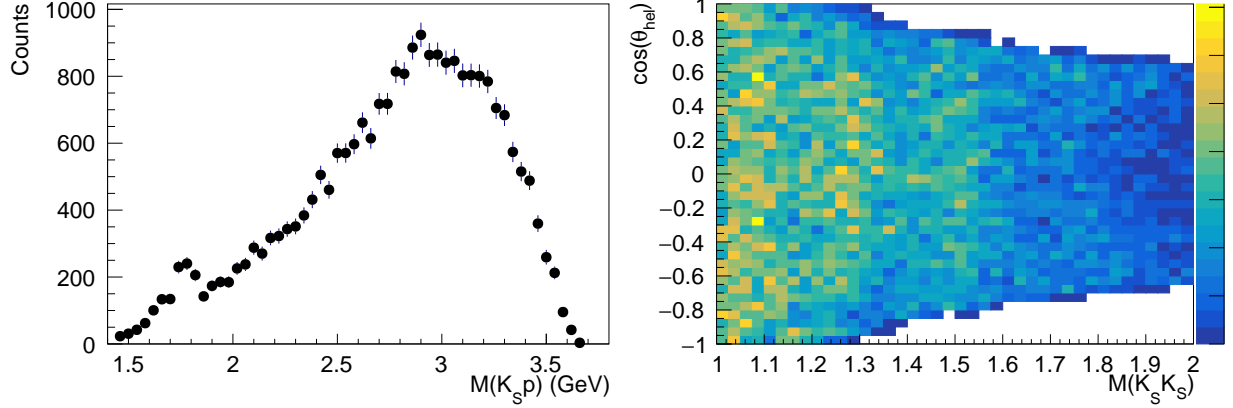


Figure 8.4: (Left) $K_S p$ invariant mass distribution. The peak at ~ 1.7 GeV is due to a $\Sigma^+ \rightarrow K_S p$ possibly the $\Sigma^+(1775)$. (Right) $M(K_S K_S)$ vs. $\cos(\theta)$ in the Helicity system after removing events below 2.0 GeV in the $K_S p$ invariant mass.

We can reject the Σ^+ contribution by removing events with a $K_S p$ invariant mass below 2.0 GeV. However, as seen in Figure 8.4, these events are strongly correlated to events at large angles in the $\cos(\theta_{\text{hel}})$ distribution where some of the distinguishing D -wave (i. e. the D_0 -wave) features are observed. The Σ^+ is a very small contribution to the whole spectrum and is unlikely to affect our angular analysis. We assume the Σ^+ contribution is negligible in the following analysis.

8.2.2 Amplitude Analysis

We follow the methodology used to study the $K_S K_L$ system to analyze the $K_S K_S$ system, see Chapter 7.2.3. This is possible because the amplitudes defined for the Partial Wave Analysis (PWA) apply for the decay to any two pseudoscalar mesons. For convenience, we write the intensity function here

$$\begin{aligned}
 I(\Omega, \Phi) = 2\kappa \sum_{k=\substack{\text{spin flip} \\ \text{non-flip}}} \left\{ (1 - P_\gamma) \left| \sum_{\ell, m} [\ell]_{m; k}^{(-)} \Re \mathfrak{e} [Z_\ell^m(\Omega, \Phi)] \right|^2 + (1 - P_\gamma) \left| \sum_{\ell, m} [\ell]_{m; k}^{(+)} \Im \mathfrak{m} [Z_\ell^m(\Omega, \Phi)] \right|^2 + \right. \\
 \left. (1 + P_\gamma) \left| \sum_{\ell, m} [\ell]_{m; k}^{(+)} \Re \mathfrak{e} [Z_\ell^m(\Omega, \Phi)] \right|^2 + (1 + P_\gamma) \left| \sum_{\ell, m} [\ell]_{m; k}^{(-)} \Im \mathfrak{m} [Z_\ell^m(\Omega, \Phi)] \right|^2 \right\}.
 \end{aligned} \tag{8.5}$$

and remind the reader that we neglect the sum of k when performing fits to data. For the $K_S K_S$ system only $\ell = \text{even}$ amplitudes contribute. We do not expect a contribution from $\ell = 4$ or higher amplitudes since only one spin-4 meson is known below 2 GeV and such states are expected

to have smaller cross sections. From our observations of Figure 8.3 we expect both $\ell = 0$ and 2 amplitudes to contribute. Considering both reflectivities and all m -projections gives a total of 12 complex amplitudes¹. Given the statistical precision of the current data set, including all $\ell = 0$ and 2 amplitudes appear to introduce too much freedom into the model which leads to unphysical behavior from one bin to the next. A reduced number of amplitudes is thus required to obtain physically meaningful information from data. We explore two approaches to choosing an appropriate set of amplitudes. First, we choose to follow the approach taken in the $a_2 \rightarrow \eta\pi^0$ analysis² of GlueX data [79]. The approach taken for the a_2 analysis is to use the set of $\ell = 2$ amplitudes predicted by the so-called Tensor Meson Dominance (TMD) model [80]. The predicted set of amplitudes, called a wave-set, for a_2 is D_{-1}^- , D_0^- , D_1^- , D_0^+ , D_1^+ and D_2^+ . We assume this wave-set is sufficient to describe f_2 and f_2' mesons. The resulting fit is shown in Figure 8.5. The bin-to-bin fluctuations resulting from the fit show unphysical behavior indicating that the statistical precision of the data is insufficient to properly constrain the fit. Another approach is to use the minimum reasonable wave-set, which our discussion in Chapter 8.2.1 indicates is S_0^- , S_0^+ and D_2^+ . The D_2^+ -wave shows smooth bin-to-bin behavior with intensity almost exclusively in the range 1.2 – 1.65 GeV, where the $f_2(1270)$, $a_2(1320)$ and $f_2'(1525)$ are expected. On the other hand, the S -waves are not stable in some parts of the mass spectrum. In particular, the behavior around the 1.4 – 1.6 GeV region, where we expect the $f_0(1500)$ and $f_2'(1525)$, is difficult to interpret. At higher mass, the intensity is almost exclusively S -wave but without introducing other D -wave components into the model we can not conclude that the resonances at ~ 1.75 GeV is the $f_0(1710)$.

We compare the data and fitted angular distributions in the 2nd, 6th, 11th, and 15th bin, see Figures 8.7, 8.8, 8.9 and 8.10 respectively. The statistical significance of including additional amplitudes (TMD wave set compared to our minimal wave set) can be estimated by the square root of the difference in likelihood. This estimator leads to a significance of 4.6σ for bin 2, 4.2σ for bin 6, 4.4σ for bin 11, and 3.9σ for bin 15. The large significance in each bin indicates that the minimal wave set is missing some features present in the data.

¹One m -projection for $\ell = 0$, five m -projections for $\ell = 2$ and two reflectivities for each m -projection.

²The η and π^0 particles are, like the K_S and K_L , pseudoscalar mesons and therefore the a_2 analysis used the same formalism as we use for the $K_S K_S$ amplitude analysis.

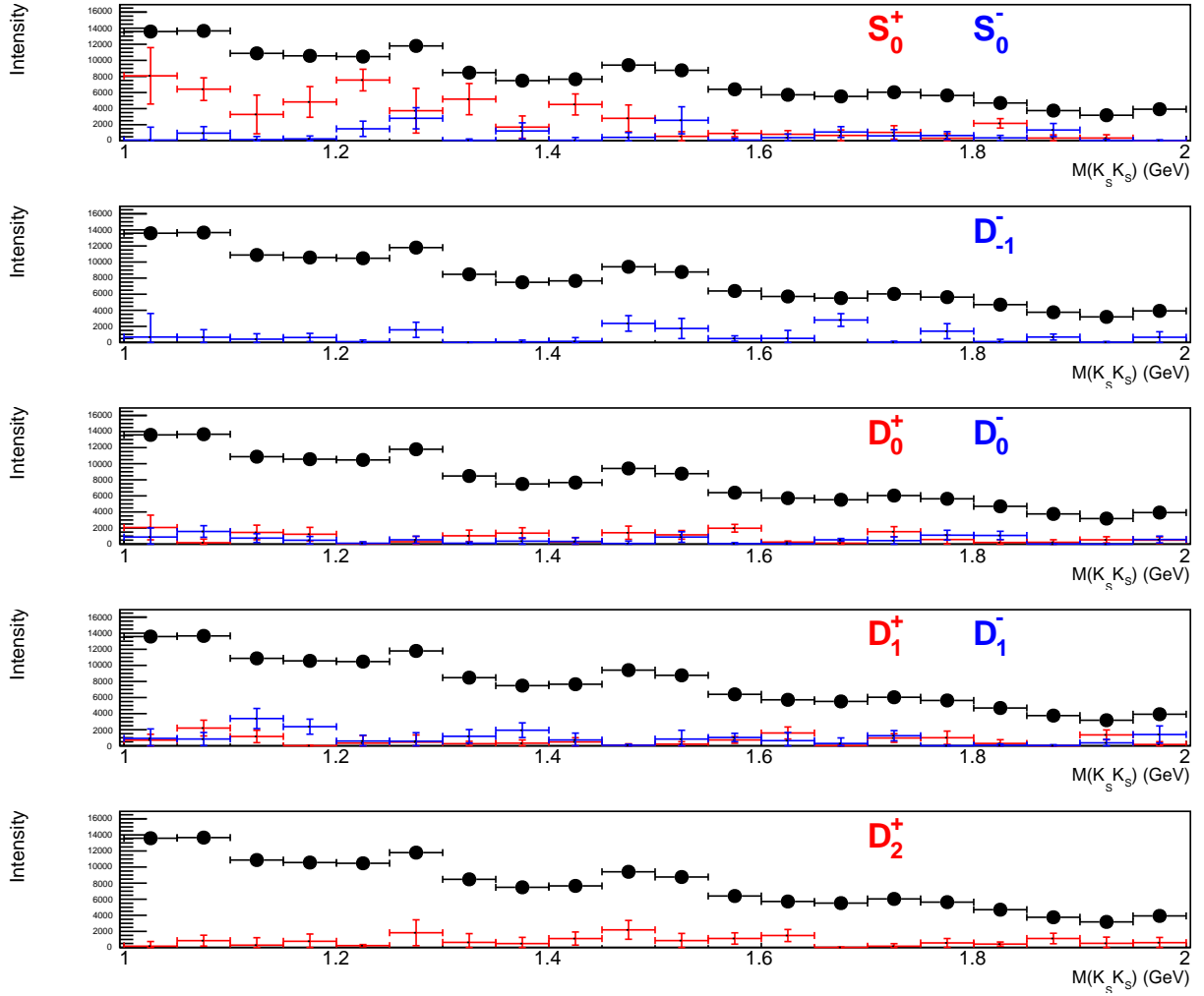


Figure 8.5: PWA of the $K_S K_S$ system using the TMD wave-set. Each panel includes the (black) total intensity and the intensity for the indicated ℓ_m amplitude with (red) positive reflectivity and (blue) negative reflectivity.

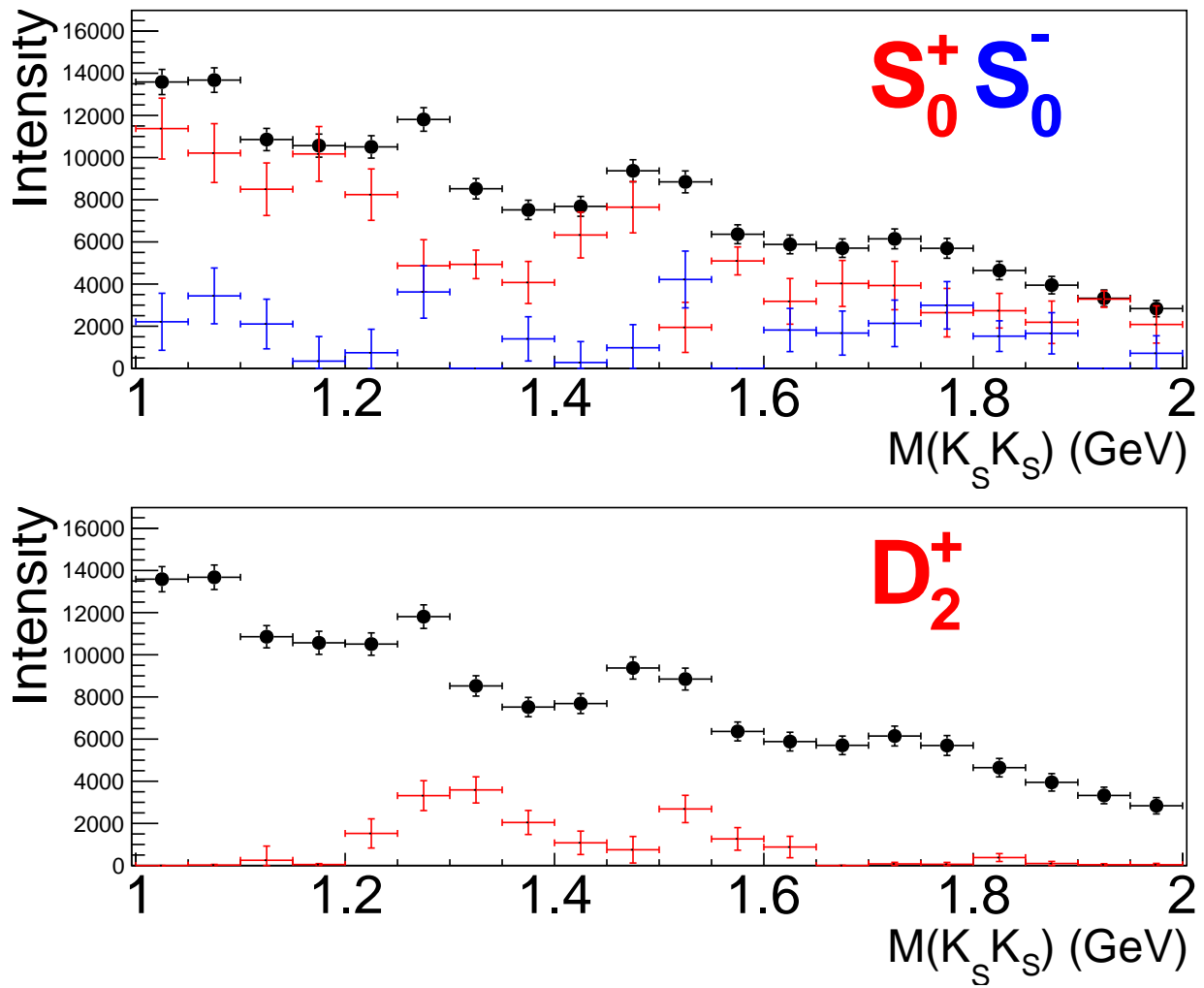


Figure 8.6: PWA of the $K_S K_S$ system using the minimum reasonable wave-set. Each panel includes the (black) total intensity and the intensity for the indicated ℓ_m amplitude with (red) positive reflectivity and (blue) negative reflectivity.

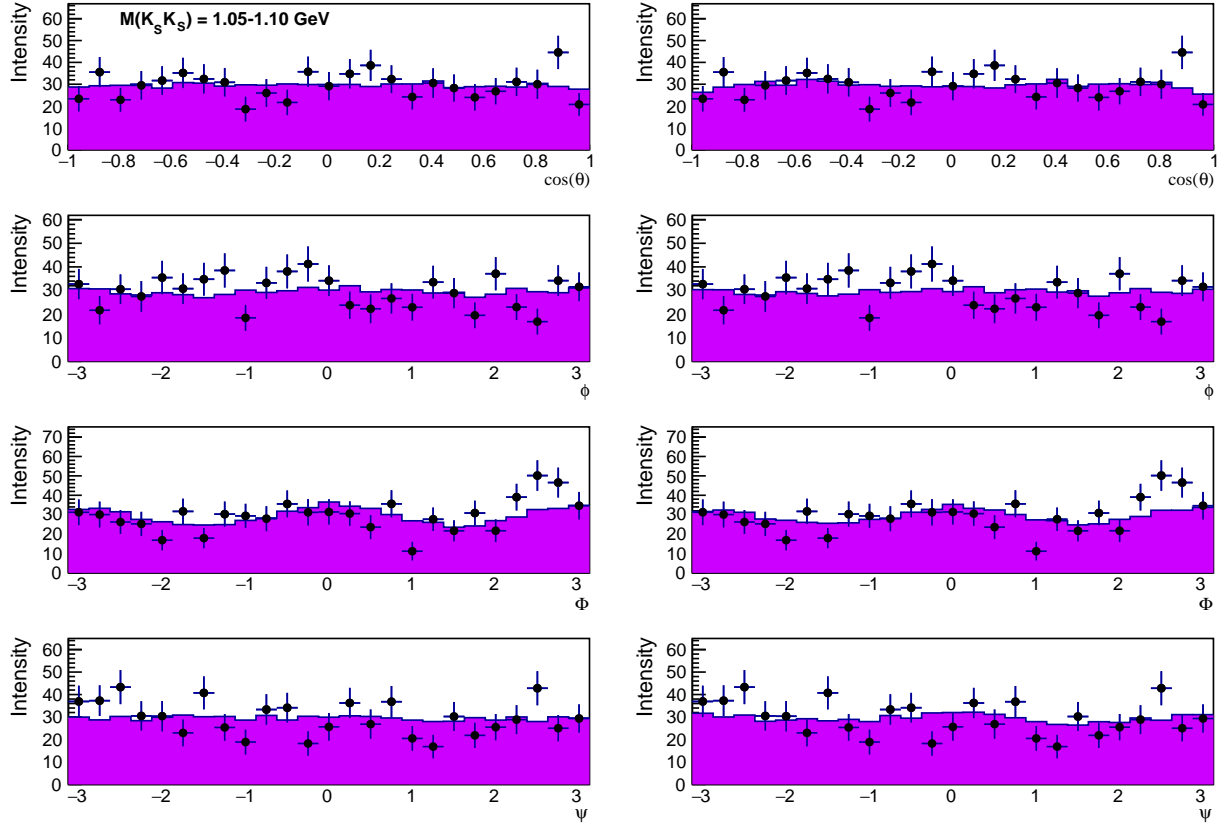


Figure 8.7: Comparison of (violet) fit to (black) data with (left) the S_0^\pm and D_2^+ wave set and (right) the TMD wave set. (From top to bottom) Polar angle and azimuthal angle of K_S in the \mathcal{H} frame, polarization angle, and (bottom right) $\psi = \phi - \Phi$ angle. These results correspond to the 2nd bin. The likelihoods obtained are $(S_0^\pm + D_2^+)$ -5199 and (TMD) -5220.

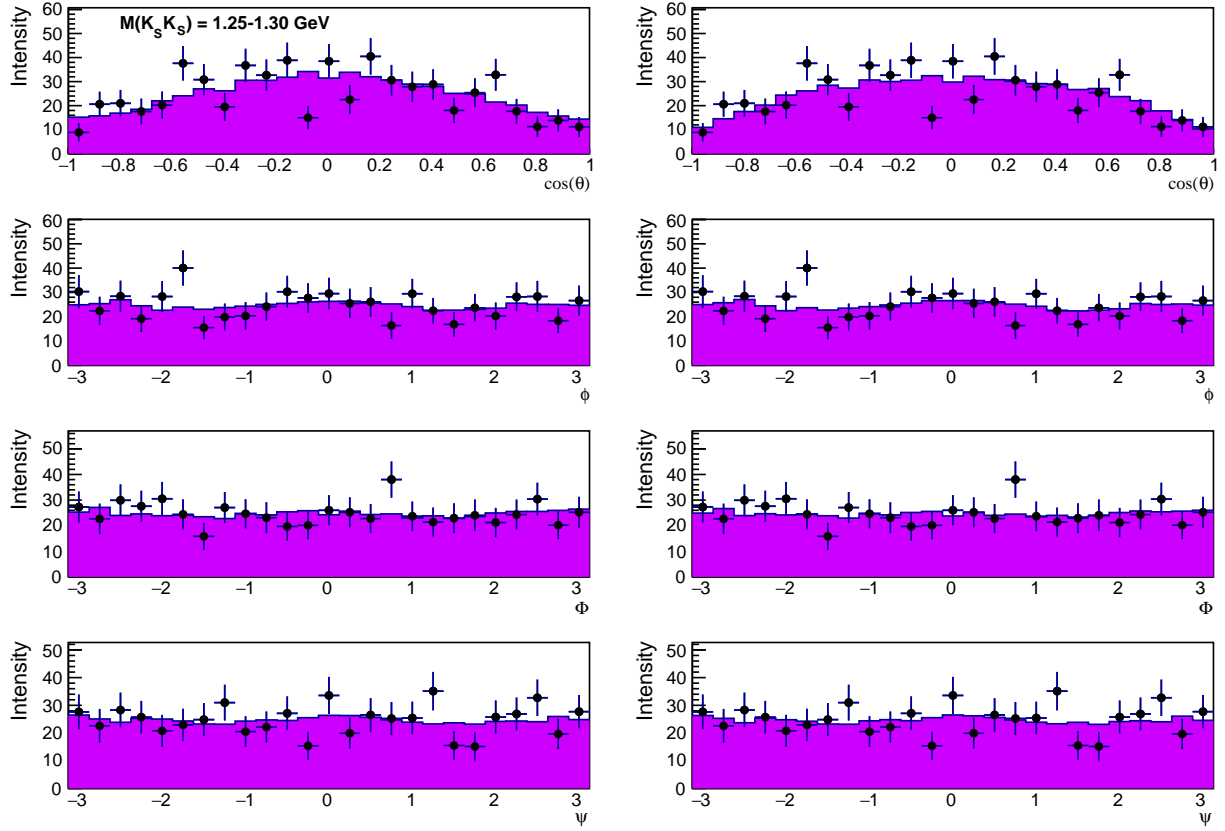


Figure 8.8: Comparison of (violet) fit to (black) data with (left) the S_0^\pm and D_2^+ wave set and (right) the TMD wave set. (From top to bottom) Polar angle and azimuthal angle of K_S in the \mathcal{H} frame, polarization angle, and (bottom right) $\psi = \phi - \Phi$ angle. These results correspond to the 6th bin. The likelihoods obtained are $(S_0^\pm + D_2^+)$ -4508 and (TMD) -4526.

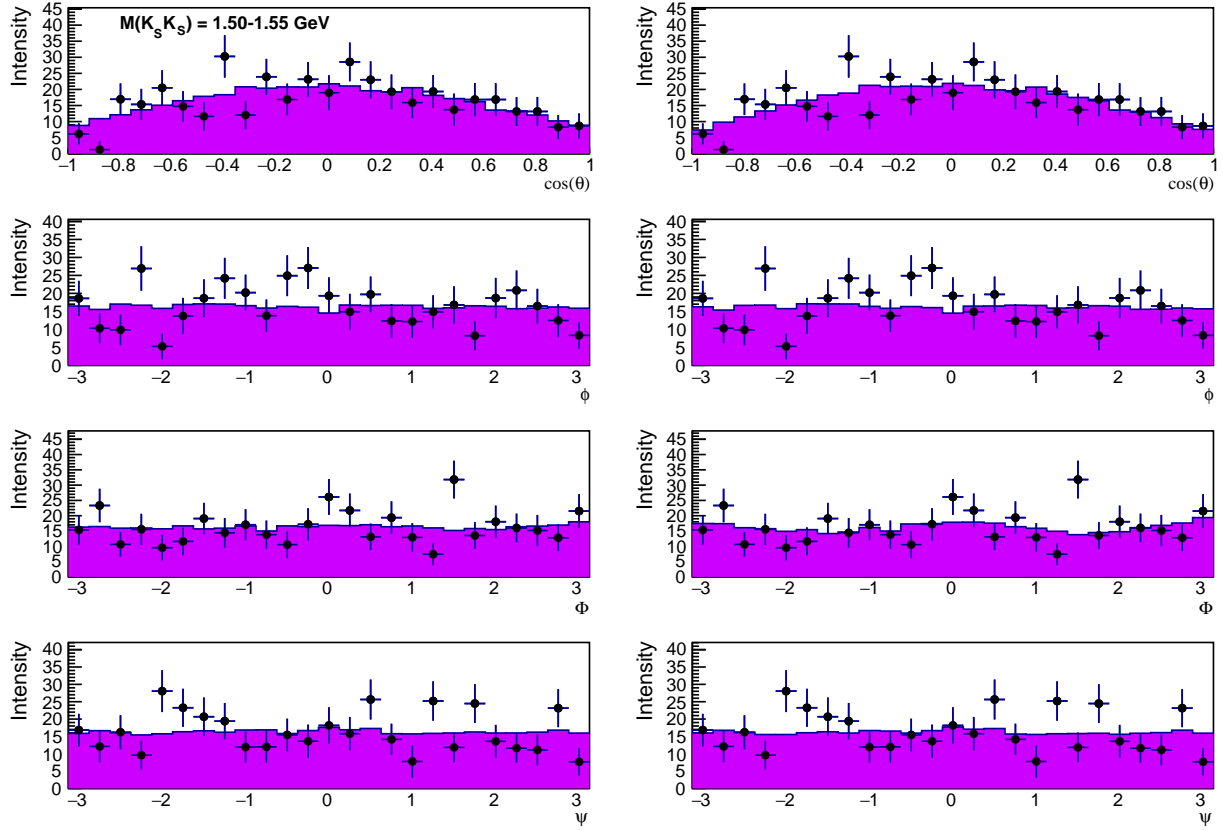


Figure 8.9: Comparison of (violet) fit to (black) data with (left) the S_0^\pm and D_2^+ wave set and (right) the TMD wave set. (From top to bottom) Polar angle and azimuthal angle of K_S in the \mathcal{H} frame, polarization angle, and (bottom right) $\psi = \phi - \Phi$ angle. These results correspond to the 11th bin. The likelihoods obtained are $(S_0^\pm + D_2^+)$ -3165 and (TMD) -3184.

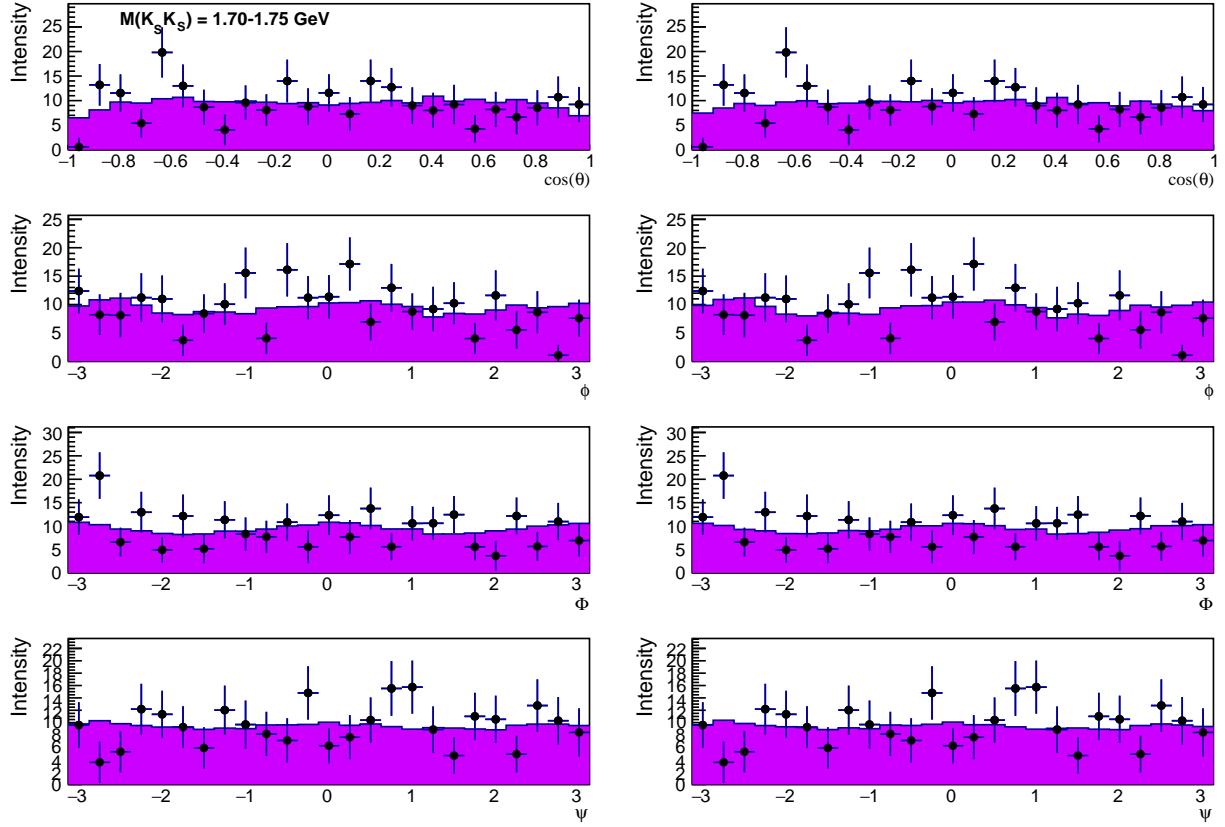


Figure 8.10: Comparison of (violet) fit to (black) data with (left) the S_0^\pm and D_2^+ wave set and (right) the TMD wave set. (From top to bottom) Polar angle and azimuthal angle of K_S in the \mathcal{H} frame, polarization angle, and (bottom right) $\psi = \phi - \Phi$ angle. These results correspond to the 15th bin. The likelihoods obtained are $(S_0^\pm + D_2^+)$ -1644 and (TMD) -1659.

CHAPTER 9

CONCLUSION

This dissertation analyzed the $\gamma p \rightarrow K_S K_L p$ and $\gamma p \rightarrow K_S K_S p$ reactions using the GlueX Phase-I (GlueX-I) data set. The aim of this dissertation was to: first, isolate the $K_S K_L p$ and $K_S K_S p$ final state in the GlueX-I data; second, measure the Spin Density Matrix Elements (SDMEs) and differential cross section of $\phi(1020) \rightarrow K_S K_L$; third, investigate the $K_S K_L$ spectrum beyond the $\phi(1020)$ and perform a Partial Wave Analysis (PWA) of the meson spectrum; and fourth, investigate the $K_S K_S$ spectrum and perform a PWA of the meson spectrum. Measurement of $\phi(1020)$ SDMEs will serve as an input to better understand meson photoproduction, a prerequisite in the search for exotic mesons. Through the PWA of the $K_S K_L$ spectrum, we explored the excited vector meson spectrum, laying the groundwork for future searches for hybrid vector mesons. We explored the $K_S K_S$ spectrum with special interest in f_0 mesons, which are believed to mix with a scalar glueball.

The $\phi(1020)$ differential cross section was measured in the range $-t = 0.15 - 1.0 \text{ GeV}^2$. Modeling the differential cross section as an exponential decay, we obtain a slope of $4.44 \pm 0.01 \text{ GeV}^{-2}$. The integrated cross section in the range $-t = 0.15 - 1.0 \text{ GeV}^2$ was $295.7 \pm 0.4 \text{ nb}$. Both measurements are consistent and far more precise than the previous measurement by Ballam et al. [1]. SDMEs of $\phi(1020)$ were measured across nine $-t$ bins in the range $0.15 - 1.0 \text{ GeV}^2$. Our measurement indicates that production through unnatural exchange is consistent with zero. At low $-t$, we find the data were consistent with s-channel helicity conservation, SCHC, i. e. the only non-zero SDMEs were $\rho_{1-1}^1 = -\text{Im}(\rho_{1-1}^2) = 1/2$. At higher $-t$, the SDMEs deviate from SCHC and our measurement indicates that this is due to natural parity exchange. The measured SDMEs were in poor agreement with theoretical predictions put forward by JPAC [35]. The deviation from SCHC observed in data might be due to a contribution of (the natural parity) f_2' exchange, this contribution was expected to be small and was therefore neglected in the JPAC model. We also find that the contribution from helicity double-flip amplitudes is consistent with zero. These measurements will serve as input to models of the production process, which will be essential for the interpretation of possible signals of exotic mesons in GlueX.

The $K_S K_L$ spectrum above $\phi(1020)$ is dominated by two peaks at ~ 1.5 GeV and ~ 1.75 GeV with no clear structures above 2 GeV. We modeled the acceptance corrected $K_S K_L$ invariant mass distribution as a sum of Breit-Wigner functions on top of a smooth background and considered models with and without interference between resonances. Based on the fits to data we could not identify the first peak as either $\omega(1420)$ or $\rho(1450)$. In principle, the peak could be due to both resonances, but we cannot make any definitive statements without a more sophisticated analysis. In line with previous photoproduction data of $K^+ K^-$, the second peak is found to be more consistent with the $X(1750)$ rather than $\phi(1680)$. We find that including a third Breit-Wigner around 2.2 GeV provides a modest improvement to the fit quality. In models without interference, the χ^2/ndf goes from 1.75 to 1.59, while in the interference model, it goes from 1.41 to 1.18. If such a state is present in the data, it can be attributed to the $\phi(2170)$ which has been observed in $K\bar{K}$ decays [4, 5] and, perhaps, at GlueX [21].

A PWA of the $K_S K_L$ spectrum from 1.1–2.0 GeV was performed. We find the spectrum below ~ 1.6 GeV was well described by $\ell = 1$ amplitudes. At higher mass, some features appear in the angular distributions that cannot be accounted for with purely $\ell = 1$ amplitudes. F_1 and F_2 amplitudes improve the description of the angular distributions while F_0 and F_3 amplitudes do not give an appreciable improvement. This indicates that the $K_S K_L$ spectrum is predominantly spin-1 with a small spin-3 contribution. The $K_S K_L$ spectrum is predominantly positive reflectivity up to ~ 1.6 GeV after which it becomes a nearly equal mix of positive and negative reflectivity. In a fit with only $\ell = 1$ amplitudes, we find that the positive reflectivity component of the spectrum reproduces the same double bump structure seen in the total intensity while the negative reflectivity distribution peaks between the two bumps. However, this peculiar feature is not always present when introducing $\ell = 3$ amplitudes into the model and therefore can only be considered suggestive at this stage. When fully available, including the GlueX Phase-II data set may be sufficient to stabilize the PWA results. This would provide a firm footing on which to interpret the $K_S K_L$ spectrum.

The $K_S K_S$ system shows a rich spectrum with multiple resonance structures but is more statistically limited than the $K_S K_L$ system. We selected $K_S K_S$ events over the full beam energy range and modeled the invariant mass spectrum as a sum of resonances on top of a smoothly varying background. We found evidence at the 10.9σ level in favor of a resonance at ~ 1.75 GeV. The

model parameters suggest this is the $f_0(1710)$. A PWA was performed up to 2 GeV in $K_S K_S$ invariant mass following the same methodology used for the $K_S K_L$ analysis. The analysis of the $K_S K_S$ spectrum was inconclusive, given the statistical precision of the data we were unable to satisfactorily measure the partial waves using a large wave-set. Using the minimum reasonable wave-set (S_0^- , S_0^+ and D_2^+) suggests that spin-2 contributions to the mass spectrum were mostly in the 1.2 – 1.6 GeV range, where the $f_2(1270)$, $a_2(1320)$ and $f_2'(1525)$ are expected.

The analyses that have been undertaken in this dissertation can be extended by including the GlueX Phase-II (GlueX-II) data set. This new data set is anticipated to be three to four times larger than that of GlueX-I, with approximately 40% of GlueX-II data already available. With an increase in statistical precision, the $\phi(1020)$ SDME analysis can be extended to higher $-t$ or increase the number of bins in the range. The statistical precision of the data is a limiting factor in establishing whether $\phi(2070) \rightarrow K_S K_L$ has been observed, this may be alleviated by expanding the beam energy range outside the coherent peak ($E_\gamma = 8.2 - 8.8$) and by including the GlueX-II data. The increased statistics of the GlueX-II data set will benefit the PWA of the $K_S K_L$ and $K_S K_S$ systems. The increased statistical precision can help stabilize the fits, perhaps enough to extract the spin-3 contribution of the $K_S K_L$ spectrum and increase the wave-set in fits to $K_S K_S$. An approach to PWA that was not explored in this dissertation is to introduce a mass dependence into the model. Given the complicated structure of both reactions, especially $K_S K_S$, developing a realistic model for the mass dependence is challenging. However, the model-dependent approach does not suffer from the unphysical bin-to-bin fluctuations we observe but introduces more bias through the model dependence. Other approaches being explored are Bayesian techniques that impose smooth bin-to-bin behavior of the amplitudes in a non-parametric way as opposed to assuming a specific biased parametric model. This approach has shown promising results, but is still in early development. To separate isoscalar and isovector components of the $K^0 \bar{K}^0$ spectrum will require a coupled channel-analysis. For example, $K_S K_S$ channel can be coupled to the $\pi^0 \pi^0$ and $\eta \pi^0$ channels to separate, respectively, f_J and a_J contributions.

APPENDIX A

TWO BODY KINEMATICS

Figure A.1 depicts a general $2 \rightarrow 2$ scattering process. The cross section for such a reaction may be expressed as a function of Mandelstam variables defined as:

$$s = (p_1 + p_2)^2 = (p_3 + p_4)^2 = m_1^2 + m_2^2 + 2(E_1 E_2 - \mathbf{p}_1 \cdot \mathbf{p}_2) \quad (\text{A.1})$$

$$t = (p_1 - p_3)^2 = (p_2 - p_4)^2 = m_1^2 + m_3^2 - 2(E_1 E_3 - \mathbf{p}_1 \cdot \mathbf{p}_3) \quad (\text{A.2})$$

$$u = (p_1 - p_4)^2 = (p_2 - p_3)^2 = m_1^2 + m_4^2 - 2(E_1 E_4 - \mathbf{p}_1 \cdot \mathbf{p}_4) \quad (\text{A.3})$$

where m_i are the masses of the final state particles and $p_i = (E_i, \mathbf{p}_i)$ are the four-momenta. The three Mandelstam variables satisfy the relation

$$s + t + u = \sum_i m_i^2 \quad (\text{A.4})$$

i.e. there are only two independent variables to fully characterize the scattering process for given masses m_i .

In the center-of-momentum frame, we have $\mathbf{p}_1 = -\mathbf{p}_2$ (and $\mathbf{p}_3 = -\mathbf{p}_4$), thus

$$s = (E_1 + E_2)^2 = (E_3 + E_4)^2 \quad (\text{A.5})$$

$$t = m_1^2 + m_3^2 - 2(E_1 E_3 - |\mathbf{p}_1| |\mathbf{p}_3| \cos \theta_s) \quad (\text{A.6})$$

$$u = m_1^2 + m_4^2 - 2(E_1 E_4 - |\mathbf{p}_1| |\mathbf{p}_4| \cos \theta_s) \quad (\text{A.7})$$

with θ_s the scattering angle between particle 1 and 3 in the center-of-momentum frame. At high energy the rest mass becomes negligible and we obtain

$$t \approx |\mathbf{p}_1| |\mathbf{p}_3| \cos \theta_s \quad (\text{A.8})$$

$$u \approx |\mathbf{p}_1| |\mathbf{p}_4| \cos \theta_s \quad (\text{A.9})$$

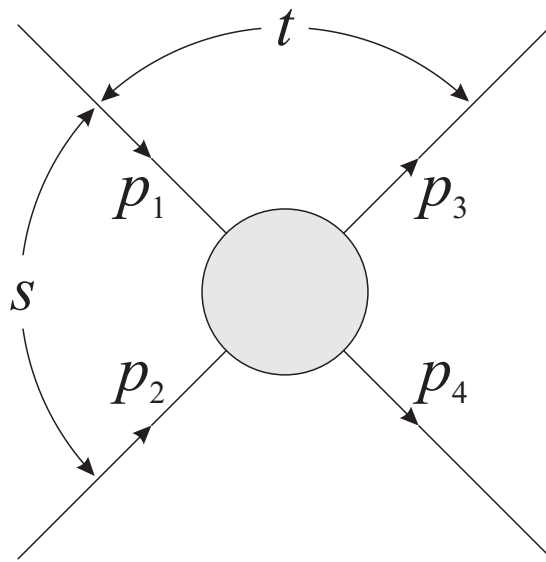


Figure A.1: Diagram of a two body scattering process $1 + 2 \rightarrow 3 + 4$. Figure is taken from Ref. [7]

APPENDIX B

BEAM POLARIZATION PARAMETERS

The angle of linear polarization of the photon beam is determined by the orientation of the diamond radiator. While collecting data, the diamond is cycled through four orientations at nominal values: 0° , 45° , 90° , and -45° . However, deviation from the nominal orientations have been observed. The deviations were determined with $\rho(770) \rightarrow \pi^+\pi^-$ data for each run period [76]. When extracting the $\phi(1020)$ SDMEs we fit the complete GlueX-I data set, so the polarization angle is set to the weighted average of the three run periods. The weights are determined by the luminosity in the coherent peak, $E_\gamma = 8.2 - 8.8$ GeV for GlueX-I and $E_\gamma = 8.0 - 8.6$ GeV for the Spring 2020 run period. All polarization angle and luminosity values are reported in Table B.1.

Table B.1: Polarization angle luminosity and fraction of GlueX-I data for each run period.

Nominal	Polarization Angle ($^\circ$)				
	Spring 2017	Spring 2018	Fall 2018	GlueX-I	Spring 2020
0	1.8 ± 0.6	4.1 ± 0.4	3.3 ± 0.4	3.4 ± 0.4	1.4 ± 1.1
45	47.9 ± 0.5	48.5 ± 0.5	48.3 ± 0.8	48.3 ± 0.6	47.1 ± 0.6
-45	-41.6 ± 0.6	-42.4 ± 0.4	-42.1 ± 0.6	-42.2 ± 0.5	-42.2 ± 0.5
90	94.5 ± 0.5	94.2 ± 0.4	92.9 ± 0.4	93.8 ± 0.4	93.4 ± 1.6
Luminosity (pb^{-1})	21.8	63.0	40.1	124.9	132.4
Fraction of GlueX-I	0.18	0.50	0.32	1.000	1.06

APPENDIX C

SYSTEMATIC TESTS OF $\phi(1020)$ SPIN-DENSITY MATRIX ELEMENTS

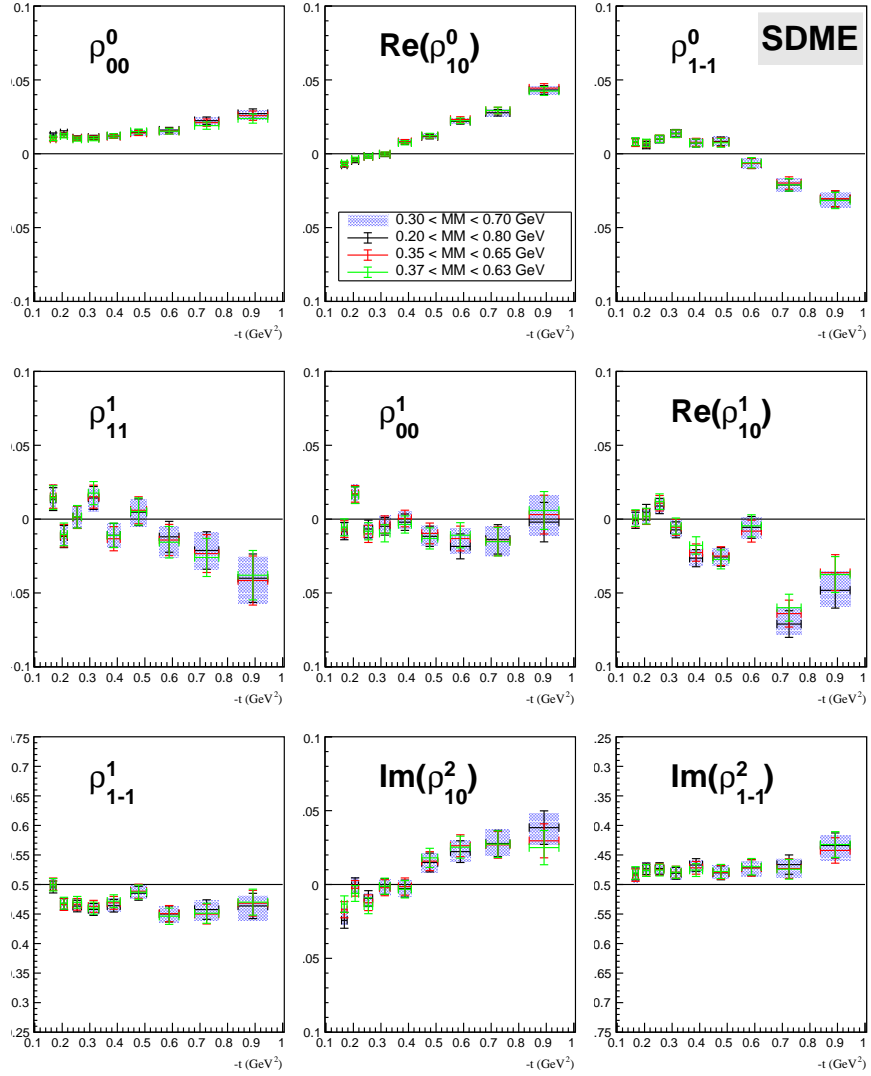


Figure C.1: Spin-Density Matrix Elements for the nominal data set and three variations on the missing mass selection.

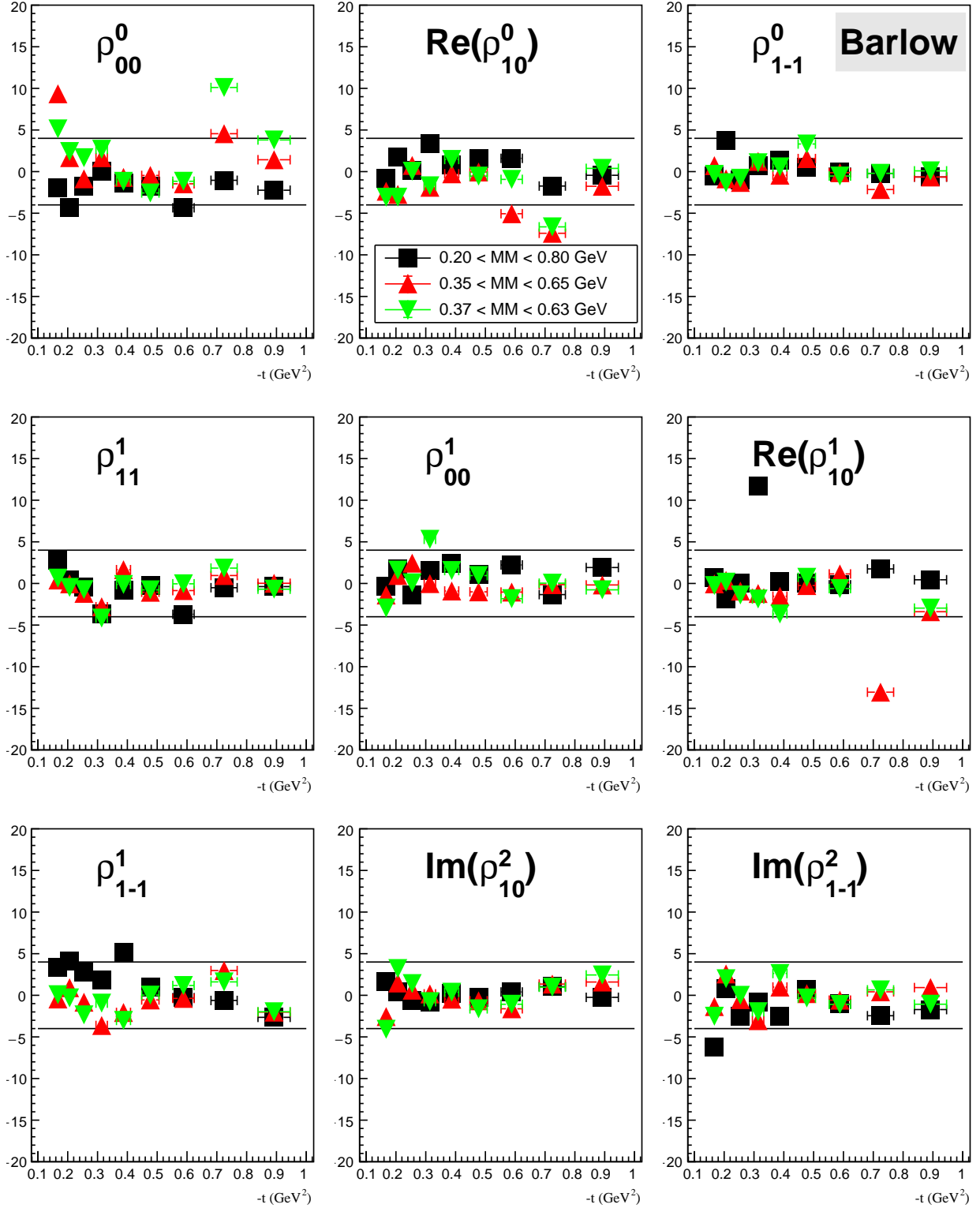


Figure C.2: Barlow significance test for each missing mass variation as a function of $-t$. Horizontal lines indicate $\pm 4\sigma_{Barlow}$.

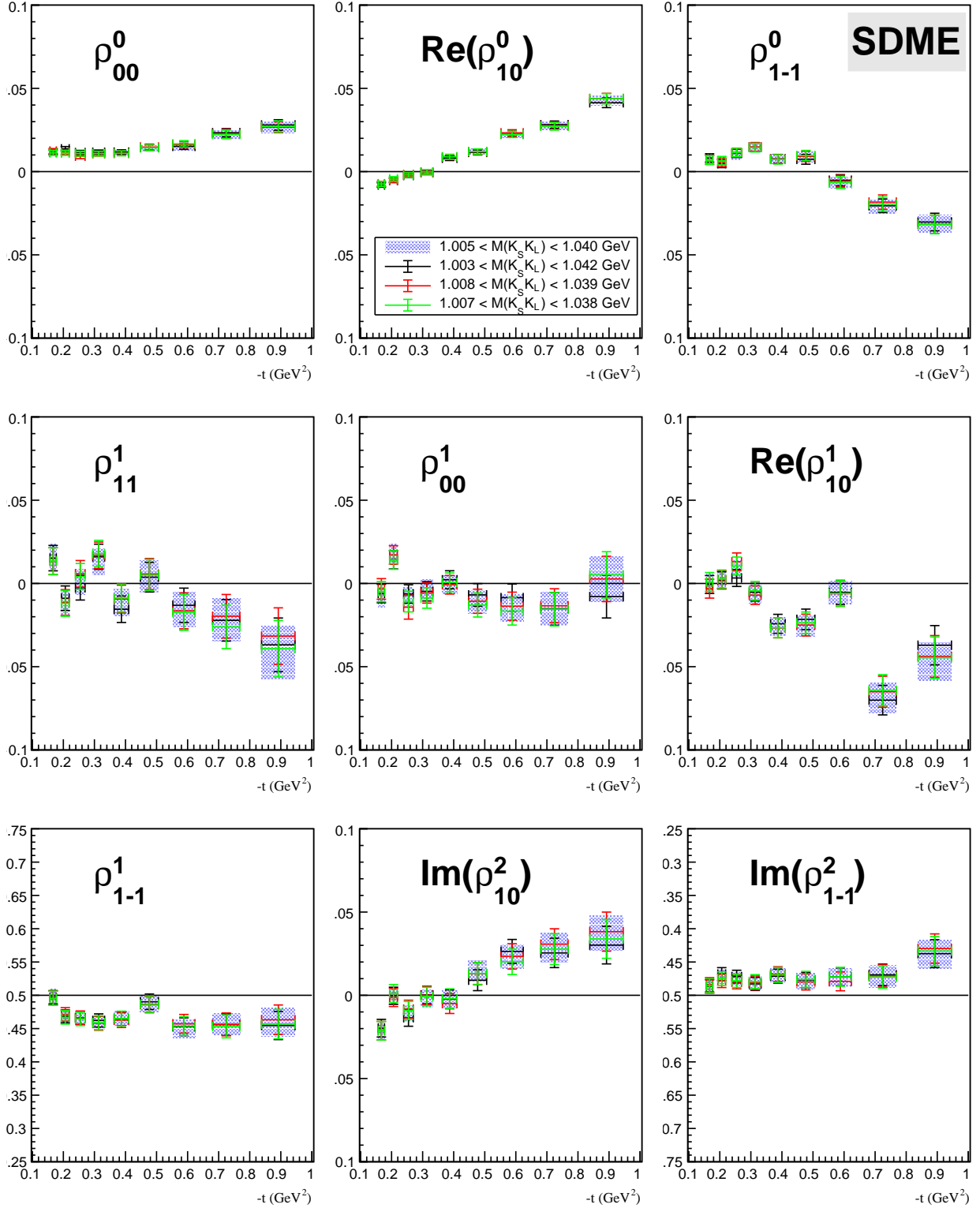


Figure C.3: Spin-Density Matrix Elements for the nominal data set and three variations on the $K_S K_L$ invariant mass selection.

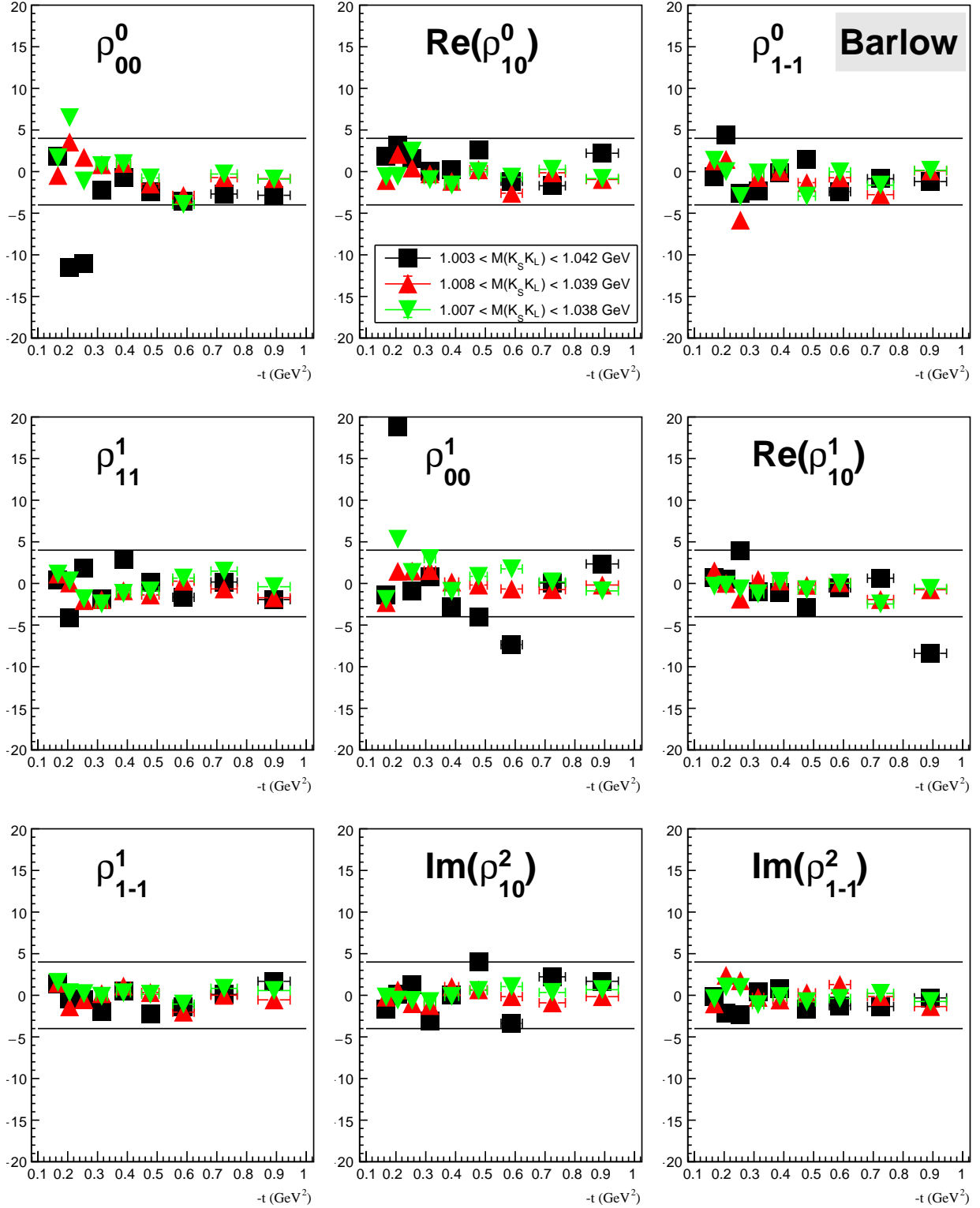


Figure C.4: Barlow significance test for each $K_S K_L$ invariant mass variation as a function of $-t$. Horizontal lines indicate $\pm 4\sigma_{\text{Barlow}}$.

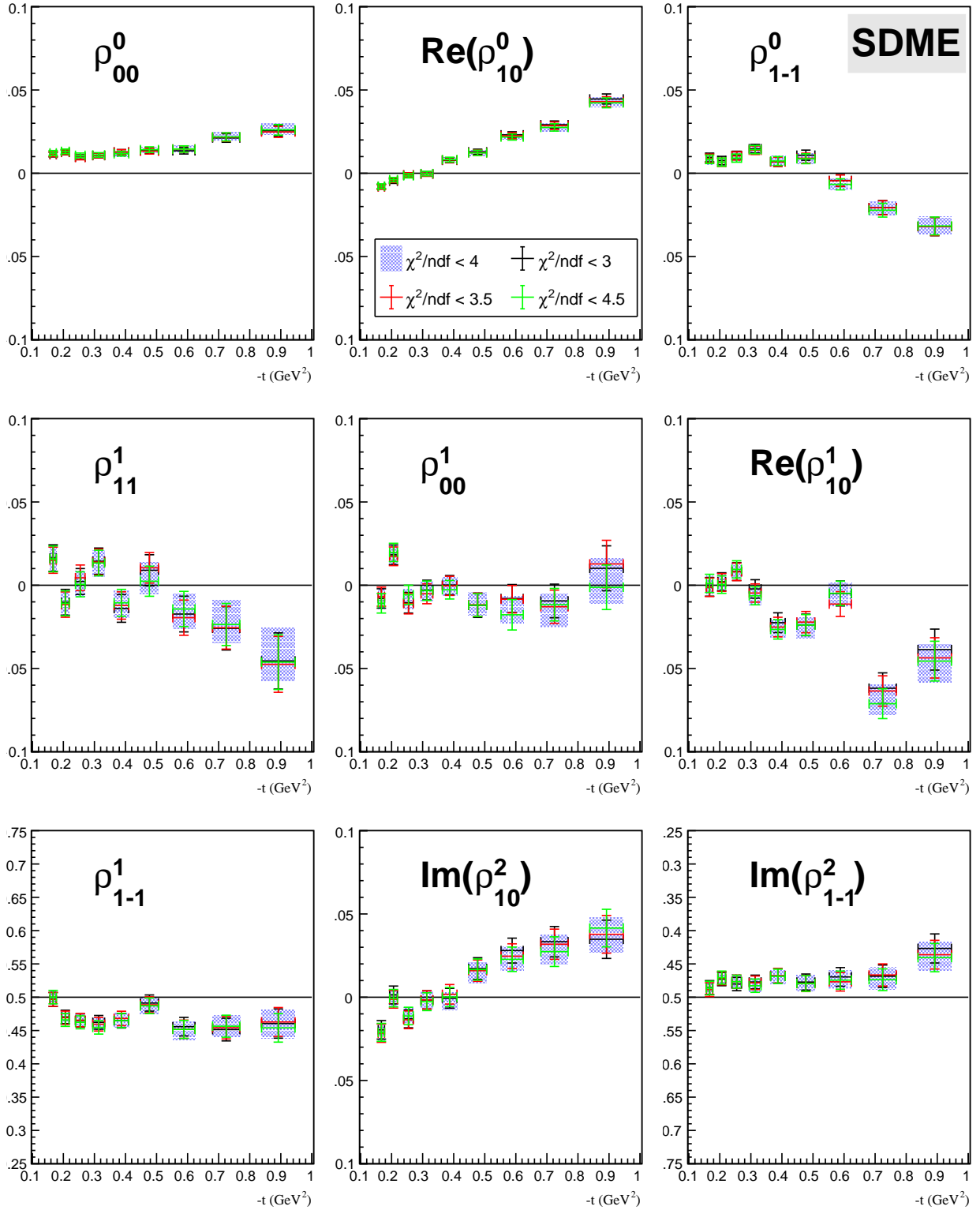


Figure C.5: Spin-Density Matrix Elements for the nominal data set and three variations on the χ^2/ndf selection.

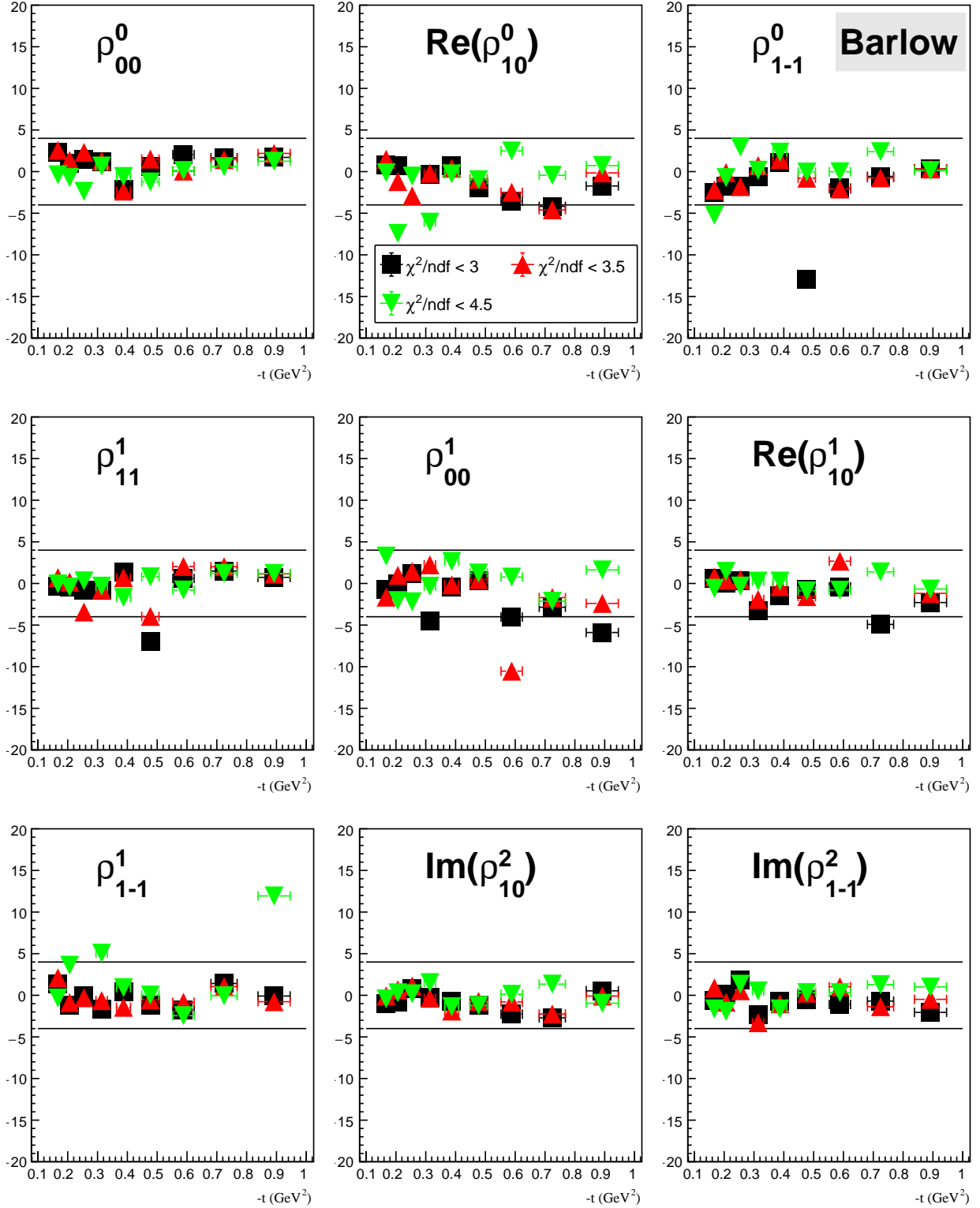


Figure C.6: Barlow significance test for each χ^2/ndf variation as a function of $-t$. Horizontal lines indicate $\pm 4\sigma_{\text{Barlow}}$.

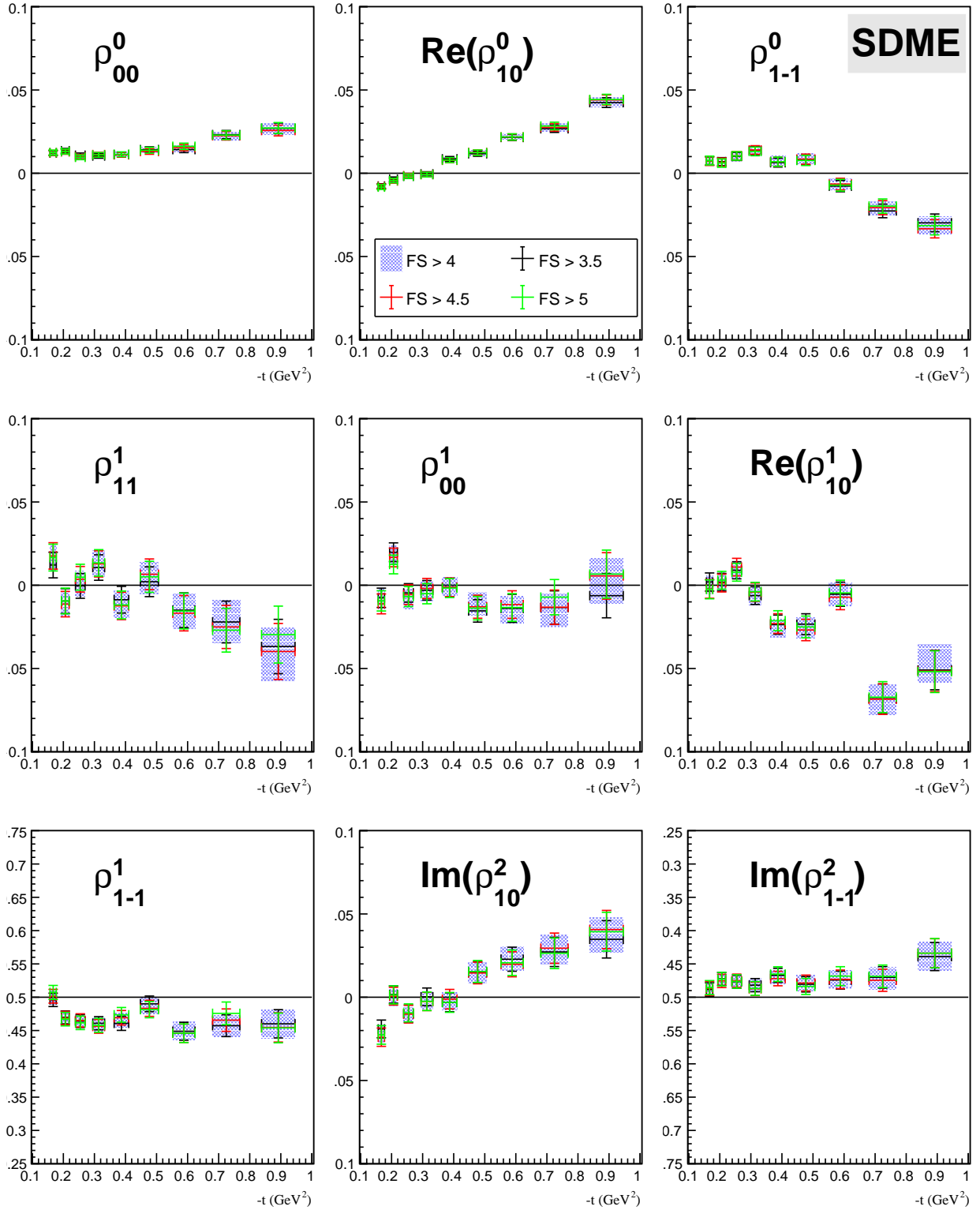


Figure C.7: Spin-Density Matrix Elements for the nominal data set and three variations on the FS selection.

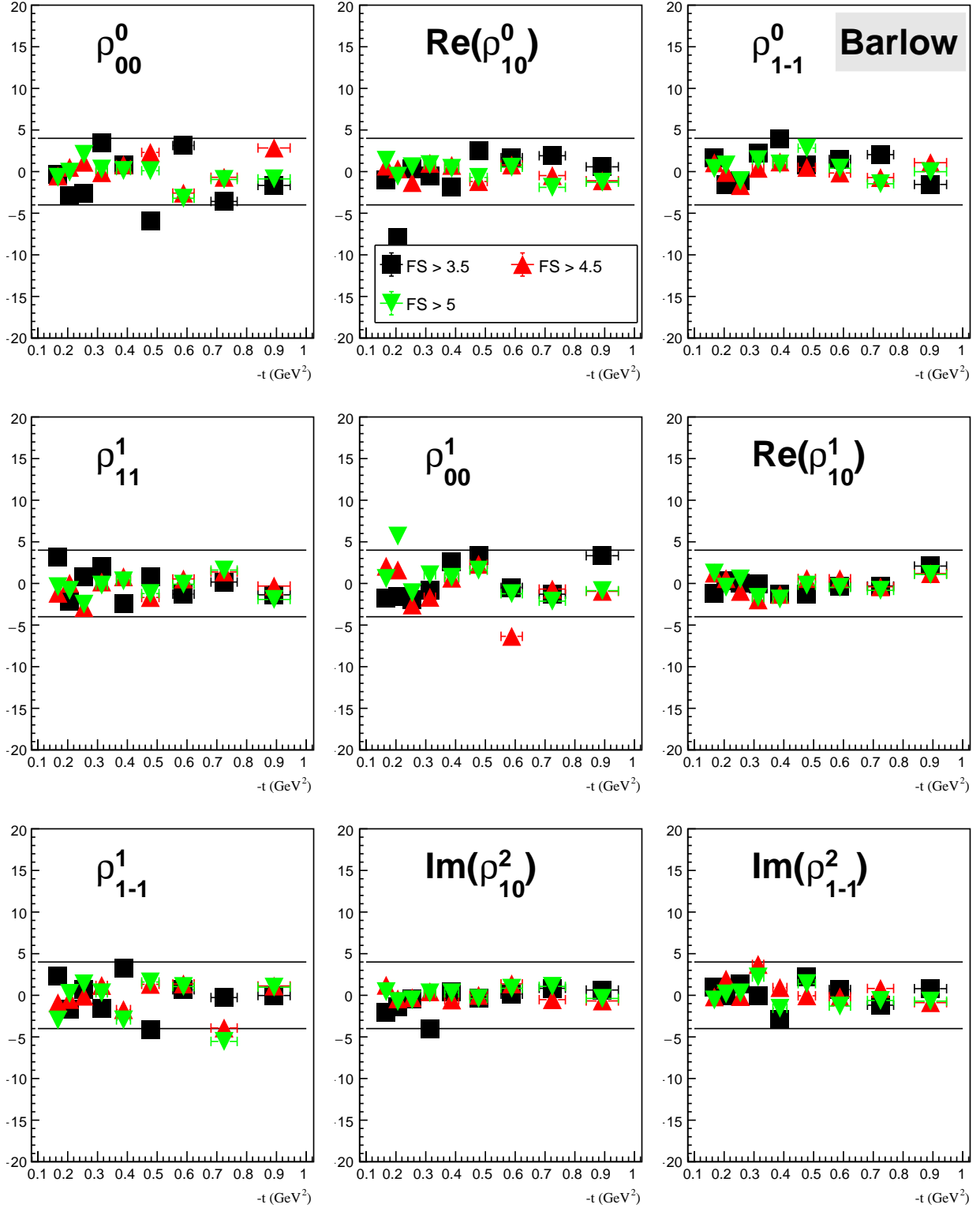


Figure C.8: Barlow significance test for each FS variation as a function of $-t$. Horizontal lines indicate $\pm 4\sigma_{\text{Barlow}}$.

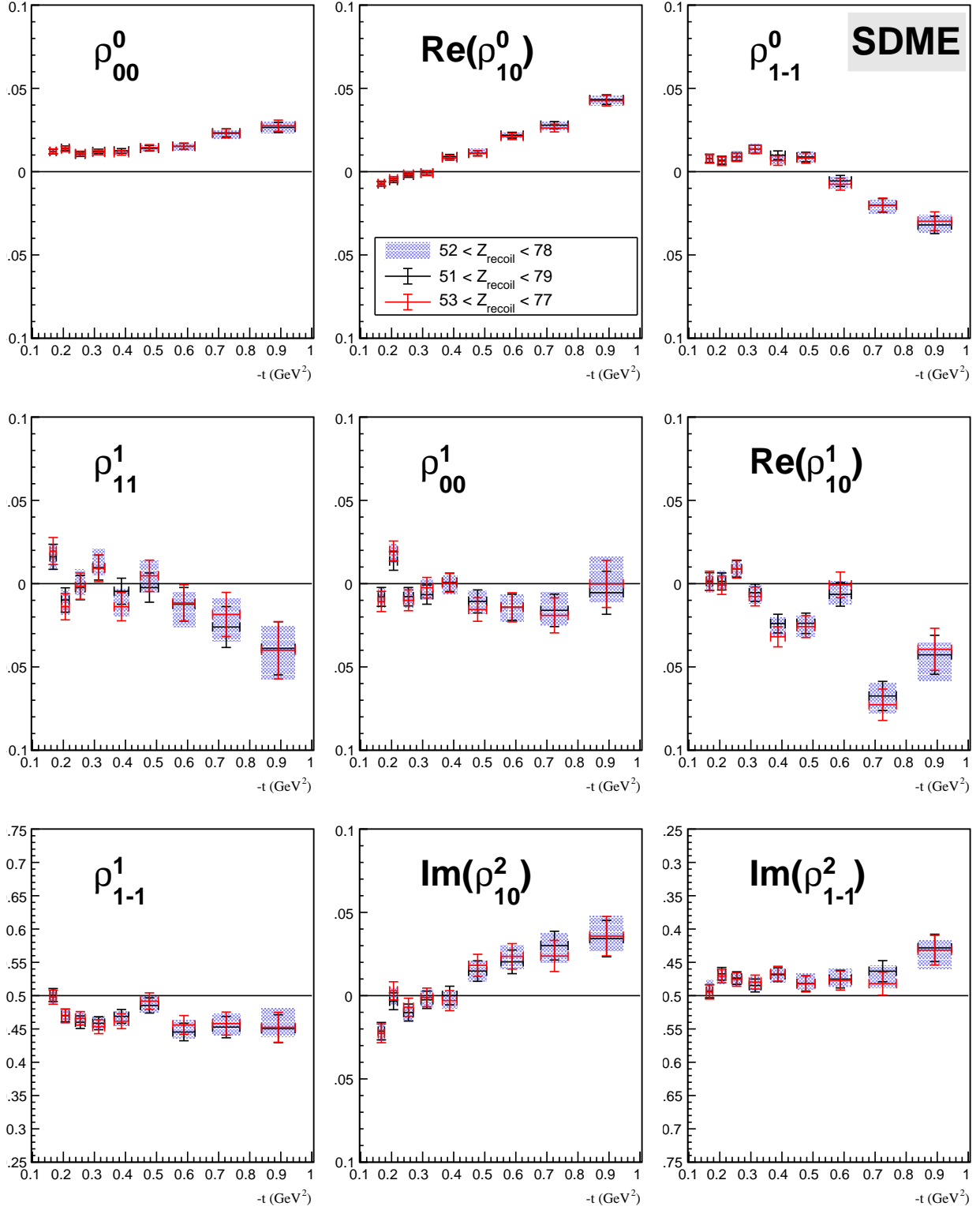


Figure C.9: Spin-Density Matrix Elements for the nominal data set and three variations on the proton z-vertex selection.

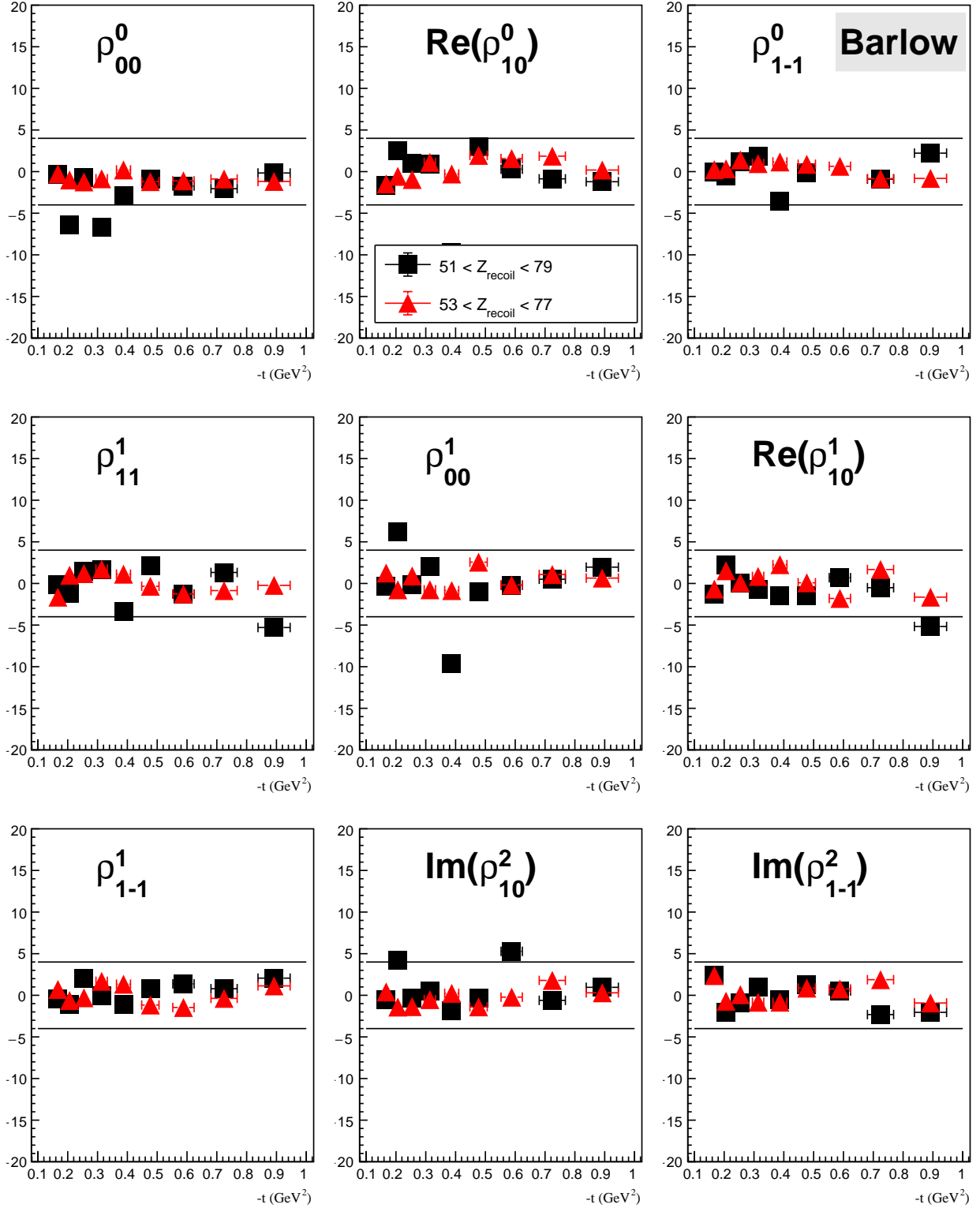


Figure C.10: Barlow significance test for each proton z-vertex variation as a function of $-t$. Horizontal lines indicate $\pm 4\sigma_{Barlow}$.

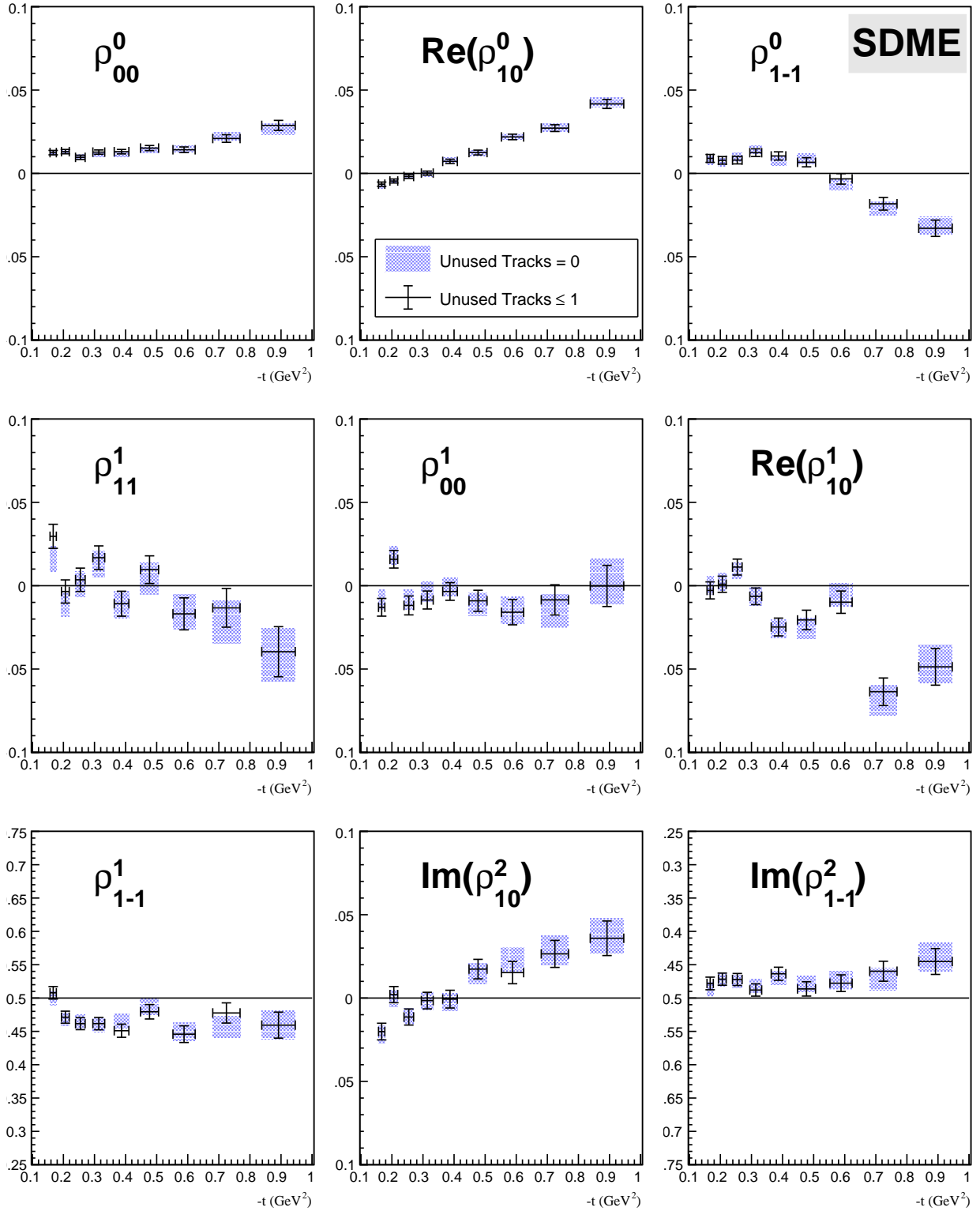


Figure C.11: Spin-Density Matrix Elements for the nominal data set and three variations on the number of unused tracks selection.

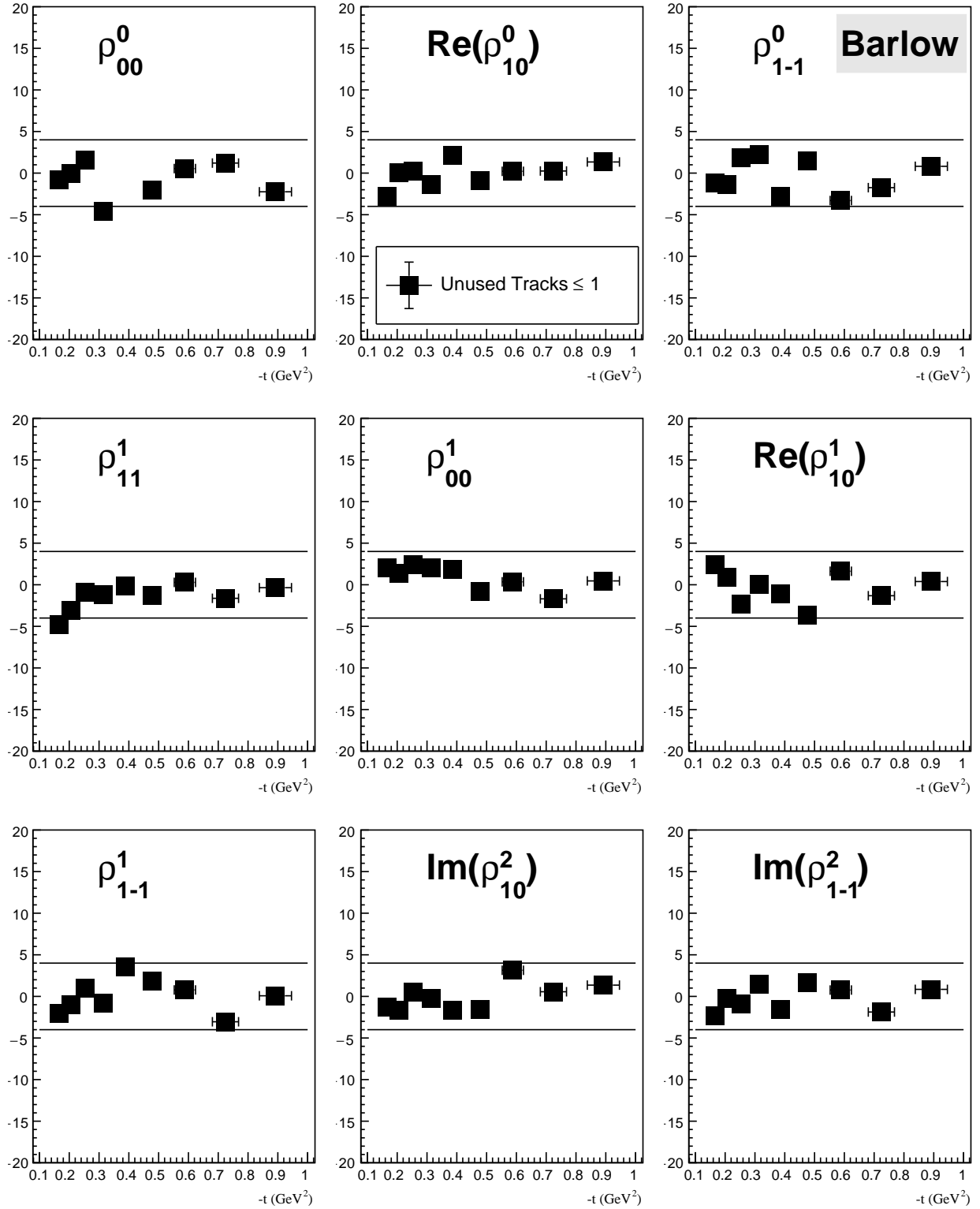


Figure C.12: Barlow significance test for each number of unused tracks variation as a function of $-t$. Horizontal lines indicate $\pm 4\sigma_{\text{Barlow}}$.

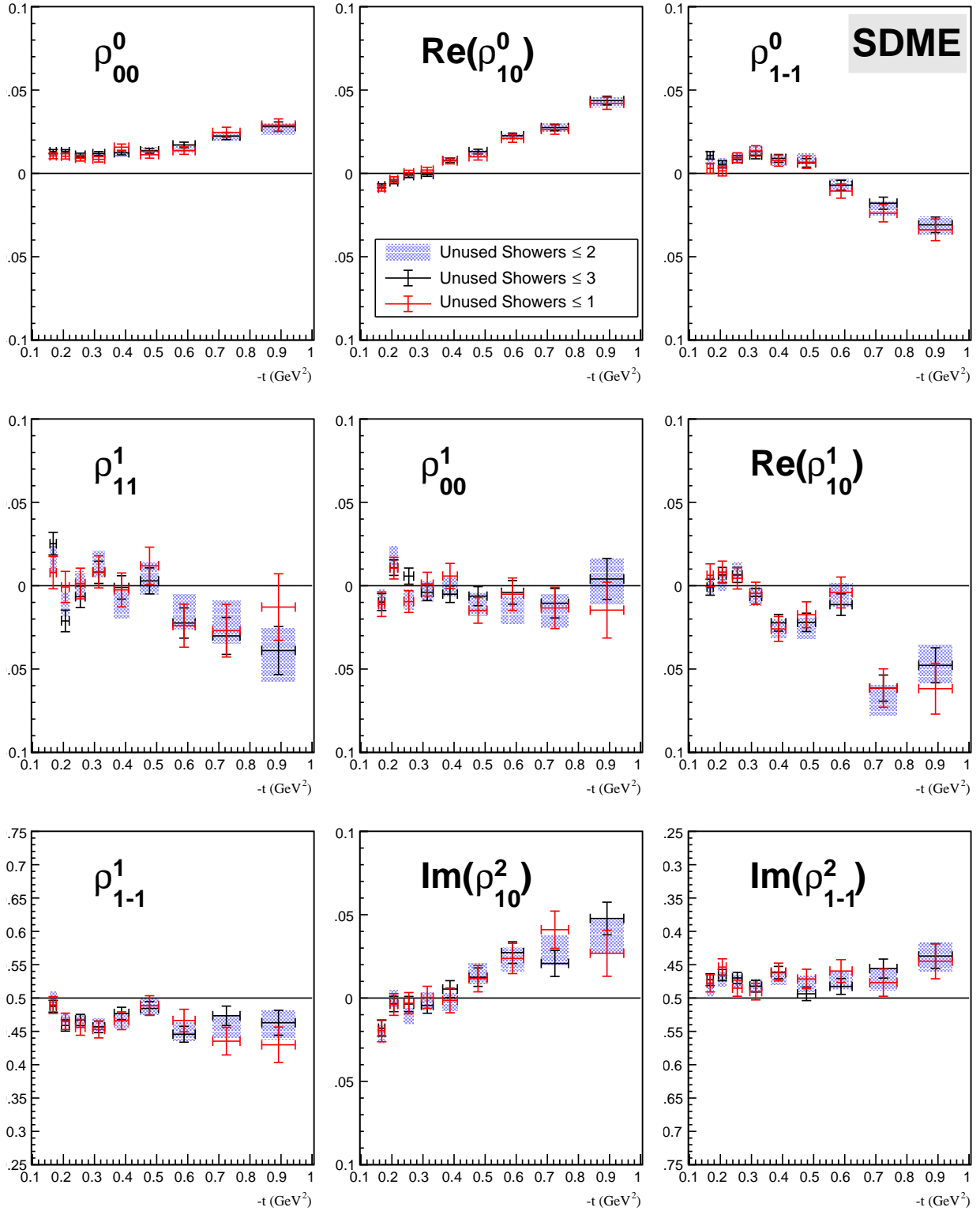


Figure C.13: Spin-Density Matrix Elements for the nominal data set and three variations on the number of unused showers selection.

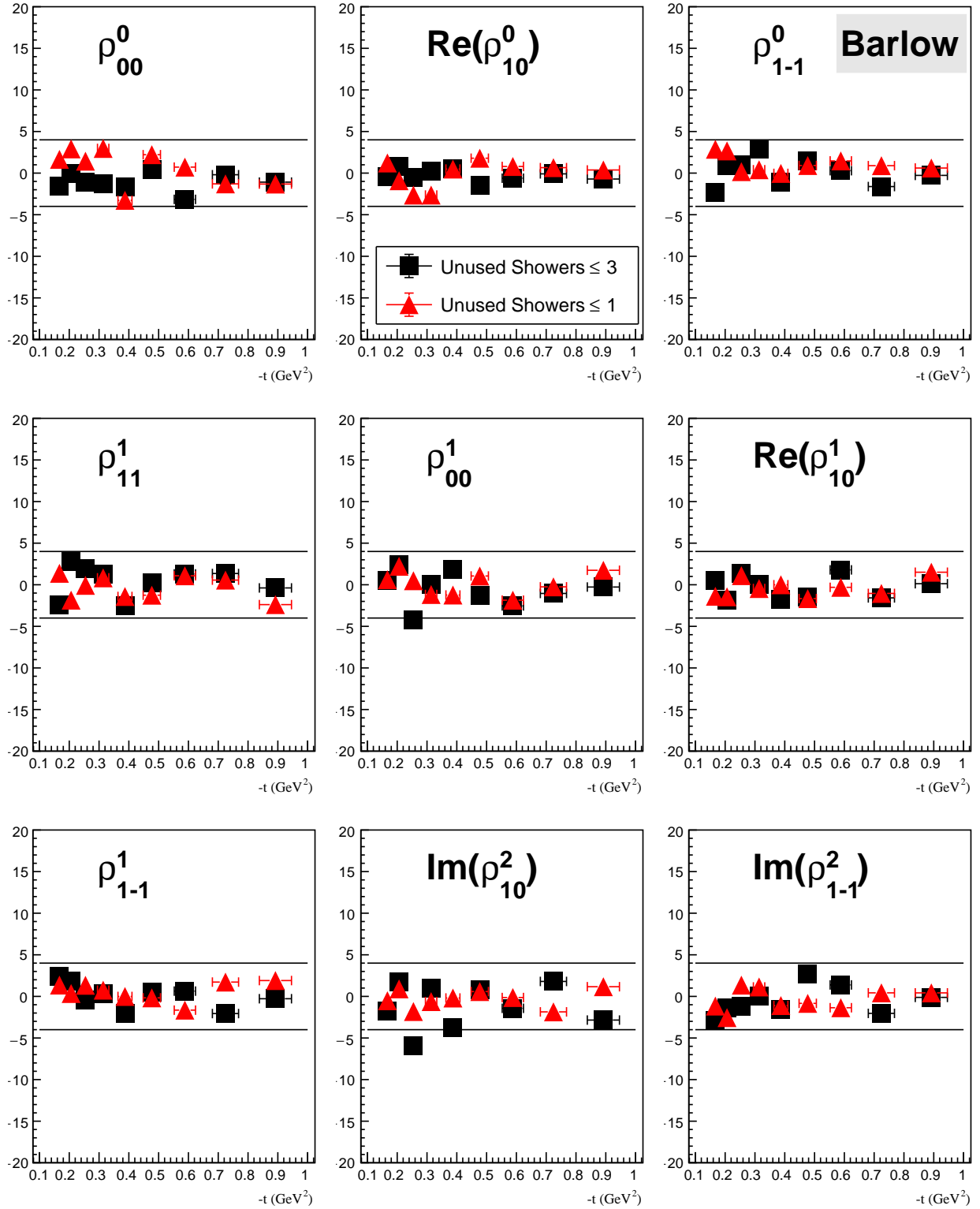


Figure C.14: Barlow significance test for each number of unused showers variation as a function of $-t$. Horizontal lines indicate $\pm 4\sigma_{Barlow}$.

APPENDIX D

HIGH MASS $K_S K_L$ PARTIAL WAVE ANALYSIS

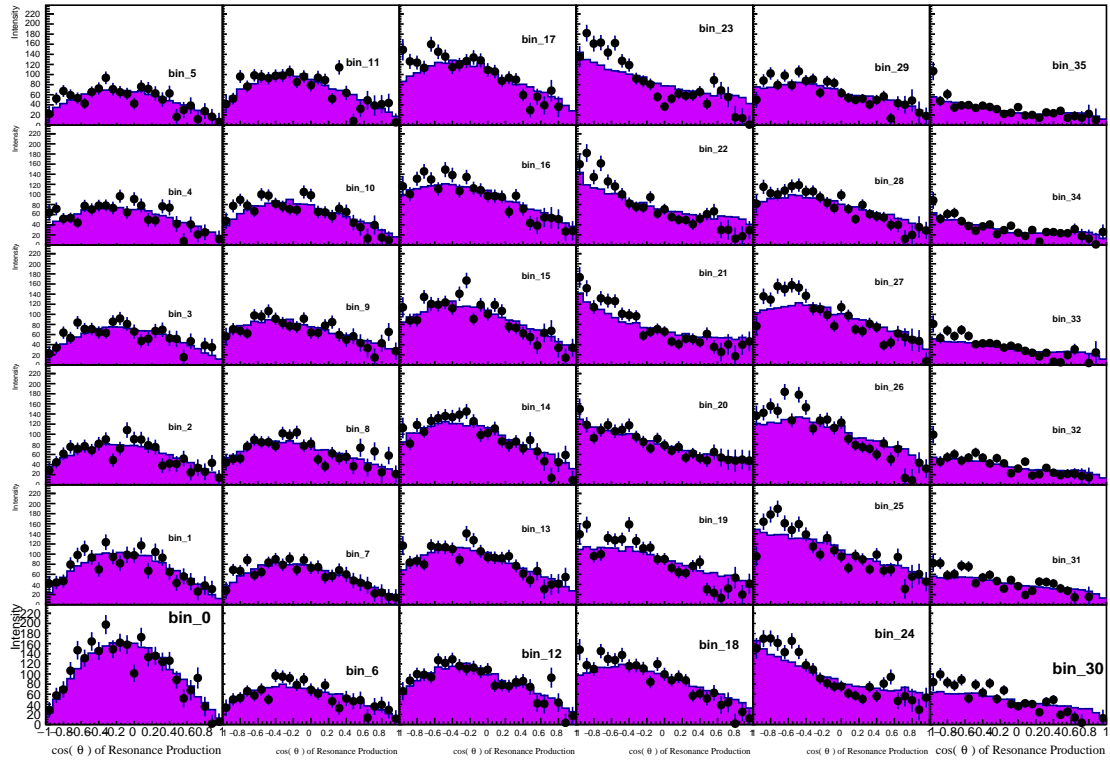


Figure D.1: Comparison of $\cos\theta$ in the helicity frame for (violet) fit to (black) data. The fit includes all $\ell = 1$ amplitudes but no $\ell = 3$ amplitudes.

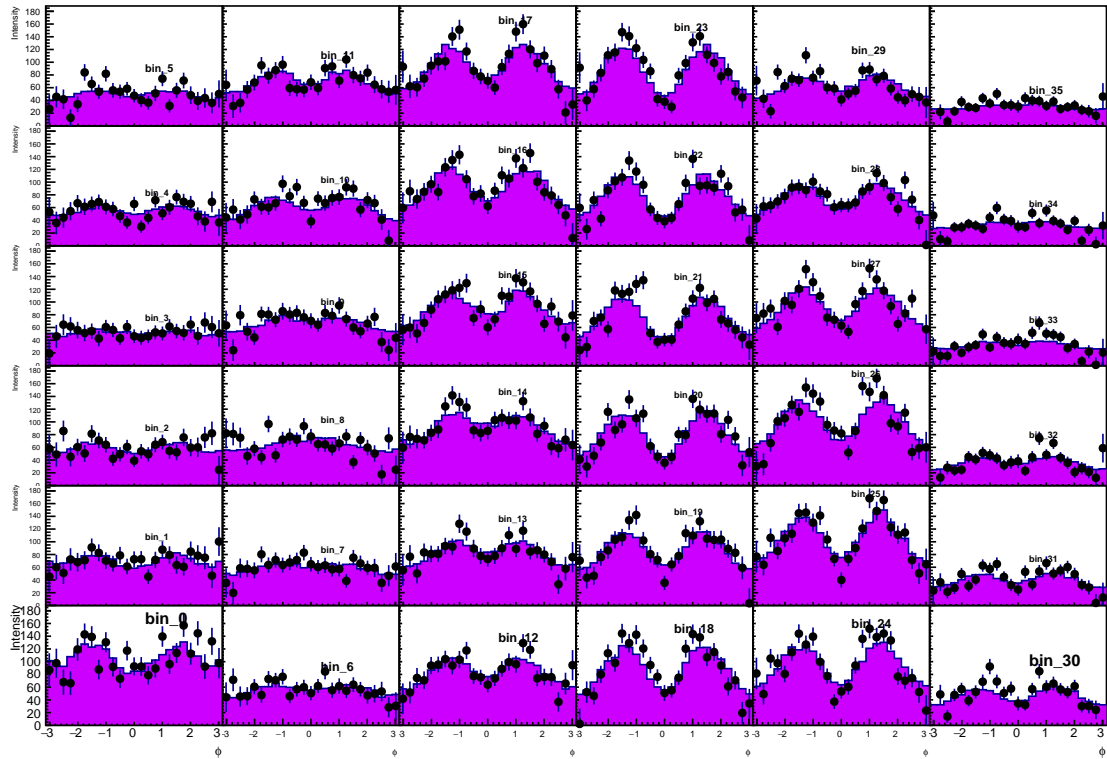


Figure D.2: Comparison of ϕ in the helicity frame for (violet) fit to (black) data. The fit includes all $\ell = 1$ amplitudes but no $\ell = 3$ amplitudes.

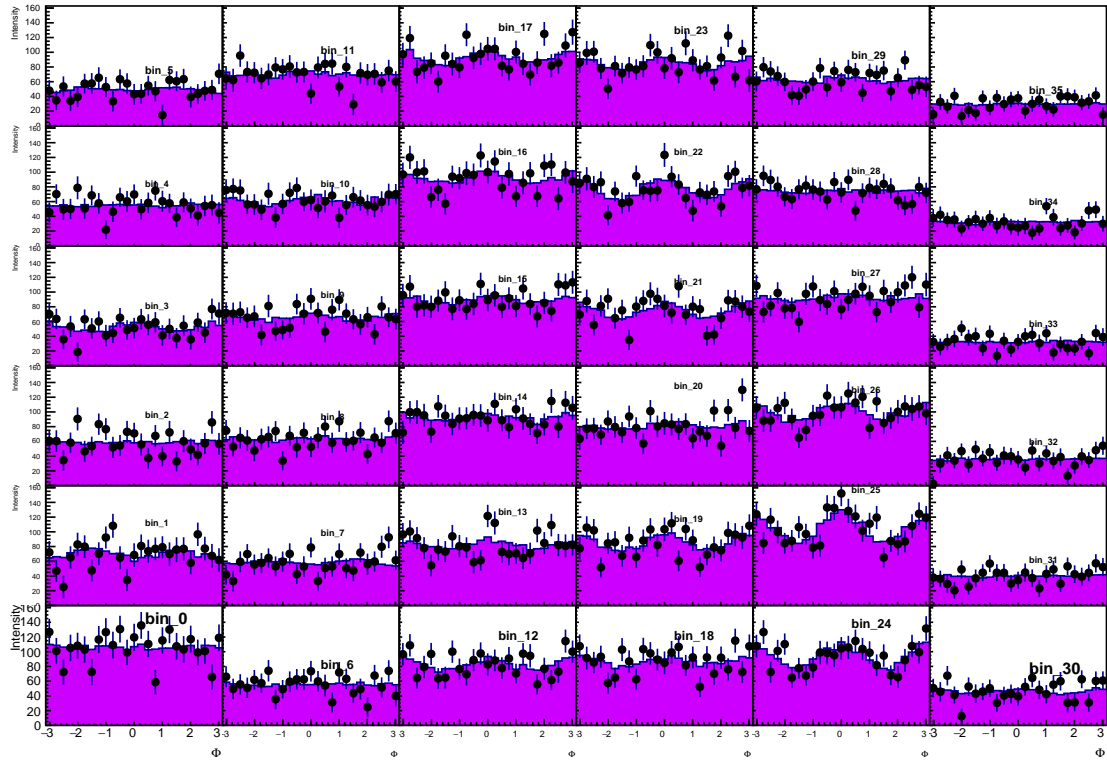


Figure D.3: Comparison of Φ in the helicity frame for (violet) fit to (black) data. The fit includes all $\ell = 1$ amplitudes but no $\ell = 3$ amplitudes.

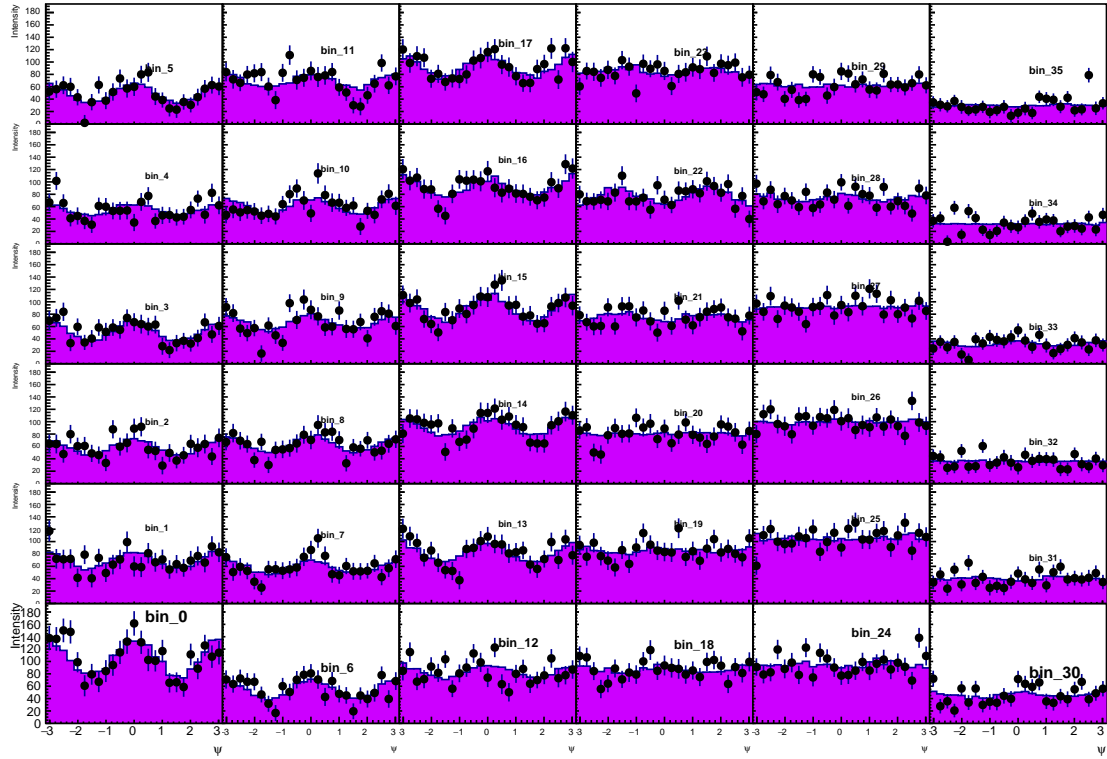


Figure D.4: Comparison of $\Psi = \phi - \Phi$ in the helicity frame for (violet) fit to (black) data. The fit includes all $\ell = 1$ amplitudes but no $\ell = 3$ amplitudes.

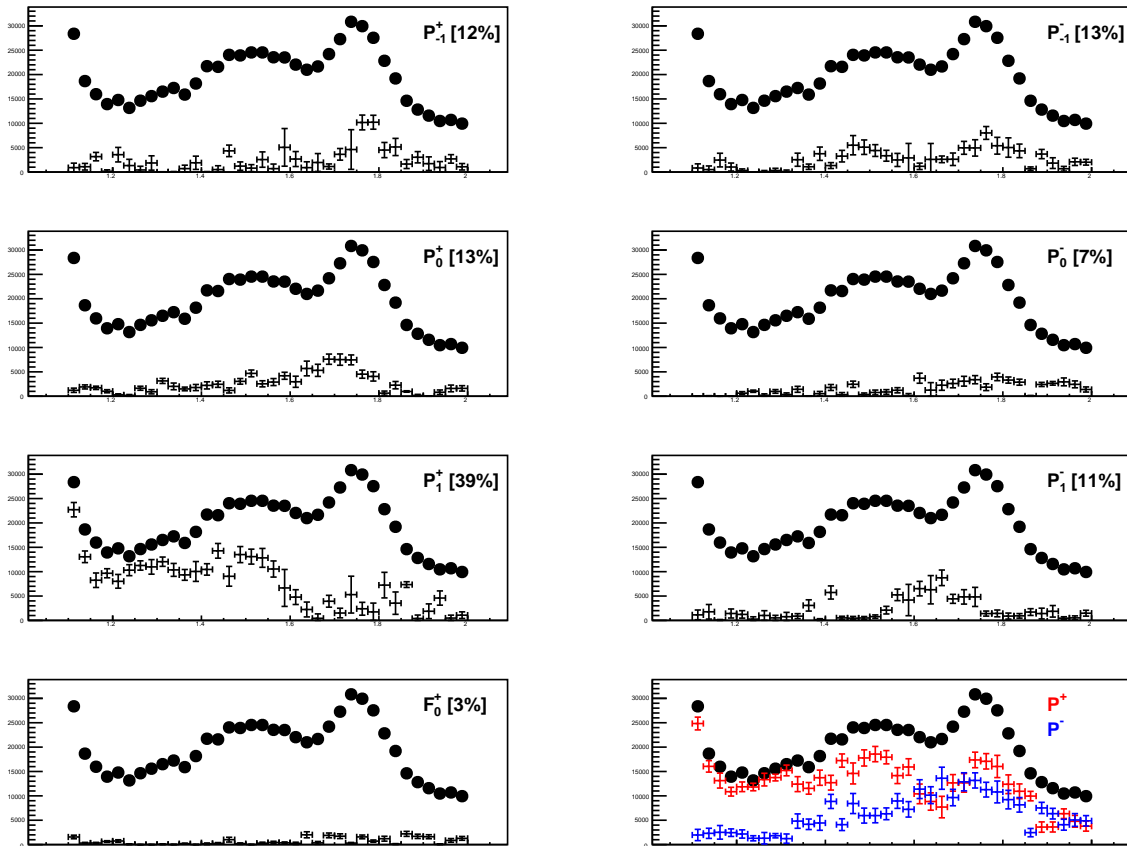


Figure D.5: Fit to data including all P-wave amplitudes and a F_0^+ amplitude. Points indicate the total intensity and crosses indicate the indicated partial wave.

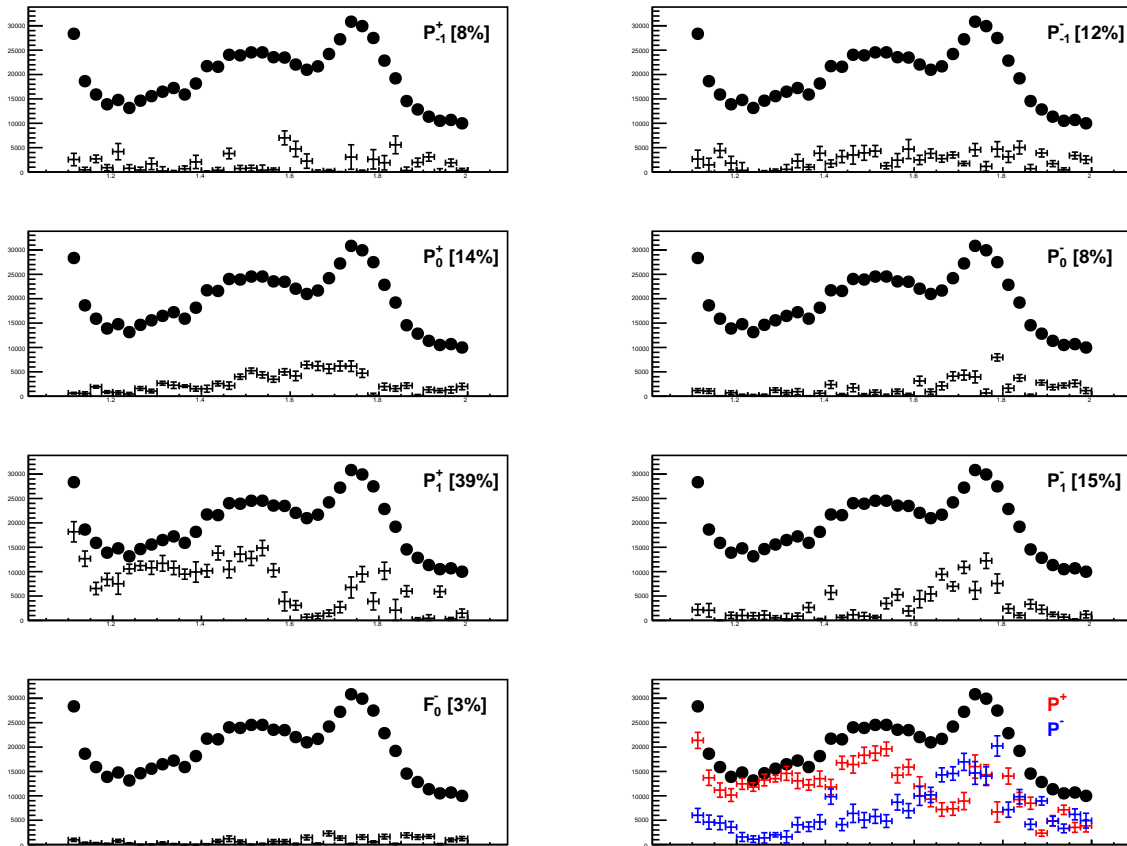


Figure D.6: Fit to data including all P-wave amplitudes and a F_0^- amplitude. Points indicate the total intensity and crosses indicate the indicated partial wave.

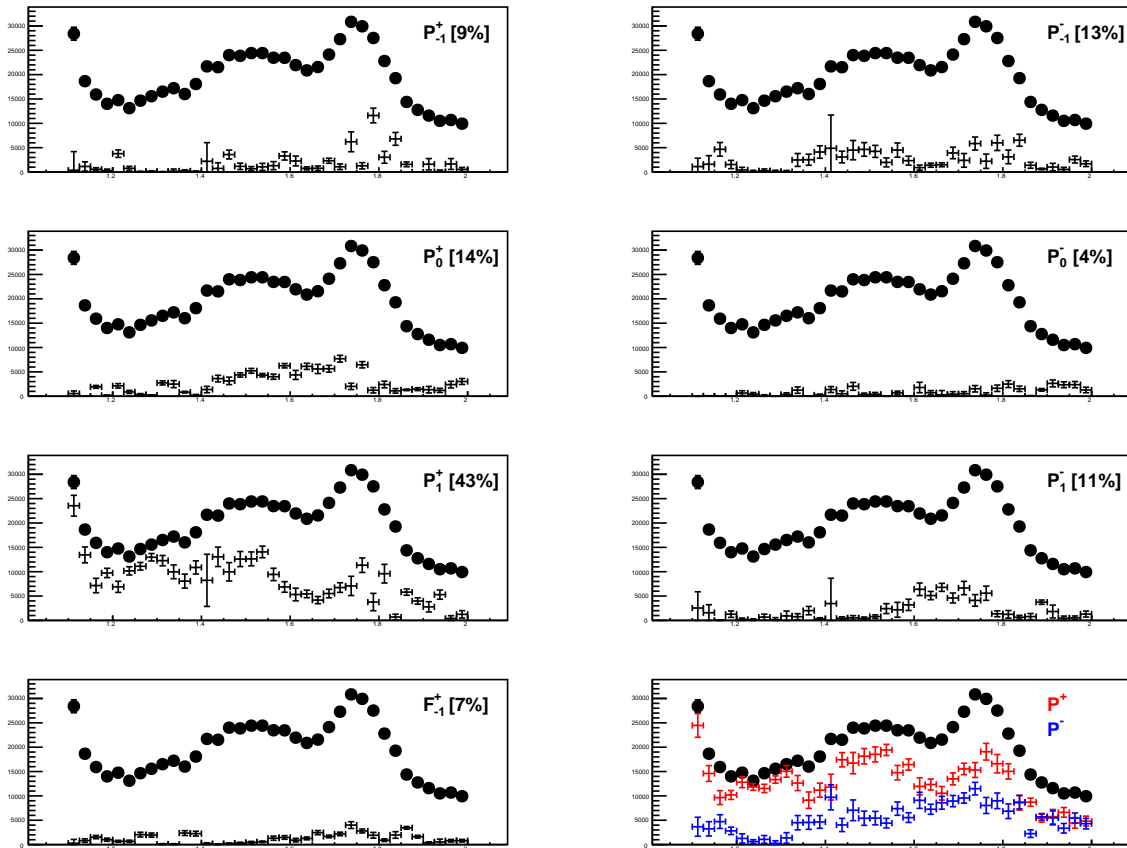


Figure D.7: Fit to data including all P-wave amplitudes and a F_{-1}^+ amplitude. Points indicate the total intensity and crosses indicate the indicated partial wave.

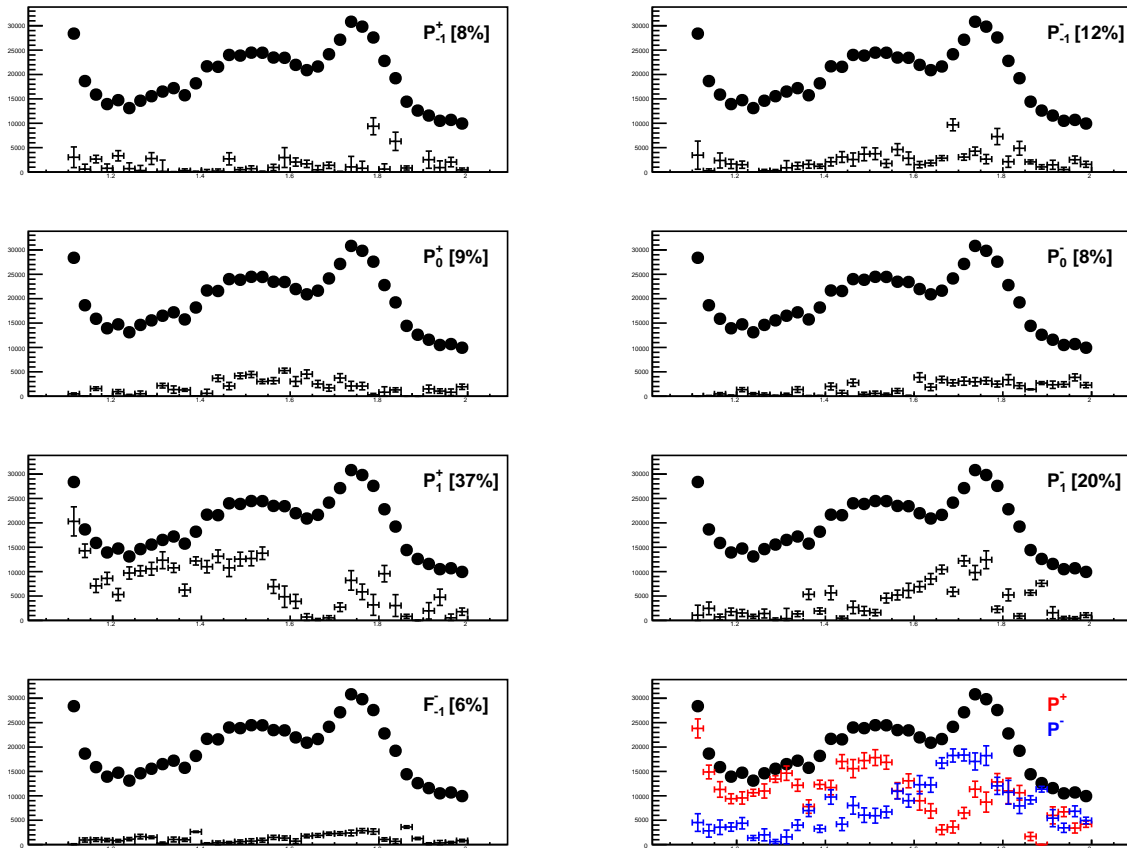


Figure D.8: Fit to data including all P-wave amplitudes and a F_{-1} amplitude. Points indicate the total intensity and crosses indicate the indicated partial wave.

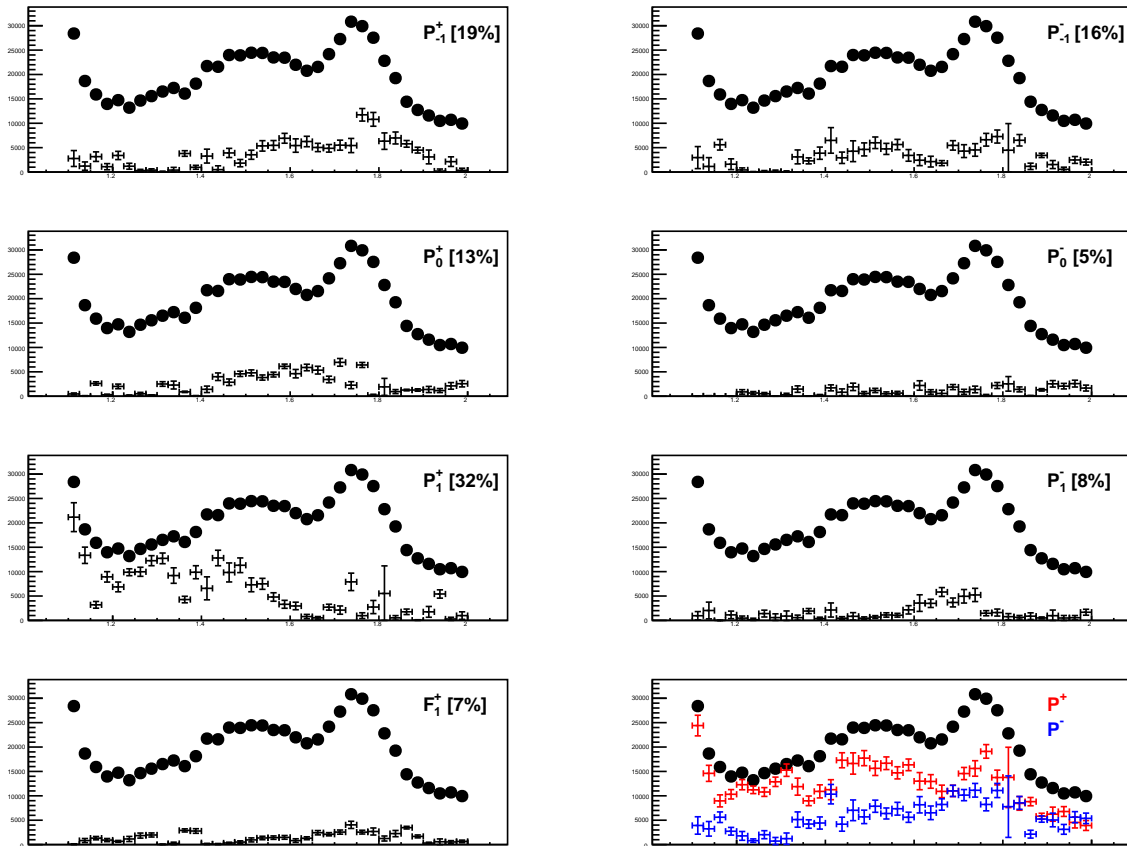


Figure D.9: Fit to data including all P-wave amplitudes and a F_1^+ amplitude. Points indicate the total intensity and crosses indicate the indicated partial wave.

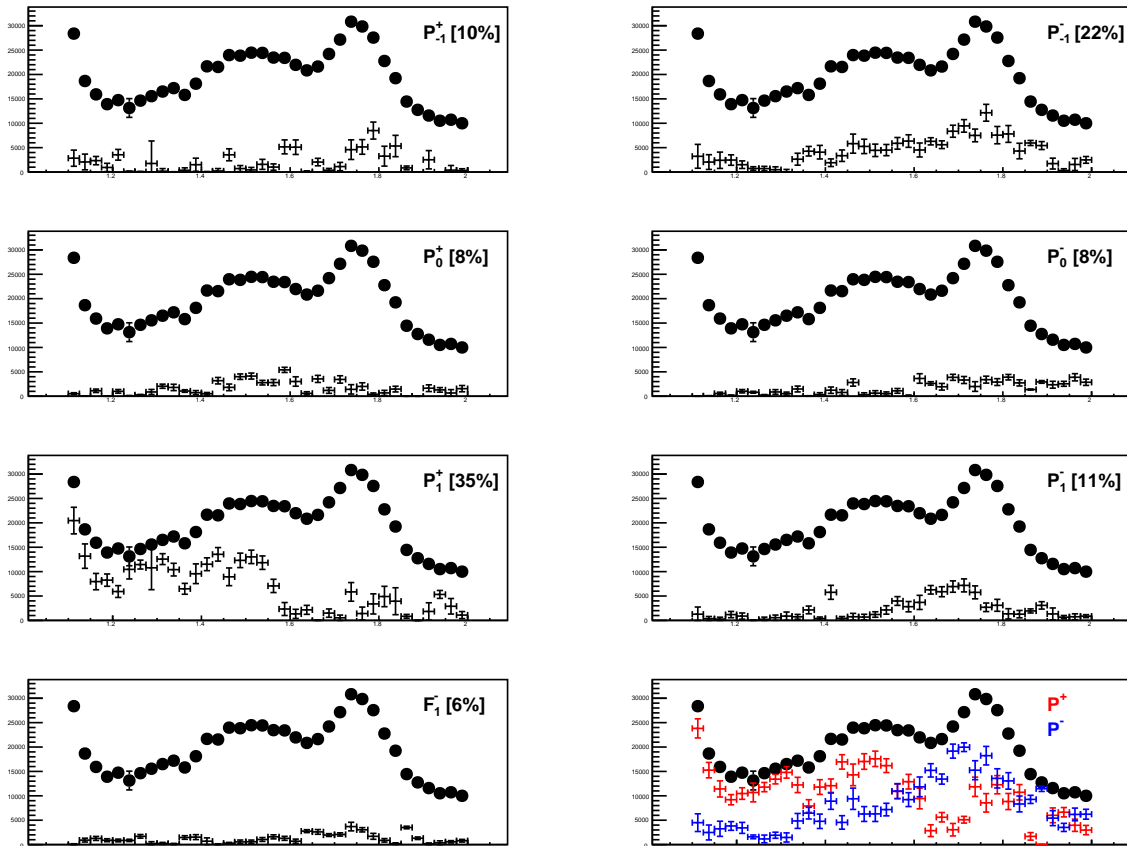


Figure D.10: Fit to data including all P-wave amplitudes and a F_1^- amplitude. Points indicate the total intensity and crosses indicate the indicated partial wave.

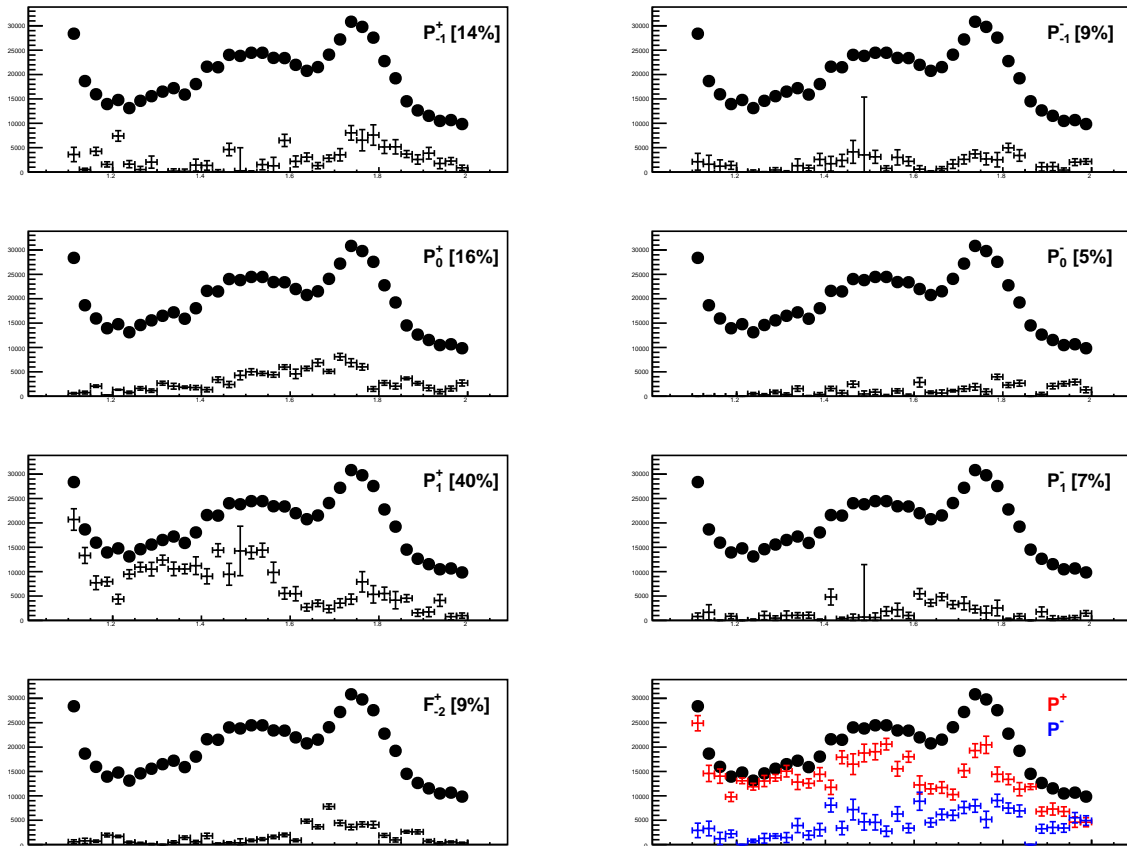


Figure D.11: Fit to data including all P-wave amplitudes and a F_2^+ amplitude. Points indicate the total intensity and crosses indicate the indicated partial wave.

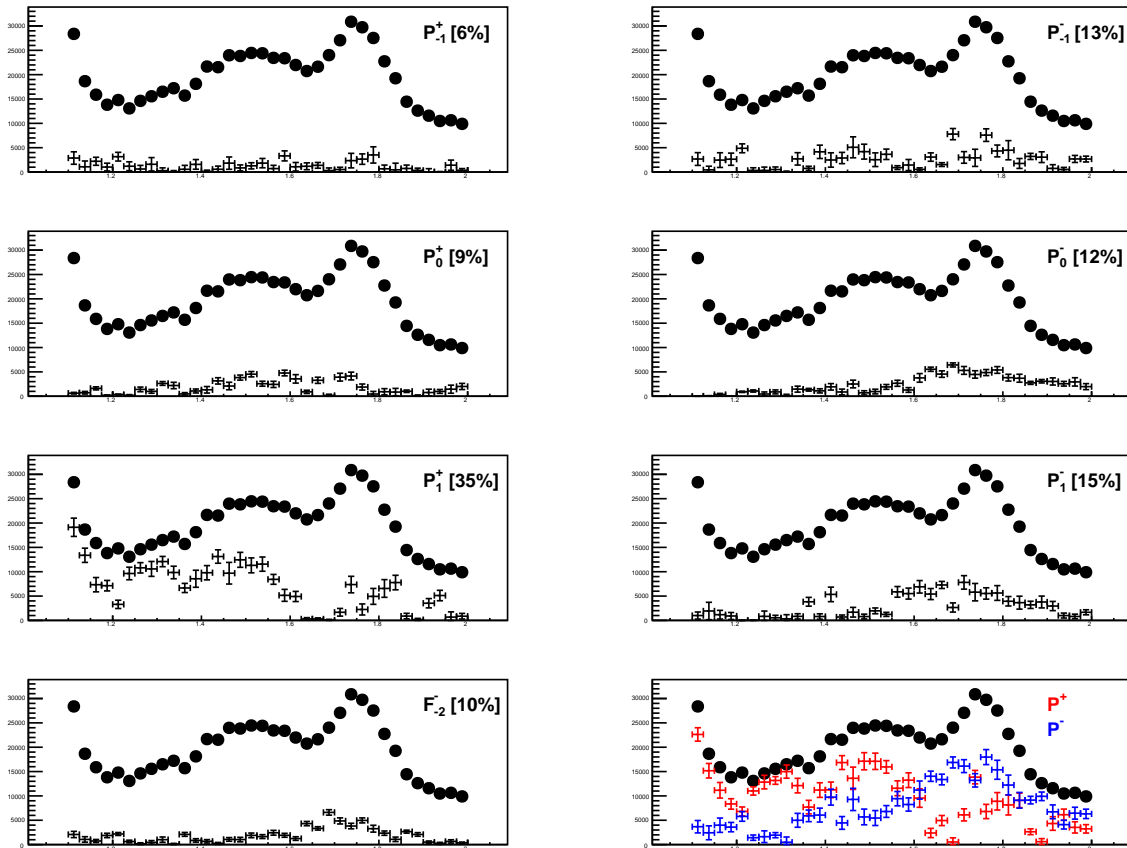


Figure D.12: Fit to data including all P-wave amplitudes and a F_{-2}^- amplitude. Points indicate the total intensity and crosses indicate the indicated partial wave.

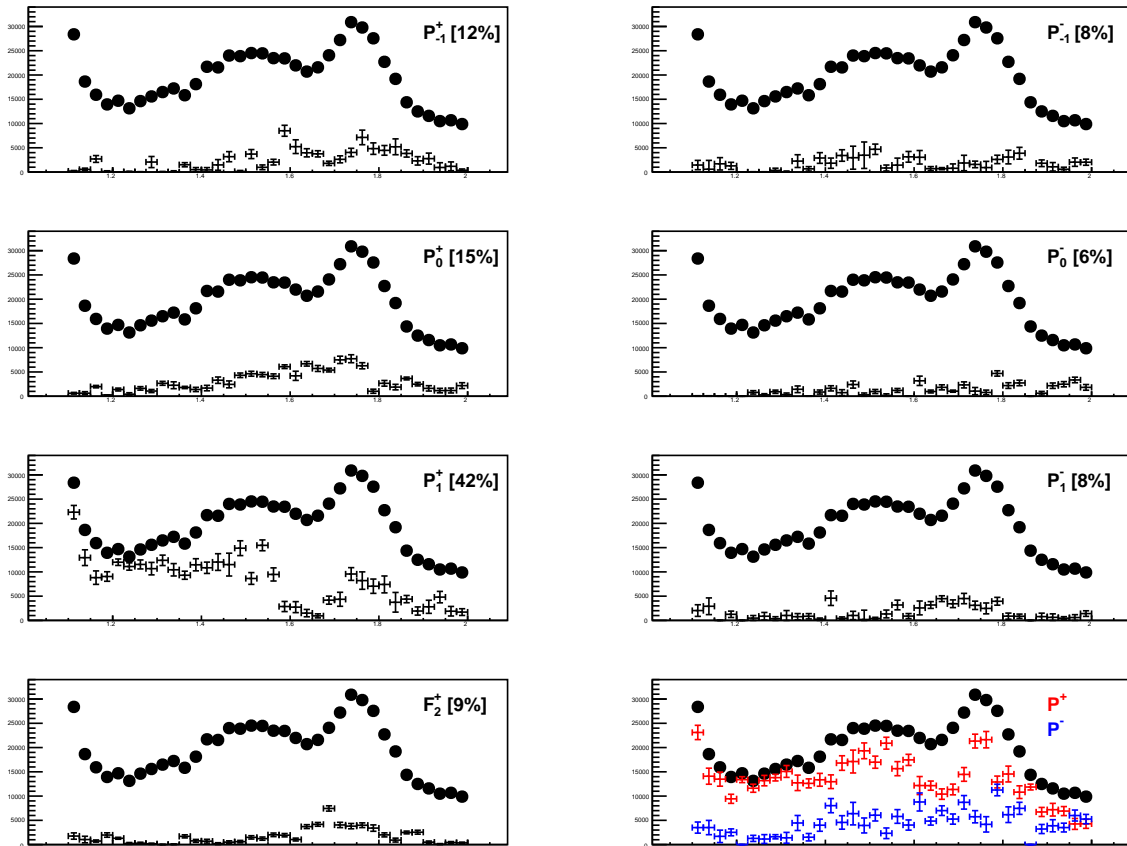


Figure D.13: Fit to data including all P-wave amplitudes and a F_2^+ amplitude. Points indicate the total intensity and crosses indicate the indicated partial wave.

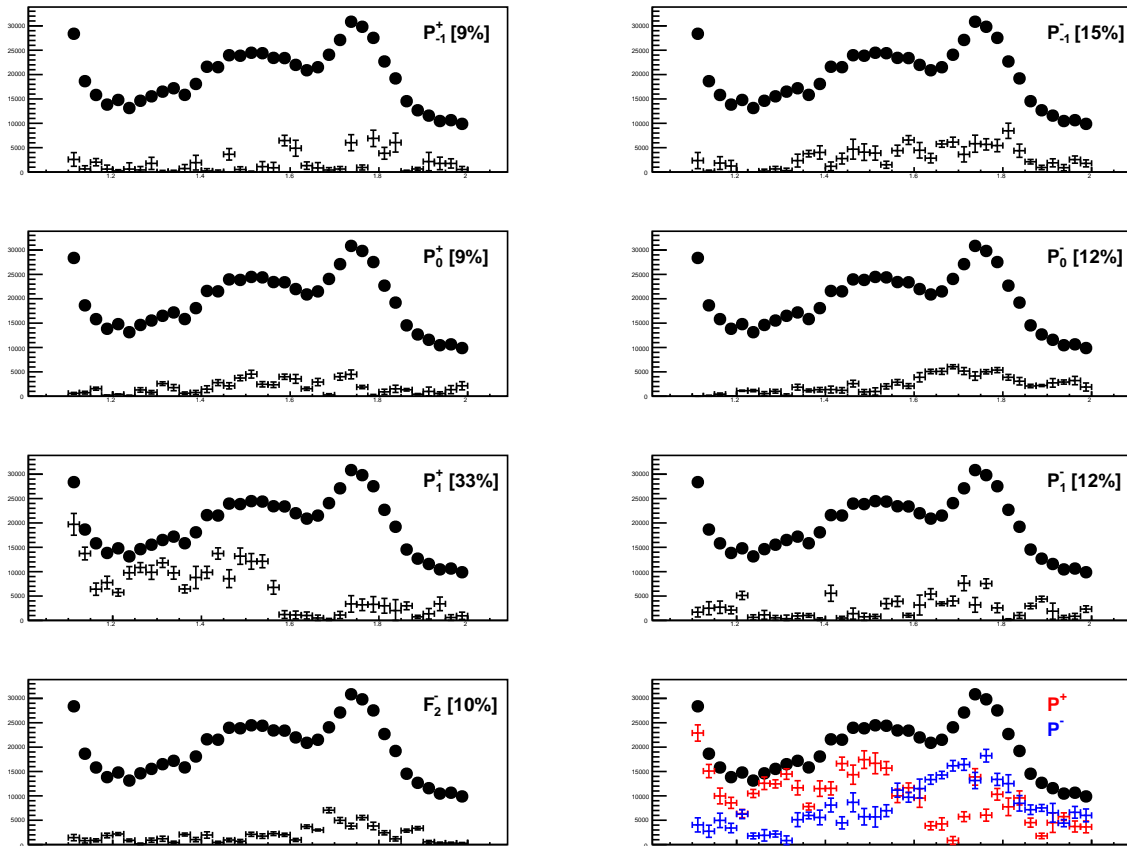


Figure D.14: Fit to data including all P-wave amplitudes and a F_2^- amplitude. Points indicate the total intensity and crosses indicate the indicated partial wave.

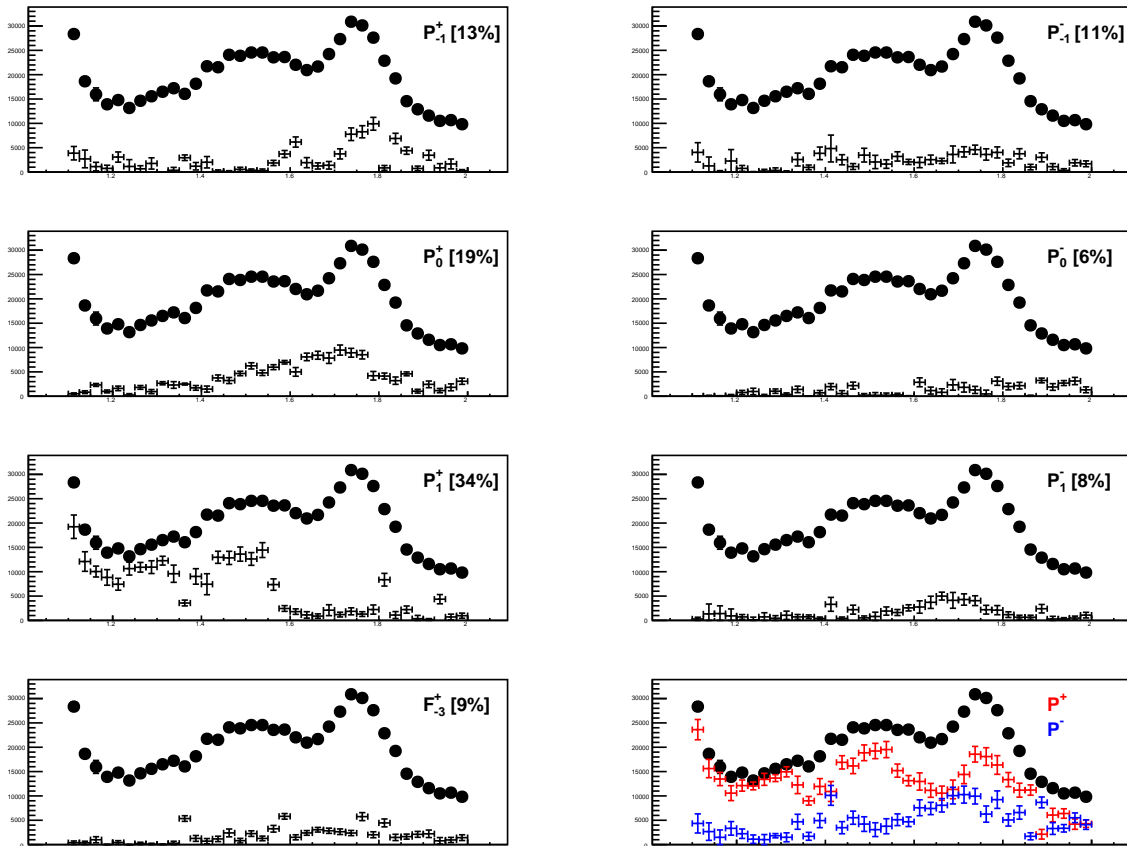


Figure D.15: Fit to data including all P-wave amplitudes and a F_3^+ amplitude. Points indicate the total intensity and crosses indicate the indicated partial wave.

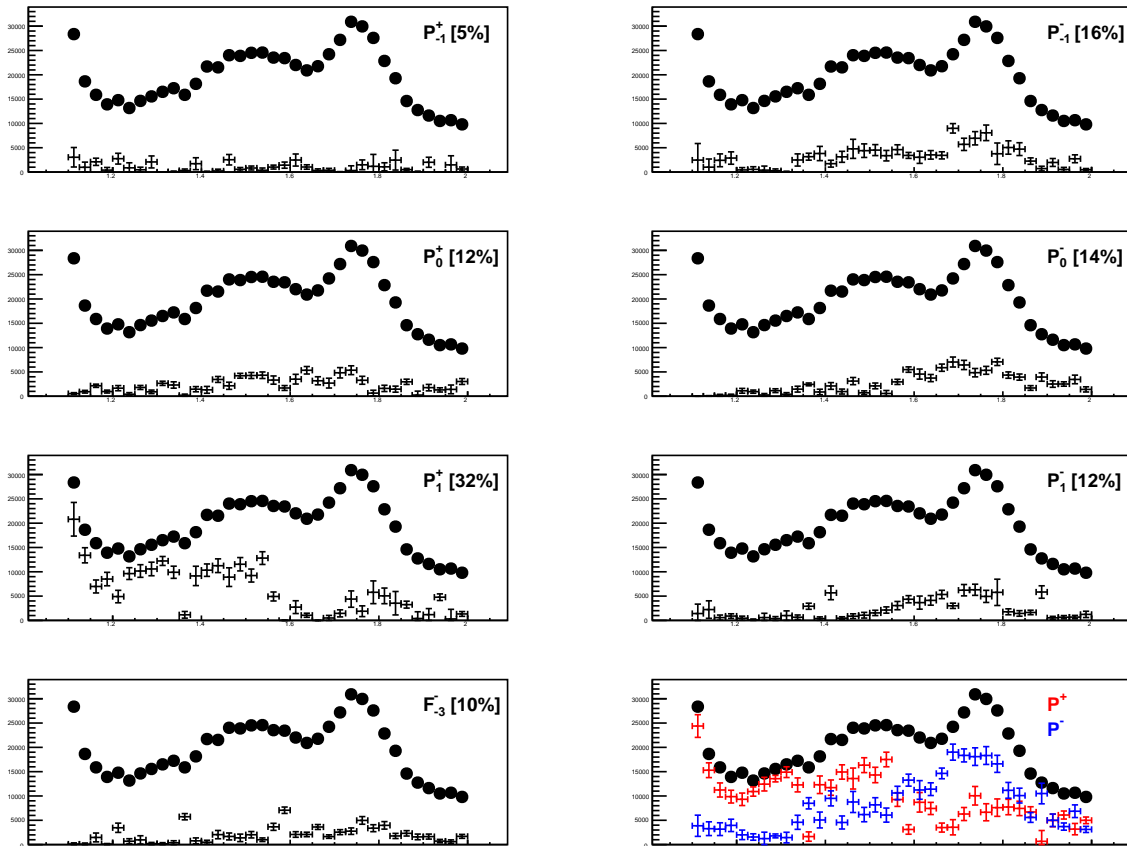


Figure D.16: Fit to data including all P-wave amplitudes and a F_{-3}^- amplitude. Points indicate the total intensity and crosses indicate the indicated partial wave.

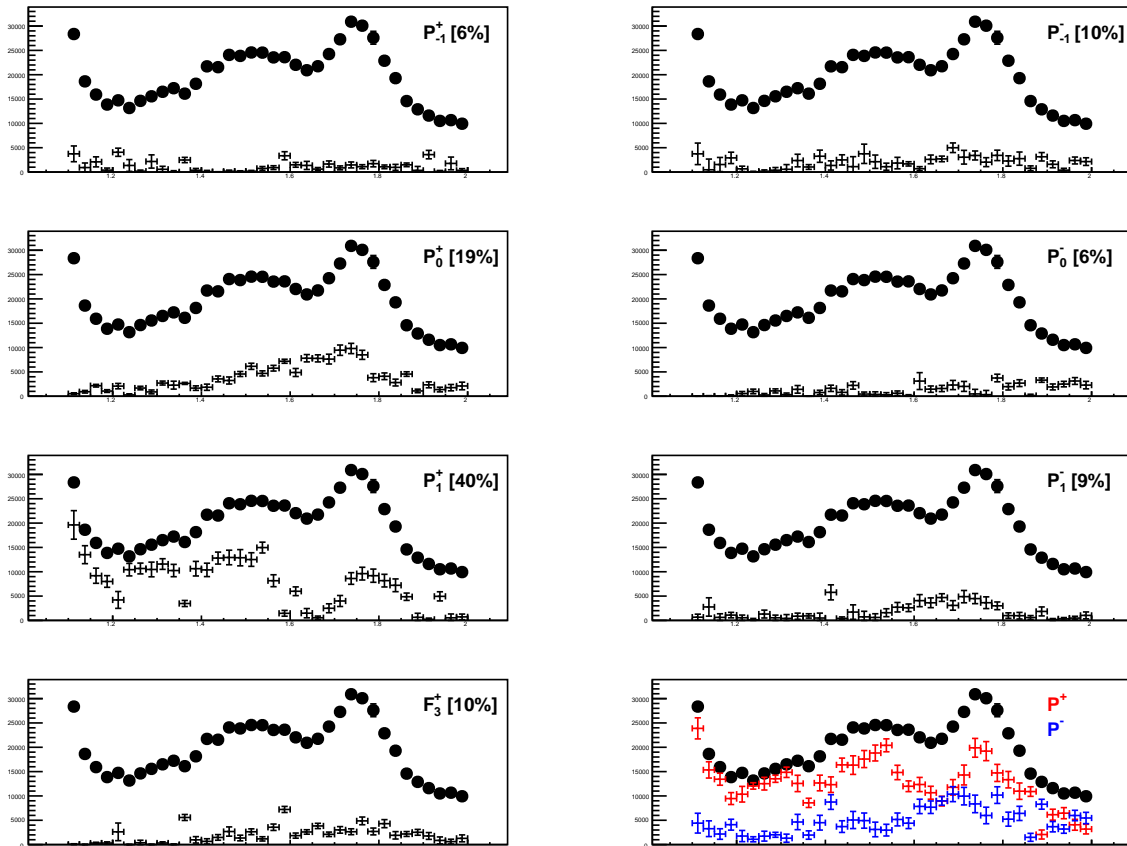


Figure D.17: Fit to data including all P-wave amplitudes and a F_3^+ amplitude. Points indicate the total intensity and crosses indicate the indicated partial wave.

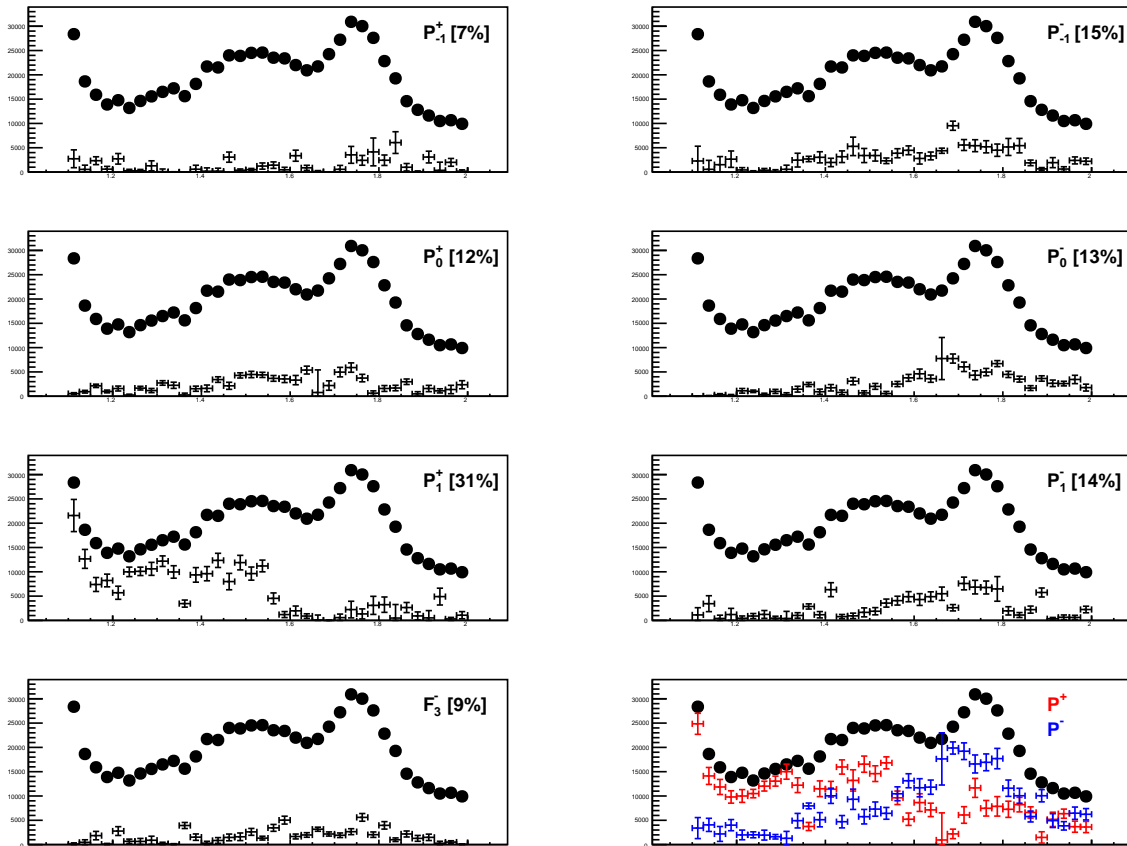


Figure D.18: Fit to data including all P-wave amplitudes and a F_3^- amplitude. Points indicate the total intensity and crosses indicate the indicated partial wave.

REFERENCES

- [1] J. Ballam *et al.*, “Vector Meson Production by Polarized Photons at 2.8-GeV, 4.7-GeV, and 9.3-GeV,” *Phys. Rev. D*, vol. 7, p. 3150, 1973.
- [2] M. Atkinson *et al.*, “Photoproduction of ϕ Mesons by Linearly Polarized Photons of Energy 20-GeV to 40-GeV and Further Evidence for a Photoproduced High Mass KK Enhancement,” *Z. Phys. C*, vol. 27, p. 233, 1985.
- [3] M. e. a. Tanabashi, “Review of particle physics,” *Phys. Rev. D*, vol. 98, p. 030001, Aug 2018.
- [4] M. Ablikim *et al.*, “Measurement of $e^+e^- \rightarrow K^+K^-$ cross section at $\sqrt{s} = 2.00 - 3.08$ GeV,” *Phys. Rev. D*, vol. 99, no. 3, p. 032001, 2019.
- [5] M. Ablikim *et al.*, “Cross section measurement of $e^+e^- \rightarrow K_S^0 K_L^0$ at $\sqrt{s} = 2.00 - 3.08$ GeV,” *Phys. Rev. D*, vol. 104, no. 9, p. 092014, 2021.
- [6] P. A. Z. et al., “Review of Particle Physics,”
- [7] B. Ketzer, B. Grube, and D. Ryabchikov, “Light-Meson Spectroscopy with COMPASS,” *Prog. Part. Nucl. Phys.*, vol. 113, p. 103755, 2020.
- [8] J. J. Dudek, R. G. Edwards, P. Guo, and C. E. Thomas, “Toward the excited isoscalar meson spectrum from lattice QCD,” *Phys. Rev.*, vol. D88, no. 9, p. 094505, 2013.
- [9] D. Vadacchino, “A review on Glueball hunting,” in *39th International Symposium on Lattice Field Theory*, 5 2023.
- [10] A. Rodas *et al.*, “Determination of the pole position of the lightest hybrid meson candidate,” *Phys. Rev. Lett.*, vol. 122, no. 4, p. 042002, 2019.
- [11] C. Adolph *et al.*, “Odd and even partial waves of $\eta\pi^-$ and $\eta'\pi^-$ in $\pi^-p \rightarrow \eta^{(\prime)}\pi^-p$ at 191 GeV/c,” *Phys. Lett. B*, vol. 740, pp. 303–311, 2015. [Erratum: *Phys.Lett.B* 811, 135913 (2020)].
- [12] M. Ablikim *et al.*, “Observation of an Isoscalar Resonance with Exotic $JPC=1-+$ Quantum Numbers in $J/\psi\gamma\eta\eta'$,” *Phys. Rev. Lett.*, vol. 129, no. 19, p. 192002, 2022. [Erratum: *Phys.Rev.Lett.* 130, 159901 (2023)].
- [13] R. Gannouji, “Introduction to Electroweak Baryogenesis,” *Galaxies*, vol. 10, no. 6, p. 116, 2022.

- [14] W. C. Chang *et al.*, “Measurement of Spin-Density Matrix Elements for ϕ -Meson Photoproduction from Protons and Deuterons Near Threshold,” *Phys. Rev. C*, vol. 82, p. 015205, 2010.
- [15] K. Mizutani *et al.*, “ ϕ photoproduction on the proton at $E_\gamma = 1.5 - 2.9$ GeV,” *Phys. Rev. C*, vol. 96, no. 6, p. 062201, 2017.
- [16] L. Clark, *Hadron spectroscopy of pseudoscalar and vector meson photoproduction using linearly polarised photons at CLAS*. PhD thesis, Glasgow U., 2022.
- [17] J. P. Lees *et al.*, “Cross sections for the reactions $e^+e^- \rightarrow K_S^0 K_L^0$, $K_S^0 K_L^0 \pi^+ \pi^-$, $K_S^0 K_S^0 \pi^+ \pi^-$, and $K_S^0 K_S^0 K^+ K^-$ from events with initial-state radiation,” *Phys. Rev. D*, vol. 89, no. 9, p. 092002, 2014.
- [18] J. Busenitz *et al.*, “High-energy Photoproduction of $\pi^+ \pi^- \pi^0$, $K^+ K^-$, and $P\bar{P}$ States,” *Phys. Rev. D*, vol. 40, pp. 1–21, 1989.
- [19] J. M. Link *et al.*, “Observation of a $1750 - MeV/c^2$ Enhancement in the Diffractive Photoproduction of $K^+ K^-$,” *Phys. Lett. B*, vol. 545, pp. 50–56, 2002.
- [20] J. P. Lees *et al.*, “Cross Sections for the Reactions $e^+e^- \rightarrow K^+ K^- \pi^+ \pi^-$, $K^+ K^- \pi^0 \pi^0$, and $K^+ K^- K^+ K^-$ Measured Using Initial-State Radiation Events,” *Phys. Rev. D*, vol. 86, p. 012008, 2012.
- [21] K. Götzen and e. a. Frank Nerling, “Measurement of the phi pi pi production cross section and search for resonances in phi pi pi ,”
- [22] S. Chandavar *et al.*, “Double K_S^0 Photoproduction off the Proton at CLAS,” *Phys. Rev.*, vol. C97, no. 2, 2018.
- [23] S. Chekanov *et al.*, “Inclusive $K_S^0 K_S^0$ resonance production in ep collisions at hermes,” *Phys. Rev. Lett.*, vol. 101, p. 112003, Sep 2008.
- [24] M. Ablikim *et al.*, “Amplitude analysis of the $K_S K_S$ system produced in radiative J/ψ decays,” *Phys. Rev. D*, vol. 98, no. 7, p. 072003, 2018.
- [25] A. Rodas, A. Pilloni, M. Albaladejo, C. Fernandez-Ramirez, V. Mathieu, and A. P. Szczepaniak, “Scalar and tensor resonances in J/ψ radiative decays,” 9 2021.
- [26] M. Ablikim *et al.*, “Amplitude analysis of the $\pi^0 \pi^0$ system produced in radiative J/ψ decays,” *Phys. Rev. D*, vol. 92, no. 5, p. 052003, 2015. [Erratum: *Phys.Rev.D* 93, 039906 (2016)].
- [27] F. Barbosa, C. Hutton, A. Sitnikov, A. Somov, S. Somov, and I. Tolstukhin, “Pair spectrometer hodoscope for hall d at jefferson lab,” *Nuclear Instruments and Methods in Physics Research Section A: Accelerators, Spectrometers, Detectors and Associated Equipment*, vol. 795, pp. 376–380, 2015.

- [28] N. Jarvis, C. Meyer, B. Zihlmann, M. Staib, A. Austregesilo, F. Barbosa, C. Dickover, V. Razmyslovich, S. Taylor, Y. V. Haarlem, G. Visser, and T. Whitlatch, “The central drift chamber for GlueX,” *Nuclear Instruments and Methods in Physics Research Section A: Accelerators, Spectrometers, Detectors and Associated Equipment*, vol. 962, p. 163727, may 2020.
- [29] T. Beattie, A. Foda, C. Henschel, S. Katsaganis, S. Krueger, G. Lolos, Z. Papandreou, E. Plummer, I. Semenova, A. Semenov, F. Barbosa, E. Chudakov, M. Dalton, D. Lawrence, Y. Qiang, N. Sandoval, E. Smith, C. Stanislav, J. Stevens, S. Taylor, T. Whitlatch, B. Zihlmann, W. Levine, W. McGinley, C. Meyer, M. Staib, E. Anassontzis, C. Kourkoumelis, G. Vasileiadis, G. Voulgaris, W. Brooks, H. Hakobyan, S. Kuleshov, R. Rojas, C. Romero, O. Soto, A. Toro, I. Vega, and M. Shepherd, “Construction and performance of the barrel electromagnetic calorimeter for the GlueX experiment,” *Nuclear Instruments and Methods in Physics Research Section A: Accelerators, Spectrometers, Detectors and Associated Equipment*, vol. 896, pp. 24–42, jul 2018.
- [30] E. Pooser, F. Barbosa, W. Boeglin, C. Hutton, M. Ito, M. Kamel, P. Khetarpal, A. LLodra, N. Sandoval, S. Taylor, T. Whitlatch, S. Worthington, C. Yero, and B. Zihlmann, “The GlueX start counter detector,” *Nuclear Instruments and Methods in Physics Research Section A: Accelerators, Spectrometers, Detectors and Associated Equipment*, vol. 927, pp. 330–342, may 2019.
- [31] A. Ali, F. Barbosa, J. Bessuille, E. Chudakov, R. Dzhygadlo, C. Fanelli, J. Frye, J. Hardin, A. Hurley, G. Kalicy, J. Kelsey, W. Li, M. Patsyuk, C. Schwarz, J. Schwiening, M. Shepherd, J. Stevens, T. Whitlatch, M. Williams, and Y. Yang, “The GLUEX DIRC program,” *Journal of Instrumentation*, vol. 15, pp. C04054–C04054, apr 2020.
- [32] A. Ali, F. Barbosa, J. Bessuille, E. Chudakov, R. Dzhygadlo, C. Fanelli, J. Frye, J. Hardin, A. Hurley, E. Ihloff, G. Kalicy, J. Kelsey, W. B. Li, M. Patsyuk, J. Schwiening, M. Shepherd, J. R. Stevens, T. Whitlatch, M. Williams, and Y. Yang, “Initial performance of the GlueX DIRC detector,” *Journal of Physics: Conference Series*, vol. 2374, p. 012009, nov 2022.
- [33] S. Adhikari *et al.*, “The GLUEX beamline and detector,” *Nucl. Instrum. Meth. A*, vol. 987, p. 164807, 2021.
- [34] V. Mathieu, M. Albaladejo, C. Fernández-Ramírez, A. Jackura, M. Mikhasenko, A. Pilloni, and A. Szczepaniak, “Moments of angular distribution and beam asymmetries in 0 photoproduction at glueX,” *Physical Review D*, vol. 100, Sep 2019.
- [35] V. Mathieu, J. Nys, C. Fernández-Ramírez, A. Jackura, A. Pilloni, N. Sherrill, A. P. Szczepaniak, and G. Fox, “Vector Meson Photoproduction with a Linearly Polarized Beam,” *Phys. Rev. D*, vol. 97, no. 9, p. 094003, 2018.
- [36] C. D. Roberts, “Hadron Physics and QCD: Just the Basic Facts,” *J. Phys. Conf. Ser.*, vol. 630, no. 1, p. 012051, 2015.

- [37] A. Deur, S. J. Brodsky, and G. F. de Teramond, “The QCD Running Coupling,” *Nucl. Phys.*, vol. 90, p. 1, 2016.
- [38] N. Brambilla and A. Vairo, “Quark confinement and the hadron spectrum,” in *13th Annual HUGS AT CEBAF*, pp. 151–220, 5 1999.
- [39] M. Gell-Mann, “A schematic model of baryons and mesons,” *Physics Letters*, vol. 8, no. 3, pp. 214 – 215, 1964.
- [40] G. Zweig, “An SU_3 model for strong interaction symmetry and its breaking,” 1964.
- [41] C. A. Meyer, “Light and exotic mesons,” 2001.
- [42] F. Gross *et al.*, “50 Years of Quantum Chromodynamics,” *Eur. Phys. J. C*, vol. 83, p. 1125, 2023.
- [43] C. J. Morningstar and M. J. Peardon, “The Glueball spectrum from an anisotropic lattice study,” *Phys. Rev. D*, vol. 60, p. 034509, 1999.
- [44] V. Crede and C. Meyer, “The Experimental Status of Glueballs,” *Prog. Part. Nucl. Phys.*, vol. 63, pp. 74–116, 2009.
- [45] S. Godfrey and J. Napolitano, “Light meson spectroscopy,” *Rev. Mod. Phys.*, vol. 71, pp. 1411–1462, 1999.
- [46] G. F. Chew and S. C. Frautschi, “Regge Trajectories and the Principle of Maximum Strength for Strong Interactions,” *Phys. Rev. Lett.*, vol. 8, pp. 41–44, 1962.
- [47] M. Thomson, *Modern particle physics*. New York: Cambridge University Press, 2013.
- [48] L. R. Dai, E. Oset, and L. S. Geng, “The $D_s^+ \rightarrow \pi^+ K_S^0 K_S^0$ reaction and the $I = 1$ partner of the $f_0(1710)$ state,” *Eur. Phys. J. C*, vol. 82, no. 3, p. 225, 2022.
- [49] T. Mibe, W. C. Chang, T. Nakano, D. S. Ahn, J. K. Ahn, H. Akimune, Y. Asano, S. Daté, H. Ejiri, H. Fujimura, M. Fujiwara, K. Hicks, T. Hotta, K. Imai, T. Ishikawa, T. Iwata, H. Kawai, Z. Y. Kim, K. Kino, H. Kohri, N. Kumagai, S. Makino, T. Matsuda, T. Matsumura, N. Matsuoka, K. Miwa, M. Miyabe, Y. Miyachi, M. Morita, N. Muramatsu, M. Niiyama, M. Nomachi, Y. Ohashi, T. Ooba, H. Ohkuma, D. S. Oshuev, C. Rangacharyulu, A. Sakaguchi, T. Sasaki, P. M. Shagin, Y. Shiino, H. Shimizu, Y. Sugaya, M. Sumihama, A. I. Titov, Y. Toi, H. Toyokawa, A. Wakai, C. W. Wang, S. C. Wang, K. Yonehara, T. Yorita, M. Yoshimura, M. Yosoi, and R. G. T. Zegers, “Near-threshold diffractive ϕ -meson photoproduction from the proton,” *Phys. Rev. Lett.*, vol. 95, p. 182001, Oct 2005.

- [50] B. Dey, C. A. Meyer, M. Bellis, M. Williams, K. P. Adhikari, D. Adikaram, M. Aghasyan, M. J. Amaryan, M. D. Anderson, S. Anefalos Pereira, J. Ball, N. A. Baltzell, M. Battaglieri, I. Bedlinskiy, A. S. Biselli, J. Bono, S. Boiarinov, W. J. Briscoe, W. K. Brooks, V. D. Burkert, D. S. Carman, A. Celentano, S. Chandavar, L. Colaneri, P. L. Cole, M. Contalbrigo, O. Cortes, V. Crede, A. D’Angelo, N. Dashyan, R. De Vita, E. De Sanctis, A. Deur, C. Djalali, D. Doughty, M. Dugger, R. Dupre, A. El Alaoui, L. El Fassi, L. Elouadrhiri, G. Fedotov, S. Fegan, J. A. Fleming, M. Garçon, N. Gevorgyan, Y. Ghandilyan, G. P. Gilfoyle, K. L. Giovanetti, F. X. Girod, D. I. Glazier, J. T. Goetz, R. W. Gothe, K. A. Griffioen, M. Guidal, K. Hafidi, C. Hanretty, N. Harrison, M. Hattawy, K. Hicks, D. Ho, M. Holtrop, C. E. Hyde, Y. Ilieva, D. G. Ireland, B. S. Ishkhanov, D. Jenkins, H. S. Jo, K. Joo, D. Keller, M. Khandaker, A. Kim, W. Kim, A. Klein, F. J. Klein, S. Koirala, V. Kubarovsky, S. E. Kuhn, S. V. Kuleshov, P. Lenisa, K. Livingston, H. Lu, I. J. D. MacGregor, N. Markov, M. Mayer, M. E. McCracken, B. McKinnon, T. Mineeva, M. Mirazita, V. Mokeev, R. A. Montgomery, K. Moriya, H. Moutarde, E. Munevar, C. Munoz Camacho, P. Nadel-Turonski, S. Niccolai, G. Niculescu, I. Niculescu, M. Osipenko, L. L. Pappalardo, R. Paremuzyan, K. Park, E. Pasyuk, P. Peng, J. J. Phillips, S. Pisano, O. Pogorelko, S. Pozdniakov, J. W. Price, S. Procureur, D. Protopopescu, A. J. R. Puckett, D. Rimal, M. Ripani, B. G. Ritchie, A. Rizzo, P. Rossi, P. Roy, F. Sabatié, M. S. Saini, D. Schott, R. A. Schumacher, E. Seder, I. Senderovich, Y. G. Sharabian, A. Simonyan, E. S. Smith, D. I. Sober, D. Sokhan, S. S. Stepanyan, P. Stoler, I. I. Strakovsky, S. Strauch, V. Sytnik, M. Taiuti, W. Tang, S. Tkachenko, M. Ungaro, B. Vernarsky, A. V. Vlassov, H. Voskanyan, E. Voutier, N. K. Walford, D. P. Watts, N. Zachariou, L. Zana, J. Zhang, Z. W. Zhao, and I. Zonta, “Data analysis techniques, differential cross sections, and spin density matrix elements for the reaction $\gamma p \rightarrow \phi p$,” *Phys. Rev. C*, vol. 89, p. 055208, May 2014.
- [51] D. Aston, M. Atkinson, R. Bailey, A. Ball, B. Bouquet, G. Brookes, J. Bröring, P. Bussey, D. Clarke, A. Clegg, D. D’Almagne, G. De Rosny, B. Diekmann, M. Draper, B. Drevillon, I. Duerdoth, J.-P. Dufey, R. Ellison, D. Ezra, P. Feller, A. Ferrer, P. Flynn, F. Friese, W. Galbraith, R. George, S. Gill, M. Goldberg, S. Goodman, W. Graves, B. Grossetête, P. Hampson, K. Heinloth, R. Hughes-Jones, J. Hutton, M. Ibbotson, M. Jung, S. Katsanevas, M. Kemp, F. Kovacs, B. Kumar, G. Lafferty, J. Lane, J.-M. Levy, V. Liebenau, J. Litt, G. London, D. Mercer, J. Morris, K. Müller, D. Newton, E. Paul, P. Petroff, Y. Pons, C. Raine, F. Richard, R. Richter, J. Roberts, P. Roudeau, A. Rougé, M. Rumpf, M. Sené, J. Six, I. Skillicorn, J. Sleeman, K. Smith, C. Steinhauer, K. Storr, R. Thompson, D. Treille, C. De La Vaissière, H. Videau, I. Videau, A. Waite, A. Wijangco, W. Wojcik, J.-P. Wuthrick, and T. Yiou, “Photoproduction of $k+k$ pairs on hydrogen at photon energies of 20 to 36 gev,” *Nuclear Physics B*, vol. 172, pp. 1–12, 1980.

- [52] R. Akhmetshin, V. Aulchenko, V. Banzarov, L. Barkov, S. Baru, N. Bashtovoy, A. Bondar, D. Bondarev, A. Bragin, S. Dhawan, S. Eidelman, D. Epifanov, G. Fedotovitch, N. Gabyshev, D. Gorbachev, A. Grebeniuk, D. Grigoriev, V. Hughes, F. Ignatov, S. Karpov, V. Kazanin, B. Khazin, I. Koop, P. Krokovny, A. Kuzmin, I. Logashenko, P. Lukin, A. Lysenko, K. Mikhailov, I. Nesterenko, V. Okhapkin, A. Pak, A. Polunin, A. Popov, B. Roberts, N. Root, A. Ruban, N. Ryskulov, A. Shamov, Y. Shatunov, B. Shwartz, A. Sibidanov, V. Sidorov, A. Skrinsky, I. Snopkov, E. Solodov, P. Stepanov, A. Sukhanov, J. Thompson, Y. Yudin, and S. Zverev, “Study of the process $e^+e^- \rightarrow K_S^0 K_L^0$ in the c.m. energy range 1.05–1.38 GeV with cmd-2,” *Physics Letters B*, vol. 551, p. 27–34, Jan. 2003.
- [53] M. N. Achasov, V. M. Aulchenko, S. E. Baru, K. I. Beloborodov, A. V. Berdyugin, A. V. Bozhenok, A. D. Bukin, D. A. Bukin, S. V. Burdin, T. V. Dimova, S. I. Dolinsky, V. P. Druzhinin, M. S. Dubrovin, D. I. Ganushin, I. A. Gaponenko, V. B. Golubev, V. N. Ivanchenko, P. M. Ivanov, I. A. Koop, A. A. Korol, M. S. Korostelev, S. V. Koshuba, A. P. Lysenko, A. A. Mamutkin, I. N. Nesterenko, A. V. Otboev, E. V. Pakhtusova, E. A. Perevedentsev, A. A. Polunin, E. E. Pyata, A. A. Salnikov, S. I. Serebnyakov, V. V. Shary, Y. M. Shatunov, V. A. Sidorov, Z. K. Silagadze, A. N. Skrinsky, Y. V. Usov, A. A. Valishev, A. V. Varganov, A. V. Vasiljev, and Y. S. Velikzhanin, “Experiments at vepp-2m with snd detector,” 1998.
- [54] F. Mane, D. Bisello, J. C. Bizot, J. Buon, A. Cordier, and B. Delcourt, “Study of the Reaction $e^+e^- \rightarrow K_S^0 K_L^0$ in the Total Energy Range 1.4-GeV to 2.18-GeV and Interpretation of the K^+ and K^0 Form-factors,” *Phys. Lett. B*, vol. 99, pp. 261–264, 1981.
- [55] P. m. Ivanov, L. m. Kurdadze, M. y. Lelchuk, E. v. Pakhtusova, V. a. Sidorov, A. n. Skrinsky, A. g. Chilingarov, Y. m. Shatunov, B. a. Shvarts, and S. i. Eidelman, “MEASUREMENTS OF THE FORM-FACTOR OF THE NEUTRAL KAON FROM 1.06-GEV TO 1.40-GEV,” *JETP Lett.*, vol. 36, pp. 112–115, 1982.
- [56] M. Atkinson *et al.*, “Photoproduction of $K\bar{K}\pi$ Final States in the Photon Energy Range From 20-GeV to 70-GeV,” *Nucl. Phys. B*, vol. 231, pp. 1–14, 1984.
- [57] G.-J. Ding and M.-L. Yan, “Y(2175): Distinguish Hybrid State from Higher Quarkonium,” *Phys. Lett. B*, vol. 657, pp. 49–54, 2007.
- [58] C.-Q. Pang, “Excited states of ϕ meson,” *Phys. Rev. D*, vol. 99, no. 7, p. 074015, 2019.
- [59] Z.-G. Wang, “Analysis of the Y(2175) as a tetraquark state with QCD sum rules,” *Nucl. Phys. A*, vol. 791, pp. 106–116, 2007.
- [60] G.-J. Ding and M.-L. Yan, “A Candidate for 1– strangeonium hybrid,” *Phys. Lett. B*, vol. 650, pp. 390–400, 2007.
- [61] L. Zhao, N. Li, S.-L. Zhu, and B.-S. Zou, “Meson-exchange model for the $\Lambda\bar{\Lambda}$ interaction,” *Phys. Rev. D*, vol. 87, no. 5, p. 054034, 2013.

- [62] L. Alvarez-Ruso, J. A. Oller, and J. M. Alarcon, “On the $\phi(1020)$ $f_0(980)$ S-wave scattering and the $Y(2175)$ resonance,” *Phys. Rev. D*, vol. 80, p. 054011, 2009.
- [63] M. Dugger *et al.*, “Design and construction of a high-energy photon polarimeter,” *Nucl. Instrum. Meth. A*, vol. 867, pp. 115–127, 2017.
- [64] I. Adam, R. Aleksan, L. Amerman, E. Antokhin, D. Aston, P. Bailly, C. Beigbeder, M. Benkebil, P. Besson, G. Bonneaud, P. Bourgeois, D. Breton, H. Briand, F. Brochard, D. Brown, A. Buzykaev, J. Chauveau, R. Cizeron, J. Cohen-Tanugi, M. Convery, S. Dardin, P. David, G. De Domenico, C. de la Vaissiere, A. de Lesquen, F. Dohou, M. Doser, S. Emery, S. Ferrag, G. Fouque, A. Gaidot, S. Ganzhur, F. Gastaldi, T. Geld, J.-F. Genat, P. Giraud, L. Gosset, P. Grenier, T. Haas, T. Hadig, D. Hale, G. Hamel de Monchenault, O. Hamon, B. Hartfiel, C. Hast, A. Hoecker, M. John, R. Kadel, J. Kadyk, M. Karolak, H. Kawahara, M. Krishnamurthy, H. Lacker, H. Lebbolo, F. Le Diberder, M. Legendre, P. Leruste, J. Libby, G. London, M. Long, J. Lory, A. Lu, A.-M. Lutz, G. Lynch, R. Malchow, J. Malcles, G. Mancinelli, M. McCulloch, D. McShurley, F. Martinez-Vidal, P. Matricon, B. Mayer, B. Meadows, S. Mikhailov, L. Mir, D. Muller, J.-M. Noppe, J. Ocariz, I. Ofte, A. Onuchin, D. Oshatz, G. Oxoby, T. Petersen, M. Pivk, S. Plaszczynski, W. Pope, M. Pripstein, J. Rasson, B. Ratcliff, R. Reif, C. Renard, L. Roos, E. Roussot, A. Salnikov, X. Sarazin, S. Schrenk, M.-H. Schune, J. Schwiening, S. Sen, V. Shelkov, M. Sokoloff, S. Spanier, H. Staengle, J. Stark, P. Stiles, R. Stone, J. Taylor, A. Telnov, G. Therin, C. Thiebaux, V. Tocut, K. Truong, M.-L. Turluer, A. Vallereau, G. Vasileiadis, G. Vasseur, J. Va’vra, M. Verderi, D. Warner, T. Weber, T. Weber, W. Wenzel, R. Wilson, G. Wormser, A. Yarritu, C. Yéche, S. Yellin, Q. Zeng, B. Zhang, and M. Zito, “The dirc particle identification system for the babar experiment,” *Nuclear Instruments and Methods in Physics Research Section A: Accelerators, Spectrometers, Detectors and Associated Equipment*, vol. 538, no. 1, pp. 281–357, 2005.
- [65] https://halldweb.jlab.org/DocDB/0041/004122/004/tagger_accidentals_doc.pdf. Accessed: 2023-17-07.
- [66] <https://halldweb.jlab.org/doc-private/DocDB/ShowDocument?docid=5338>. Accessed: 2023-17-07.
- [67] T. Sjöstrand, L. Lönnblad, and S. Mrenna, “Pythia 6.2 physics and manual,” 2001.
- [68] C. A. Meyer, “Coordinate systems in gluex.”
- [69] K. Schilling, P. Seyboth, and G. E. Wolf, “On the Analysis of Vector Meson Production by Polarized Photons,” *Nucl. Phys. B*, vol. 15, pp. 397–412, 1970. [Erratum: *Nucl.Phys.B* 18, 332 (1970)].
- [70] S. Adhikari *et al.*, “Measurement of spin-density matrix elements in $\rho(770)$ production with a linearly polarized photon beam at $E_\gamma=8.2\text{--}8.8$ GeV,” *Phys. Rev. C*, vol. 108, no. 5, p. 055204, 2023.

- [71] C. Meyer and A. Austregesilo, “Relationships between vector-meson s-dmes,”
- [72] M. Shepherd, “Amptools implementation of polarized production,”
- [73] S. M. Flatte, “Coupled - Channel Analysis of the π eta and K anti-K Systems Near K anti-K Threshold,” *Phys. Lett. B*, vol. 63, pp. 224–227, 1976.
- [74] C. A. Meyer, “The Flatte Parametrization of the $a_0(980)$,”
- [75] B. Kopf, M. Albrecht, H. Koch, M. Küßner, J. Pychy, X. Qin, and U. Wiedner, “Investigation of the lightest hybrid meson candidate with a coupled-channel analysis of $\bar{p}p$ -, π^-p - and $\pi\pi$ -data,” *The European Physical Journal C*, vol. 81, Dec. 2021.
- [76] A. Austregesilo, “Orientations of the Photon Beam Polarization from $\rho(770)$ Decay Asymmetries,”
- [77] R. Barlow, “Systematic errors: facts and fictions,” 2002.
- [78] M. Shepherd, “Amptools user guide,”
- [79] L. Ng, “PHOTOPRODUCTION OF THE $\eta\pi\pi^0$ SYSTEM OFF A PROTON TARGET AT $E_{\text{gamma}} = 8.5$ GEV,”
- [80] V. Mathieu, A. Pilloni, M. Albaladejo, L. Bibrzycki, A. Celentano, C. Fernández-Ramírez, and A. P. Szczepaniak, “Exclusive tensor meson photoproduction,” *Phys. Rev. D*, vol. 102, no. 1, p. 014003, 2020.

BIOGRAPHICAL SKETCH

Education

Doctor of Philosophy in Physics (2020-2024)

Florida State University

Dissertation: Photoproduction of $K^0\bar{K}^0$ with the GlueX Experiment

Advisor: Dr. Sean Dobbs

Master of Science in Physics (2017-2020)

Florida State University

Thesis: A Study of $\gamma p \rightarrow K_S^0 K_S^0 p$ With The GlueX Experiment

Advisor: Dr. Sean Dobbs

Bachelor of Science in Physics (2010-2017)

Universidad de Puerto Rico, Recinto de Río Piedras

Conferences

Two-Pseudoscalar Spectroscopy at GlueX (*Invited talk*)

2023 JLUO Annual Meeting · Indico

Jefferson Lab, Virginia, United States of America, June 26-28, 2023

Photoproduction of $K^0\bar{K}^0$ with the GlueX Experiment (*Talk*)

2022 Fall Meeting of the APS Division of Nuclear Physics

New Orleans, Louisiana, United States of America, October 27-30, 2022

A study of $\gamma p \rightarrow K_S K_S p$ with the GlueX Experiment (*Talk*)

88th Annual Meeting of the Southeastern Section of the American Physical Society

Tallahassee, Florida, United States of America, November 18-20, 2021

A Study of $\gamma p \rightarrow K_S K_S p$ with the GlueX Experiment (*Poster*)

2021 JLUO Annual Meeting

Jefferson Lab, Virginia, United States of America, June 21-23, 2021

Publications

(GlueX Collaboration) **Measurement of the J/ψ photoproduction cross section over the full near-threshold kinematic region**

Phys. Rev. C 108, 025201 · arXiv:2304.03845

(GlueX Collaboration) **Measurement of Spin-Density Matrix Elements in $\rho(770)$ Production with a Linearly Polarized Photon Beam at $E_\gamma=8.2-8.8\text{GeV}$**

Phys. Rev. C 108, 055204 · arXiv:2305.09047

(GlueX Collaboration) **Measurement of Spin Density Matrix Elements in $\Lambda(1520)$ Photoproduction at 8.2 GeV to 8.8 GeV**

Phys. Rev. C 105, 035201 · arXiv:2107.12314

(GlueX Collaboration) **Search for photoproduction of axion-like particles at GlueX**

Phys. Rev. D 105, 052007 · arXiv:2109.13439

(GlueX Collaboratino) **Measurement of beam asymmetry for $\pi^-\Delta^{++}$ photoproduction on the proton at $E_\gamma=8.5\text{ GeV}$**

Phys. Rev. C 103, L022201 · arXiv:2009.07326

Skills

Programming languages

C++ · Python · Bash

Software, Libraries and Frameworks

CERN ROOT	Extensively used throughout my graduate studies
AmpTools	Used for unbinned maximum likelihood fits
Swif2	Jefferson Lab framework for managing batch systems
HTCondor	Used for distributing jobs across multiple serves
L ^A T _E X	Preparation of technical documents (i.e. papers and presentations)
Open MPI	Used together with AmpTools to do complicated parallelized fits
Aptainer	A container platform designed to create and run containers optimized for HPC

Languages

Spanish (native) · English (fluent) · German (beginner)

Teaching

Thermal and Statistical Physics (Grader)	2023 Spring Semester
Classical Mechanics-II (Grader)	2022 Fall Semester
Physics-I Laboratory (Algebra based)	2019 Fall Semester
Physics-II Laboratory (Calculus based)	2019 Spring Semester
Physics-I Laboratory (Calculus based)	2018 Fall Semester